Professional Report 123

GEOLOGY OF KASATOCHI VOLCANO, ALEUTIAN ISLANDS, ALASKA

Christopher J. Nye, William E. Scott, Owen K. Neill,
Christopher F. Waythomas, Cheryl E. Cameron,
and Andrew T. Calvert

Published by
STATE OF ALASKA
DEPARTMENT OF NATURAL RESOURCES
DIVISION OF GEOLOGICAL & GEOPHYSICAL SURVEYS
2017

Front cover: Oblique aerial view of Kasatochi volcano; view is toward the north. Photograph by Roger Clifford, February 12, 2013.

GEOLOGY OF KASATOCHI VOLCANO, ALEUTIAN ISLANDS, ALASKA

Christopher J. Nye, William E. Scott, Owen K. Neill, Christopher F. Waythomas,
Cheryl E. Cameron, and Andrew T. Calvert

Professional Report 123

State of Alaska
Department of Natural Resources
Division of Geological & Geophysical Surveys

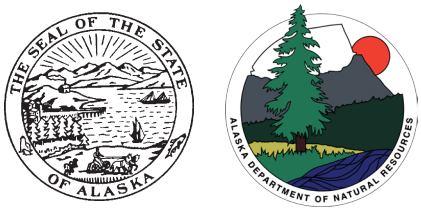

STATE OF ALASKA

Bill Walker, *Governor*

DEPARTMENT OF NATURAL RESOURCES

Andrew T. Mack, *Commissioner*

DIVISION OF GEOLOGICAL & GEOPHYSICAL SURVEYS

Steve Masterman, *State Geologist and Director*

Publications produced by the Division of Geological & Geophysical Surveys (DGGS) are available for download from the DGGS website (dggs.alaska.gov). Publications on hard-copy or digital media can be examined or purchased in the Fairbanks office:

Alaska Division of Geological & Geophysical Surveys
3354 College Rd., Fairbanks, Alaska 99709-3707
Phone: (907) 451-5010 Fax (907) 451-5050
dggspubs@alaska.gov
dggs.alaska.gov

Alaska State Library
Historical Collections &
Talking Book Center
395 Whittier Street
Juneau, Alaska 99811

Alaska Resource Library &
Information Services (ARLIS)
3150 C Street, Suite 100
Anchorage, Alaska 99503-3982

CONTENTS

Abstract **1**
Introduction **1**
Location 1
Previous Studies 2
2008 Eruption 2
Geologic Mapping 5
Base map 5
Geographic and map unit names and symbols 5
Fieldwork and data acquisition 6
Dynamic landscape 6
Description and Discussion of Map Features **6**
Crater lake minimum elevation contour 6
Gullies 7
Tension Cracks 8
Loafing Gull lake 8
Post-eruption Shorelines 8
Pre-eruption shoreline 9
Pre-eruption crater rim 9
Description and Discussion of Map Units **9**
Overview 9
Post Eruption 10
Beach deposits (Qb) 10
Lag beach deposits (Ql) 10
Back-beach deposits (Qm) 10
Alluvial fans (Qf) 10
Talus (Qt) 11
Slump (Qs) 12
2008 mass-flow deposits (Qd) 12
2008 eruption deposits 12
Pyroclastic deposits (Q8p) 12
Pyroclastic fans (Q8f) 14
Pre-Eruption 14
Luna pyroclastic deposits (Qlp) 14
Lava units 18
Monkeys Forehead basaltic andesite (Qmfm) 18
Tundering basaltic andesite (Qtm) 19
Mount Kasatochi andesite (Qmka) 20
Ogres Brow basaltic andesite (Qobm) 21
Rye basaltic andesite (Qrm) 21
Rye basalt (Qrb) 22
Whiskey andesite (Qwa) 22
Gregs Mighty basalt (Qgmb) 23
Peregrine lava (Qpl) 24
Peregrine glaciovolcanic deposits (Qpg) 24
Crater Wall 28
Colluvium (Qwc) 28
2008 pyroclastic deposits (Qw8) 28
Dikes (Qwd) 28
Fragmental volcanic deposits (Qwf) 29
Lava (Qwl) 29
Thin lava flows (Qwtf) 29

Lower crater wall deposits (Qwh) 29
Thin tephra (Qwp) 30
Petrography 30
Lavas and scoriae 30
Cumulate mafic and ultramafic inclusions 31
Mineral Compositions 32
Lavas and scoriae 32
Gabbroic inclusions 34
Geochemistry 35
Major element classification 35
Trace elements 36
Cumulate gabbroic and ultramafic inclusions 40
Gabbro control of magma chemistry 41
Summary 42
Acknowledgments 43
References 44

SHEETS

1. Geologic map of Kasatochi volcano; scale 1:5,000 pocket ..... pocket

TABLES

1. Changes in beach area and length measured from satellite images from immediately after the eruption, through February 2, 2012 9

FIGURES

1. Geography of the Aleutian Arc, showing location of Kasatochi volcano 2
2. Bathymetry of the Kasatochi region 3
3. Summary of geophysical data from the 2008 eruption 4
4. Views of the northwestern coast of Kasatochi before and after the 2008 eruption 5
5. Detailed views of gullies in 2008 eruption deposits 7
6. Photographs showing post-eruption formation and growth of Whiskey talus 11
7. Photographs showing formation of Monkey talus between 2009 and 2013 12
8. Examples of 2008 mass-flow deposits (map unit Qd) formed by the sloughing of the uppermost portion of 2008 eruption deposits 13
9. Height of 2008 deposits above the pre-eruption shoreline 15
10. Views of the southern coast of Kasatochi before and after the 2008 eruption 15
11. View of Luna pyroclastic deposits (Qlp) exposed in the southern crater wall 16
12. View of the western coast of Kasatochi, showing extent of Luna pyroclastic deposits prior to the 2008 eruption 17
13. Detailed pre-eruption view of Luna pyroclastic deposits on the western coast 17
14. View of the northern coast of Kasatochi, showing The Monkeys Forehead and nearby lava outcrops 19
15. Two views showing spatial relationship of Tundering basaltic andesite (Qtm) and mount Kasatochi andesite (Qmka) 20
16. View of the northwestern coast of Kasatochi, showing outcrops of Whiskey andesite (Qwa), Tundering basaltic andesite (Qtm), and Mount Kasatochi andesite (Qmka) 20
17. View of The Ogres Brow on the northeastern coast of Kasatochi 21
18. View of the eastern coast of Kasatochi, showing outcrops of Rye basalt (Qrb), Rye basaltic andesite (Qrm), Ogres Brow basaltic andesite (Qobm), and a 2008 pyroclastic fan(Q8f) 22
19. View of the north–northwestern coast, showing outcrops of Whiskey andesite (Qwa), Monkeys Forehead basaltic andesite (Qmfm), mount Kasatochi andesite (Qmka), and 2008 deposits 22

20. Photograph of Gregs Mighty rock 23
21. Pre-eruption photograph of the north–northeastern coast of Kasatochi, showing the extent of Gregs Mighty basalt (Qgmb) 24
22. View of the southwestern flank and coast of Kasatochi, showing the extent of Peregrine glaciovolcanic deposits (Qpg) and Peregrine lava (Qpl) 25
23. Photographs of Peregrine glaciovolcanic deposits (Qpg) at Shag rock 25
24. Outcrop photograph of a representative laharic debris flow in upper Peregrine glaciovolcanic deposits (Qpg) 26
25. Outcrop photograph, showing dike and folding and slumping of beds in upper Peregrine glaciovolcanic deposits (Qpg) 27
26. Aerial view of Kasatochi's eastern, northern, and lower western crater wall and the northern part of the crater lake 28
27. Photographs showing details of the northwestern crater wall 29
28. Photographs of the southeastern and southwestern crater wall 30
29. Modal analyses of Kasatochi samples 31
30. Hand-specimen photographs and a photomicrograph of amphibole gabbro inclusions from 2008 pyroclastic deposits 32
31. Summary of compositions of minerals in Kasatochi samples 33
32. Histograms of core and rim compositions of minerals in Kasatochi samples 34
33. Whole-rock SiO_2 of Kasatochi samples by unit 35
34. Plots of K_2O and FeO*/MgO vs. SiO_2 for Kasatochi samples and regional Aleutian Arc samples 36
35. Multi-element variation diagram of Kasatochi samples normalized to primitive mantle 37
36. Multi-element variation diagram, showing the range of basalt compositions and the relationship between basalts and more silicic samples 37
37. Selected silica variation diagrams of all Kasatochi samples 38
38. Multi-element variation diagrams by unit 39
39. Multi-element variation diagram showing lava and scoria compositions compared to gabbroic and ultramafic inclusions 40
40. Selected silica variation diagrams showing relationship of lava and scoria samples to gabbroic and ultramafic inclusions and calculated average phenocryst compositions 42

APPENDICES

1. Panoramic Photographs 46
A1.00. Approximate orientation and viewshed of panoramic coastal photographs 46
A1.01. Photograph of western part of north shore of Kasatochi 47
A1.01. Photograph of western part of north shore of Kasatochi 47
A1.02. Photograph of northwestern coast of Kasatochi between Tundering head and Barabara ridge 47
A1.03. Photograph of western coast of Kasatochi 48
A1.04. Photograph of western coast of Kasatochi from a few hundre meters south of where photograph in A1.03 was taken 48
A1.05. Photograph of northern part of southwestern coast of Kasatochi 48
A1.06. Photograph of southwestern coast of Kasatochi 49
A1.07. Photograph of southern coast of Kasatochi 49
A1.08. Photograph of south–southeast coast of Kasatochi 49
A1.09. Photograph of southeastern coast of Kasatochi 50
A1.10. Photograph of eastern coast of Kasatochi 50
A1.11. Photograph of northeastern coast of Kasatochi 51
A1.12. Photograph of north–northeast coast of Kasatochi 51
A1.13. Photograph of northern coast of Kasatochi 51

A1.50. Approximate orientation and viewshed of panoramic photographs of crater walls, taken from crater rim 52
A1.51. Panoramic photograph of northern, eastern, and southern crater walls, taken from crater rim immediately south of mount Kasatochi 53
A1.52. Panoramic photograph of southern and eastern crater walls, taken from southwest 53
A1.53. Panoramic photograph of western, northern, and eastern crater walls taken from Luna summit, on crater's south rim 54
A1.54. Panoramic photograph of western and northern crater walls, taken from southeast crater rim. 54
A1.55. Panoramic photograph of southern, western, and northern crater walls, taken from southeastern crater rim 54
Table A1. Full resolution copies of the panoramic images are in Electronic Supplement E1 55
2. Satellite images used in this study 56
3. Sample list and descriptions 57
A. Table A3a. Sample list and metadata 57
B. Table A3b. Sample descriptions 61
4. $^{40}Ar/^{39}Ar$ age data 73
A. Table A4a. $^{40}Ar/^{39}Ar$ ages 75
B. Age Spectra 76
C. Table A4b. $^{40}Ar/^{39}Ar$ tabulated data 81
5. Whole-rock compositions 86
A. Silica variation diagrams 86
Figure A5a.1. Silica variation diagrams of major oxides (wt%, normalized to 100%) and trace elements (ppm) 86
Figure A5a.2. Silica variation diagrams of all rare-earth elements (REE, ppm) 87
B. Enrichment spectrogram 88
Figure A5b. Enrichment spectogram 88
C. Precision 89
Table A5c.1. Summary of intra-duplicate variation and compositional range of AVO samples analyzed by Washington State University GeoAnalytical Laboratory between 2004 and 2016 89
Figure A5c.1. Variation between duplicate pellets vs. concentration for major elements (normalized to 100%) measured by XRF 91
Figure A5c.2. Variation between duplicate pellets vs. concentration for trace elements measured by XRF 92
Figure A5c.3. Variation between duplicate pellets vs. concentration for REE measured by ICP/MS 93
Figure A5c.4. Variation between duplicate pellets vs. concentration for trace elements other than REE measured ICP/MS 94
Figure A5c.5. Variations between duplicate pellets vs. concentration for trace elements measured by both XRF and ICP/MS 95
D. Data 96
6. Modal data 108
A. Methods and discussion 108
B. Mode summary by unit 108
7. Photomicrographs 109
A7.1. Plane-polarized photomicrographs of representative samples of 2008 scoria (Q8p) 109
A7.2. Plane-polarized photomicrographs of representative samples of amphibole gabbro inclusions in 2008 pyroclastic deposits (Q8g) 110
A7.3. Plane-polarized photomicrographs of representative samples of Luna pyroclastic deposits (Qlp). A7.4. Plane-polarized photomicrographs of samples of Tundering basaltic andesite (Qtm) and Monkey's Forehead basaltic andesite (Qmfm) 111

A7.4. Plane-polarized photomicrographs of samples of Tundering basaltic andesite (Qtm) and Monkeys Forehead basaltic andesite (Qmfm) 112
A7.5. Plane-polarized photomicrographs of samples of Mount Kasatochi andesite (Qmka), Ogres Brow basaltic andesite (Qobm), and a gabbroic inclusion in Ogres Brow basaltic andesite (Qobg) 113
A7.6. Plane-polarized photomicrographs of samples of Rye basaltic andesite (Qrm), Rye basalt (Qrb), and Gregs Mighty basalt (Qgmb) 114
A7.7. Plane-polarized photomicrographs of samples of Whiskey andesite (Qwa) 115
A7.8. Plane-polarized photomicrographs of juvenile clasts in Peregrine glaciovolcanic deposits (Qpg) and Peregrine lava (Qpl) samples 116
A7.9. Plane-polarized photomicrographs of lithic clasts in 2008 pyroclastic deposits derived from pre-existing portions of the volcanic edifice 117
8. Mineral compositions 118
A. Data summary 118
Table A8. Numbers of points, analyzed by sample and phase 118
B. Plot of Compositions 119
Figure A8. Mineral analyses by sample and rank 119
C. Analytical details 120
D. Microprobe data 123
9. Componetry of 2008 pyroclastic deposits 123
A. Lithologic components 124
Table A9a. Clast counts from composite stratigraphic sections through units 2 and 3 of 2008 pyroclastic deposits 124
B. Clast-size distribution 126
Table A9b. Particle-size distribution of samples from 2008 units 2 and 3 pyroclastic deposits 126
C. Density of juvenile scoria 127
Table A9c. Clast density measured after Houghton and Wilson (1989), using clasts from the -4 phi (16–32mm) size fraction, wrapped in parafilm 127

ELECTRONIC SUPPLEMENT

Electronic data files available at http://doi.org/10.14509/29718 include sample metadata and major and trace element XRF and ICP/MS data also included in the appendices; electron microprobe mineral analyses which are discussed in the report, but not tabulated elsewhere; and high resolution versions of panoramic photographs (appendix 1) and photomicrographs (appendix 7).

GEOLOGY OF KASATOCHI VOLCANO, ALEUTIAN ISLANDS, ALASKA

Christopher J. Nye[1], William E. Scott[2], Owen K. Neill[3,4], Christopher F. Waythomas[5], Cheryl E. Cameron[1], and Andrew T. Calvert[6]

Abstract

Kasatochi is a small, isolated island volcano in the center of the Aleutian Island chain. It consists of a roughly circular cone ~3 km in diameter with a lake-filled central crater that is 1.2 km in diameter and extends from the highest point on the island to sea level. The oldest unit recognized is a thick series of mid-Pleistocene glaciovolcanic deposits consisting of autobrecciated lava, lahars, and volumetrically minor lava masses that we believe to have been emplaced underneath a regional ice cap. This unit is unconformably overlain by several massive Holocene lavas, above which lies a thick sequence of latest-Holocene pyroclastic deposits likely deposited during the crater-forming eruption. The 2008 eruption enlarged the preexisting crater, and produced pyroclastic density currents, surges, and fall that blanketed the entire island except for the crater wall and steep, seaward-facing cliffs on the flanks. 2008 deposits initially extended the shoreline seaward by up to 500 m.

Kasatochi lava and scoria are porphyritic basalt, basaltic andesite, and andesite, all of which bear trace-element evidence for prolonged crustal residence and equilibration with an amphibole-rich gabbroic residue. Lavas from individual effusive eruptions have limited compositional range, whereas juvenile scoriae from explosive eruptions span the majority of the compositional range of the entire volcano. 2008 pyroclastic deposits contain texturally diverse amphibole gabbro clasts and smaller, less abundant, plagioclase-free pyroxenitic and peridotitic cumulate inclusions. We infer that the gabbroic inclusions are from the margins of regions of crustal magma storage and evolution and that equilibration with the amphibole plays an important role in the evolution of mafic and intermediate magmas.

INTRODUCTION

Kasatochi volcano is located at the intersection of the flat, shallow Aleutian platform and the Bering slope rise, an area of high biologic productivity. As a result, the island hosts a large sea lion colony and nesting sites for hundreds of thousands of seabirds. A large eruption in 2008 blanketed the island in pyroclastic deposits, covering nesting sites and almost all existing vegetation. A multidisciplinary effort to document recovery of the ecosystem was initiated, and this study of the geology of the island was undertaken as part of that effort.

LOCATION

The subaerial portion of Kasatochi volcano comprises the entirety of Kasatochi Island, an isolated 6.5 km^2 island in the center of the Andreanof Island region of the Aleutian Islands, 19 km north of the western tip of Atka Island, its closest neighboring island. From west to east, Kasatochi is about a quarter of the way along the Aleutian Arc, a chain of subduction-zone volcanoes that lie along the Aleutian Islands and the Alaska Peninsula and extend into central Alaska (fig. 1). Volcanoes in the eastern half of the arc sit on continental crust of the North American plate. Volcanoes in the western half sit on the summit platform of the Aleutian Ridge, a roughly 100-km-wide welt built on oceanic crust since the middle of the Eocene by subduction-zone magmatism and erosion and redeposition of primary igneous rocks. The Aleutian Ridge abruptly rises about 3,500 m above the Bering Sea floor to the north, 5,000 m above the Pacific Ocean floor to the south, and 7,000 m above the Aleutian Trench, which marks the location of subduction. The Aleutian Ridge has steep flanks on both the Bering Sea and Pacific Ocean sides, and a broad, low-relief summit platform formed by subaerial erosion since mid-Eocene time (for example, Scholl and others, 1975). Measured along the Bering–Pacific divide, fifty percent of the Aleutian Ridge is subaerial, and twenty-seven percent is less than 130 m below sea level (bsl). The portion of the ridge between sea level and 130 m bsl was likely emergent during low Pleistocene sea levels. The remaining twenty-three percent of the Aleutian Ridge is cut by passes up to 75 km wide and a few hundred meters to 1,100 m deep.

Kasatochi is on a portion of the Aleutian summit platform that is about 340 km long and has a total area above 130 m bsl of about 11,600 km^2. Kasatochi itself sits on a spur protruding from the northern side of the summit platform (fig. 2), directly above the rise of the Bering slope. The island sits at the northern tip of the spur, and at the northern edge of a gently sloping, low-relief platform that extends from sea level to about 50 m bsl with a slope of about one degree. Below the 50 m isobath the western, northern, and eastern margins of the spur abruptly steepen to a slope of about ten degrees, parallel to the slope between the Aleutian Ridge and the Bering Sea floor. South of Kasatochi the spur feathers into the Aleutian platform. The 50 m isobath—presumably the approximate base of the volcano—encloses about 60 km^2, nearly ten times the area of the island.

The position of Kasatochi at the break in slope between the summit platform and ridge flank is important biologically because upwelling along the ridge dramatically increases productivity, providing abundant food for nesting seabirds and

[1] Alaska Volcano Observatory, Alaska Division of Geological & Geophysical Surveys, 3354 College Road, Fairbanks, Alaska 99709-3707
[2] Cascades Volcano Observatory, U.S. Geological Survey, 1300 SE Cardinal Court, Vancouver, Washington 98683
[3] University of Alaska Fairbanks, Geophysical Institute, 903 N Koyukuk Drive, Fairbanks, Alaska 99775
[4] Peter Hooper GeoAnalytical Lab, School of the Environment, 1228 Webster Physical Science Building, Washington State University, Pullman, Washington 99164
[5] Volcano Science Center- Alaska Volcano Observatory, U.S. Geological Survey, 4210 University Drive, Anchorage, Alaska 99508
[6] Volcano Science Center, U.S. Geological Survey, 345 Middlefield Road, Menlo Park, California 94025

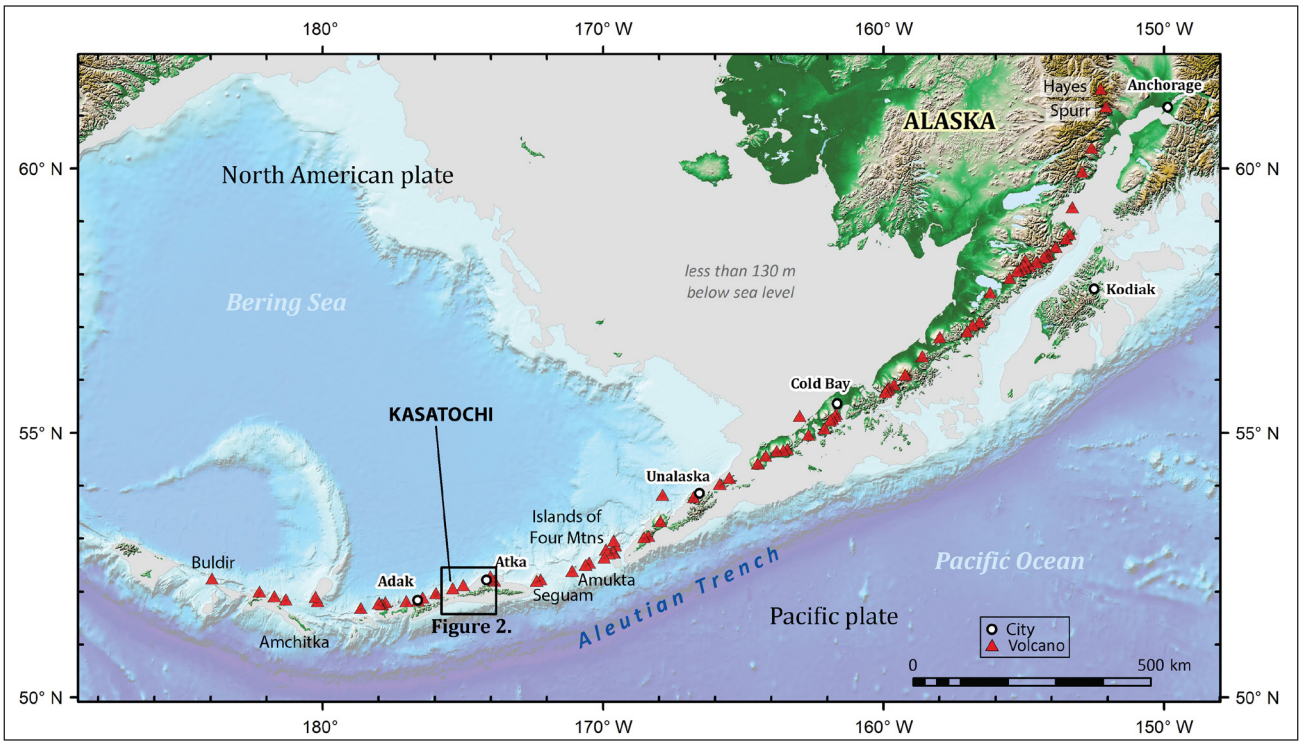

Figure 1. Geography of the Aleutian Arc. Red triangles denote subaerial volcanoes or volcanic centers, from Buldir (farthest west) to Hayes (farthest north) and Spurr (farthest east). The portion of the continental shelf and Aleutian ridge between sea level and 130 m bsl, which was likely emergent during low Pleistocene sea levels, is shown in gray (data from Lim and others, 2011). Projection is The ARC System (Equal Arc-Second Raster Chart/Map System), Zone 4, central meridian 165°W, standard parallel 58°N. (Higher-resolution [600 dpi] versions of all figures are in electronic supplement E10.)

resident sea lions (for example, DeGange and others, 2010). The position of Kasatochi on a large, areally extensive portion of the summit platform, which was likely emergent during low Pleistocene sea levels and thus could have supported an ice cap, is important to our interpretation that the basal unit was erupted subglacially.

PREVIOUS STUDIES

Previous geologic studies at Kasatochi are sparse. A program of systematic mapping of the geology of the majority of Aleutian Islands was undertaken by the U.S. Geological Survey (USGS) in the 1940s and 1950s, resulting in the 1028-series of USGS Bulletins. As part of this program, Robert Coats led geologic reconnaissance in the western Aleutian Islands (Coats, 1956). Coats identified Kasatochi as a recent volcanic island, but its stratigraphy was not subdivided beyond "Late Tertiary and Quaternary basaltic rocks", and the island was only described in a few passing sentences. The next pulse of geologic study of Aleutian volcanoes was in the 1970s and 1980s. This work was aimed at sampling and analyzing the chemistry of Aleutian lavas, and using those data to understand magma genesis and evolution. During this work Robert Kay made one visit to Kasatochi and published the analysis of one sample (Kay and Kay, 1985, 1994). The location of Kay's sample is not given, but it is a close match to the basalt unit on Kasatochi's northeast coast that we map as Gregs Mighty basalt (Qgmb). The next geologic visit was in 2005. Prompted by effervescence and roiling noted in the crater lake by U.S. Fish and Wildlife Service (USFWS) biologists, Christina Neal (USGS, Alaska Volcano Observatory [AVO]) made a one-day, helicopter-supported visit. She recognized, among other features, the widespread geologically young pyroclastic deposits that revealed the volcano's recent explosive history. The present study is the first attempt to systematically define, map, sample, and describe all geologic units.

While geologic work at Kasatochi has been minimal, biologic work has not. Kasatochi is one of nine ecological monitoring sites in the Alaska Maritime National Wildlife Refuge. Starting in 1996, USFWS biologists have conducted annual intensive summer-season fieldwork there, aimed primarily at collecting baseline data and identifying trends in seabird populations. Prior to 1996, USFWS conducted episodic investigations, notably during the 1980s eradication of non-native foxes, which had been introduced by 1927 (for example, Drummond and Larned, 2007; Buchheit and Ford, 2008). USFWS biologists prompted the 2005 AVO field visit and first reported emerging seismic unrest immediately prior to the 2008 eruption.

2008 ERUPTION

Scott and others (2010) and Waythomas and others (2010b) provide detailed descriptions of the 2008 eruption of Kasatochi, which are summarized below. Prior to 2008, Kasatochi had not had a confirmed magmatic eruption in the 250-year span of historic time. However, anecdotal reports from the 18th and 19th centuries suggest that there may have been episodic elevated fumarolic activity (Grewingk, 1850; Coats, 1956). The only report of 20th-century unrest is from USFWS observers, who reported "increased steaming" in 1996 at Kasatochi (as well as Gareloi, 230 km to the west) following a M 6.0 regional earthquake (Neal and McGimsey, 1997). In 2005, USFWS observers noticed bubbling in the crater lake for the first time. The onset of bubbling is bracketed between June 23 and July 27 observations of the lake from the crater rim. There

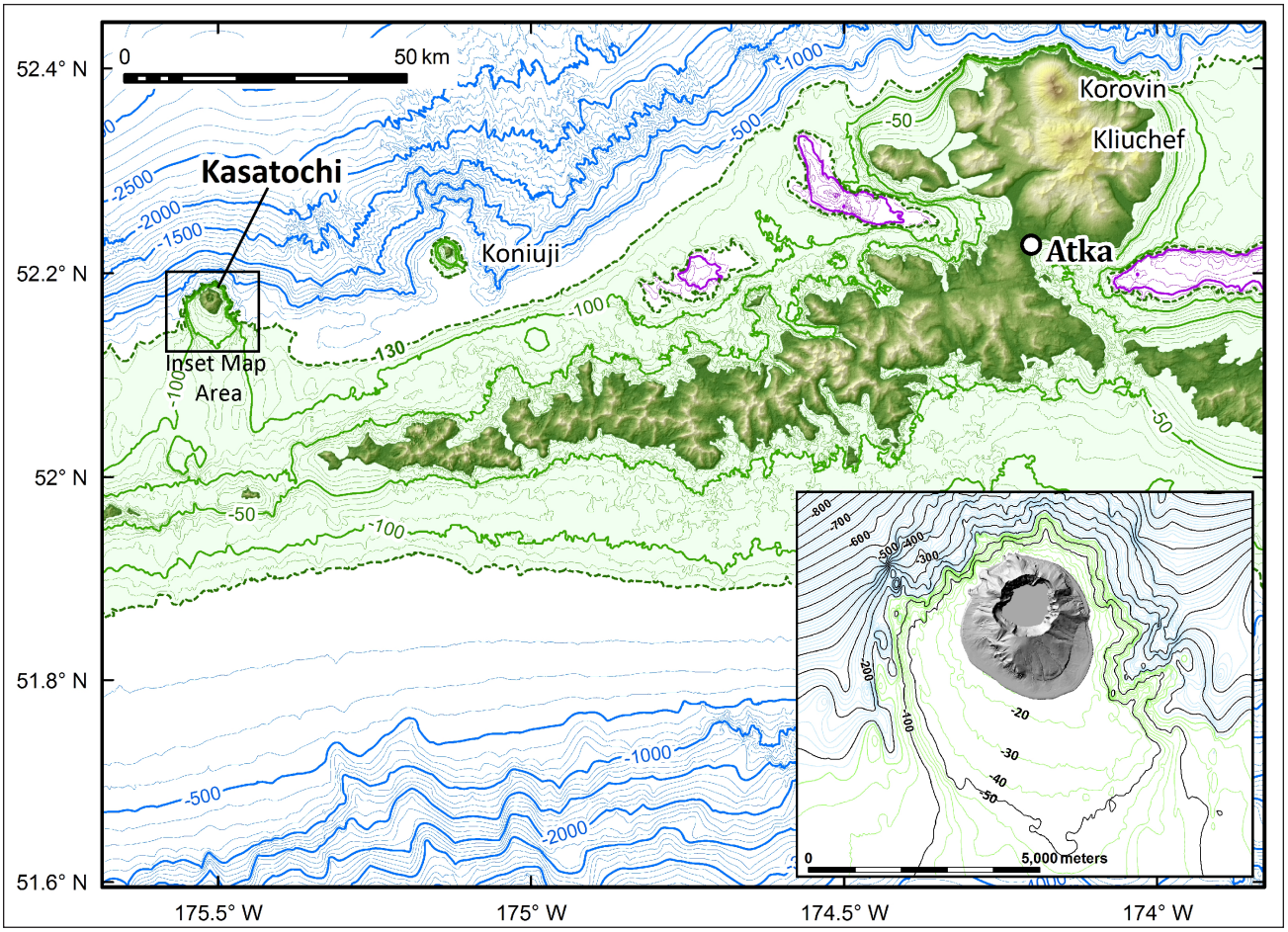

Figure 2. Geography of Atka Island and surrounding area, including Kasatochi. All contours are in meters. The area below 130 m bsl has blue 100 m contours; the area between sea level and 130 m bsl is shaded green with 10 m contours. Shaded-relief topography is based on ASTER DEM data (http://reverb.echo.nasa.gov/reverb). Enclosed basins in the Aleutian platform deeper than 130 m bsl are shown with 10 m purple contours; these basins have floors 40–60 m below the surrounding topography. Bathymetric data from Friday and others, 2011. The inset map shows detailed bathymetry near Kasatochi. Pre-eruption ocean depths from sea level to 130 m are shown in 10 m green contours; depths below 130 m are shown in blue 10 m contours; black contours are at 50 m intervals. The post-eruption Kasatochi shaded-relief image is from this study, and sea level in the image overlies most of the pre-eruption-10 m isobath.

was no apparent steam or odor and no associated felt seismicity. Bubbling was concentrated in the western half of the lake and was also noted in the same general location in 2006. It is likely that the bubbling resulted from increased fumarolic flux at the lake bottom, and that the bubbles contained gases with limited solubility in the lake water, such as CO_2, rather than high-temperature, water-rich steam. USFWS biologists at the Kasatochi field camp began feeling repetitive earthquakes on August 2, 2008. This was the earliest notice of pre-eruptive seismicity, although retrospective analysis by the Alaska Earthquake Information Center (AEIC; now Alaska Earthquake Center) showed that pre-eruptive seismicity had begun by early July 2008 (Ruppert and others, 2011).

The rate of earthquakes felt by the USFWS crew increased to 2–3 events every 5 minutes by August 6, and by the end of the day of August 6 earthquake magnitudes had increased to as large as M 4. On August 6 USFWS scientists also observed multiple rockfalls and small avalanches from diverse locations on the crater wall and rim. Such rockfalls were previously uncommon and isolated; however, the August 6 rockfalls were likely a direct result of seismic shaking. In addition to documenting the rockfalls, the scientists noted discolored plumes in the lake, separated on all sides from the lakeshore and thus likely not generated by rockfall. These events may represent entrainment of lake-bottom mud by increasingly vigorous lake-bottom fumaroles. The USFWS crew was evacuated from the island about noon on August 7, shortly before the eruption's onset.

The record of pre-eruptive unrest from instrumental measurements is different from the intimate record provided by USFWS scientists, largely because the seismometers closest to Kasatochi were ~40 km to the west and ~85 km to the east, so small earthquakes such as those felt by USFWS personnel starting August 2 were not detectable because of seismic wave attenuation. Additionally, all seismometers in the region are roughly collinear, so earthquake source locations determined by triangulation are poorly constrained. AEIC detected M 1–2 earthquakes near Kasatochi as early as July 8, with a cluster of events around July 24. At the time, these early earthquakes did not seem substantially different than the diffuse tectonic seismicity common along the arc—it was only retrospectively that they were understood to be precursors. In part, they were not recognized as being related to Kasatochi because of ambiguous locations. On August 6, the pre-eruptive swarm bloomed (fig. 3); seismicity prior to August 6 ultimately amounted to only 4 percent of the earthquakes and released 0.006 percent of the energy associated with the eruption. The very thin resorption

rims on amphibole phenocrysts in 2008 magma, and the rapidity at which those rims form once amphibole is below the P and pH_2O of its stability, suggest that the onset of the main swarm and the beginning of magma transport to the surface coincide.

During the 18 hours after the main swarm onset, both the earthquake rate and the rate of seismic energy release increased dramatically. M 3+ and M 4+ earthquakes became commonplace, and seismic energy release increased from 10^7 to 10^{11} joules/hour. The rate of seismic energy release began to decrease early on August 7, but was punctuated by a single M 5.8 earthquake, the largest of the entire swarm, at about 10:30 (times based on 24-hour clock). Episodes of volcanic tremor were recorded starting about 45 minutes and 2.7 hours after the M 5.8 earthquake (earlier tremor may have existed, but their seismic signals would have been masked by attenuation or overlapping earthquakes).

At 14:23 on August 7, 34 hours after the start of the main seismic swarm, weather satellites detected the first eruption plume, at least the top of which was ash poor and reached an altitude of 14 km. This plume corresponds to peaks in seismic and infrasound energy. A second explosion 3.6 hours later produced another plume, also ash poor and also corresponding to seismic and infrasound energy peaks. After a 2.7-hour hiatus the third and last major eruptive phase began. The opening of

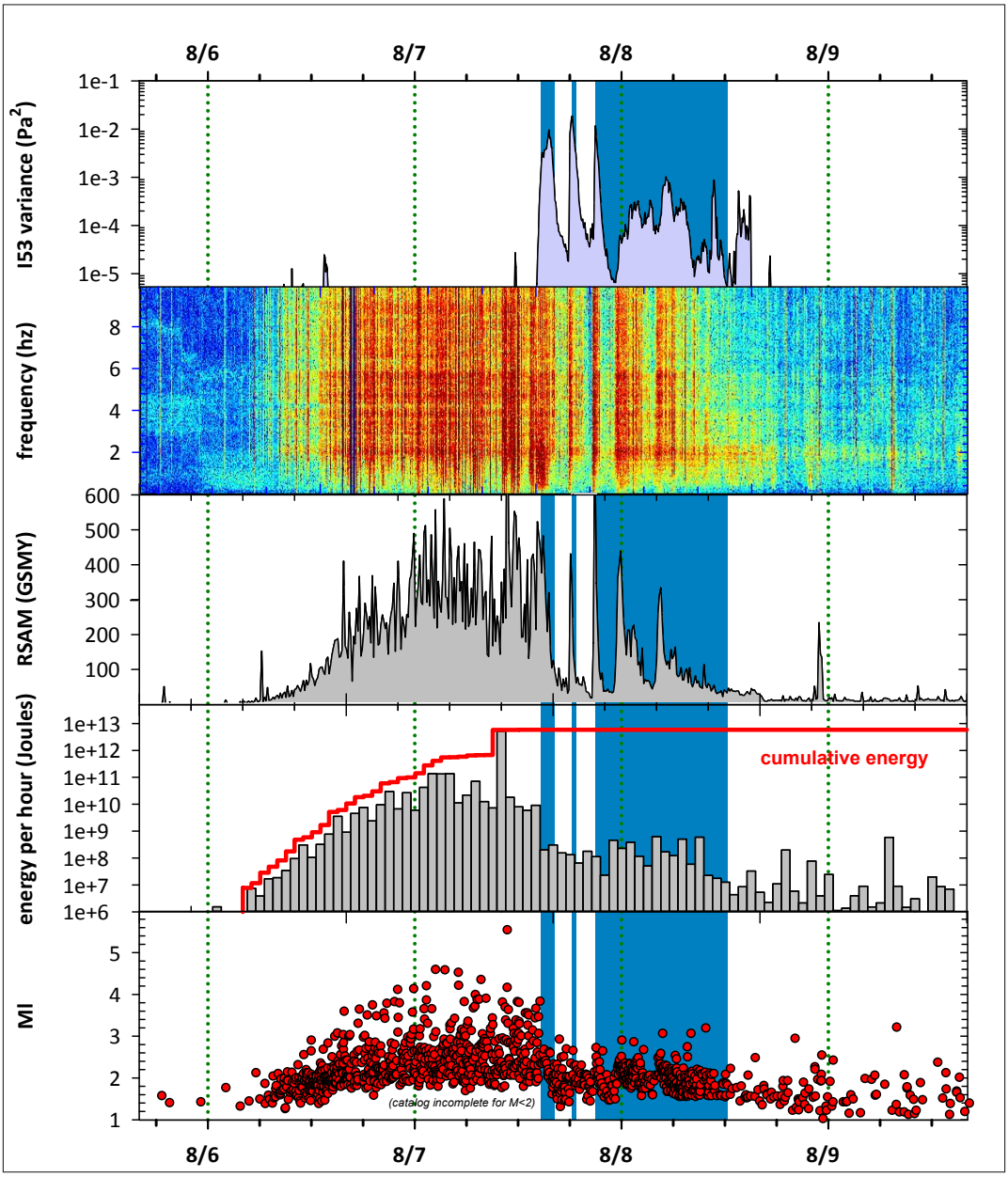

Figure 3. Summary of geophysical data from the 2008 Kasatochi eruption. The eruption had rapid onset, the highest-energy earthquakes of any recorded Alaska eruption since the Novarupta eruption of 1912, and broadband seismicity during major explosive episodes, which contrasts strongly with typical Alaska eruptions, which have had more monotonic low-frequency seismicity. Earthquake data are from the Alaska Earthquake Center (see Ruppert and others, 2011). Real-time seismic amplitude (RSAM) data are from the Alaska Volcano Observatory (AVO) and were recorded at Great Sitkin seismic station GSMY. The seismic frequency spectrogram was prepared by Glenn Thompson (AVO, unpublished). Infrasound data were recorded at station I53 (Fairbanks, Alaska; Arnoult and others, 2010). Eruption plume production (Waythomas and others, 2010b) is shown by blue bars extending behind all panels. Note that times are given in Alaska daylight time (AKDT), which is one hour earlier than local Hawaii–Aleutian daylight time (HADT).

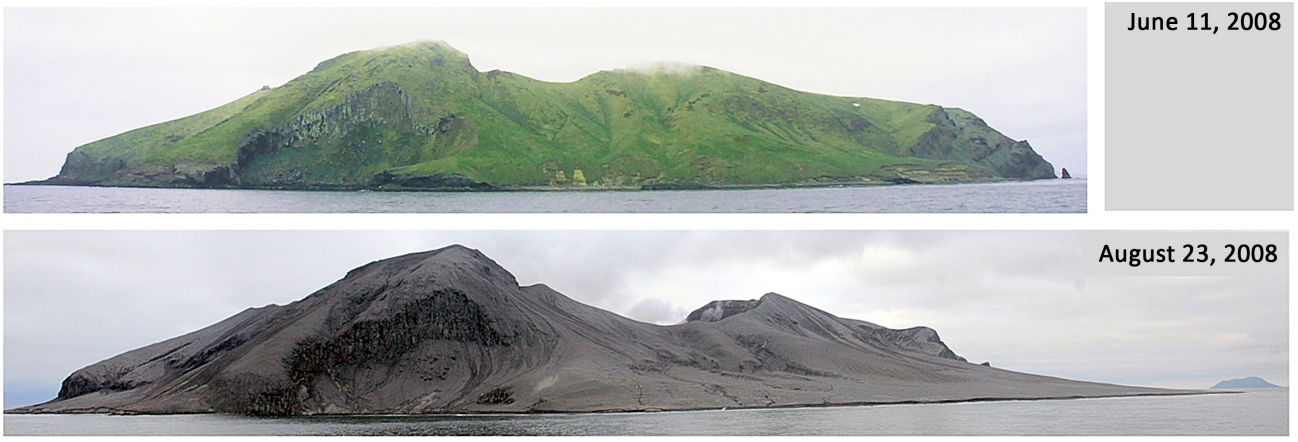

Figure 4. Photographs of the northwestern coast of Kasatochi two months prior and two weeks after the 2008 eruption. Note the complete burial of vegetation, the fans of pyroclastic debris that extend the shoreline outward, and the dramatic lowering of the crater rim. Photographs by J. Williams, USFWS.

the third phase was marked by sharp seismic and infrasound peaks, similar to the two previous plume-producing events, but unlike the previous two plumes, this plume was ash-rich and eruption was continuous for 16 hours. The continuous phase contained two seismic pulses that did not noticeably affect the plume as observed by satellite and had a variable but continuous infrasound signal.

By the close of the eruption, which seismic, satellite, and infrasound data indicate was some 62 hours from the onset of the main precursory seismic swarm and 28 hours from the first ash-poor eruption plume, the island was radically transformed (fig. 4). The area of the island had been increased by nearly 40 percent by fans of pyroclastic debris shed into the ocean; the area enclosed by the crater rim had increased by nearly 30 percent, chiefly by erosion of the western crater wall and incorporation of the resulting lithic blocks and fragments into the pyroclastic deposits; and the area of the crater floor had increased by nearly 70 percent. The formerly lush maritime tundra, which had been composed mainly of forbs, graminoids, mosses, and lichens, was covered in unconsolidated pyroclastic deposits many centimeters to many tens of meters thick—only largely unvegetated outward-facing cliffs were left uncovered. Passerines, gulls, eagles, and falcons were displaced or killed, unfledged seabirds (mostly fork-tailed storm petrels at this time of year) were killed in their burrows, and sea lions were pushed off their haul-outs, although only briefly (Williams and others, 2010). Surprisingly, the pyroclastic flows were only minimally destructive to preexisting vegetation despite the extreme proximity to the vent and the high magmatic temperature (~900–1,000°C). While preexisting vegetation was buried, it was generally not charred, and generally not ripped out of place. When subsequent erosion and gullying exposed the pre-eruption sod, the vegetation generally sprouted in the spring and grew through the summer.

The 2008 eruption of Kasatochi volcano had a rapid onset and was short-lived, but by many measures was exceptionally large, especially compared to other eruptions in the Aleutian Arc since the (much larger) 1912 Katmai eruption. The total energy released by earthquakes, not including energy released by explosions, exceeded that of any eruption monitored by AVO in prior decades by several orders of magnitude. Even the hourly seismic energy release dwarfed the total months-long seismicity preceding the 2009 Redoubt eruption and the 2005–2006 Augustine eruption by more than three orders of magnitude. The eruption cloud contained more than 1 Tg (teragram) of SO_2, the largest of any eruption worldwide since that of Chile's Mount Hudson in 1991 (for example, Corradini and others, 2010; Prata and others, 2010; total erupted SO_2 is a proxy for magma volume). The eruption cloud circled the globe, causing vivid sunsets as far downwind as the mid-western United States and Iceland. Finally, the infrasound signal was exceptionally energetic and was detected more than 5,000 km away (Fee and others, 2010).

GEOLOGIC MAPPING

Base map

The morphology of Kasatochi Island was radically changed by the 2008 eruption, rendering all preexisting basemaps obsolete. The basemap for this study was derived from a stereo pair of 58-cm-resolution WorldView1 satellite images taken April 18, 2009. The images were orthorectified and a two-meter horizontal resolution digital elevation model (DEM) was produced and then adjusted to Kasatochi mean sea level. The topographic base for the current map was derived from the DEM.

A small steam cloud in the images precludes any meaningful depiction of topography along the southeastern crater wall—contours are not shown in this region. Additionally, in the many areas of near-vertical topography parallax issues are not completely resolved, and the orthorectified satellite images deviate from the DEM produced from those images by as much as tens of meters. In these areas topography was favored over imagery as a guide to placing unit contacts and other geologic data. In areas of moderate to low slope, which constitute the majority of the island, coincidence of satellite images and topography is within a few meters.

Geographic and map unit names and symbols

Kasatochi Island is the only formally named geographic feature in the map area. This report uses informal geographic names from, or derived from, common and longstanding usage by USFWS scientists for geographic reference. Even though informal, we capitalize the names except for the parts of the names denoting a type of geographic feature (such as mount, point, ridge, cove, etc.). The geographic names are used throughout this report for spatial reference, and are shown on sheet 1.

All map units are informal stratigraphic units. Volcanic unit names combine geographic (capitalized) and compositional

attributes (not capitalized) except for 2008 eruption deposits, which include "2008" in the names and "8" in unit symbols.

We refer to the geographic feature that underlies the highest elevation on the island as mount Kasatochi, and the stratigraphic unit named for that feature Mount Kasatochi andesite.

Map-unit symbols all have an initial "Q" indicating Quaternary age. Unconsolidated, non-volcanic units have a single lower-case letter following "Q" indicating general lithology or depositional environment. Volcanic units on the flanks, some of which extend to the uppermost crater wall, have one or two lower-case letters following the "Q" derived from geographic features and a final letter indicating either average chemical composition or lithology. Meanings of the final letter of map unit symbols are:

Non-volcanic units:

b	beach deposits
l	beach-lag deposits
m	back-beach deposits
t	talus
s	slump deposits
d	mass-flow deposits

Volcanic units:

b	basalt (<53% SiO_2)
m	basaltic andesite (53-57% SiO_2)
a	andesite (57-63% SiO_2)
p	pyroclastic density current and rare fall deposits
f	thick fans of pyroclastic deposits
g	glaciovolcanic deposits

Units exposed exclusively in the crater wall have symbols starting with "Qw", followed by one or two letters indicating gross lithology. Samples of 2008 ejecta are subdivided in some geochemical figures, and those symbols are explained on the figures or in the figure captions. Subdivisions of 2008 samples are not shown on the map.

Fieldwork and data acquisition

Geologic field mapping and sampling were conducted during short trips on 18 days—nominally 2 to 3 days in mid-June and mid- to late-August—from 2009 through 2013. Fieldwork was supported by the USFWS using the *M/V Tiĝlax̂*. Dates and amount of fieldwork were constrained by the schedule of the *Tiĝlax̂*, which travels over 15,000 miles each field season supporting more than 130 scientists at more than 50 locations. Eruption response fieldwork at Kasatochi was multidisciplinary: the June dates coincided with auklet nesting and the August dates coincided with maximum seasonal vegetation growth and storm petrel nesting. One advantage of short periods of geologic fieldwork conducted over several years is that we could monitor the rapid post-eruption morphological changes to the shoreline and the extensive gully network.

More than 110 rock samples were collected during the course of mapping. One hundred one of these samples were analyzed for major and trace elements by the Peter Hooper GeoAnalytical Lab at Washington State University. Detailed petrographic descriptions and 1,000-point modes were made using thin sections of 67 of the samples. Electron probe microanalysis (EPMA) at the Advanced Instrumentation Laboratory at the University of Alaska Fairbanks produced 3,364 mineral analyses, including core-rim pairs from 1,385 grains, from 24 representative samples, spanning all lithologic units. In addition, $^{40}Ar/^{39}Ar$ ages were obtained for three samples by the USGS, Menlo Park, California. Sample descriptions and analytical data are in the appendices of this report.

Dynamic landscape

The 2008 eruption changed Kasatochi Island dramatically (fig. 4; Waythomas and others, 2010a,b; Scott and others, 2010). The island increased by 40 percent in total area by deposition of eruption deposits beyond the pre-eruptive shoreline; the area enclosed by the crater rim grew by nearly 30 percent by the explosive removal of tens of millions of cubic meters of older volcanics; and the island was blanketed with millions of cubic meters of unconsolidated volcanic deposits. The island is responding very quickly to the new load of nearshore and shallow marine sediment, and is rapidly shedding 2008 deposits from its flanks.

As a result, the map presented here shows the island at a moment in time—April 18, 2009—when the only stereo pair of satellite images was obtained. The stereo images permit the construction of a digital elevation model and contour map; however, in the few years since those images were acquired there have been significant geomorphic changes to the shoreline, gully system, and even to the exposure of lithologic units that underlie the 2008 deposits.

As a result of ongoing changes some features of this map are already obsolete: the coastline is inaccurate, some sample locations are now offshore, and other sample locations were covered in 2009, but uncovered and sampled subsequently. We note post-map-base changes in the text. Statements about the geology of the island in the present tense should, unless otherwise noted, be understood to carry the caveat "as of April 18, 2009."

Appendix 1 contains high-resolution panoramic photographs of the island flanks taken from offshore, and of the crater wall taken from the rim. These are intended to augment the figures and serve as reference photographs for use by scientists in the future.

DESCRIPTION AND DISCUSSION OF MAP FEATURES

CRATER LAKE MINIMUM ELEVATION CONTOUR

At the time the base images for this map were acquired (April 18, 2009, 8.3 months post-eruption), the surface elevation of the crater lake was 10.8 m below local mean sea level (bsl) (see map metadata for description of the map datum). Field observations by AVO and USFWS personnel two weeks after the eruption showed a small, slate-gray lake in the crater surrounded by a wide, gently sloped shore, which was likely at or near the bottom of the pre-eruption lake, as well as a small island toward the center of the lake. The island, which was not seen in any subsequent imagery, may have been part of a slightly irregular lake bottom, and thus provided some sense that the lake was very shallow. Field investigators also noted a spring below the 2009 crater lake level (10.8 m bsl) that was feeding water into the crater. Excessive steam in the crater during the field visit precluded obtaining photographs that would allow accurate estimation of the lake height by comparison to the 2009 DEM. Oblique photographs taken from a commercial flight on September 8, 2008 (B. Mees, AVO image database), show a portion of the north crater wall with some recognizable features. These images, compared with 2009 imagery and the

DEM, suggest the lake may have risen about 10 m between the eruption and April 2009, and thus that the lake bottom is about 21 m bsl.

GULLIES

A robust system of gullies dissects the 2008 deposits (sheet 1; fig. 5). Sheet 1 shows minor gullies (1–5 m wide at their top) and major gullies (greater than 5 m wide). Gullies less than 1 m wide were not mapped because they could not be uniformly identified on the base imagery. The map shows 173 km of minor and 12 km of major gullies cutting the 3.9 km^2 of the volcano's flanks mantled by 2008 deposits. The gullies shown have an average lateral spacing of about 25 m; the actual lateral spacing ranges from meters to tens of meters on individual surfaces. We estimate that about 10 percent of the surface area of 2008 deposits was gullied within 9 months of the eruption.

The gullies developed early and rapidly. The first field visit (September 22; two weeks after the eruption) found fine-scale dendritic gullies at high elevations; straight, branching gullies; and well-established larger gullies at lower elevations. Once gullies were established they deepened in place but did not migrate laterally over time by more than a few meters.

Gullies are the most important agent for delivering sand, gravel, and boulders derived from 2008 deposits to tidewater.

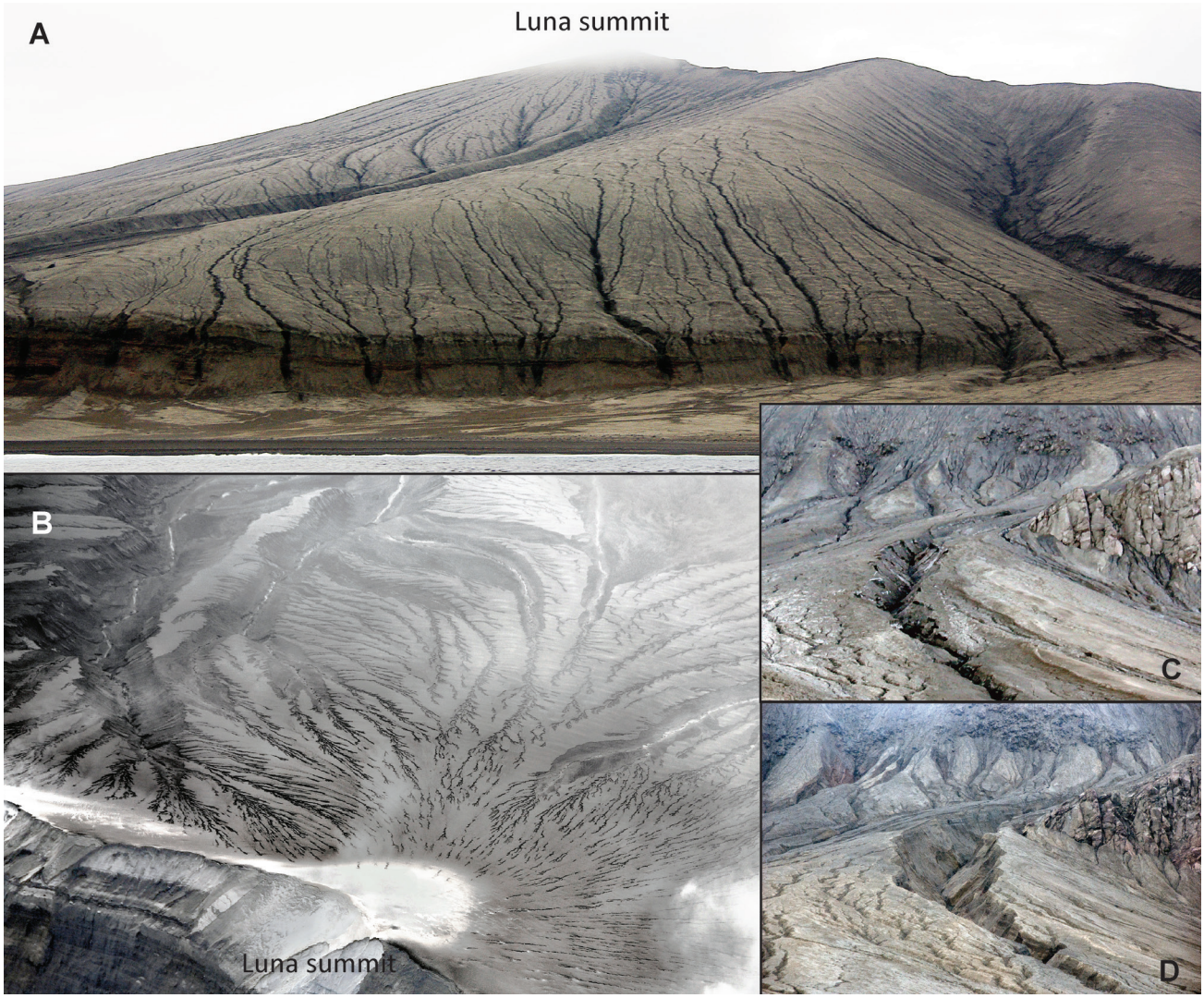

Figure 5. Detailed views of post-eruption gullies. **A.** View to northwest of the southeastern flanks of Kasatochi immediately south of The Ogres Toes (sheet 1). Luna summit is the high point on the skyline. The vertical bluffs in the foreground are pre-eruption sea cliffs of Luna pyroclastic deposits and are up to 29 m tall. The width of the foreground view is 500 m. Photograph by C. Nye, August 11, 2010. **B.** Downward and southeast-looking oblique aerial view taken from above Luna summit 14 days after the eruption, showing that intricate gullying from the crater rim downward was established very rapidly. The foreground width of the field of view is about 300 m. Elevations shown range from 320 m asl at the rim to about 120 m asl, encompassing about half of the upper southeast flank. The smallest gullies in the foreground are less than 1 m wide, and therefore are not shown on sheet 1. Photograph by R. Buchheit, USFWS, August 22, 2008. **C, D.** Nearly identical views of the largest gully as it exits Peregrine ravine, as well as larger gullies at lower elevations. The 40-m-high cliffs on the right edge of the photographs are of Peregrine lava, the source of the now-buried Troll talus, an important auklet nesting colony prior to the eruption. The mid-field width of each scene is 140 m. The photograph in C was taken by J. Williams, USFWS, June 12, 2009. Field observations at that time showed the gully to be about 28 m wide with steeply-sloping upper walls extending to a depth of about 8 m. A narrow, vertical-walled slot extended several meters deeper. In contrast, field photographs from August 22, 2008 (not shown), show that two weeks after the eruption this gully was about 3 m wide and 1–2 m deep with vertical walls and a flat bottom. The photograph in D was taken by C. Nye, August 24, 2013. In five years the gully had grown to 46 m wide, with steep-sloped upper walls about 24 m deep above a narrow, deeper slot.

Field investigations show that a major mechanism for downgully movement of 2008 deposits involves failure of gully walls along near-vertical tension cracks, producing gully-blocking debris dams, which are subsequently mobilized as debris flows that deliver large volumes of boulder- to sand-sized debris to the gully mouth. Field evidence supporting this mechanism includes observation of tension cracks that had not yet failed parallel to gully walls, debris dams in gully bottoms, and fresh boulder-bearing flowage deposits that were delivered to the beach and eroded by the next high tide.

Gullies are steep-sided, and those of small to moderate size remained steep-sided through 2013, the final year of field investigations associated with this map. In contrast, some of the larger gullies evolved morphologically, becoming deeper and wider over 5 years of periodic observations (figs. 5C and D). The best-documented example of the rapidity of large gully change is the morphology of the large gully exiting Peregrine ravine that was (at a set reference point) a few meters wide 2 weeks post-eruption, 28 m wide 8.5 months post-eruption, and 46 m wide 5 years post-eruption. During the 5-year period the gully deepened from 1–2 m to more than 24 m. In 2009 this gully had a roughly funnel-shaped cross section with very steep walls at the bottom and more flared walls near the top. Over time, the upper flared walls widened faster than the bottom near-vertical-walled section deepened. If this change continues, with additional time the gully will change from slot-shaped to funnel-shaped to V-shaped, and will ultimately be closer in cross section to the Ogres Toes—presumably analog relict gullies developed in the Luna pyroclastic deposits—and the rate of erosion will decrease.

TENSION CRACKS

Tension cracks parallel to the northeastern and southeastern crater rim are visible on satellite imagery postdating, but not predating, the eruption. The existence of those near the southeastern crater wall was confirmed during field investigations. These cracks are tens to several tens of centimeters wide and up to 200 m long. They may have formed either by the unusually energetic seismic shaking associated with the eruption or as a result of erosion and steepening of the walls during the eruption. Satellite imagery subsequent to the base imagery used for this map suggests that the system of cracks parallel to the northeastern crater rim failed sometime prior to March 2011, and that a slab of crater wall approximately 20 m wide and 175 m long fell into the crater.

LOAFING GULL LAKE

Loafing Gull lake is a shallow, freshwater pond near the southernmost point of the island. It is a common resting place for gulls, perhaps attractive as a water source. It sits in a depression formed by 2008 pyroclastic fans on the east and west and the beach ridge formed during post-eruption aggradation of the southern beach. It formed sometime between mid-September (not present in satellite imagery) and October 23, 2008 (clearly visible in oblique aerial photography by J. Morris), and has persisted since. At the time the base satellite images used for mapping were acquired (April 18, 2009), Loafing Gull lake was about 0.9 ha, had a surface elevation of 2.6 m, and was surrounded by topographic barriers to drainage at least 90 cm high. On March 9, 2011, its surface elevation had increased to about 3.3 m, its area had increased to 2.1 ha, and topographic barriers to drainage were only a few tens of cm higher than the lake level. In 2011 satellite imagery it appears that at some prior point the lake had been deep enough to partially drain to the east along the base of the 2008 pyroclastic fan. On February 2, 2012, the lake level was slightly higher than in 2011, and the surface area had increased to 3.0 ha. What we interpret to be a relict shoreline in the 2012 imagery suggests that prior to data acquisition the lake had been as large as 4.4 ha and deeper by at most a few tens of centimeters. Unlike in 2011, there is no indication of eastward drainage despite the higher lake level, likely because the alluvial fan at the base of the major gully to the southeast of Luna summit had increased in size enough to wrap around the southern toe of the pyroclastic fan just east of Loafing Gull lake and block that drainage, as well as to shed at least some debris into the lake. In 2012 that fan was 5.7 times the area it was in 2009, and the elevation at its apex had increased from 9.5 m to 16 m.

POST-ERUPTION SHORELINES

The locations of shorelines before the eruption and at four different times after the eruption were mapped using orthorectified satellite imagery (sheet 1, appendix 2). Individual shorelines were drawn through the center of the surf zone, an easily identifiable feature on each image. They were not corrected for tidal stage, but the tidal range at Kasatochi is about 1 m, indicating that tidal correction of shorelines would be relatively minor. Sheet 1 also shows relict bluff locations from winter 2008–2009. These are bluffs that were cut into 2008 deposits, but were not being actively eroded at the time the satellite image was acquired. Instead, they were protected by sandy beaches that had formed in late winter and early spring 2009.

The eruption shed lithic pyroclastic debris into the sea beyond the pre-eruption shoreline in all directions. Wave erosion and submarine slumping started eroding the deposits immediately. When the island was visited by AVO and USFWS personnel on August 22, 2008, just two weeks after the eruption, wave-cut bluffs were around 1 m high on the western side of the island, centimeters or less on the south, and up to 3 m high on the northeastern coast, and the bluffs were separated from the sea by steep, coarse beaches a few tens of meters wide. Shoreline erosion most likely continued into September, when the first satellite images were obtained from which we can draw an accurate shoreline, so the post-eruption shoreline shown on sheet 1 is somewhat landward of the true post-eruption shoreline.

Erosion continued through winter 2008–2009, pushing the shoreline tens of meters farther landward before downslope erosion supplied enough material to the shore to allow longshore transport to start building protective beaches on the southern and eastern sides of the island.

By April 18, 2009, new beaches had been built along the southern coast between Peregrine peak and Rye point, and sand beaches separated the winter bluffs from the sea from Rye point north along the eastern coast. Relict wave-cut bluffs inside these beaches record the maximum landward extent of the shoreline during winter 2008–2009.

By April 18, 2009, the northwestern coast headlands were fully exposed, although beaches between the headlands were still seaward of their pre-eruption location. Forty-two hectares (42 ha) of land had been eroded from the western, northern, north–northeastern, and eastern shores, and 27 ha of new beaches had extended the shoreline seaward along the southwestern, southern, southeastern, and northeastern coasts (table 1; sheet 1).

By March 9, 2011, another 28 ha of the western, northern,

Table 1. Changes in beach area and length measured from satellite images from September 3, 2008 (26 days after the eruption) through February 2, 2012. Losses of beaches and 2008 deposits through landward erosion and gains through seaward building of new beaches are listed by size (hectares). The percentage of stable pre-eruption shoreline exposed and forming the shore on successive dates is also listed.

Image Date	September 3, 17, and 29, 2008	September, 2008 through April 18, 2009	April 18, 2009 through March 9, 2011	March 9, 2011 through February 2, 2012
elapsed time (yrs)	–	0.55	1.89	0.90
loss (ha)	–	42	28	25
gain (ha)	207	27	17	3.7
net (ha)	207	-15	-11	-21
net change (ha/y)	–	-27	-5.8	-24
Date	**September 29, 2008**	**April 18, 2009**	**March 9, 2011**	**February 2, 2012**
percent of pre-eruption shoreline exposed	3	16	24	48

and eastern shores had been eroded; 17 ha had been added to the southern quadrant, and twenty-four percent of the shoreline had reached erosional stability. Between 2011 and February 2, 2012, erosion continued along seventy-eight percent of the coast, removing another 25 ha, and beach growth was restricted to the southern thirteen percent of the coast, adding only another 3.7 ha. By 2012 the rest of the northeastern coast had eroded back to its stable pre-eruption position, and most of the northern half of the island (except primarily the pocket beaches in the northwestern coves) had reached stability. In 2012 there was still a beard of 2008 deposits up to 500 m wide on the southern half of the island. Field observations indicate that the 2008 deposits may have a sufficient volume of large lithic fragments to form a persistent new boulder-armored shoreline at some intermediate point between the current shoreline and the pre-eruption shoreline.

PRE-ERUPTION SHORELINE

The pre-eruption shoreline is digitized from an April 9, 2004, QuickBird satellite image. Prior to the eruption the shoreline consisted of boulder lags and bare rock. After repeat visits, USFWS personnel reported that the shoreline was relatively stable over many years.

PRE-ERUPTION CRATER RIM

The pre-eruption crater rim is digitized from an April 9, 2004, QuickBird satellite image. Lack of evidence for large rockfalls inside the crater between 2004 and the last pre-eruption observation of the crater (USFWS photographs from August 6, 2008) suggest the 2004 rim was identical, or close to, the pre-eruption rim.

DESCRIPTION AND DISCUSSION OF MAP UNITS

OVERVIEW

The stratigraphically lowest, and thus oldest, units on the island are composed of massive to thickly bedded autobrecciated lava and lahars that carry abundant angular monolithologic juvenile lava clasts; and a few stubby, thick lava flows (map units Peregrine glaciovolcanic deposits [Qpg] and Peregrine lava [Qpl], sheet 1). We believe these units were emplaced in subglacial lakes beneath a Pleistocene ice cap grounded on the ~40-km-wide summit platform of the Aleutian Ridge, which was likely subaerial during low Pleistocene sea levels. They are exposed in 150–200-m-high southwest-facing cliffs on the island's southwestern flank and, apparently, in the lowermost northwestern crater wall. A single $^{40}Ar/^{39}Ar$ age of 131 ± 2.5 ka from one of the Qpl lavas suggests a mid-Pleistocene age for these units.

Next in age are at least eight thick basalt, basaltic andesite, and andesite flows, which form cliffs, headlands, and steep outer slopes on the northern half of the island (sheet 1). Compositional dissimilarities between individual units suggest these formed from a number of discrete eruptive episodes. All are subaerial, rather than subaqueous or englacial, and thus are likely of interglacial or post-glacial age. Two of the units, both stratigraphically below five of the six other lava units, yielded $^{40}Ar/^{39}Ar$ ages of 8.9 ± 2.0 and 4.0 ± 2.5 ka, thus we infer Holocene ages for at least most of the eight flank lava units.

A thick sequence comprising numerous deposits of pyroclastic density currents and related processes (Luna pyroclastic deposits [Qlp]; sheet 1), discontinuously overlies all older units, particularly on the southern, southeastern, and southwestern sides of the island. Soil development on top of the Luna pyroclastic deposits is poor, and regional tephras, common on nearby islands, are notably absent on top of the pyroclastic deposits. This suggests that at least the upper surface of the Luna pyroclastic deposits is quite young, although prehistoric, perhaps several hundreds to at most a few thousands of years.

All these older units are mantled by deposits of the 2008 eruption except where the older units form near-vertical cliffs (sheet 1). The thickness of 2008 deposits is highly variable and controlled by funneling of pyroclastic density currents (PDCs) by preexisting topography, forming pronounced fans (Q8f) in many areas. In the absence of funneling by preexisting topography, 2008 PDCs form sheets of multiple flow units (Q8p). Immediately after, or during the waning phase of the eruption, the uppermost unit within the 2008 deposits—finer-grained surges and flows—slid off the steep upper surface and formed fans and sheets of mass-flow deposits (Qd) at lower elevations and on gentler slopes, thereby stripping 2008 PDCs of their relatively impermeable cap of surge deposits. The majority, but not all, of these mass flows formed by the time of first visual observations, about two weeks after the eruption.

The 2008 eruption deposited pyroclastic material that ex-

tended the pre-eruption shoreline by as much as 500 m laterally, and up to approximately the pre-eruption 10 m isobath. During the course of this study the northern extended shorelines retreated rapidly, while longshore and downslope transport of material from the 2008 deposits built beaches that continued to extend the southern shoreline seaward.

A robust system of gullies formed very quickly in the 2008 deposits, and during the course of this investigation those gullies have deepened but not migrated significantly laterally, delivering material either to tidewater or to lower elevation fans (Qf). This material, mobilized by southerly longshore transport, built the southern beach seaward during the course of this study.

POST ERUPTION

Beach deposits (Qb)

Beach deposits (Qb) include fines-depleted, cobble- and gravel-bearing, coarse sand of active beaches. In 2009 these beaches were 70–200 m wide, with a lower beach face 20–30 m wide, increasing in elevation from sea level to about 3 m asl. The active beach face was backed by a wide, gently sloped to flat section, often with localized concavities. These beaches are restricted to the southern third of the island, and straddle the shoreline as it was immediately after the eruption (sheet 1). The seaward limit of these beaches is up to 150 m seaward of the post-eruption shoreline, and the landward limit of these beaches is up to 130 m landward of the post-eruption shoreline. The beaches are likely the product of a combination of processes including reworking of local 2008 deposits, and downslope and longshore southerly transport and redeposition of 2008 deposits. Because these beaches, at least in part, extend seaward of the post-eruption shoreline it is clear that there was active beach construction on the southern part of the island.

Along the northeastern shore, sandy beaches 40–100 m wide between the shore and the bluffs eroded during winter 2008–2009; at the time of satellite image acquisition (April 18, 2009) the bluffs were not being actively eroded. These beaches were short lived. The September 13, 2009, satellite image shows that along the north–northeast coast the beach was gone and waves were actively eroding the bluffs of 2008 deposits; along the east–northeast coast the width of the beach had been reduced by half.

Between 2009 and 2012 the southernmost beach continued to expand southward. On February 2, 2012, the southern tip of the island was 120 m farther south than in 2009, when the base imagery for this map was acquired (sheet 1).

Lag beach deposits (Ql)

Sand-poor boulder beaches formed, and continue to form, during retreat of shorelines extended by deposition of 2008 ejecta. In April 2009 beaches on the west side of the island were 10–30 m wide, composed of coarse sand, gravel, and cobbles, and located midway between the maximum post-eruption shoreline and the pre-eruption shoreline and at the base of bluffs of 2008 ejecta. Bluffs eroded into 2008 deposits thinned from more than 25 m high at the north to 0 m at the south. Pocket beaches in Tundering and Whiskey coves were sandier and asymmetric—wider at the west end of each cove. Beaches on the northeastern part of the island, between the north point and Gregs Mighty rock, were 40–70 m wide, at the base of 30-m-high bluffs of 2008 deposits, and with shorelines as far as 150 m landward of the maximum post-eruption shoreline (sheet 1).

These beaches are dynamic and continued to migrate inward toward the pre-eruption shoreline. By early 2012 the shoreline on the northern half of the island was essentially at its pre-eruption location and the beaches consisted of coarse boulder lag. Beaches on the southwestern side of the island that had grown outward beyond the post-eruption shoreline had also begun to retreat.

The preferential beach erosion and landward migration of the shoreline on the northern half of the island presumably reflects the greater power of northerly storm waves, which have a longer fetch and approach the island through deeper water than waves from other directions (fig. 2). Shallower water and less powerful storm waves permit accumulation of beach sands to the south.

Back-beach deposits (Qm)

Back-beach deposits (Qm) comprise clay, silt, fine sand, and subordinate gravel deposited from ephemeral ponds in closed depressions behind the active beach ridge. The surfaces of back-beach deposits are easily recognized in the field by polygonal desiccation cracks that contrast strongly with adjacent coarse beach sand. Along Kasatochi's southern shore between Peregrine peak and The Ogres Toes, more than two-thirds of the beach has such depressions, typically in areas between the lateral margins of large fans of 2008 pyroclastic debris. Not all depressions are filled with back-beach deposits.

The westernmost back-beach deposits are below Peregrine peak. The outboard of this pair of deposits is in a 600-m-long trough 40–60 m wide, with stepped elevations of 2, 1.8, and 1.4 m asl, and with a seaward ridge of sand between 60 cm and 1.5 m higher than the trough. This deposit was removed by landward erosion of the shoreline between satellite images acquired April 9, 2011, and February 2, 2012. Landward of this occurrence is a separate, higher trough immediately seaward of the maximum winter 2008–2009 erosion limit. It is about 200 m long, with a base elevation of 3.8 m, and with a seaward ridge of beach sand about 60 cm high.

A smaller back-beach deposit lies about 700 m to the southeast, below the southern end of the cliffs of Peregrine glaciovolcanic deposits, and adjacent to the lateral edge of the westernmost large fan of pyroclastic debris on the south flank of the island. It has a surface elevation of 3.2 m, and is enclosed by a seaward rise of beach sand about 40 cm higher.

The largest back-beach depression is occupied by Loafing Gull lake. Sheet 1 shows back-beach deposits on the western, southern, and eastern shores of the lake. The surface elevation of the deposits is 3 m or less, and they are surrounded by topography at least 50 cm higher. Growing alluvial fans shed from major gullies to each side covered the western and eastern ends of the mapped deposits by early 2012.

Two more small areas of back-beach deposits are mapped about 700 m northeast of Loafing Gull lake, between major pyroclastic fans shed from the gully southeast of Luna summit and the southern Ogres Toes gully. The surface of these deposits is about 3.2 m asl, and a beach ridge up to 1.2 m higher lies seaward. Floodwaters that pond in this depression drain to the northeast, obliquely to the beach, along a channel with outlet elevation of 3.5 m asl. These deposits were buried by progradation of adjacent alluvial fans in late 2011 or earliest 2012.

Alluvial fans (Qf)

Fans of fines-depleted sand, gravel, and small boulders are formed by intermittent streamflow and debris flows that course down gullies to an elevation, or slope, where they start deposit-

ing their sediment load. Apices of these fans are at the mouths of gullies. The majority of these fans have formed on the southern and southwestern flanks behind post-2008 beaches where gullies flatten out to a gently dipping, low-elevation slope. In contrast, on the northern part of the island gullies are relatively steep all the way to the tide line and deposit their sediment load below the high tide line.

The dominant source of material is presumably 2008 deposits, but some gullies have eroded to below the pre-eruption surface and fans sourced by these gullies must incorporate older material. One clear example of this is on the low southeastern flank (fig. 5A), where gullies have eroded through the vegetation mat into Luna pyroclastic deposits.

Talus (Qt)

Talus deposits are jumbled piles of angular boulders up to many meters in diameter that have accumulated at the bases of cliffs. Taluses are key features at Kasatochi; prior to the 2008 eruption Tundering and Troll taluses provided nesting habitat for hundreds of thousands of seabirds, mostly crested and least auklets. Those taluses were deeply buried by the eruption, thus unavailable for nesting in 2009. There was doubt among ornithologists about how the auklets would adapt to the sudden and total loss of their nesting burrows as they are known to have high nest-site fidelity (Williams and others, 2010; Drew and others, 2010).

The map shows new taluses built on top of 2008 eruption deposits in areas away from the previously heavily used, and now buried, nesting taluses. The most prominent is Whiskey talus, located above Whiskey cove and under the north-facing cliffs of Mount Kasatochi andesite (Qmka). Immediately after the August 23, 2008, eruption, a discontinuous scattering of individual boulders had fallen on top of the 2008 deposits. Year by year additional rockfall added new material and as of 2013 the talus extends for about 130 m along the base of the cliff and 65 m perpendicular to the cliff face (fig. 6). Individual boulders are angular fragments of lava columns and are routinely meter-sized; the largest are up to 7 or 8 m in diameter. The position of the toe of the talus has been fairly stable since 2010; growth of the talus has been in thickness and in length along the cliff face. The toe of the talus was initially 50 m or more from the active beach, but rapid erosion of the beach and bluffs of 2008 deposits behind the beach have lessened the protection the talus once had from active erosion. Still, the majority of the talus is landward of the pre-eruption shoreline, which was presumably much more stable than the present shoreline, and beach retreat will likely stop before the talus is heavily eroded.

Colonization of the talus by least and crested auklets in substantial numbers began in 2010 and has increased to many tens of thousands of birds.

A smaller talus is forming about 150 m west of the main Whiskey talus. It is about 20 m in diameter and in a concave re-entrant in the cliff face. It extends from the base of the cliff across the surface of 2008 deposits, then down the bluff face carved in the 2008 deposits by subsequent erosion. The lack of a vibrant green, guano-fertilized algal bloom as late as August 2013 suggests that this smaller talus has not been extensively colonized by seabirds.

Another post-2008 talus lies high on the northern flank, between 160 and 210 m elevation, and about 80 m long measured along slope and 40 m wide. We refer to it as Monkey talus because it sits above The Monkeys Forehead, the informal USFWS name for a prominent, protruding block of lava lower on the north flank. The talus developed on the surface of a Monkeys Forehead basaltic andesite (Qmfm) flow unit, only thinly covered by 2008 deposits, which dips northward with a surface slope of about 40 degrees.

Visual observations of this slope were precluded by fog or clouds during many of our field visits, so our photographic record is sparse. The slope where the talus now sits was boulder free in June 2009 (fig. 7). Our next view was in June 2012, when the upper part of the slope on which Monkey talus sits was in clouds, but the lower part was visible. Monkey talus was present and consisted of dun-colored boulders similar in appearance

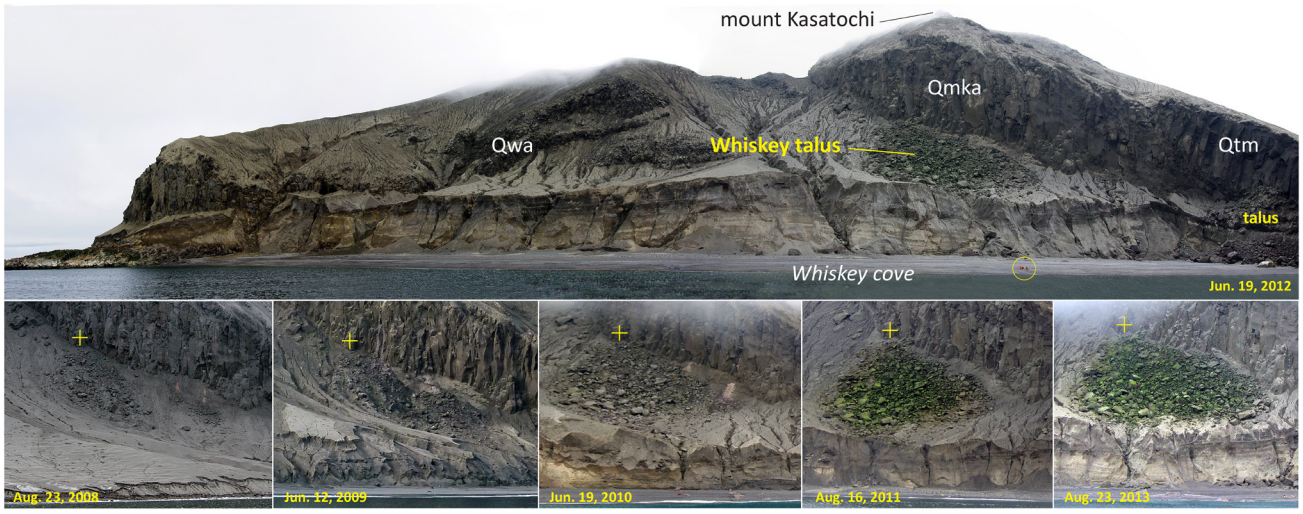

Figure 6. Whiskey talus, above Whiskey cove and below north-facing cliffs of Mount Kasatochi andesite (Qmka) and Tundering basaltic andesite (Qtm) shown at six different times over the course of this study. A single feature common to all photographs is indicated by a yellow plus. Scattered boulders lay on the surface of 2008 deposits two weeks after the eruption. Ten months later additional rockfall had added material, most notably to the right (northwestern side) of the earlier talus. The talus was not used for nesting by auklets in 2009 (Williams and others, 2010). By 2011, the talus was being used for nesting, as evidenced by the bright green color produced by guano-based algae and confirmed by field observations. By 2013 the talus had enlarged to the northwest (right of photograph) and thickened. Cliffs behind the talus are 70–120 m tall. Note geologists sitting on beach in top photo, circled in yellow. Photographs by J. Williams, USFWS, and C. Nye.

to nearby lava. In August 2013 the arrangement of boulders in the talus was similar or identical to 2012, suggesting there had not been significant additional rockfall in the past year. Unlike in 2012, in 2013 the talus was vibrant green, suggesting that it had been colonized and that guano was hosting algae. Although we have no direct evidence for precisely when, between 2009 and 2012, the talus formed, it is logical to infer that it occurred at the same time that the portion of crater wall failed (see Tension Cracks) and thus was likely sometime before March 2011.

Slump (Qs)

Two slumps of 2008 deposits are shown along the northeastern shore. These deposits were ephemeral and are the two that were mappable on our base imagery; they were in place on April 18, 2009, when the imagery was acquired, but were removed soon after by ongoing erosion and shore retreat. Presumably many similar deposits were formed and removed by wave action in time intervals between satellite observations. The northern slump deposit is outboard of the 2011 shoreline, and the southern slump deposit is outboard of the 2012 shoreline. Slump deposits are sections of 2008 pyroclastic flows that have dropped downward along shoreline-parallel failures and, in the case of the northern slump, translated seaward enough to produce a crude, fan-shaped deposit with irregular hummocky surface.

2008 mass-flow deposits (Qd)

The surface of 2008 pyroclastic deposits, dominantly thin beds of ash and accretionary lapilli, sloughed at the close of, or shortly after, the eruption and flowed down slopes as mud-lump debris flows (fig. 8C) that came to rest on surface slopes of 15 degrees or less, compared to the greater-than-25-degree slopes where they originated (fig. 8). These form unit Qd. The deposits are generally less than a few meters thick, composed chiefly of sand- to clay-sized material; and have a characteristically lumpy surface, with individual lumps a few decimeters in diameter, and blunt lobate margins many centimeters to many decimeters high.

2008 ERUPTION DEPOSITS

Pyroclastic deposits (Q8p)

The 2008 eruption produced deposits chiefly of pyroclastic density currents (PDC) and only minor fall deposits. On broad upland slopes and on top of previous topographic highs the 2008 deposits form a sheet-like package composed of multiple subparallel units of varying composition, grain size, and depositional mechanism. We map these as 2008 pyroclastic deposits (Q8p). Cumulative thickness is variable, from about 10 m on the middle of the southern flank, to greater than 10 m at the southern crater rim, to a few decimeters on the lower eastern flank, which was both upwind during the eruption and relatively steep.

The deposits contain both andesite and basaltic andesite juvenile scoria, as well as gabbroic inclusions, which are described in the Petrography and Geochemistry sections. Basaltic andesite scoria (52–56.5% SiO_2) are dark- to medium-gray and have phenocrysts of plagioclase (22–34%, 0.3–1 mm), clinopyroxene (3–8%, 0.3–1 mm), orthopyroxene (2–6%, 0.2

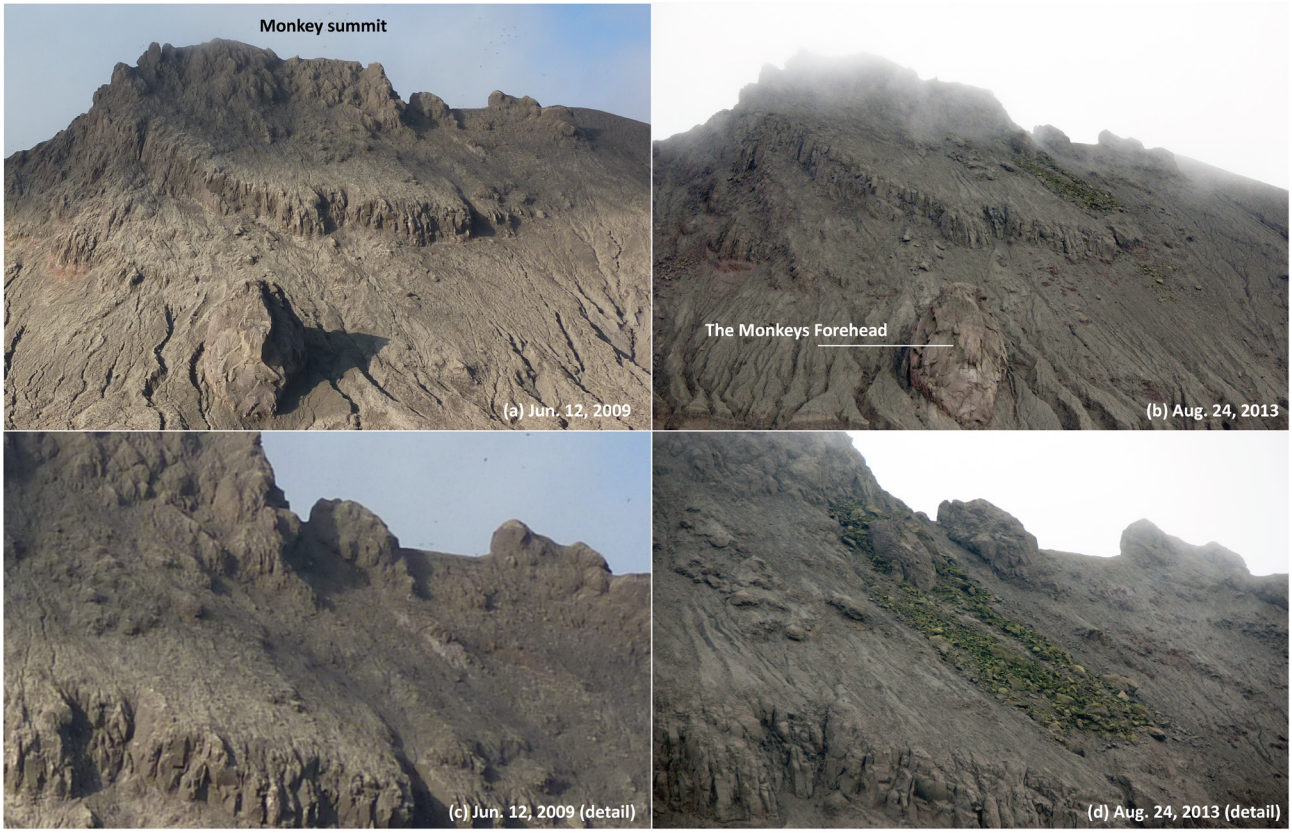

Figure 7. Monkey talus, high on the outer northern flanks above and west of The Monkeys Forehead. **A, C**. In June 2009, ten months after the eruption, the ground slope was bare. **B, D.** The upper slopes were covered by fog or clouds during most of our field visits, but on August 24, 2013, chance visibility revealed a roughly 40 by 80 m talus that had formed since 2009. The green color indicates that the talus is an active nesting site. Panels A and B are views of the upper 80 percent of the northern flank; panels C and D are expanded views of portions of the same photographs showing talus details. Photographs by C. Nye.

mm), amphibole (1–8%, 0.5–1.2 mm), opaque oxides (2–4%, 0.2 mm), and olivine (0–1%, 0.1–0.2 mm), and 47–70 percent groundmass composed of microlites and brown glass (see appendix 7 for photomicrographs). The plagioclase is typically zoned, and has concentric, frittered, inclusion-bearing bands, which mark episodes of disequilibrium. Amphibole phenocrysts have thin (~5 µm) reaction rims. The basaltic andesite also contains xenocrysts of large unzoned plagioclase crystals and poikilitic amphibole enclosing plagioclase and pyroxene, which are presumably fragments of disaggregated gabbro. Andesite scoria (58.3–60.6% SiO_2) are light gray to white and have phenocrysts of plagioclase (12–21%, 0.3–1.1 mm), clinopyroxene (0–7%, 0.4–1 mm), orthopyroxene (1–3%, 0.2–0.3 mm), opaque oxides (1–4%, 0.2 mm), and amphibole (0–4%, 0.5–0.8 mm), and 68–86% groundmass composed of clear glass and microlites. Some andesite scoria have bulk densities <1 g/cc, and thus float in seawater. Basaltic andesite and andesite scoria both have large compositional ranges, but there is a 2 weight percent (wt.%) SiO_2 compositional gap between the two. Banded scoria is common, and consists of sharp bands of basaltic andesite and andesite at scales from a few centimeters to as small as five microns (µm). The sharpness of even the thinnest bands indicates that mingling of basaltic andesite and andesite occurred shortly enough before eruption that there was insufficient time for diffusive equilibration.

The stratigraphy, composition, and depositional mechanisms are discussed in detail by Scott and others (2010), Waythomas and others (2010b) and Neill (2013), and are summarized below. They recognize a basal layer (Unit 1) of thin fall and surge deposits that are dark, muddy, pumice-bearing, and acidic, and presumably derived from lake-bottom mud during the opening phreatomagmatic explosion, which apparently ejected the lake entirely. Unit 1 is not seen everywhere, and is never exposed seaward of the pre-eruption shoreline, where deposits, if they exist, would be below sea level. It is generally centimeters to decimeters thick.

Unit 2 is a thick sequence of vaguely bedded, coarse-grained pyroclastic flows. At shoreline exposures, much of Unit 2 is presumed to be below sea level. Unit 3 is a distinctly stratified sequence of interbedded, coarse pyroclastic deposits of flow and fall origin. The distinct bedding between Unit 3 flows, including intervals of pumiceous and fines-depleted fall, suggests that Unit 3 accumulated during a time of more episodic deposition than when Unit 2 was deposited. Units 2 and 3

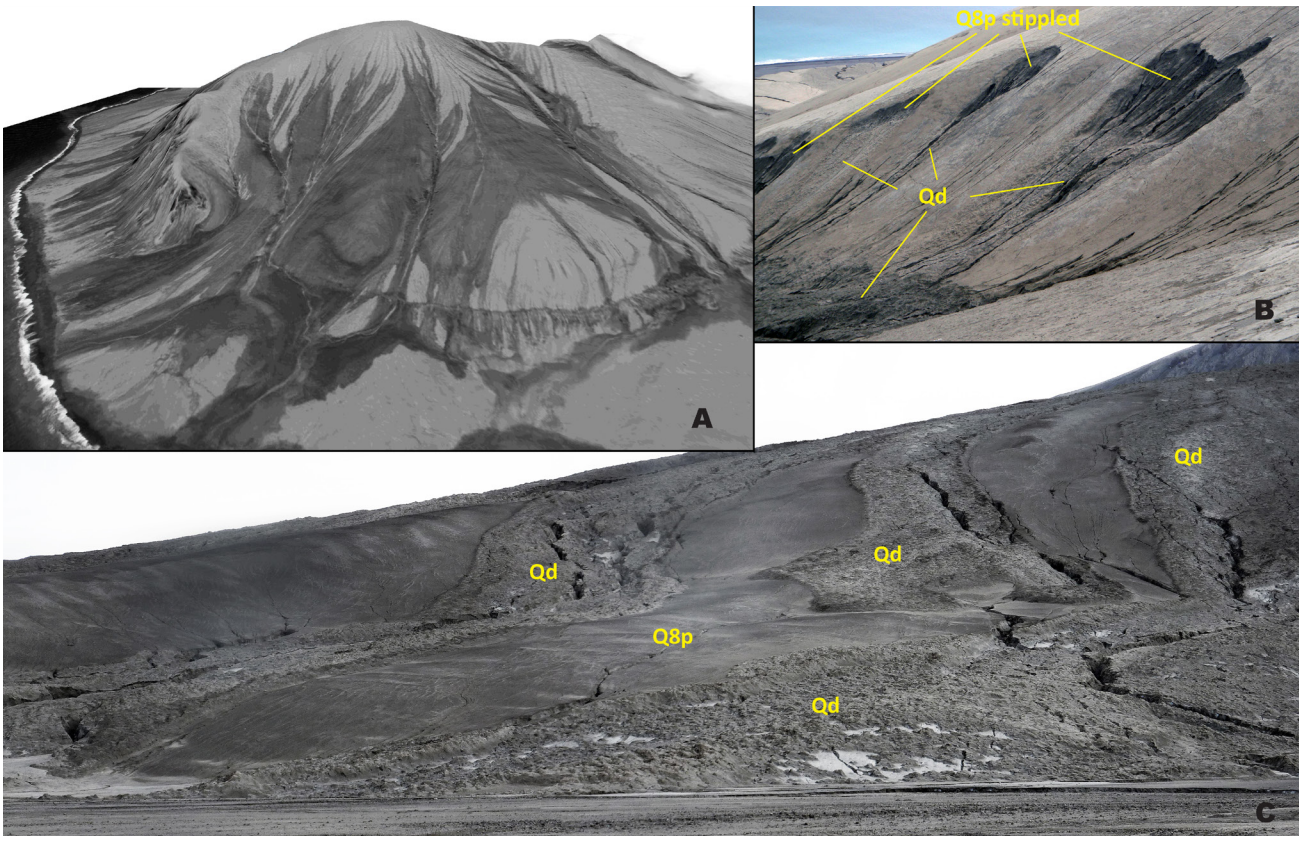

Figure 8. Examples of 2008 mass flows (map unit Qd) and the primary 2008 deposits denuded primarily of their uppermost, fine-grained layer (Unit 4; see text). **A.** Oblique view 41 days after the eruption of September 17, 2008, satellite imagery draped on the April 2009 DEM. The extensive dark areas (stippled Q8p on sheet 1) show where the upper part of 2008 deposits have detached, flowed to lower elevations, and redeposited as unit Qd, illustrating widespread and rapid erosion of 2008 deposits through sloughing and slab avalanches that produced mass flows. **B.** Photograph taken in the uppermost part of a prominent gully about 400 m east of Luna summit. It shows four small scarps, each about 10 m across, where Unit 4 deposits have slumped, generating mass flows (Qd) and leaving behind patches of 2008 deposits stripped of their uppermost surface. Photograph by J. Williams, USFWS, June 13, 2009. **C.** View northward of the southern side of the pyroclastic fan built from 2008 pyroclastic density currents channeled by Peregrine ravine. It shows the distal ends of four flows, three toward the camera and one on the skyline, which originated on the upper slopes of Peregrine ravine. The steepest parts of the two center mass flows are 18 and 16 m wide. The termini of the flows are covered by subsequent alluvial deposits seen in the foreground. Photograph by C. Nye, June 13, 2009. The two mass flow deposits in the center are among the few that were emplaced during the winter of 2008–2009 rather than immediately after the eruption.

both contain abundant non-juvenile lithic fragments presumably mostly derived from the portions of the crater wall that were removed during the eruption. Non-juvenile lithic clasts comprise an average of 70 percent of fragments in the 16–32 mm size class (appendix 9). The largest lithic block we have seen is about 7 m long and a few meters wide and thick; it sits about 850 m seaward of the nearest part of the crater rim on the south–southeast flank. Numerous lithic blocks greater than 3 m long sit on the surface of 2008 deposits about a kilometer from the crater rim and a few hundred meters seaward of the pre-eruption shoreline.

Units 2 and 3 contain basaltic andesite, andesite, and banded scoria in roughly equal proportions. Andesite scoriae dominate juvenile ejecta in the bases of Units 2 and 3. Basaltic andesite dominates the middle of Unit 3, and andesite and basaltic andesite are in subequal proportions in the tops of both Unit 2 and Unit 3. Unit 3 also contains texturally diverse, amphibole-rich, cumulate gabbroic blocks and minor cumulate pyroxenitic and peridotitic blocks. Gabbros are often extremely friable and contain intergranular voids, some of which contain interstitial basalt melt slightly more mafic than the most mafic juvenile basaltic andesite scoriae. Some cumulate blocks are coated with basalt rinds of the same composition as the interstitial basalt in the gabbros.

Units 2 and 3 comprise the bulk of the 2008 deposits, and are overlain by Unit 4, which is composed of millimeters- to centimeters-thick beds of ash and accretionary lapilli that were deposited by falls and surges during the waning stage of the eruption. Individual beds are composed of fine sand, silt, and clay-sized particles. Low-angle crossbedding is common. Accretionary lapilli are abundant, suggesting that water was incorporated in the eruptions that produced Unit 4. Aggregate thickness of Unit 4 is decimeters to a few meters.

Boundaries between units are not differentiated on the map and are only visible in near-vertical exposures. Pyroclastic density currents from the 2008 eruption were only locally erosive, as shown by occasional rip-ups of underlying turf, and often not erosive, as shown by undisturbed turf below the deposits. Despite the expected high magmatic temperature (~900°C) and the proximity to the vent, the pyroclastic deposits were in general not hot enough to char underlying turf or rare manmade artifacts (for example, a plywood observation blind at Tundering talus that was exposed by erosion some years after the eruption).

We observed Unit 4 becoming mobilized under light rain, presumably because its fine-grained, interbedded nature promotes rapid buildup of pore pressure and loss of shear strength. Unit 4 initially capped all 2008 deposits, but soon after deposition it commonly sloughed off steeper slopes, producing mud-lump debris flows (fig. 8; see 2008 mass-flow deposits [Qd]) that moved downslope and came to rest on shallower slopes, leaving behind large areas of 2008 deposits largely denuded of their Unit 4 cap. Such areas are bounded by headwall and sidewall scarps a meter or two high, and are shown with a stippled pattern on sheet 1. Differences in their surface characteristics may be relevant to revegetation. Where Unit 4 is fine-grained enough, and where it is still in place capping 2008 deposits, even light rainfall migrates downslope as sheet-flow before dropping into gullies. In the absence of Unit 4 the upper surface of 2008 deposits is much more porous, and rainfall is more likely to infiltrate.

Most sloughing of Unit 4 and the subsequent formation of mass flows occurred very soon after the eruption. The first post-eruption visual observations of Kasatochi were from the *M/V Tiĝlax̂* shortly after sunset August 10, about two and a half days after the eruption ceased. While low light, low clouds, scattered fog, and intermittent rain significantly degrade the available photographic record, it is clear that many Unit 4 debris flows had formed. A helicopter-supported visit to the island by USFWS and AVO scientists on August 22, and observations from the *M/V Tiĝlax̂* on August 29, show widespread areas where Unit 4 sloughed, forming mass-flow deposits at lower elevation. Satellite images acquired as early as September 3 show most of the sloughed areas and mass-flow deposits essentially as they have been since (fig. 8A); some additional mass flows were emplaced during winter 2008–2009, but prior to April 18, 2009, the date of the satellite images used as a base for this study. The sloughing of Unit 4 was an early post-eruptive process, largely completed within at most two weeks, and fully complete within at most eight months, and was not ongoing during the course of our study.

The surface of about 30 percent of the original pyroclastic deposits sloughed. While there is broad overlap of surface slopes where sloughing did and did not occur, the areas that sloughed have a higher proportion of steeper slopes (for example, 35 percent of the sloughed areas, but only 15 percent of the areas where Unit 4 remained in place have surface slopes greater than 30 degrees). Perhaps slumping was initiated on steeper slopes and then propagated across shallower slopes.

Pyroclastic fans (Q8f)

2008 pyroclastic density currents were largely channeled by preexisting topography despite their proximity to the vent. As a result, thick fans formed with apices at the lower ends of canyons and valleys. These fans are mapped as a separate unit (Q8f). The lack of precise pre-eruption topographic data makes determination of the three-dimensional morphology of the fans difficult. However, the position of the pre-eruption shoreline—a pre-eruption zero-elevation marker—is known, and the elevation of the surface of the 2008 deposits above this zero-elevation line can be determined.

Figure 9 shows the thickness of 2008 deposits at the pre-eruption shoreline along the western, southern, and eastern shore between Barabara ridge and Rye point. The thickest fan, at the mouth of Peregrine ravine (fig. 9, point A), is 50 m thick. Other thick fans are seaward of the lowest point on the crater rim (north of point A in fig. 9), at the south end of the cliffs of Peregrine glaciovolcanic deposits (Qpg) (fig. 9, point B), at the mouth of the broadest valley below Luna Summit (fig. 9, point C), and seaward of The Ogres Toes (fig. 9, point D), a triplet of pre-eruption valleys presumably cut into the Luna pyroclastic deposits. All of these fans stand more than 20 m above the pre-eruption beach and thin dramatically landward because they cover steep pre-eruption topography. Thickness of 2008 deposits along this transect range from 6 m at the edges of fans to 50 m at the peak of the largest fan, with an average of about 23 m. The surface slopes of the fans average about 13 degrees, about half as steep as the upper slopes of the volcano, where 2008 pyroclastic deposits form sheet-like bodies.

PRE-ERUPTION

Luna pyroclastic deposits (Qlp)

The stratigraphically highest unit prior to the 2008 eruption was a thick package of beds formed principally by deposition from pyroclastic flows. The name for this unit, Luna pyroclastic deposits (Qlp), is taken from Luna Insularis—the USFWS

name for the area surrounding Luna summit, which was a bare, unvegetated surface prior to the 2008 eruption. In all exposures, including those inferred from pre-eruption photography, Luna pyroclastic deposits overlie all other units, and underlie only 2008 deposits.

The Luna pyroclastic deposits map unit consists of stacks of individual flow units. Each flow unit is meters to several meters thick and poorly sorted, containing juvenile pyroclasts up to tens of centimeters in diameter, and angular lithic blocks of preexisting lava up to a few meters in diameter, in a sandy to ashy matrix. Individual flow units are usually uniform in thickness over horizontal distances of hundreds of meters. However, in some localities there are flattened, lens-shaped bodies, apparently formed both by scouring of underlying flows by overlying flows and by deposition of leveed lobes of pyroclastic flow deposits.

Three main outcrop areas of Luna pyroclastic deposits existed prior to the 2008 eruption: the south shore, the southern crater rim, and the west shore. The south shore exposure consisted of a continuous beach bluff that rose above a 20–50-m-wide sand, gravel, and boulder beach (fig. 10) and ran in a 2-km-long arc from the southernmost point eastward and then northward to Rye point, a distance of about a quarter of the pre-eruption circumference of the island. The bluff was

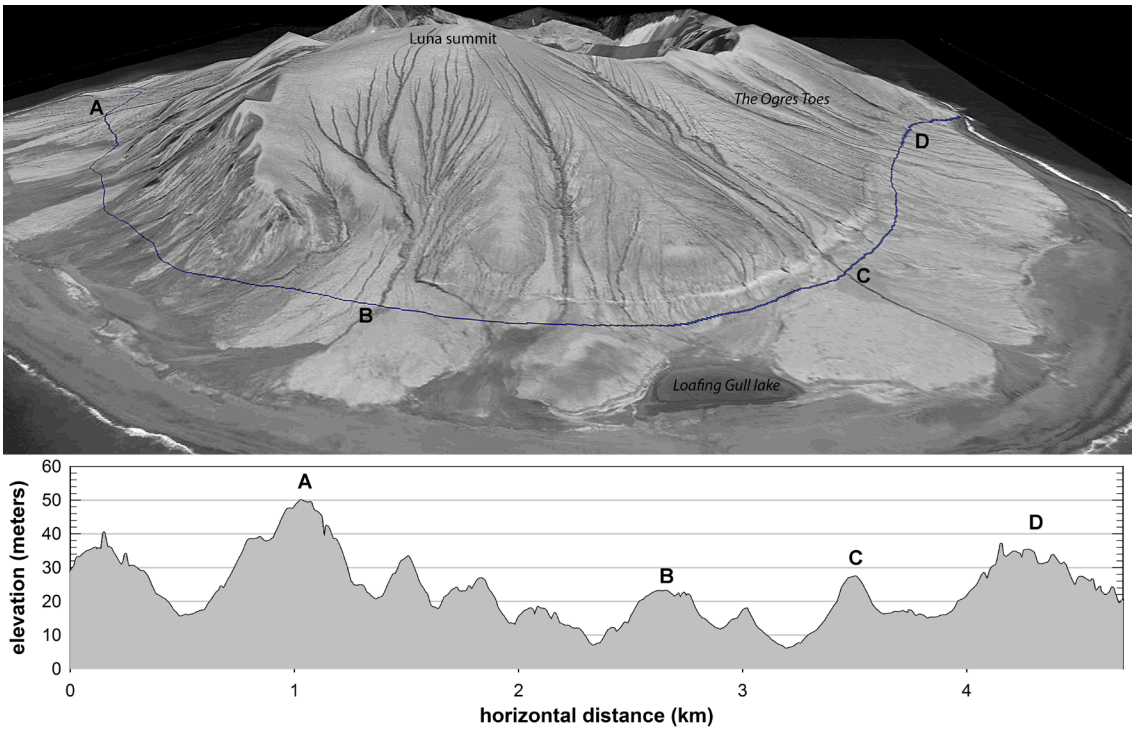

Figure 9. Upper panel is a north-looking perspective of the April 18, 2009, satellite image used as a map base, showing the western, southern, and eastern flanks of Kasatochi, as well as the surface projection of the pre-eruption shoreline (dark blue line) taken from April 4, 2004, satellite imagery. Lower panel is an elevation profile of the projected pre-eruption shoreline (vertical exaggeration 15x), showing higher elevations at apices of fans of 2008 pyroclastic deposits than between the fans. Letters show matching features between panels.

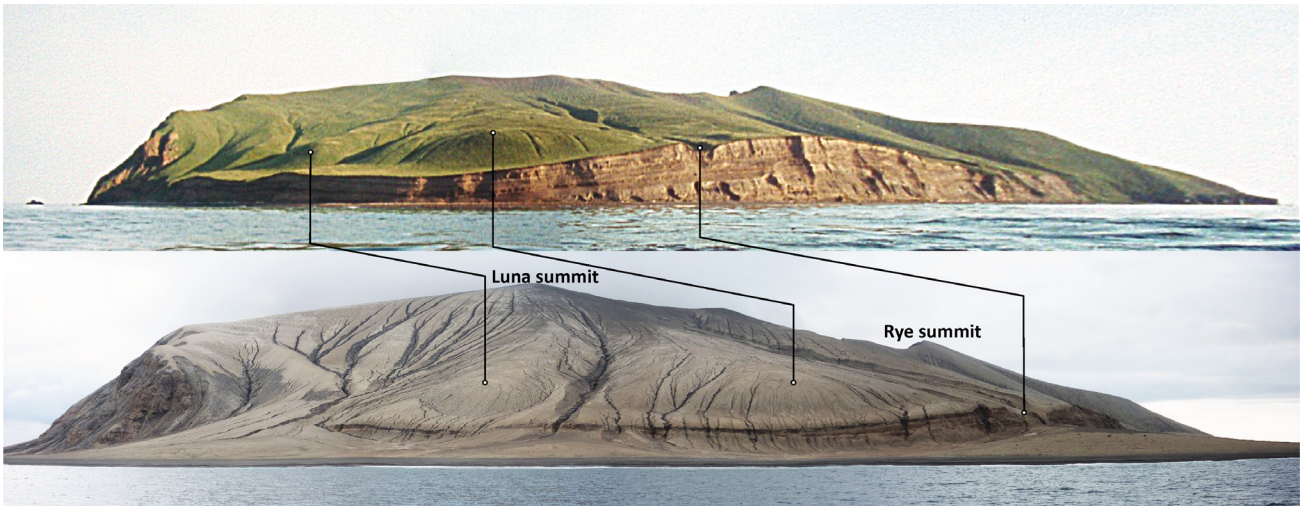

Figure 10. Views of the southern shore of Kasatochi before and after the 2008 eruption. Lines indicate the positions of the same three major features on each photograph. Upper photograph by USFWS, 1996. Lower photograph by C. Nye, June 12, 2009.

about 50 m high at the mouth of a shallow radial valley (250 m wide and 20 m deep measured midway between shore and rim) and thinned to about 20 m high to the north and south. Individual flow units mirror the top edge of the bluff, showing that the thickened central portion is constructional. Deposits from 2008 have buried the lower 20 m of the pre-eruption bluff, completely burying the bluff on the northern and southern ends, and leaving about 30 m of the bluff exposed at its thickest part. From the top of the bluff to the crater rim, the surface slope of Kasatochi is generally smooth and 10–15 degrees at lower elevations and 15–20 degrees nearer the rim. Comparison with pre-eruption photographs suggests that deposition of meters to several meters of 2008 deposits did not significantly change the slope. The smooth surface slope is presumed to be the original depositional slope of Luna pyroclastic deposits slightly modified by erosion. The major exception to the generally constant flank slope is near the south point of the island where a gently lobate band about 30 m high with a surface slope of 25–40 degrees lies about 50 m behind the beach bluff (fig. 10). It is likely that these steeper bluffs reflect preexisting topography, and perhaps a preexisting shoreline, which Luna pyroclastic deposits flowed over and around, building the island seaward in a manner similar to the 2008 event.

The southern crater wall, upslope from the southern beach bluffs, contains a composite section of pyroclastic deposits up to 200 m thick (fig. 11). None of these deposits are accessible, so our description is based on observations from the crater rim and from photographs. The basal 50 m appears to consist of massive, poorly stratified, lithic-rich pyroclastic flow deposits. The basal unit is overlain by about 80 m of reddish and dark-gray pyroclastic flow deposits. The deposits include 10-m-thick layers containing dense lithic blocks, but fewer than the lower massive section, and are interbedded with thinner, finer-grained pyroclastic flows and falls. This intermediate section also includes a few thin, light-colored deposits that define wavy unconformities. Next there is a package of about 70 m of ~1-m-thick parallel pyroclastic-flow deposits that are mostly free of large lithic blocks and are also lighter in color than the lower units. The thinner-bedded section may reflect either a period of lower-energy explosive eruptions or a period of inflated flow with little deposition. In the crater wall Luna pyroclastic deposits are overlain by about 10 m of 2008 deposits.

The third area with large pre-eruption exposures of Luna pyroclastic deposits was on the western flanks. With the exception of three small outcrops totaling less than 0.2 ha, all Luna pyroclastic deposit outcrops on the western flanks are completely buried by 2008 deposits, hence the only available information comes from pre-eruption photographs. Pyroclastic flows formed the uppermost deposits from Barabara ridge southward for 1.2 km to the shoreline below Peregrine peak. An impressive bluff that cut into these fans from below the USFWS cabin 550 m southward (fig. 12), was about 40 m high beneath the cabin and rose to a maximum height of nearly 50 m near the end of Peregrine ravine before tapering away beneath Peregrine peak.

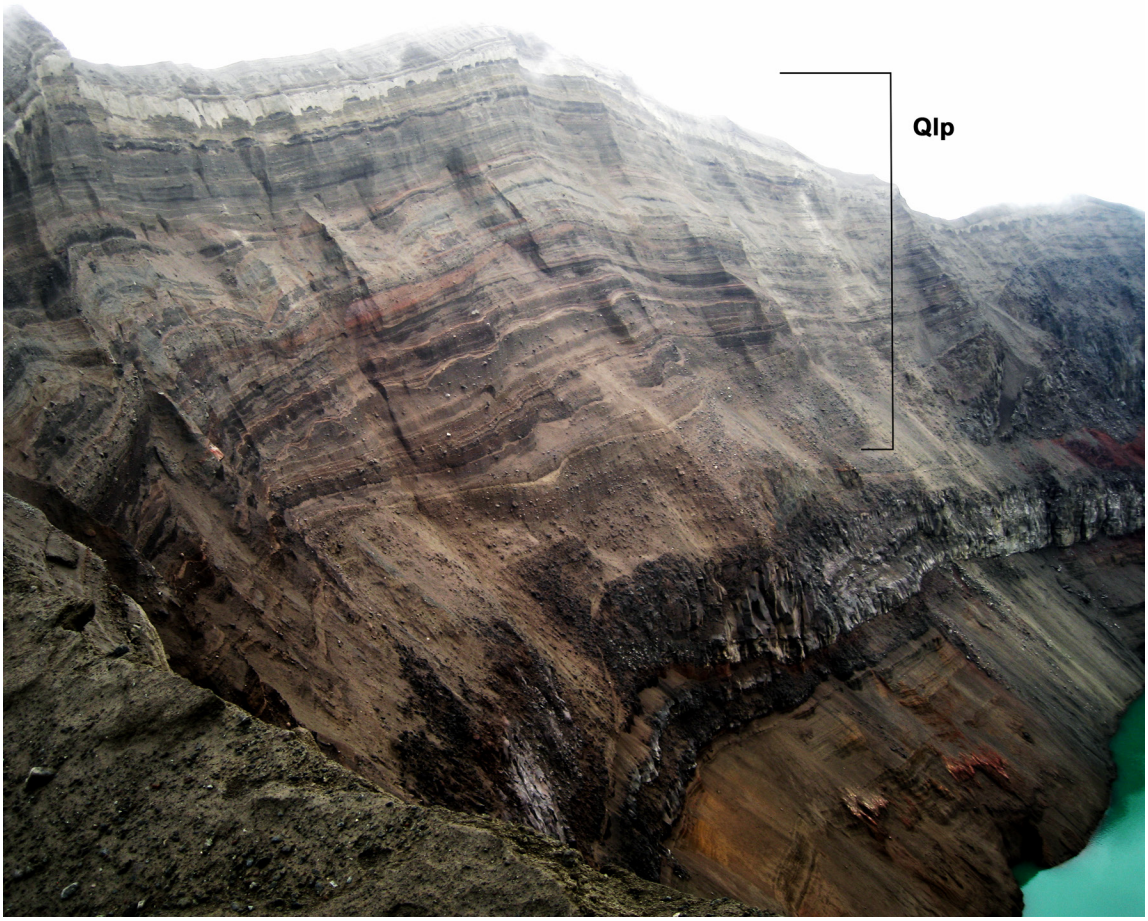

Figure 11. View of the southern crater wall, showing 200-m-thick Luna pyroclastic deposits (Qlp) above lava and thin tephra exposed only in the lower crater wall. Photograph by W. Scott, August 11, 2010.

The bluff consisted of four or five major packages of pyroclastic flow deposits, each composed of multiple crudely stratified subunits (fig. 13). Pronounced low-angle crosscutting between packages presumably reflects deposition from successive major pulses of pyroclastic flows. The pyroclastic-flow deposits apparently contain occasional lithic blocks up to a few meters in diameter. The beach below the bluffs was 15–25 m wide and composed of meter-sized boulders that presumably are the lag deposit left from erosion of the pyroclastic fan. The Luna pyroclastic fans presumably extended several hundred meters seaward immediately after eruption, similar to the way the 2008 fans extended the pre-eruption shoreline, and were eroded back over time, leaving the bluffs protected from all but large storms by the boulder beach.

From the cabin north to Barabara ridge, bluffs were not as well developed as those south of the cabin, although slumps did expose pyroclastic-flow deposits discontinuously. Prior to 2008, lava bedrock was exposed immediately below the cabin, at Barabara ridge, and midway between the two. These lava outcrops may represent more continuous lava slightly below the pre-2008 beach, which might have protected the Luna pyroclastic fans from erosion. About 15 vertical meters of Luna pyroclastic deposits were exposed on the north-facing flank of Barabara ridge prior to 2008. The upper crater wall upslope from the northern part of this western package of Luna pyroclastic deposits exposes 50–100 m of presumably correlative bedded pyroclastic-flow deposits.

The western package of Luna pyroclastic deposits was well exposed prior to the 2008 eruption, but is now almost entirely covered by 2008 deposits. The estimated thicknesses of 2008 deposits above the pre-eruption bluff edge range from 3 to 10 m. The few currently accessible outcrops are only several tens of meters long and several meters high. Those outcrops are along the sides of small, pre-2008 radial valleys and 250–300 m from the low spot in the 2008 crater rim. The 2008 pyroclastic flows were uncharacteristically erosive

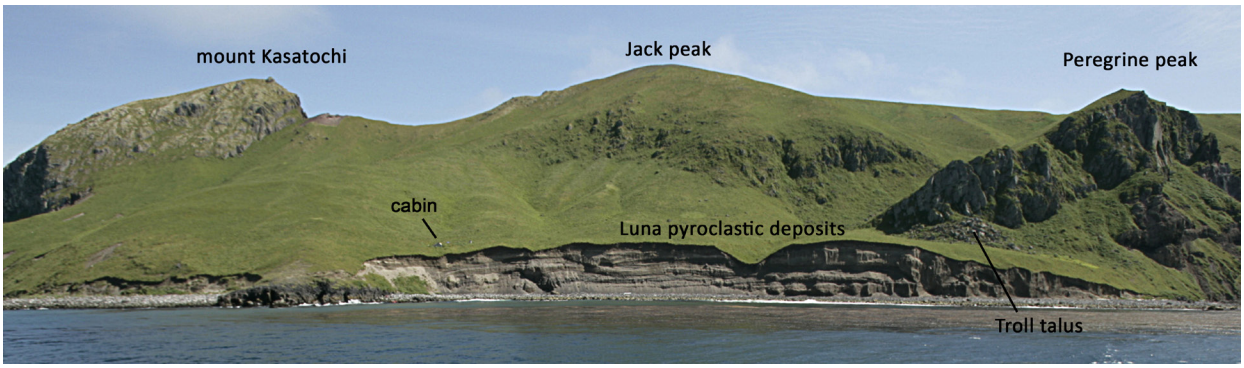

Figure 12. Pre-eruption photograph of the western coast of Kasatochi, showing a large fan of Luna pyroclastic deposits exposed in the beach bluff. This fan is now entirely buried by 2008 deposits, as are the cabin and Troll talus. Photograph by USFWS, August 7, 2006.

Figure 13. View of western shore of Kasatochi, showing Luna pyroclastic deposits below the cabin and boulder beach deposits at the shoreline. The cabin, Luna pyroclastic deposits outcrop, and beach deposits are buried beneath 2008 deposits. Photograph by USFWS, August 7, 2006.

in this area, peeling away the pre-eruption vegetation to expose the underlying Luna pyroclastic deposits.

The age of Luna pyroclastic deposits is not precisely known, nor is the amount of time required to accumulate the 200 m of stacked flow units exposed in the southern crater wall. However, we see no soils or significant erosional breaks in the Luna pyroclastic deposits, suggesting the unit formed during a single, large, relatively brief eruptive episode. The youngest dated underlying lava unit is 4.0 ± 2.5 ka, but our interpretation of stratigraphy indicates that there are several undated overlying lava units that are younger still, so we consider 4 ka to be a maximum age, and substantially older than Luna pyroclastic deposits. Luna pyroclastic deposits are overlain by very thin, poorly developed soils, even at very low elevations, which also suggests a very young age. Minor radial valleys cut into Luna pyroclastic deposits, most prominently on the eastern flank of the island (forming The Ogres Toes), and on the western flank between the cabin site and Barabara ridge. At mid elevation these valleys are 100–250 m wide and 30–50 m deep. They are V-shaped, and the slopes of the valley walls are generally less than 30 degrees. Presumably these started as steep-walled gullies similar to those in the 2008 deposits and evolved over time from a box-shape profile to the current V shape as the gully walls eroded from near-vertical to the angle of repose or less. The amount of time required for this erosional modification to the gullies is unknown, but we note that similar modification of the largest gullies in 2008 deposits was well underway during the course of this study. Prior to the 2008 eruption the sides and bottoms of the valleys were entirely vegetated, thus the valleys were no longer being formed by active erosion. During the 2008 eruption the bottoms of some of these valleys were scoured, exposing Luna pyroclastic deposits that had previously been vegetated.

Juvenile pyroclasts were collected from the upper exposed portion of the pre-eruption southern beach bluffs and from other smaller outcrops. The full stratigraphic extent of Luna pyroclastic deposits is only exposed in the crater wall, and is inaccessible. Luna pyroclastic deposit samples range from 52.8 percent SiO_2 basaltic andesite through 59.4 percent SiO_2 andesite, and incompatible element abundances vary regularly with SiO_2, so there is limited dispersion of concentrations about trendlines of specific elements vs. SiO_2. Luna samples are similar to 2008 deposits only in having a large compositional range with little spread about trendlines. Pyroclasts have phenocrysts of plagioclase (14–39%, 0.2–0.8 mm), clinopyroxene (2–12%, 0.3–0.7 mm), orthopyroxene (0–5%, 0.2 mm), oxides (0–3%, 0.3–0.5 mm), amphibole (0–1%, 0.5–1 mm), and 46–82 percent groundmass consisting of glass plus microlites. Groundmass is more abundant and phenocrysts less abundant in samples with higher SiO_2 (see appendix 7 for photomicrographs).

Lava units

Eight prominent lava-flow units form the flanks of the northern half of the island. They are generally steep, thick flows with surface slopes of 25–50 degrees with tall cliffs at their margins. The lavas are uniformly medium-gray and dense and are difficult to distinguish from each other in hand specimen. Twenty-five lava samples collected from outcrop and three additional lava samples collected from lithic blocks in the 2008 pyroclastic flows were analyzed for major and trace elements; modal mineralogy was determined for 21 of these. We identified several separate lava units based on geographic contiguity and petrographic and chemical similarity. Those units from which we have multiple samples have restricted ranges of concentrations of certain key trace elements and inter-unit variations that suggest that the units are genetically different and therefore likely represent temporally distinct eruptions. Some lava exposures that are not contiguous are correlated on the basis of distinctive chemical composition. Most of the units are basaltic andesite and andesite with 50 ± 10 percent crystals, although notable basalt units exist.

An unequivocal field-based stratigraphy cannot be established because overlapping relationships from one unit to the next spanning all units were not found. Lava units are listed in order of what we interpret to be increasing apparent age based on field relationships, geomorphology, and limited $^{40}Ar/^{39}Ar$ dating.

Monkeys Forehead basaltic andesite (Qmfm)

The Monkeys Forehead is the name given by USFWS personnel to a large, isolated block of lava on the northern flank of Kasatochi, about 500 m east of the northernmost point of the island (fig. 14). The roughly triangular seaward-facing surface of The Monkeys Forehead is near-vertical, 45 m wide at the base, and about 40 m tall. It stands about 35 m above adjacent lower slopes, and 5 m above adjacent upper slopes. The base of the block is 80 m laterally behind and 60 m above the beach. The block does not seem to be morphologically connected to any adjacent lava flow or dome. We believe The Monkeys Forehead is a roughly equant 40–50-m-diameter block that slid a few hundred meters or less to its present position. Presumably the massive nature and lack of internal fractures helped keep the block intact during transport.

During field investigations neither The Monkeys Forehead nor any of the outer slopes of the north–northeast sector of the volcano were accessible because unbroken bluffs that cut into the 2008 deposits were up to 30 m tall, friable, and too steep to climb.

Sample 1010KCnye004, which we believe is a piece of The Monkeys Forehead, is taken from an area of large, angular, 5–10 m homogeneous blocks on the beach directly below The Monkeys Forehead. The sample area was buried by 2008 deposits during 2009 fieldwork, but was exposed in 2010. These blocks are distinctly different morphologically from the heterogeneous, rounded 0.5–1.5 m boulders that form the beach on either side, as well as petrographically and chemically different from the nearest unequivocal outcrops in either direction along the beach.

Lavas high on the cone directly upslope from The Monkeys Forehead (fig. 15) have been assigned to the Qmfm map unit because they are the uppermost units on this flank, thus stratigraphically equivalent to The Monkeys Forehead itself. The upper units were inaccessible during field investigations and have not been sampled. The upper units appear, based on oblique field photographs, to consist of two to about six flow lobes, each 200–300 m wide and 5–15 m thick. The best exposed of these flow lobes is about 80 m upslope from The Monkeys Forehead, and is divided into fairly regular vertical columns 3–5 m wide. Other upper flow units appear to have similar columnar fracture. The maximum total thickness of these upper units as exposed in the crater wall is about 75 m, extending from Monkey summit to 10–15 m below the low spot on the rim just southeast of Monkey summit. The upper flow units have an original depositional slope of about 45 degrees.

Monkeys Forehead basaltic andesite contains phenocrysts of plagioclase (28%, 0.2–0.8 mm), clinopyroxene (5%,

0.4–0.8 mm), orthopyroxene (2%, 0.1–0.2 mm), oxides (2%, 0.2–0.3 mm), amphibole (4%, 0.3–0.6 mm), and 50 percent microcrystalline groundmass (see appendix 7 for photomicrographs). Plagioclase crystals typically are zoned and have concentric spongy, inclusion-rich regions. Atypical large, unzoned, inclusion-free plagioclase crystals are likely xenocrysts. Amphibole crystals have an opaque reaction rim at least 100 µm thick; smaller amphibole crystals are often completely replaced by reaction products. Monkeys Forehead basaltic andesite is distinguished from the more silicic Whiskey andesite immediately to the west by having more amphibole and a more inequigranular texture. Qmfm is distinguished from Gregs Mighty basalt immediately to the east by its higher silica content, absence of large euhedral olivine and clinopyroxene, and much higher relative proportion of plagioclase.

Tundering basaltic andesite (Qtm)

Tundering basaltic andesite (Qtm) consists of two large flow lobes embracing Tundering cove on the northwestern side of the island. The northern flow lobe is the largest, and forms Tundering head. It is about 600 m long, widening from about 90 m at its top to 150 m on the lower flank, before flaring to a 250-m-wide bulbous terminus near sea level. Pre-eruption imagery shows that this flow lobe does not extend to the crater rim; instead, it originates at an elevation of about 300 m, high on the outer flank of mount Kasatochi (fig. 15). Whether this flow is a rootless, spatter-fed flow or erupted from a vent that penetrated Mount Kasatochi andesite is unknown; the uppermost part of the flow was inaccessible during this study and is also blanketed with 2008 deposits. The surface of the flow slopes about 25–30 degrees, somewhat less steep than the Mount Kasatochi andesite surface it overlies. The upper part of the flow appears to be 15–30 m thick. The lateral margins of the lower, widened part of the flow are cliffs 40–90 m tall, formed by a single massive lava flow that forms vertical, subparallel, blocky columns several meters thick.

The other Tundering basaltic andesite flow unit underlies Barabara ridge and forms the headland bounding Tundering cove on the south. It is exposed immediately behind the beach in the southern third of Tundering cove, and extends to the crater rim where it is truncated and exposed in lava flows many tens of meters thick. Barabara ridge is currently covered by 2008 deposits. Pre-eruption photography shows that at about 80 m elevation on the ridge, 25 m of poorly sorted pyroclastic bluff deposits, presumably Luna pyroclastic deposits, overlie the lava and presumably are still present beneath the 2008 deposits.

Lavas have 53.8–55.7 weight percent SiO_2 and phenocrysts of plagioclase (26–41%, 0.1–0.7 mm), olivine (1–3%, 0.2–0.2 mm), clinopyroxene (5–7%, 0.3–0.5 mm), orthopyroxene (0–2%, 0.3–0.3 mm), oxides (3–4%, 0.1–0.3 mm), amphibole (1–2%, 0.3–0.5 mm), and 44–63 percent fine-grained microlitic groundmass (see appendix 7 for photomicrographs). Plagioclase crystals typically are zoned and have concentric spongy, inclusion-rich regions. One magmatic inclusion (09KC-wes024) was also examined. It has 55.5 weight percent SiO_2 and consists of sparse phenocrysts of plagioclase and heavily-rimmed amphibole in a matrix of interlocking 100-µm-wide acicular plagioclase and pyroxene, abundant void space, and some glass.

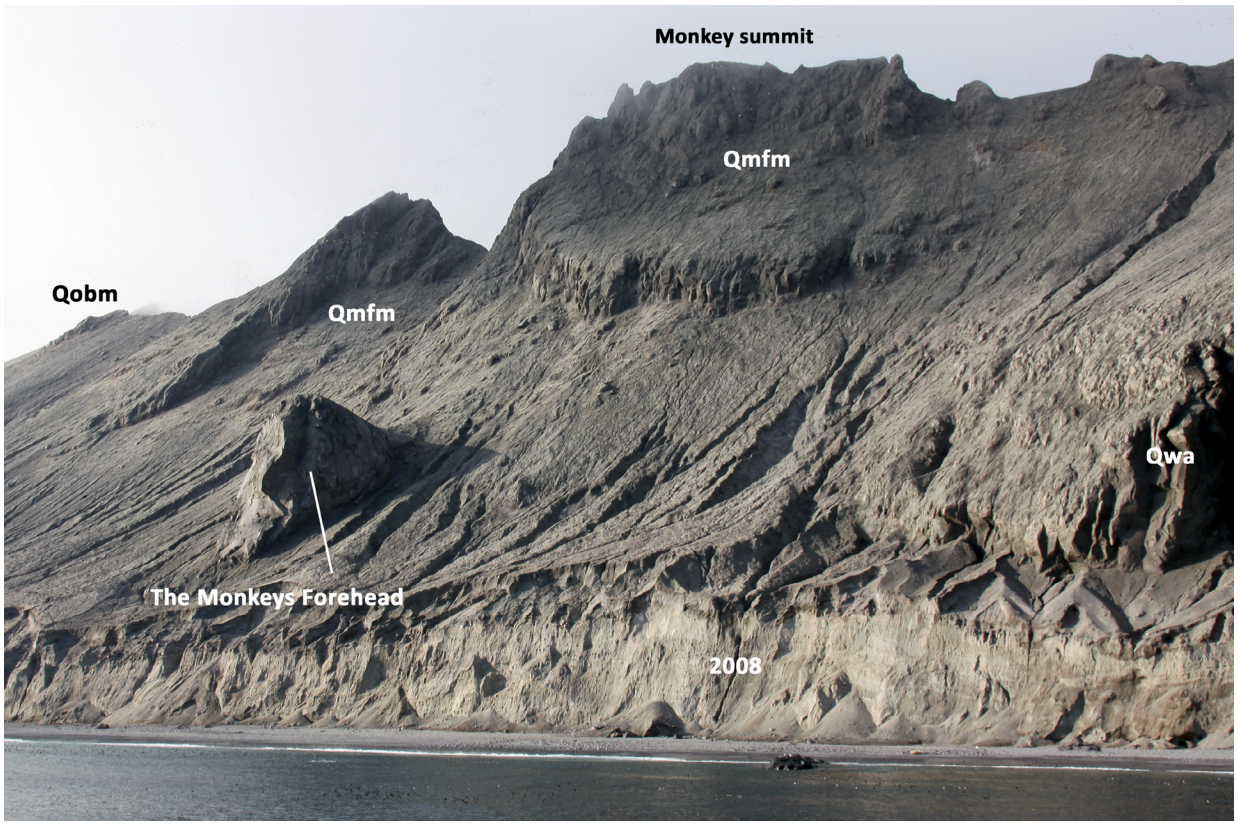

Figure 14. View of the northern shore of Kasatochi, showing The Monkeys Forehead and inaccessible lavas mapped as Monkeys Forehead basaltic andesite (Qmfm). The easternmost outcrop of Whiskey andesite (Qwa) is on the right side of the photograph. The outcrop on the distant far left rim is Ogres Brow basaltic andesite (Qobm). Nearly vertical bluffs of 2008 deposits (2008) up to 32 m tall and continuous for more than 1.2 km along the shoreline prevented access to outcrops upslope during the course of this study. Photograph by J. Williams, USFWS, June 12, 2009.

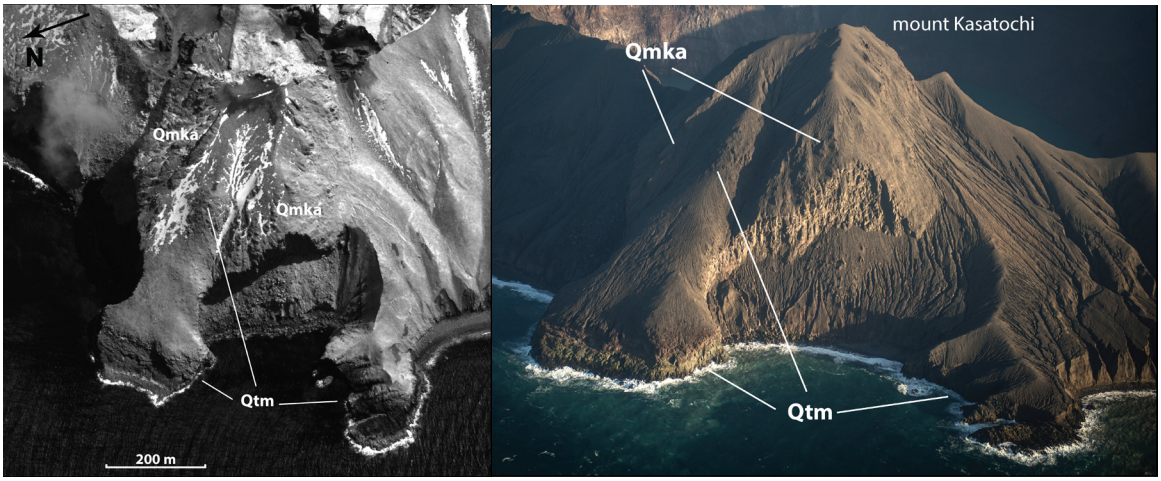

Figure 15. Two views, showing both Tundering basaltic andesite (Qtm) flow lobes and Mount Kasatochi andesite (Qmka). The proximal end of the left (northern) lobe appears to be high on the outer slope of the mount Kasatochi dome, and to not extend to the crater rim. Left frame is a portion of the April 9, 2004, pre-eruption QuickBird image that shows the different surface textures of Qtm and Qmka. The right frame shows 2008 deposits covering and obscuring the flow surfaces. Photograph by R. Clifford, February 14, 2013.

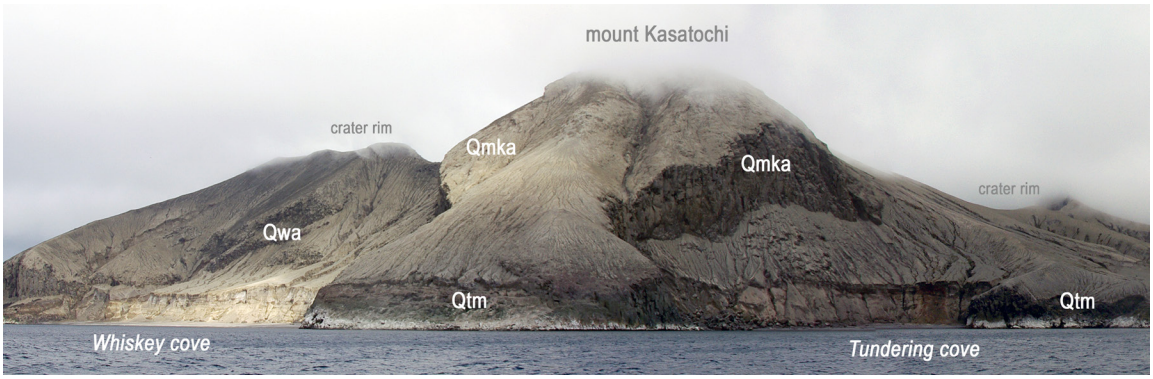

Figure 16. View of the northwestern shore of Kasatochi, showing outcrops of Whiskey andesite (Qwa), Tundering basaltic andesite (Qtm), and Mount Kasatochi andesite (Qmka), all blanketed by 2008 eruption deposits. Outcrops in the left third of the photograph are also shown in figure 6. Photograph by C. Nye, June 19, 2012.

Mount Kasatochi andesite (Qmka)

Mount Kasatochi andesite (Qmka) forms a dome of massive, dense, medium-gray andesite with amphibole phenocrysts that are conspicuous in hand specimen. The unit is located above Tundering and Whiskey coves on the northwestern side of the island and is the island's most prominent region of high topography (fig. 16). It is approximately 550 m long and 450 m wide, forming a dome-like lava mass elongated radially outward to the northwest. The surface has a characteristic fracture pattern that forms a fan-like texture composed of lines of blocks a few tens of meters wide and several meters higher or lower than adjacent blocks. These are likely spines and creases that formed during dome growth. The highest point, also the highest point on the island, is the summit of mount Kasatochi, which is 315.3 m asl. The outward-facing portion of the exposed cliff above Tundering cove is 85 m tall. Here, the unit is composed of 3–5-m-wide, poorly developed, vertical columns that extend from the base to the top of the cliff without pervasive horizontal disruptions. Thus the unit appears to be a single lava body rather than a package of flow units. The base of the unit consists of increasingly friable, sugary blocks grading down to angular cobble- to sand-sized lava fragments, and forms an uneven surface between 110 and 80 m asl. A steep talus pile between the lower contact and the beach covers underlying units. Prior to the 2008 eruption this talus, named Tundering talus by USFWS, hosted one of the largest least and crested auklet nesting colonies in the north Pacific. The surface of this talus is deeply buried by 2008 deposits, but is morphologically similar to the post-eruption surface. The unit is also well exposed, but unreachable, in the crater wall. From the summit of mount Kasatochi inward, the surface of the unit drops to about 240 m elevation with a surface slope of 50–60 degrees, then steepens to the near-vertical cliff that extends to the base of the unit at about 140 m asl, roughly 50 m higher than the base above Tundering cove. In the crater wall Mount Kasatochi andesite also consists of massive, poorly formed vertical columns. Mount Kasatochi andesite forms a single massive unit up to 150 m thick that we interpret to be a dome emplaced on the moderately dipping outward slopes of the preexisting volcano.

One sample of Mount Kasatochi andesite was chemically and petrographically analyzed. It has 59.4% SiO_2 and phenocrysts of plagioclase (35%, 0.3–1 mm), clinopyroxene (3%, 0.3–0.7 mm), orthopyroxene (1%, 0.2–0.3 mm), oxides (2%, 0.2–0.3 mm), amphibole (3%, 0.3–0.7 mm), and 56 percent fine-grained groundmass (see appendix 7 for pho-

Figure 17. View of the northeastern shore of Kasatochi, showing The Ogres Brow, the most prominent outcrop of Ogres Brow basaltic andesite (Qobm). The cliff of Ogres Brow is about 360 m wide and up to 80 m high. A small outcrop of Gregs Mighty basalt underlies the far lower right corner of The Ogres Brow, separated from it by a red scoriaceous interval. Areas other than cliff faces are blanketed with 2008 eruption deposits. The lateral edges of 2008 pyroclastic fans extend to the beach on the left and right sides of the photograph. Photograph by J. Williams, USFWS, June 12, 2009.

tomicrographs). Plagioclase crystals typically are zoned and have concentric spongy, inclusion-rich regions, which suggest transient disequilibrium during growth. Amphibole crystals have opacite rims about 40 μm wide.

Ogres Brow basaltic andesite (Qobm)

The Ogres Brow is an informal name given here to a prominent cliff on the northeastern flank of Kasatochi (fig. 17). The name is an extension of "The Ogre's Toes", a traditional USFWS name for the large parallel ridges that descend the southeastern flank of Kasatochi. The cliff is the most prominent exposure of Ogres Brow basaltic andesite (Qobm), and is formed of a single lens-shaped flow unit of massive lava cut by vertical, through-going cooling fractures defining moderately-well-developed columns 2–4 m wide. At its center the flow is 80 m thick, and the thickness tapers to zero across the 440 m width of the outcrop. The base of the unit is 50–60 m asl, and is exposed in outcrop and visible in pre-eruption photographs. The surface of the unit is covered with thin layers of pre-eruption soil and vegetation and 2008 pyroclastic flows and surges totaling a few meters in thickness. The surface of the unit climbs 135 m to the crater rim with a slope of about 25 degrees along a central spine and 25–35 degrees to each side of the central spine. A subdued outcrop at 180–185 m elevation, assumed to be Ogres Brow basaltic andesite, also is visible and recognizably similar in pre-eruption photography, underscoring the thinness of 2008 deposits here.

Ogres Brow basaltic andesite underlies the third highest elevation on the crater rim (274 m asl), referred to here as Ogre summit. In the crater wall Ogres Brow basaltic andesite forms a single massive body 120 m thick and 250 m wide that is cut by through-going, nearly vertical cooling fractures at intervals of 5–7 m.

Ogres Brow basaltic andesite is similar to other Kasatochi lavas in being porphyritic. It has 56.6–56.8 weight percent SiO_2, phenocrysts of plagioclase (29–33%, 0.3–0.7 mm), clinopyroxene (6–8%, 0.3–0.7 mm), orthopyroxene (7%, 0.3–0.7 mm), oxides (1–2%, 0.2–0.3 mm), amphibole (3–5%, 0.4–2.6 mm), and 54% fine-grained aphanitic to cryptocrystalline groundmass (see appendix 7 for photomicrographs). The amphibole is typically dark brown with well-developed opaque reaction rims about 180 μm wide. Plagioclase crystals typically are zoned and have concentric spongy, inclusion-rich regions.

Amphibole gabbro inclusions are common in at least the lower part of Ogres Brow basaltic andesite. One of the inclusions (09KCnye107, see photomicrograph in Appendix 7) was examined. It contains 47% amphibole, 23% clinopyroxene, 11% plagioclase, 9% void space, 8% interstitial magma, 1% opaque oxides, and 1% olivine, The amphiboles are brown to dark reddish brown, euhedral, and 5-7 mm in diameter. Opaque reaction rims on the amphiboles are about 20 μm wide—a small fraction of the width of reaction rims on amphibole phenocrysts in the enclosing lava. Clinopyroxenes are subhedral and as large as 3 mm when not included in amphibole, but rarely more than 1 mm when surrounded by amphibole. Plagioclase crystals are anhedral, rarely larger than 1 mm, and in most cases included in amphibole. Voids are angular, and defined by the euhedral amphibole crystal faces. About half the voids are filled with magmatic material consisting of very elongated (up to 0.8 mm long, aspect ratio >10), hollow quench plagioclase crystals with small amounts of interstitial brown glass.

Rye basaltic andesite (Qrm)

Rye basaltic andesite (Qrm) lies between Rye point and the Ogres Brow on the east flank of Kasatochi (fig. 18). At low elevation it forms East point and an unnamed point 90 m south. Other exposures are in a 30-m-high cliff starting at 40 m asl that is 200 m northwest of Rye point and a 20-m-high cliff starting at 50 m asl that is 150 m west of East point. Scattered outcrops define a band that increases in elevation northward to about 150 m asl. We infer that Rye basaltic andesite continues upslope, although buried below 2008 eruption and perhaps earlier deposits because there are no major breaks in slope between the tops of the cliff exposures and the crater rim. It

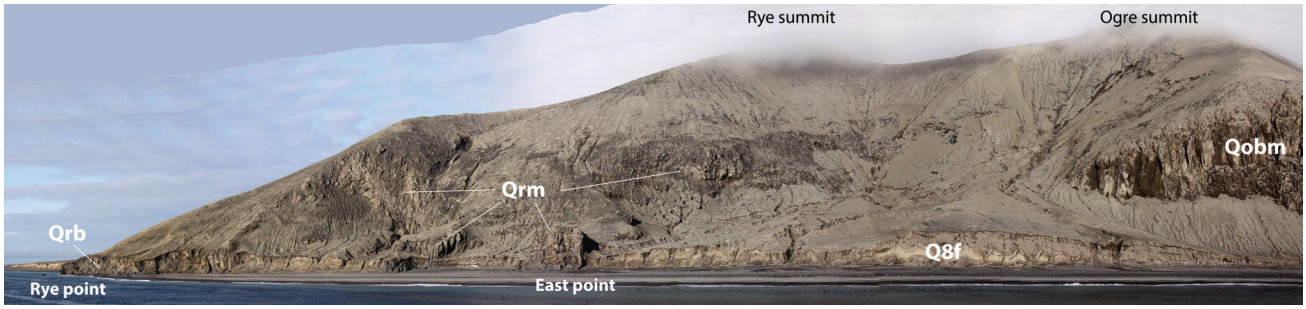

Figure 18. View of the eastern shore of Kasatochi, showing outcrops of Rye basalt (Qrb), Rye basaltic andesite (Qrm), Ogres Brow basaltic andesite (Qobm), and a 2008 pyroclastic fan (Q8f). Photograph by J. Williams, USFWS, June 12, 2009.

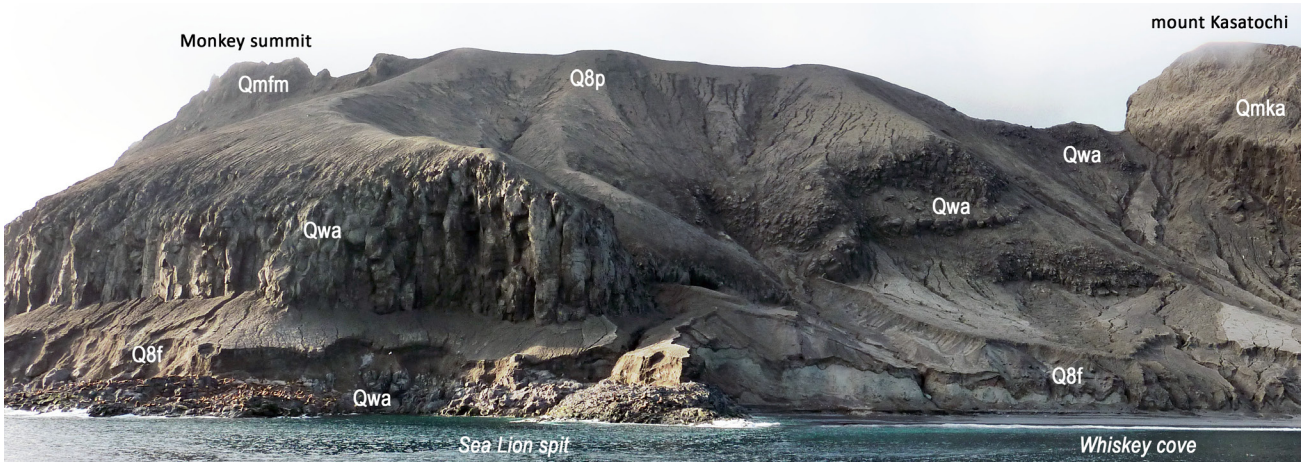

Figure 19. Photograph of the north–northwestern coast of Kasatochi, showing outcrops of Whiskey andesite (Qwa), Monkeys Forehead basaltic andesite (Qmfm), Mount Kasatochi andesite (Qmka), 2008 pyroclastic deposits (Q8p), and 2008 pyroclastic fans (Q8f). Photograph by C. Nye, June 12, 2009.

may underlie Rye summit. Thick lavas exist in the crater wall upslope from Rye basaltic andesite outcrops, and the uppermost of these may be the same flow as is exposed on the flanks, but crater wall lavas could not be sampled for verification. Because Rye basaltic andesite could not be traced unequivocally to any of the crater wall lavas, none are shown as Rye basaltic andesite.

On its southern margin Rye basaltic andesite appears to overlie Rye basalt, although the contact itself is not exposed. We infer that Rye basaltic andesite is younger than Rye basalt based on this geometry. On its northern margin the stratigraphic relationship between Rye basaltic andesite and Ogres Brow basaltic andesite is unclear. It appears that the boundary between the two units lies in a steep, broad gully system and overlapping relationships are hidden. If the thick lava mass below Rye summit is Rye basaltic andesite then stratigraphic relations exposed in the wall favor the interpretation that Rye basaltic andesite is older than Ogres Brow basaltic andesite.

Rye basaltic andesite (56.5–56.6 wt.% SiO_2) is porphyritic, with phenocrysts of plagioclase (33–37%, 0.3–1.2 mm), clinopyroxene (8–10%, 0.3–1.2 mm), orthopyroxene (2–4%, 0.3–0.4 mm), oxides (2–3%, 0.2–0.3 mm), amphibole (0–1%, 0.4–1.3 mm), and 49–53 percent aphanitic groundmass. Plagioclase crystals typically are zoned and have concentric spongy, inclusion-rich regions. Amphiboles are dark brown, and have opaque reaction rims up to 90 μm thick.

Rye basaltic andesite is petrographically and geochemically nearly indistinguishable from Whiskey andesite, described below. Rye basaltic andesite is a very-high-silica basaltic andesite, and Whiskey andesite is a very-low-silica andesite. We map these as two separate units because the stratigraphic relationships and geochronologic data indicate that they are significantly different in age. If a more thorough dating program were undertaken the stratigraphic relationships might necessarily be revised.

Rye basalt (Qrb)

Rye basalt (Qrb) is exposed at and near Rye point on the eastern coast of the island (fig. 18). Here, dense lava forms sea cliffs 10–12 m high composed of parallel vertical columns about 2 m wide. The total width of continuous, unbroken, homogeneous outcrop is 175 m. Upslope from this outcrop the topography is smooth. The lava appears to underlie Rye basaltic andesite, but the contact is covered and not observable. It is not possible to trace Rye basalt to units exposed in the crater wall.

Rye basalt (50.9–51.3 wt.% SiO2) is a fine-grained plagioclase basalt with phenocrysts of plagioclase (42–46%, 0.2–0.6 mm), olivine (2–4%, 0.2–0.4 mm), clinopyroxene (8–11%, 0.3–1.2 mm), oxides (2%, 0.1–0.3 mm), and 36–45 percent coarse (70 μm) nearly holocrystalline groundmass (see appendix 7 for photomicrographs). Its $^{40}Ar/^{39}Ar$ age is 4.0 ± 2.5 ka (appendix 4).

Whiskey andesite (Qwa)

Several lobes of lava with similar and distinctive trace-element geochemistry exist on the north and west flanks of Kasatochi. These are collectively referred to as Whiskey andesite (Qwa), because their average composition is andesite, although as a group they straddle the basaltic andesite–andesite boundary.

The largest outcrop of Whiskey andesite is on the northernmost point of the island and in adjacent flow lobes in the bluffs and cliffs above Whiskey cove, extending to the crater rim north of mount Kasatochi (fig. 19). The maximum width of this package of flow lobes is 665 m. The longest lobe extends from the rim 560 m downslope to the shore. The shortest flow lobe is about 200 m long, terminating in a 30-m-high cliff midway between the rim and shoreline. The large flow lobe that forms the northernmost point on the island has a curved central spine with a slope of ~17 degrees, which dips northward then northwestward from the rim. The broad, upper surface of this flow lobe extends many tens of meters perpendicularly to the central spine, which drops both seaward and away from the spine with a composite slope of about 25 degrees. The distal end consists of three low, relatively flat lobes that extend into the Bering Sea at Sea Lion spit. These lobes are 50–100 m in width and length, with upper surfaces as high as 6 m asl, and are the haul-out of a large sea lion colony. Directly behind these shoreline platforms, the lava forms near-vertical cliffs 60–80 m tall. Presumably the sea lion platforms are wave-cut, and the thick flow lobe once extended farther seaward. Within the 60–80 m sea cliffs the lava is dense, and in moderately-well-developed vertical columns 2–3 m wide, with column sides composed of multiple successive chisel marks. Subhorizontal fracture of individual columns is present, but through-going horizontal structures formed by platy lava or intra-flow breccia are absent, which indicates that this is a single lava flow.

Immediately to the southwest of the main flow lobe, at mid slope above Whiskey cove, are two or three smaller flow lobes of andesite similar in hand-specimen appearance, petrography and geochemistry to the main lobe. These flow lobes end at smaller cliffs 20–30 m high at mid-slope. They are separated from each other by areas of lower slope, now covered by 2008 deposits, which are presumably intra-flow breccias, formed when a pulse of the larger flow unit broke out at the surface and overran the rubbly surface of earlier parts of the flow. Lava exposed in the upper crater wall forms relatively thin flows separated by breccia.

Lava that is petrographically and geochemically similar to, and is correlated with, the northern Whiskey andesite, crops out on the southwestern upper flank between Peregrine ravine and Jack peak. This lava forms a broad band of large blocks with an aggregate thickness of about 20 m. The immediately adjacent crater wall contains a massive lava 110 m thick, overlain by about 50 m of Luna pyroclastic deposits, in turn overlain by 2008 deposits. The thick lava is presumably correlative with the band of lava blocks on the slope, although it was not accessible for sampling or detailed inspection.

Whiskey andesite (56.0–58.3 wt.% SiO_2) is porphyritic, and contains phenocrysts of plagioclase (34–42%, 0.2–0.9 mm), clinopyroxene (7%, 0.4–1.5 mm), orthopyroxene (3–4%, 0.3–0.6 mm), oxides (2–4%, 0.2–0.4 mm), amphibole (2%, 0.4–0.8 mm), and 43–53 percent fine-grained groundmass (see appendix 7 for photomicrographs). Plagioclase phenocrysts are zoned and contain extensive sieved regions. Unzoned, unsieved plagioclase crystals occur in crystal clots in some samples. Reaction rims on amphiboles are about 90 μm thick, and completely replace smaller amphibole crystals. There are two petrographic subtypes of Whiskey andesite (see photomicrographs, appendix 7); one is more vesicular and has less groundmass, and the other has fewer vesicles, more groundmass, and about one weight percent higher silica. Both subtypes have the same mineralogy and relative proportions of mineral species.

A $^{40}Ar/^{39}Ar$ age of 8.9 ± 2.0 ka (appendix 4) was obtained from a sample on the northernmost point of the island.

Gregs Mighty basalt (Qgmb)

Gregs Mighty rock is a name given by USFWS to a fin of porphyritic olivine clinopyroxene basalt just north of the northern end of the Ogres Brow. Prior to the eruption, it extended 75 m perpendicularly to the coast, was about 5 m wide and 12 m tall (fig. 20), and is the basis for the unit name Gregs Mighty basalt (Qgmb).

The base of Gregs Mighty rock comprises unusually straight, vertical columns about 80 cm wide with well-developed horizontal bands at 10–20 cm intervals. (The horizontal bands, often called 'chisel marks' or 'striae', form by the episodic advance

Figure 20. Gregs Mighty rock, viewed from the north on August 8, 2011. The 2008 eruption covered Gregs Mighty rock and the adjacent beach with tens of meters of pyroclastic debris. By late 2011 the beach and sea-level outcrops had been re-exposed, and 10–12 m of 2008 eruption deposits remained capping the rock. By late 2013 the eruption deposits had been eroded from the top of the rock. Photo by J. Williams, USFWS, June 18, 2010.

of cooling fractures, forming columns as the lava cools and contracts in place.) Many, but not all, of the vertical cooling fractures between columns continue into the upper two-thirds of the unit. The upper part of Gregs Mighty rock consists of poorly formed, irregular columns and fracture-bounded blocks 2–4 m in diameter.

Pre-eruption photographs show that Gregs Mighty rock is part of a package of lava flows that extends 800 m northward along the coast from stratigraphically beneath the northern part of the Ogres Brow to just east of The Monkeys Forehead (fig. 21). This package is up to 60 m thick and consists of a lower ~10-m-thick unit of one to two flows characterized by moderately-well-formed vertical columns 1–3 m in diameter and an upper unit of thin, parallel, laterally extensive monolithologic flows separated by breccias composed entirely of fragments of the lava. There are at least 15 dark-gray stacked lavas, each about 1.5 m thick and of constant thickness for more than 200 m. Individual lavas are separated by about 1.5 m of red scoria and interflow breccia. It is likely that the individual lava layers are successive flow lobes formed during a single effusive eruption.

Gregs Mighty basalt was almost completely buried by the 2008 eruption; in June 2009 only a few meters of Gregs Mighty rock protruded from the beach bluff cut into the 2008 deposits, and a small exposure of the thin stacked flows was visible beneath the northern part of the Ogres Brow (sample 09KCwes001). As the beach and beach bluff eroded, more and more of the unit was exposed, and the extent of exposure of Gregs Mighty rock became a key visual indicator of the rate of geomorphic change. By 2010 there were beach exposures of the lower unit, permitting the collection of samples 10KCnye005 and 10KCnye006 (note that those sample locations plot in 2008 pyroclastic flow fan deposits on the geologic map, sheet 1). With continued erosion and the reappearance of the pre-eruption boulder beach and cliff shoreline, the beach became unwalkable and sea conditions did not permit landing for additional sampling of the newly exposed thin stacked lavas.

A visually similar package of lower, thicker, lavas and upper thin stacked lavas is exposed low on the north–northeast wall of the crater, a lateral distance of only 300 m. This is the only other exposure of thin stacked lavas on the island, thus it is likely they are the same unit as Gregs Mighty basalt, but because they could not be sampled and the correlation confirmed, they are shown on sheet 1 as unit Qwtf.

Gregs Mighty rock is unlike any of the other mapped lavas in that hand-specimen appearance is dominated by large clinopyroxene and olivine phenocrysts. It contains phenocrysts of plagioclase (22–28%, 0.3–0.9 mm), olivine (6–9%, 0.7–2.7 mm), clinopyroxene (15–20%, 0.4–3.5 mm), oxides (0–1%, 0.1 mm), and 50–53 percent groundmass composed of 5–10-µm-diameter microlites of plagioclase, opaque oxides, and ferromagnesian minerals (see appendix 7 for photomicrographs). Plagioclase phenocrysts are much smaller than pyroxene or olivine phenocrysts, and are zoned with concentric sieved regions. Clinopyroxene phenocrysts are euhedral crystals or crystal fragments. Olivine phenocrysts are euhedral to subhedral and contain opaque spinel inclusions (magnetite) rather than translucent brown chromite.

Peregrine lava (Qpl)

Peregrine lava (Qpl) consists of two lava masses at the northern end of the southwest-facing cliffs on the southwest flank of Kasatochi (fig. 22). The northernmost is about 90 m long and 40 m thick and was the source of the now-buried Troll talus auklet nesting colony. The other is about 180 m long and 80 m thick. Both lava masses overlie and are overlain by diamicts. They are roughly lens shaped, and broken into massive blocks and irregular columns meters to several meters in diameter. Margins of the lava lenses are only observable from a distance, but are more finely jointed, blocky, and rubbly. These two lava masses are interpreted to be near-vent flow lobes.

One sample from the northern end of the northern lava mass was collected and analyzed for this study; another sample was collected in 2005 from a now-buried location at lower elevation than our sample and its analysis is included (T. Neal, USGS, oral commun.). The lava is oxidized, pinkish-gray basaltic andesite (55.6–57.0 wt.% SiO_2), and contains phenocrysts of plagioclase (30–30%, 0.2–0.9 mm), amphibole (18%, 0.4–1.7 mm), clinopyroxene (2%, 0.2–0.5 mm), oxides (1%, 0.1–0.1 mm), and 49% aphanitic groundmass. Opaque reaction rims on amphibole crystals are 150 µm thick, thick enough to entirely replace smaller amphibole fragments. Peregrine lava is the only unit in this study with substantially more modal amphibole than pyroxene.

Peregrine glaciovolcanic deposits (Qpg)

The Peregrine glaciovolcanic deposits (Qpg, sheet 1) comprise a 1.2-km-long section of volcaniclastic rocks exposed primarily in outward-facing cliffs on the southwestern part of

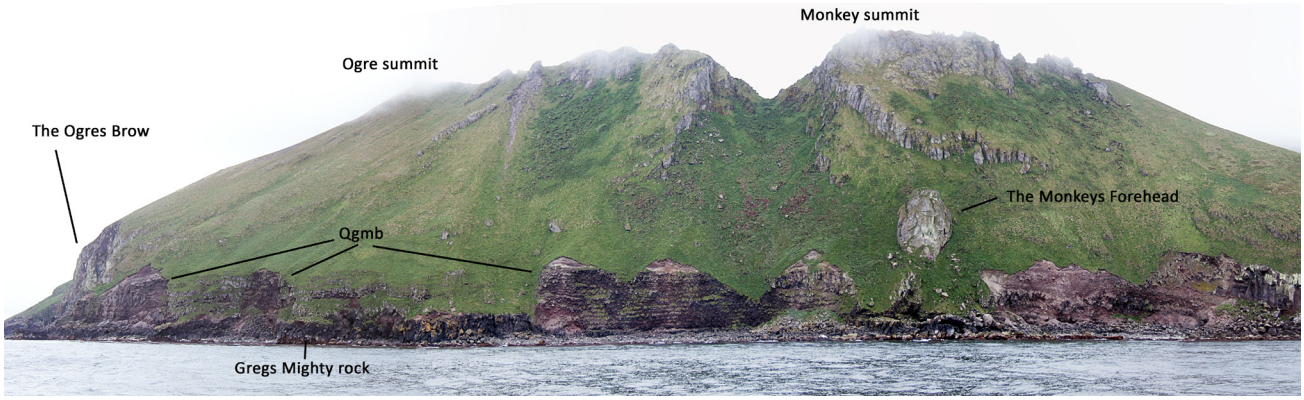

Figure 21. Pre-eruption photograph of the north–northeastern coast of Kasatochi, showing the extent of Gregs Mighty basalt (Qgmb) (thin lavas in sea cliffs), the Monkeys Forehead (large outcrop in midslope, right-center), and The Ogres Brow (midslope cliff on left skyline). Eruption deposits initially covered Qgmb outcrops almost entirely, but subsequent erosion during the course of this study exposed portions of the preexisting outcrop. The field of view is approximately 850 m wide. Photograph by Brie Drummond, USFWS, August 23, 2007.

the island (fig. 22). The unit name is adopted from the informal USFWS names Peregrine ravine and Peregrine peak. The base of the exposed section was at sea level prior to the 2008 eruption; the highest exposed outcrops range in elevation from about 190 m in the north to 200 m midway to 100 m in the south.

The base of the section is now covered by 2008 eruption deposits that decrease in thickness from 45 m in the north to 15 m in the south at crests of pyroclastic fans, and from 20 m in the north to 8 m in the south between fans. The top of unit is roughly parallel to the bedding in the upper part of the unit.

Bedding attitudes are consistent to a first order, but there is crosscutting between major packages of beds as well as local crosscutting of individual beds. As a whole, the apparent dip is to the southeast, but true dip is southerly.

There are two principal facies in the unit. The first, dominantly at the unit's base, is massive, poorly sorted volcanic debris (hyaloclastite). It contains monolithologic angular blocks of basalt from a few centimeters to many tens of centimeters in diameter and a small proportion of centimeter-sized, subrounded, variegated lava clasts supported by a gravelly, variously red, orange, yellow, and brown matrix of lava fragments and volcanic debris (fig. 23). The presence of pristine clinopyroxene megacrysts floating in the matrix suggests that the matrix was produced virtually in situ by fragmentation of the lava on contact with water. An origin by subaqueous autobrecciation is also supported by the lack of well-defined bedding, high matrix volume relative to clasts, and faceted, primary lava clasts with jigsaw fractures characteristic of quenched magma. This unit, most accessible at Shag rock, has many of the characteristics of peperite, but the lack of incorporated preexisting sediments argues against use of the strictly defined term (Skilling and others, 2002). The basalt (50.9 wt.% SiO_2) has phenocrysts

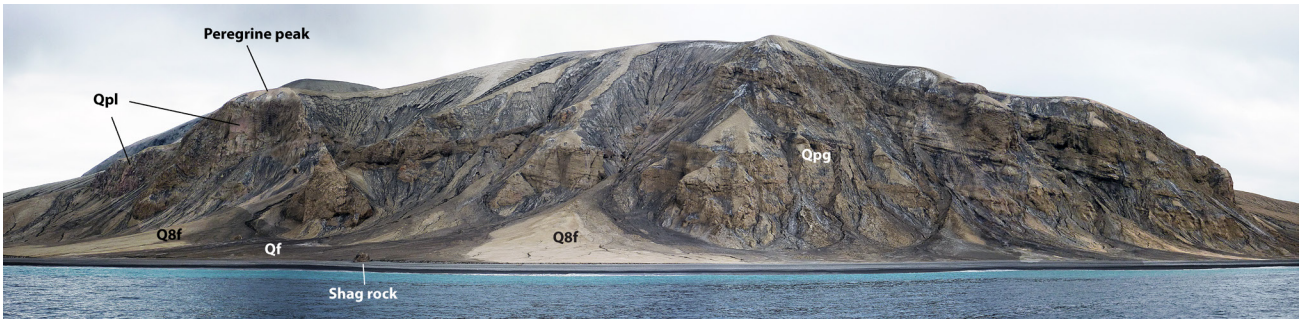

Figure 22. Panorama of the southwestern flank of Kasatochi; view is to the northeast. The field of view is 1.3 km wide, and the maximum elevation is about 200 m. The strongly layered units on the right are Peregrine glaciovolcanic deposits (Qpg). Shag rock is embedded in the beach in the left foreground. Massive cliffs near the left skyline are Peregrine lava (Qpl). Fans of 2008 pyroclastic deposits emanate from small, steep, bedrock basins (Q8f). Alluvium (Qf) has been deposited on top of 2008 deposits. See appendix 1 for high-resolution coastal panoramas. Photograph by C. Nye, June 12, 2009.

Figure 23. Peregrine glaciovolcanic deposits (Qpg) at Shag rock. Dominantly massive, matrix-supported unit of monolithologic angular to subangular clasts centimeters to tens of centimeters in diameter in a coarse matrix. Some clasts have poorly developed radial fracture. Hammer handle is 40 cm long. Inset shows close-up of the matrix (~10 cm wide), showing coarse matrix and free-floating euhedral clinopyroxene megacrysts up to 5 by 10 mm.

of plagioclase (33%, 0.2–0.8 mm), relict olivine (3%, 0.2–0.5 mm), clinopyroxene (5%, typically 0.8–2 mm, occasional larger megacrysts), and oxides (1%, 0.2 mm), and 59 percent fine-grained (10–50 μm) nearly holocrystalline groundmass (see appendix 7 for photomicrographs). Plagioclase phenocrysts typically have spongy cores and clean, euhedral rims, but show less complicated crystallization histories than plagioclase phenocrysts from most other units. Plagioclase and clinopyroxene phenocrysts show no evidence of alteration, but the olivines are mostly to completely replaced by brown to green fibrous cryptocrystalline material, although original euhedral crystal forms are preserved.

The other prominent facies, which constitutes the majority of the Peregrine glaciovolcanic deposits (Qpg), consists of bedded, volcaniclastic, laharic debris flows. Individual beds are decimeters to meters thick and most can be traced laterally for many hundreds of meters. They consist of angular, poorly sorted monolithologic lava fragments with meter- to decimeter-sized clasts supported by a gravelly matrix (fig. 24). At the southern end of the unit there is slumping and soft-sediment deformation of bedding, which is presumably syneruptive, as well as a small dike, the radially fractured tip of which is apparently broken off and laterally displaced (fig. 25). The dike (52.0 wt.% SiO_2) is petrographically similar to the basalt in the Shag rock hyaloclastite, although plagioclase phenocrysts are somewhat larger, and clinopyroxenes less numerous. Similar to the Shag rock basalt, plagioclase and pyroxene crystals are unaltered, while olivine crystals are relict—the euhedral crystal forms are replaced by cryptocrystalline material. Juvenile fragments from the lahars are monolithic within individual beds, but heterolithic between beds.

These volcaniclastic deposits are water-laid flows that require a source higher in elevation than the deposits and imply some sort of lateral restriction (such as valley walls) to contain the flows. Neither a higher-elevation source nor a way to confine the flows such that they stack to an aggregate thickness of at least 200 m is currently present. Among potential geologic explanations for the origin of the deposits are: (1) deposition in a subglacial vault, with ice providing the necessary confinement to hold water well above current sea level and to provide the lateral confinement necessary for the observed stratigraphic thickness to accumulate; (2) deposition in a shallow marine environment, followed by uplift of hundreds of meters and subsequent erosion; and (3) deposition on the slopes of a larger ancestral volcano, most of which has since been eroded.

We consider the first explanation—eruption and deposition in a subglacial vault—to be the most plausible. The Peregrine glaciovolcanic unit seems to have been deposited during the time of MIS 6 glaciation (see discussion of the age of Peregrine lava, below). While the record of Pleistocene glaciation is less complete in the Aleutian Islands than elsewhere in Alaska it is known that at least Wisconsin-aged glaciation was widespread; that ice extended from the islands onto insular shelves; and that at least at Adak the top of the ice cap might have been hundreds of meters above topographic high points (Karlstrom, 1964; Thorson and Hamilton, 1986). Thorson and Hamilton (1986) make the point that "Extensive ice caps covered most of the Aleutian Islands during late Wisconsin time; hence, it is not surprising that little evidence of earlier glaciation has been recognized on land." However, fragments of older till

Figure 24. A representative portion of upper Peregrine glaciovolcanic deposits (Qpg). The dark gray bed is approximately 2 m thick. Photograph by C. Nye, August 10, 2009.

presumed to have been deposited during MIS 6 glaciation have been described from Amchitka (Gard, 1980) west and south of Kasatochi and, like Kasatochi, isolated and distant from high, mountainous areas. The hypothesis that an ice cap existed over Kasatochi at the time Qpg was deposited is supported by geologic evidence for widespread ice caps in the Aleutians, likely grounded on the extensive portions of the summit platform of the Aleutian Ridge that were emergent during low sea levels during major glaciations. Other examples of potentially subglacial volcanics are not common in the Aleutians, but they exist. At Okmok, for instance, fragmental, apparently glaciovolcanic rocks exist as high as 1,000 m on ridges outside the caldera rim, and tuyas on the outer southwestern flank suggest formation in water depths of up to 350 m (note that these are not the tuyas that formed inside the caldera during the time a large intracaldera lake existed).

While eruption within a subglacial lake seems entirely plausible, hypotheses involving submarine eruption and rapid uplift or erosion of most of an ancestral volcano, leaving behind only the Peregrine units, require either uplift or erosion at rates that seem unlikely given the young age of Peregrine deposits.

We interpret the Peregrine glaciovolcanic deposits unit (Qpg) to have formed during Pleistocene time in a subglacial lake, the lower unit to have formed by autofragmentation of lava erupted into water, and the upper unit to have formed by remobilization of erupted breccia in water-rich flows.

Detailed stratigraphically controlled sampling was not possible because most exposures are in cliffs. The samples we were able collect vary from 51 weight percent SiO_2 basaltic andesite to 59 weight percent SiO_2 andesite. All are porphyritic, and have modes dominated by plagioclase and clinopyroxene; none have amphibole phenocrysts. Groundmasses vary from microcrystalline to fine grained; none are glassy. In all Peregrine lavas plagioclase and pyroxene show no visible alteration, but analyses have variably low analytical totals (as low as 94.9%), presumably reflecting the hydration and alteration of the groundmass,

Figure 25. A 35-m-tall outcrop at the southernmost end of the Peregrine glaciovolcanic deposits (Qpg). Note the vertical, gray, meters-wide dike (center left) with lateral offsets and a truncated, radially-fractured tip (arrow); folding and slumping (lower right); and vegetation sprouting from pre-eruption root mats. Photograph by C. Nye, June 18, 2012.

which is visible in thin section.

Variations in diagnostic trace-element ratios (such as Th/Nb) span the range of all Kasatochi samples, rather than being restricted to a subset of the compositional space, as are samples from other units. Our interpretation is that the entire Qpg unit represents deposits from multiple discrete eruptive episodes, with hiatuses of hundreds to thousands of years. Our sample density is not sufficient to subdivide Qpg based on chemical stratigraphy.

CRATER WALL

The crater wall exposes a variety of volcanic lithologies, including lava flows, volcaniclastic breccias, pyroclastic flow deposits, tephra, and dikes. However, outcrops of lithologic units exposed solely below the crater rim were not accessible because the steepness of the crater walls ranges from the angle of repose to vertical (fig. 26). Furthermore, because of safety concerns it was agreed that attempts to work inside the crater were strictly prohibited during fieldwork supported by the *M/V Tiĝlax̂*. Therefore, most crater wall units were defined morphologically and mapped using panoramic photographs taken from various positions on the rim during the few clear days available, satellite images, and oblique aerial photographs made available to us by pilots. Some units primarily exposed in the crater wall were also exposed along the rim; those were sampled wherever accessible and correlated with units exposed on the flanks on the basis of petrography, geochemistry, and geomorphology. Lava exposed on the northeastern crater rim was not visited because of terrain, time, and weather constraints.

Colluvium (Qwc)

Fans and sheets of colluvium (Qwc) on the crater wall overlie and obscure underlying units. These necessarily postdate the 2008 eruption because the eruption removed most of the pre-existing wall. The unit consists of poorly sorted boulder debris derived from farther upslope.

2008 pyroclastic deposits (Qw8)

Relatively thin deposits of undifferentiated 2008 eruption pyroclastic flow and fall (Qw8) mantle some areas of the crater wall, typically where slopes are less than about 50 degrees. This unit is shown where it is thick enough to obscure underlying units.

Dikes (Qwd)

A fang-shaped remnant of northwest-trending dikes (Qwd) exists along the northern crater wall (fig. 27). There are about a dozen tan-weathering gray dikes. Remnants of preexisting rock are not visible between individual dikes. The total outcrop is about 75 m wide perpendicular to the dikes and tapers to a point about 125 m asl, forming a fang that is free standing on all but the northeastern side. The dikes trend toward the northern crater wall, about 200 m distant, but are not present in that wall. Whether this is a function of the original lateral extent of the dikes or truncation of the dikes by explosion or erosion is unclear. It is also not known which, if any, of the lava units were fed by these dikes.

These dikes are the only exposed feeders; dikes generally are not seen elsewhere in the crater wall or at the surface on the flanks; thus, the conduits that fed most of the eruptions must have been confined to the area below the crater lake for

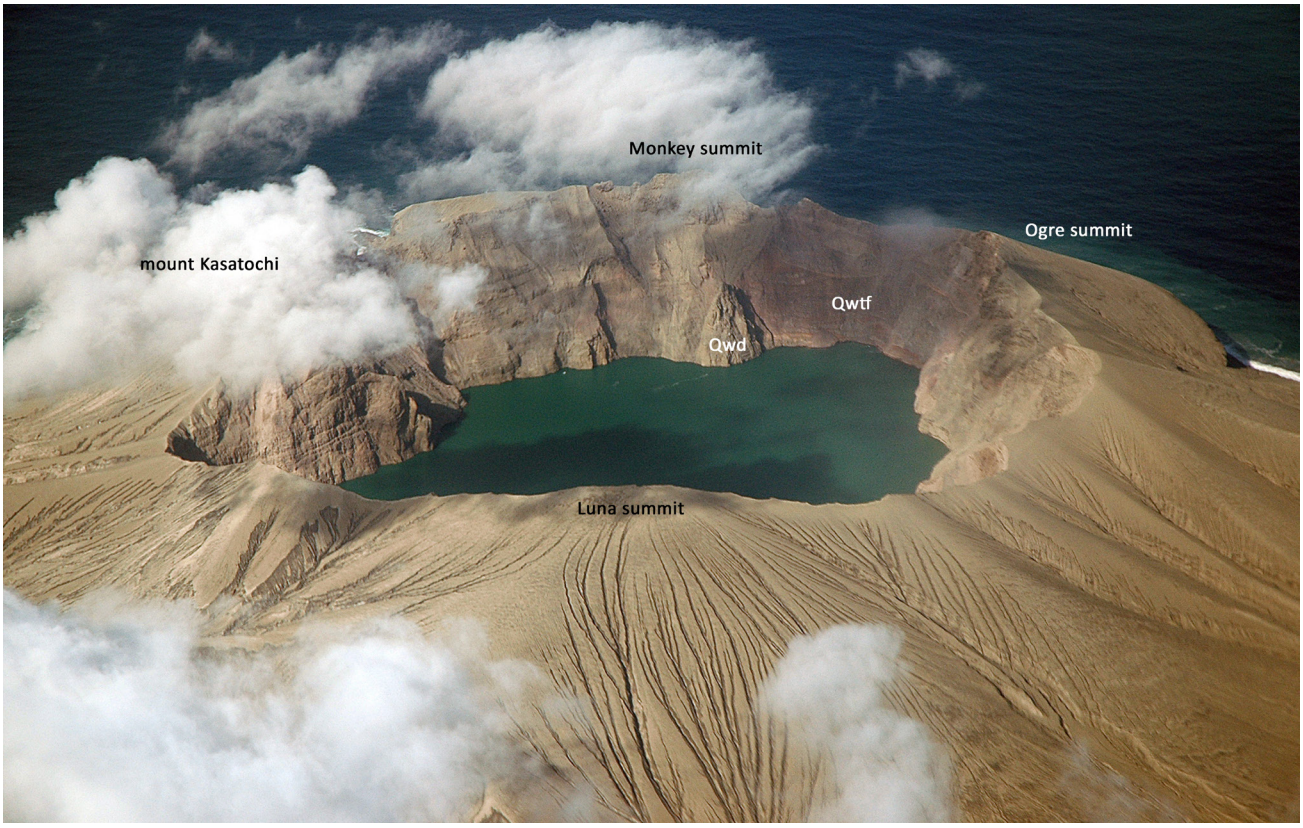

Figure 26. Aerial view of Kasatochi's eastern, northern, and lower western crater wall. The greenish color of the crater lake contrasts with the blue of the Bering Sea beyond, and is likely the result of ongoing fumarolic emissions into the base of the lake. Photograph by Burke Mees, September 8, 2011.

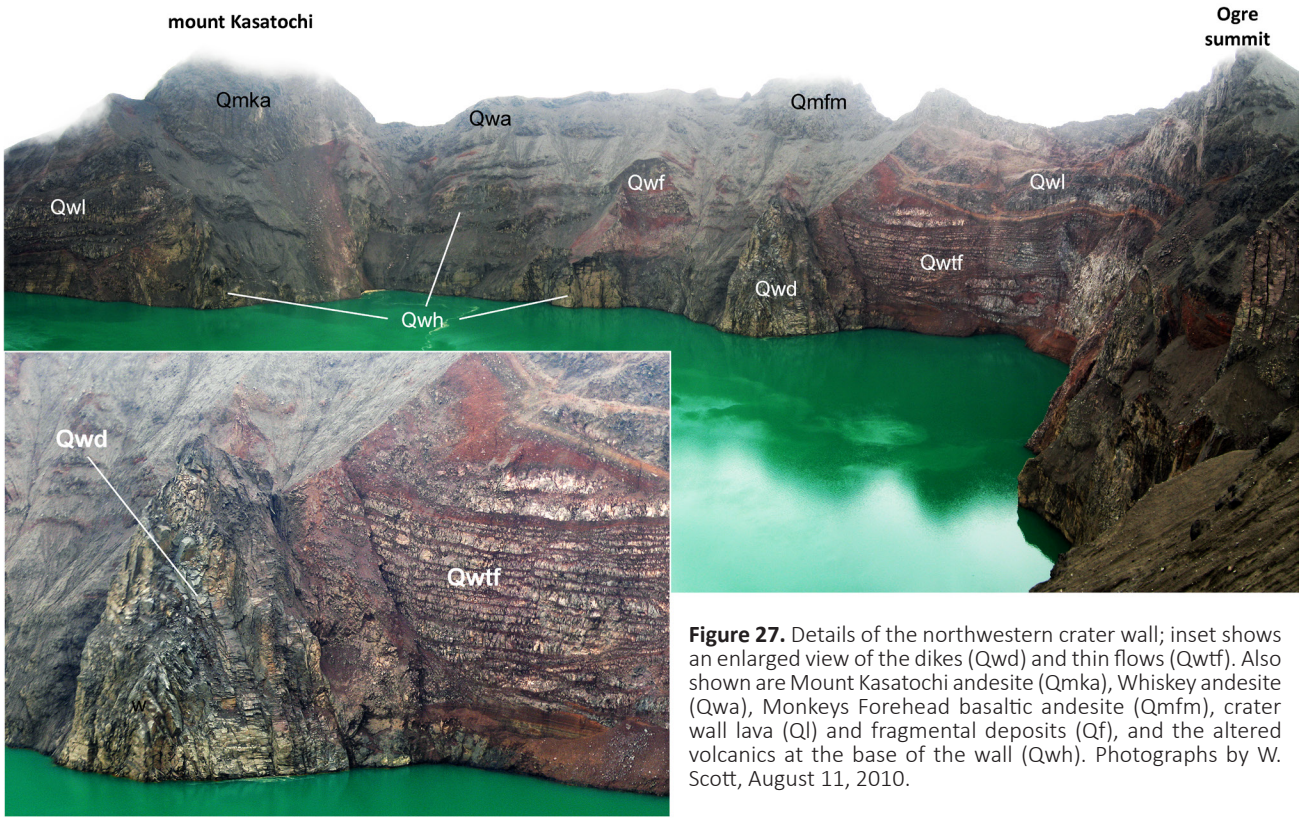

Figure 27. Details of the northwestern crater wall; inset shows an enlarged view of the dikes (Qwd) and thin flows (Qwtf). Also shown are Mount Kasatochi andesite (Qmka), Whiskey andesite (Qwa), Monkeys Forehead basaltic andesite (Qmfm), crater wall lava (Ql) and fragmental deposits (Qf), and the altered volcanics at the base of the wall (Qwh). Photographs by W. Scott, August 11, 2010.

the duration of volcanism at Kasatochi. The sole exception is the small dike seen in the southernmost part of the Peregrine glaciovolcanic deposits (fig. 25).

Fragmental volcanic deposits (Qwf)

Portions of the crater wall dominated by coarse, fragmental deposits are mapped as unit "fragmental volcanic deposits" (Qwf). The unit contains poorly sorted, crudely bedded red to brown volcanic debris apparently from scoria deposition, as well as marginal lava-flow breccia and rubble. In general, individual beds are meters thick. Also included are a few thicker units that are more uniformly buff colored and appear to be localized channel-filling pyroclastic flows.

Lava (Qwl)

Portions of the wall dominated by dense lava are mapped as "wall lava" (Qwl). Areas shown as a single outcrop of Qwl may contain multiple overlapping lava masses. Individual lava units are lens shaped, but with varying aspect ratios, and are a few meters to 65 m thick. Lava masses are apparently all lava flows, and are shades of gray, with rubbly black to reddish margins with more massive interiors that have crude, vertical, meters-thick columns. Importantly, lavas with small-diameter curved, radiating, or fanning columns suggesting ice-contact volcanism are absent.

Thin lava flows (Qwtf)

A package of thin, parallel, lava flows is exposed in the north crater wall (fig. 27). The entire package is 45–65 m thick and contains more than 20 individual flow units. Individual flow units are 1–4 m thick, and separated by red scoriaceous layers that are generally about one-quarter of the thickness of adjacent flows. Individual flow units are laterally continuous for a few to several hundred meters, and often pinch out. We interpret this package to have formed from a single eruptive event of lava with lower viscosity than other flows at Kasatochi, and the individual flow units to be successive lobes of that flow.

This package is mapped separately because it is morphologically unique among crater wall exposures. Similar-appearing, stacked flows were also known from the island's outer northern flank near sea level, about 300 m laterally north of the crater wall exposure. The outer flank stacked flows were mostly buried by the 2008 eruption, but were partly re-exposed by erosion of the 2008 eruption deposits during the timespan of this study. The north flank exposures are all Gregs Mighty basalt (Qgmb), and we interpret the inner crater wall unit (Qwtf) to be the same basalt.

The stacked flow unit (Qwtf) overlies the thin tephra unit (Qwp), the heterogeneous lower wall deposits unit (Qwh), and some older, more massive lavas (Qwl). It also appears to be cut by the wall dike unit (Qwd), and a fracture in Qwp parallel to, but tens of meters from, the margin of the dike swarm. The fracture may be a fault that developed as the dike swarm was intruded.

Lower crater wall deposits (Qwh)

A package of heterogeneous volcanic deposits (unit Qwh) from tens of meters to about 140 m thick is exposed at the base of the northwestern crater wall (fig. 28). In part this unit consists of massive lava that lacks clear flow margins and interior columns. Other parts of this unit include thick beds of coarse material with up to subvertical dips. Rocks in this unit commonly have a greenish to tannish cast that is distinct from the gray and red of upper units, suggesting pervasive low-grade alteration, perhaps during subaqueous deposition. We interpret this unit to be the proximal stratigraphic equivalent of Peregrine glaciovolcanic deposits (Qpg) exposed in outward-facing cliffs

on the southwestern part of the island. It appears this unit unconformably overlies a package of thin tephras (wall thin tephra, unit Qwp) on the southwestern end, terminates against the wall dikes (Qwd) to the northeast, and is unconformably overlain by apparently unaltered, recognizably subaerial, lava flows and fragmental debris.

Thin tephra (Qwp)

Tan to reddish-brown, uniformly thin, parallel-bedded deposits (Qwp) form the base of the southern crater wall (fig. 28). There is also an isolated outcrop of apparently similar beds in the western crater wall, presumably the continuation of the southern wall deposits, and small outcrops that were visible at the base of the northeastern crater wall in 2009, and that are now mostly below lake level. There are at least 50 beds, and the aggregate thickness is about 60 m. Individual beds are laterally continuous for hundreds of meters and of constant thickness. Crossbedding, draping, or other depositional variability is not apparent, at least at the scale that can be seen from the crater rim. Grain size is unknown, but there appear to be at least some isolated, matrix-supported clasts decimeters in diameter. We interpret these beds to be thin tephra or pyroclastic flows that record an early phase of explosive volcanism at Kasatochi. This unit may be correlative with distal Peregrine glaciovolcanic deposits (Qpg), but without closer access it cannot be determined if the unit was deposited subaerially or subaqueously.

The eastern end of the unit terminates laterally against lavas along a near-vertical contact, and is unconformably overlain by another lava flow at the top. The western end of the unit is beveled, apparently by erosion, and overlain by the heterogeneous lower wall deposits (Qwh) at the base and lava (Qwl) at the top.

The thin tephra unit (Qwp) is arguably the lowest stratigraphic unit exposed in the crater wall.

PETROGRAPHY

LAVAS AND SCORIAE

Kasatochi lavas consist of porphyritic basalt, basaltic andesite, and andesite. Most samples have 40–60 percent phenocrysts (by volume, normalized void-free) with the exception of some of the most silicic samples that have 15–30 percent phenocrysts (fig. 29); detailed modal data and photomicrographs are in appendix 6. (The term "phenocryst" is used as a general term for crystals notably coarser than those in the groundmass, which may include true phenocrysts precipitated from the host magma as well as preexisting crystals from prior magmas [antecrysts] inherited from elsewhere in the larger magmatic system.) In most samples plagioclase is the volumetrically dominant phenocryst, comprising 60–80 percent of all phenocrysts; clinopyroxene is the next most abundant phase, comprising 10–20 percent of the phenocrysts. Olivine comprises 13–18 percent of the phenocrysts in Gregs Mighty basalt and 3–8 percent in other basalts. Occasional olivines exist in many orthopyroxene-bearing basaltic andesites and andesites. Orthopyroxene forms a

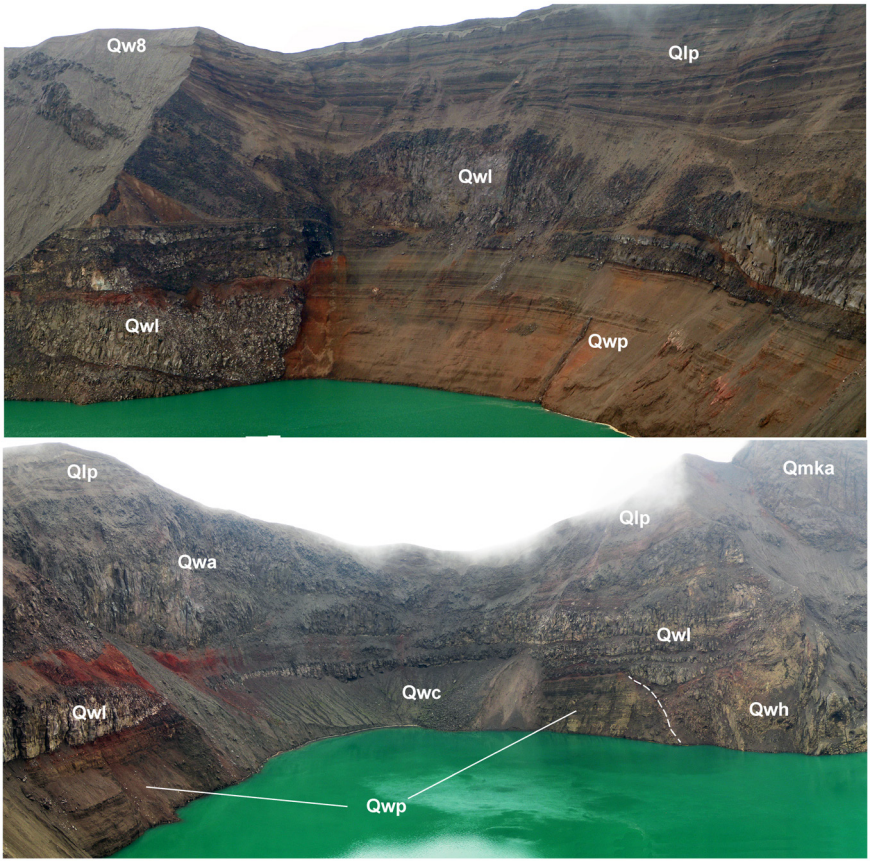

Figure 28. Photographs of the southeastern crater wall taken from the southwestern crater rim (top; photograph by J. Williams, USFWS, August 10, 2010) and the southwestern crater wall taken from the southeastern crater rim (bottom; photograph by W. Scott, August 11, 2010). Crater wall outcrop units also exposed on the flanks are of Luna pyroclastic deposits (Qlp), Whiskey andesite (Qwa), and Mount Kasatochi andesite (Qmka). Units only exposed in the crater walls are lava (Qwl), tephra (Qwp), colluvium (Qwc), and heterogeneous lower wall deposits (Qwh). Qw8 denotes 2008 eruption debris accumulated on less-steep slopes inside the crater. Note the steeply north- (right) dipping planar surface in lower right third of the bottom panel (dashed white line) that separates Qwp from Qwh.

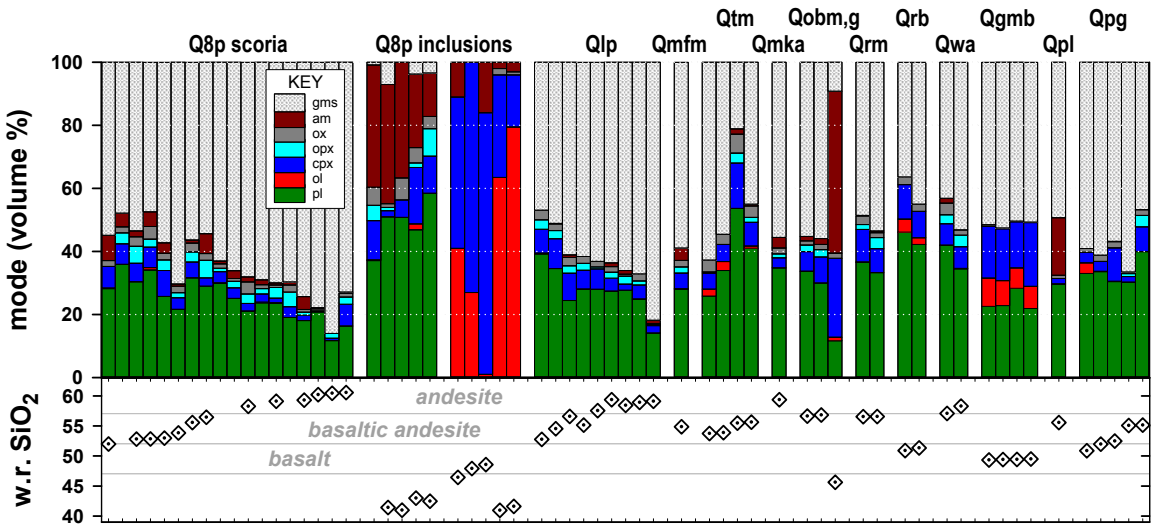

Figure 29. Modal analyses of Kasatochi samples. Modes from this study are based on 1,000-point counts using transmitted light microscopy (data from appendix 6). Modes for plagioclase-free 2008 inclusions are from Kentner (2013). Dotted diamonds (lower panel) are whole-rock SiO_2 contents (appendix 5).

few percent of the mode in most basaltic andesite and andesites.

Amphibole phenocrysts occur in all 2008 scoria, most Luna scoria, and are variably present in other basaltic andesite and andesite units. They generally constitute 1–10 volume percent of phenocrysts when present, but are more abundant in samples from Peregrine lava, Monkeys Forehead basaltic andesite, and Mount Kasatochi andesite. Thick reaction rims on amphibole phenocrysts in basaltic andesite and andesite lavas are typical—reaction rims on amphibole phenocrysts in scoria from 2008 and Luna deposits are less than 10 µm. Amphibole phenocrysts are absent from Gregs Mighty basalt, Rye basalt, and basalt through andesite scoria from Peregrine glaciovolcanic deposits.

Olivine is abundant in Gregs Mighty basalt, common in Rye basalt, present in trace to several volume percent in about 40 percent of other samples, and absent in those few samples with more than 60 weight percent SiO_2. Olivine crystals in orthopyroxene-bearing basaltic andesite and andesite are sparse, corroded or rimmed, and presumably xenocrystic. A few to several volume percent orthopyroxene is present in all samples with greater than about 52.5 percent SiO_2, and is generally subordinate to clinopyroxene in volume.

The groundmasses of all lava samples are microcrystalline, precluding direct measurement of their glass composition by electron microprobe.

Gregs Mighty basalt is petrographically distinct from all other mapped units in that only about half the phenocrysts are plagioclase, with coarse clinopyroxene and olivine constituting most of the remainder in proportions of about 2:1. The olivine and clinopyroxene crystals are up to 2–3 mm wide and 5 mm long, and generally larger than plagioclase crystals.

CUMULATE MAFIC AND ULTRAMAFIC INCLUSIONS

Cumulate mafic and ultramafic inclusions, rounded to subrounded and several centimeters to a several tens of centimeters in diameter, are common in the upper portion of 2008 pyroclastic deposits, occurring with basaltic andesite-dominated scoriae. Gabbroic inclusions similar to those in the 2008 deposits are only rarely found in situ in the lava units, but gabbroic inclusions encased in dense lava are a common minor constituent of beach cobbles.

Gabbroic inclusions are far more abundant than ultramafic (plagioclase-free) inclusions, and are much more common in 2008 deposits than in other units; thus this discussion is primarily about 2008 inclusions, but may be generalizable to other Kasatochi units. 2008 gabbroic inclusions fine-grained enough to have meaningful modes determined in a single thin section have an average of 50 percent plagioclase, 30 percent amphibole, 10 percent clinopyroxene, 3 percent orthopyroxene, 5 percent opaque oxides, up to 7 percent quenched intergranular basalt, up to 9 percent void space, and occasional olivine. For brevity, we use the term "gabbro" for these amphibole gabbros, despite their having lower modal pyroxene and higher modal amphibole than typical gabbros. Amphibole-poor or amphibole-absent pyroxene gabbros or gabbronorites are absent from the inclusion suite. All crystals are exceptionally fresh and unaltered, indicating that the gabbros are portions of a high-temperature crystal "mush", perhaps directly related to the 2008 scoria. Amphibole crystals in the gabbros in contact with magma have very thin reaction rims, which indicates rapid transit from source to surface. Amphibole crystals in the gabbros without magma contact are necessarily unrimmed.

During the course of this study we did find a small number of granitic xenoliths, which are identifiable as such in thin section because the crystals betray low-temperature crustal residence by the presence of small amounts of alteration: clays in plagioclase and chloritic alteration along cracks and margins of pyroxenes. These samples are not included in this study.

The gabbros have widely variable textures (fig. 30). Many are equigranular with evenly distributed grains a few millimeters in diameter. In larger samples mineralogical banding is often pronounced, with irregular bands of amphibole alternating with bands of plagioclase. Grain-size banding also occurs—layers of centimeter-sized grains abruptly transition to bands of millimeter-sized grains. In coarse-grained samples preferential parallel alignment of amphibole prisms is common. Extremely large crystals are not uncommon; in one sample amphibole prisms up to 12 cm long and 2–3 cm wide are set in a matrix of plagioclase only a few millimeters in diameter. Isolated amphibole crystals larger than 3 cm in diameter are present in 2008 basaltic andesite scoria, suggesting that at least some of the inclusions have disaggregated during transport.

Importantly, the gabbros have as much as 16 volume percent intercrystalline space, some of it filled with quenched basalt.

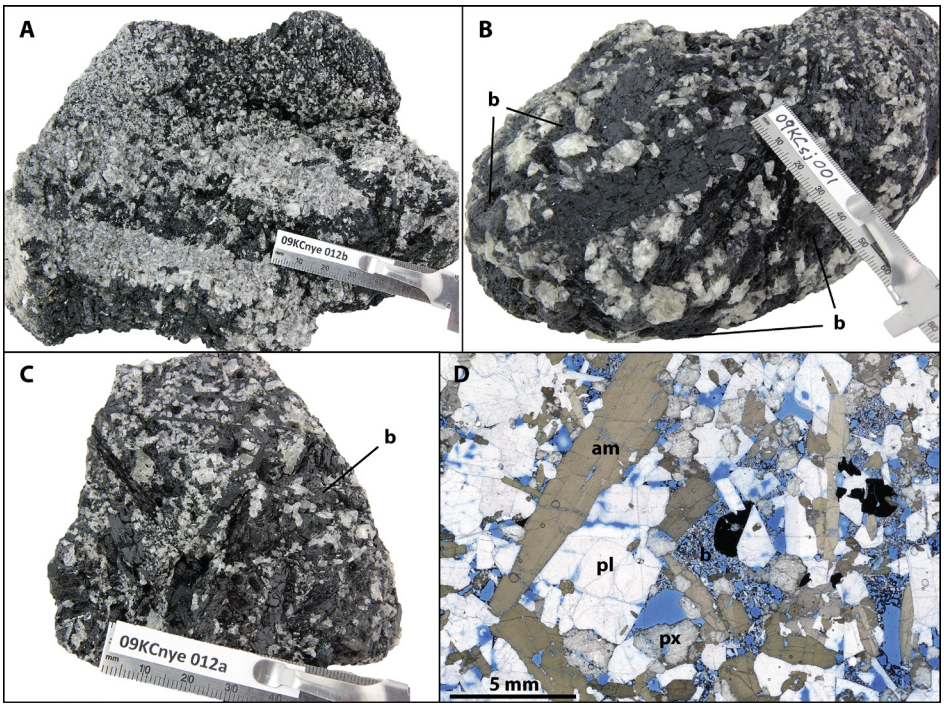

Figure 30. Amphibole gabbro inclusions from 2008 pyroclastic deposits. **A**. An inclusion with pronounced mineralogical layering. **B, C**. Examples of inclusions with elongate amphibole crystals (black), which are often aligned and penetrate a matrix of more equant and smaller amphibole and plagioclase (white). Also shown are small patches of vesicular basalt (b) filling irregular voids bounded by crystal margins. **D.** 20 x 14 mm plane-polarized photomicrograph of a gabbro with representative amphibole (am), plagioclase (pl), and clinopyroxene (px) in addition to basalt (b) that fills or partially fills most, but not all, void spaces (voids are impregnated with blue epoxy). Hand specimen photographs are in full color.

These voids are the highly angular spaces between euhedral crystal faces. In part because of the voids, gabbroic samples are very friable and can be reduced to individual euhedral crystals with light hammer taps. Thus the gabbros are fragile and easily destroyed by wave action; in 2009 gabbroic inclusions were common in beach gravels, by 2011 they were rare. Some of the larger voids are filled or partially filled with dark-gray, vesicular basalt that is more mafic than the most mafic 2008 scoria analyzed. The same basalt also occurs as a thin rind on some samples. It is noteworthy that most of the voids are not filled with magmatic groundmass, despite all the surrounding crystals presumably having crystallized from a melt. This suggests that interstitial melt in the crystal mush was displaced by non-silicate fluid or gas, perhaps derived from the advancing vapor-saturated basalt that entrained fragments of the mush shortly before eruption.

Amphibole-free and amphibole-poor peridotitic and pyroxenitic inclusions were also entrained and erupted in 2008 (Kentner, 2013; this study). Some of the inclusions have a 1–2-mm-thick rind of basalt that is compositionally identical to the basalt that coats and fills voids of some of the 2008 gabbro inclusions.

In some samples amphibole crystals in the gabbros poikilitically enclose small anhedral pyroxene and plagioclase crystals, suggesting they grew by late-stage reaction.

MINERAL COMPOSITIONS

Lavas and scoriae

Plagioclase crystals in the lavas and scoriae have a wide range of compositions in individual samples (fig. 31). An_{95} plagioclase crystal cores occur in all studied lavas and scoriae except for the most silicic sample (a 2008 scoria with ~61.5 percent SiO_2), in which the most anorthitic core was An_{87}. The uniformly anorthitic cores are present despite the linear decrease in whole-rock Ca# (100 × Ca/[Na+Ca], in moles) from 75 to 45 with increasing SiO_2, which would drive plagioclase precipitated from the magmas to more sodic compositions at constant or decreasing total pressure (P_{tot}) or partial pressure of water (pH_2O). Analyzed crystal cores range from at least An_{95} in all but the most silicic sample to as low as An_{80} in basalts, An_{58} in basaltic andesites, and An_{50} in andesites. Crystals in lavas and scoriae typically have large, corroded, optically uniform cores with abrupt transitions to thinner, more sodic rims. Those rims are variable in composition, but the majority are An_{55}–An_{70} (fig. 32).

Clinopyroxene crystals are ubiquitous, and second to plagioclase in abundance. They have Mg# ranging from 94 to 74 (Mg# = 100 × Mg/[Mg + Fe^{2+}], molar), but 80 percent of clinopyroxene cores in most samples lie in the restricted range of Mg# 86–78, regardless of whole-rock SiO_2 or Mg#. The most mafic samples analyzed have clinopyroxenes that are more magnesian by 5 mol. percent on average. Occasional crystals with Mg# as high as 94 are found in samples throughout the compositional range of Kasatochi lavas. 2008 basaltic andesite scoria have clinopyroxenes that are about 5 mol. percent more iron-rich than samples from other units with similar silica contents.

In any closed-system magma the first-formed crystals of liquidus phases will be the most refractory (for example, highest An plagioclase; highest Mg# olivine or pyroxene) and the compositions of those crystals will be determined by the composition and oxygen fugacity (fO_2) of the host magma and, especially in the case of plagioclase, P_{tot} and pH2O. Subsequently nucleated crystals and outer portions of already-formed crystals will be less refractory, and in equilibrium with the evolving melt fraction. The last of any phase crystallized, typically rims on zoned crystals, will be in equilibrium with the final evolved groundmass. The composition of crystals that precipitate from melt is determined by the exchange coefficient, $K_D^{xl/liq}$ (Fe^{2+}/Mg), which in pyroxenes and olivine is, at least to a first order, independent of pressure and temperature. Thus we can test the hypothesis that crystals in a porphyritic lava are true phenocrysts that formed by closed-system cooling and progressive crystallization. If the most refractory cores are in equilibrium with the whole rock, and the least refractory rims

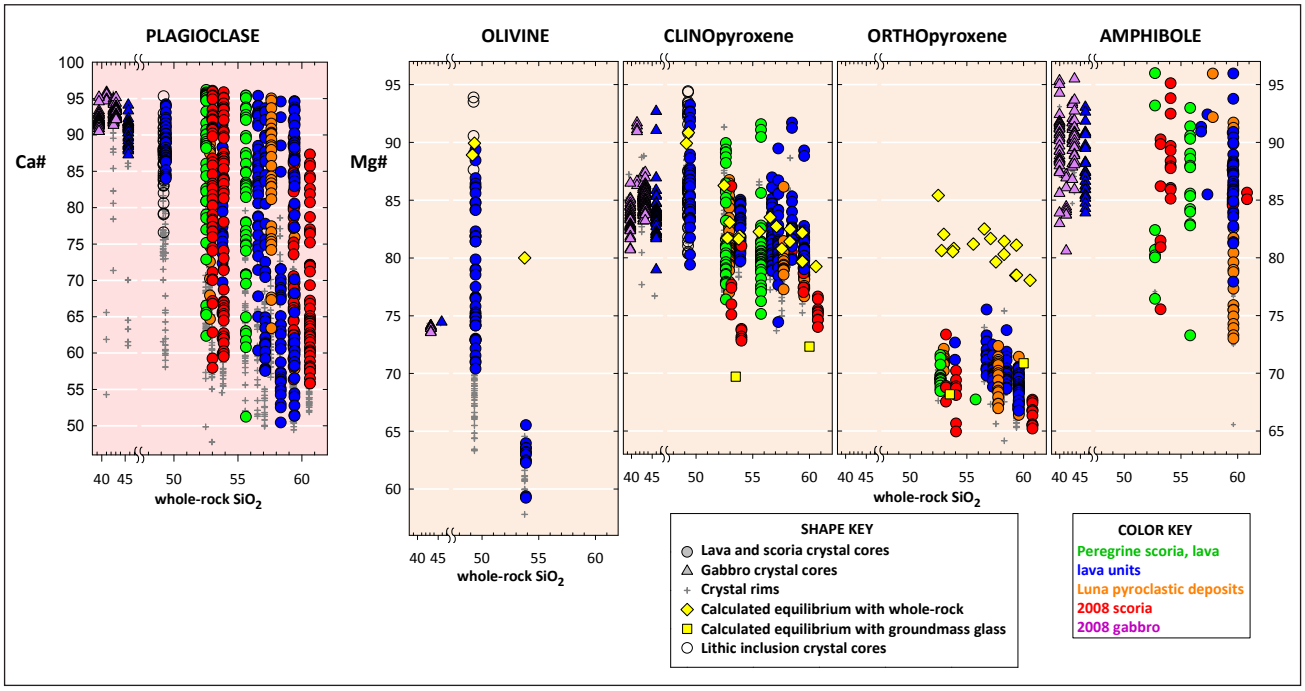

Figure 31. Mineral compositions of map units. Lava and scoria crystal cores (circles) and gabbro crystal cores (triangles) are color-coded by unit; rims are plotted as gray plus signs. Yellow diamonds in olivine and pyroxene panels are the compositions calculated to be in equilibrium with the whole-rock composition at fO_2 of NNO + 1 and $K_D^{xl/liq}(Fe^{2+}/Mg)$ of 0.30 for olivine, 0.27 for clinopyroxene, and 0.29 for orthopyroxene (Roeder, 1974; Grove and others, 1982; Lindsley, 1983). Most samples contain some clinopyroxene crystals that are too magnesian to be in equilibrium with the host whole-rock composition, and all orthopyroxene compositions are too ferric to be in equilibrium with the whole-rock composition. See text for additional discussion. Yellow squares are in equilibrium with 2008 dacitic to rhyodacitic groundmass glass (Neill, 2013; Neill, unpublished data). Oxygen fugacity was determined on 2008 magmas (Neill, unpublished data) and is assumed to be generally correct for earlier Kasatochi magmas. During the calculation of equilibrium compositions weight percent Fe_2O_3/FeO was varied linearly as a function of SiO_2 from 0.39 at 50 weight percent SiO_2 to 0.62 at 62 weight percent SiO_2 (calculated using the method of Sack and others, 1981). Scale break at ~47 weight percent SiO_2 separates gabbros from lavas and scoriae. Open circles are from a lithic, likely Gregs Mighty basalt, included in 2008 pyroclastic deposits. Sensitivity analysis shows that one log unit difference in assumed oxygen fugacity results in a two-unit shift in calculated equilibrium values of Mg# in basalts, and a four-unit shift in andesites. The calculation is less sensitive to reasonable variations in $K_D^{xl/liq}(Fe^{2+}/Mg)$, and much less sensitive to reasonable variations in temperatures used during calculation.

are in equilibrium with the residual groundmass liquid, then the crystals may be, but are not necessarily, true phenocrysts. If the crystals are too refractory to have precipitated from the host magma then they must have been added to that magma by entrainment of preexisting antecrysts or some other open-system process.

In Kasatochi lavas, an average of about a quarter of the clinopyroxenes in each sample are too magnesian to have crystallized from their host magmas (fig. 31). In some samples (for example, 2008 scoria, some Luna pyroclastic deposits samples) only a tenth of the clinopyroxene cores are too magnesian, but there are no analyzed samples without excessively magnesian clinopyroxene cores.

Core-to-rim zoning in Kasatochi clinopyroxenes is minimal, and both normal and reversed (fig. 32). In 60 percent of the crystals analyzed, rims have Mg# 2.6 ± 2.4 lower than their cores, and in 40 percent of the crystals the rims have Mg# 1.9 ± 1.6 higher. We did not measure zoning profiles across individual crystals, but the fact that cores and rims are the same composition implies that zoning is minimal.

Orthopyroxene crystals comprise up to 6 percent of the mode in samples with whole-rock SiO_2 greater than 52.5 weight percent. In each sample, regardless of whole-rock Mg# or SiO_2, orthopyroxenes have Mg# 69 ± 4. As with the clinopyroxenes, individual orthopyroxene crystals are only slightly zoned, with Mg# of rims generally within 2 mol. percent of cores, and with fewer reversely than normally zoned crystals (fig 32). Orthopyroxene cores have Mg# at least 5 mol. percent lower than expected had they been in equilibrium with their host magmas, unlike clinopyroxenes, in which the most magnesian cores are generally too magnesian to be in equilibrium with the whole-rock values. Orthopyroxenes are also too iron-rich to have co-precipitated with the clinopyroxenes, but they are approximately the composition in equilibrium with the dacitic to rhyolitic 2008 groundmass glass. Alternatively the orthopyroxenes could be antecrysts that were mechanically added to the host magmas, but which formed elsewhere in the larger magmatic system and were added recently enough that they didn't have time to begin to re-equilibrate. Neill and others (2015) describe an analogous process for the entrainment of high-An microlites into the 2008 basaltic andesite; it is likely that a similar entrainment process is responsible for the addition of antecrysts into the crystal cargo of Kasatochi eruptive products.

Forty-five olivine crystals were analyzed from a representative sample of Gregs Mighty basalt—a number likely large enough to define the actual population of all olivines. The most magnesian cores ($Fo_{89.4}$) are in equilibrium with the whole-rock analysis at the NNO + 1 oxygen fugacity buffer. Individual crystals are normally zoned with $Fo_{68 \pm 2}$ rims. Twelve olivine crystals from a Tundering basaltic andesite sample were also analyzed. They are minimally zoned $Fo_{65–60}$ crystals, but the relatively small number analyzed may not accurately reflect the full compositional range in the sample.

Amphibole compositions are roughly normally distributed

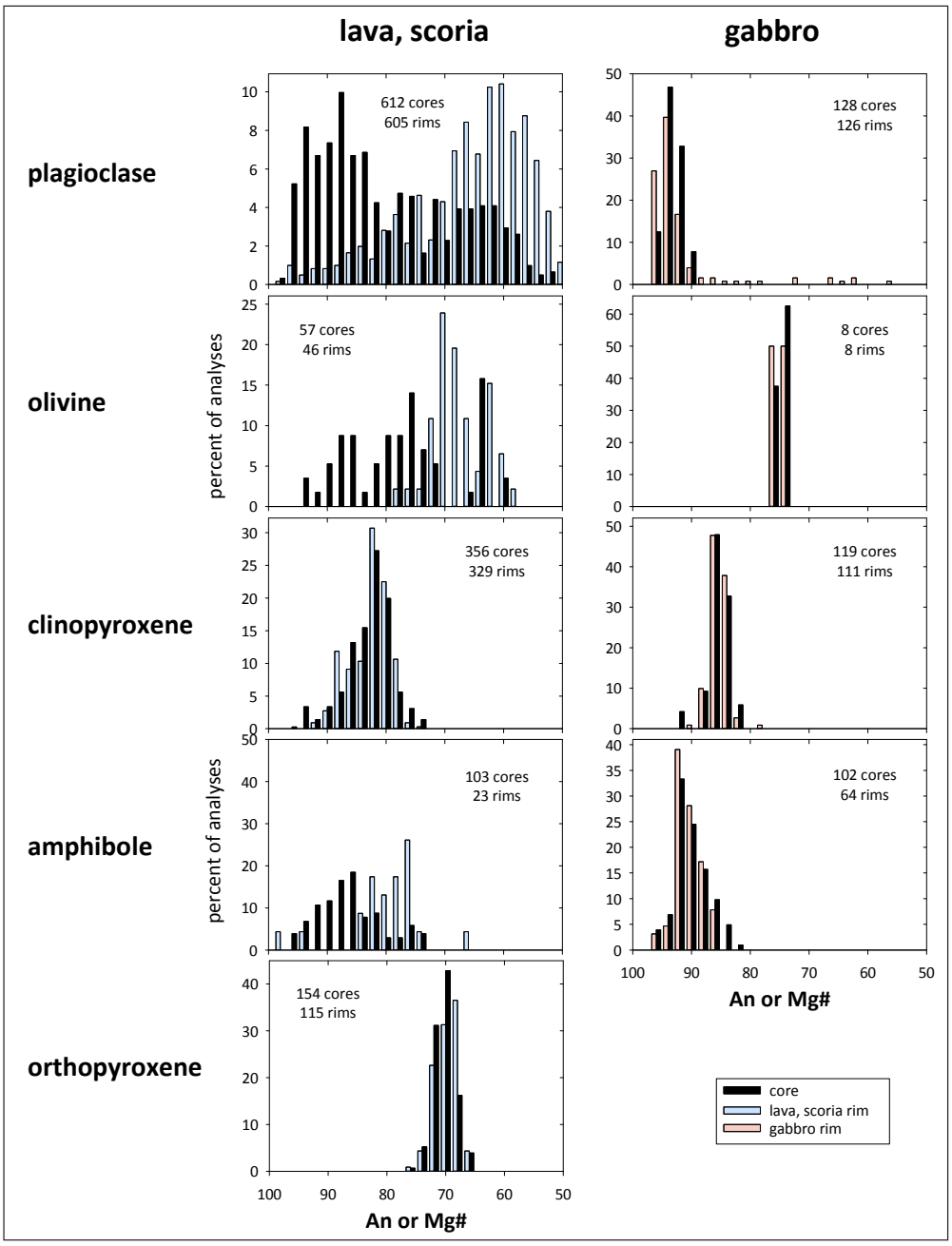

Figure 32. Histograms of analyses of mineral cores and rims with percent of analyses shown vs. An (plagioclase) or Mg# (olivine, pyroxenes, and amphibole). The total numbers of analyses plotted are shown in each plot. Cores are black bars; rims are colored bars.

in lava and scoria samples with Mg# mode of cores near 86, and individual values between 96 and 74 (fig. 31). Most crystals with cores more magnesian than average are normally zoned, and most crystals with cores less magnesian than average are reversely zoned.

Gabbroic inclusions

Crystals of four samples from gabbroic inclusions erupted in 2008 were analyzed along with a single sample of a gabbroic inclusion from Ogres Brow basaltic andesite. Mineral compositions are equivalent among all samples, so are discussed together.

Plagioclase crystals' cores are very calcic (An_{96^-88}) (fig. 32). Eighty-five percent of the crystals analyzed have only minimal zoning, with rims between 3 mol. percent An more calcic and 2 mol. percent less calcic than the cores (fig. 32). However, a few crystals in three of five gabbro samples analyzed have thin rims that are variably more sodic than the cores by up to 40 mol. percent An. Together, these comprise 15 percent of all gabbro plagioclase crystals analyzed.

Gabbro clinopyroxene crystals are relatively homogenous, with core Mg# 84.6 ± 1.9 (fig. 31). Two of the four samples analyzed have a few out-range cores with Mg# 90–93. The gabbro clinopyroxenes are also minimally zoned, with average rim Mg# 84.3 ± 1.4. Individual crystals have rims either more or less magnesian by an average of one Mg# unit (fig. 32).

Seven olivine crystals from a single 2008 gabbro sample and a single olivine from the Ogres Brow gabbro were analyzed. They have the same composition among samples and within the 2008 gabbro sample, and are unzoned, with $Fo_{74 \pm 0.2}$ cores. These olivines are dramatically less magnesian than gabbro clinopyroxenes, so it is unlikely that they precipitated from the dominant melt that formed the gabbros.

Ninety-five percent of analyzed amphiboles from gabbro samples range between Mg# 94 to 83; there are a few

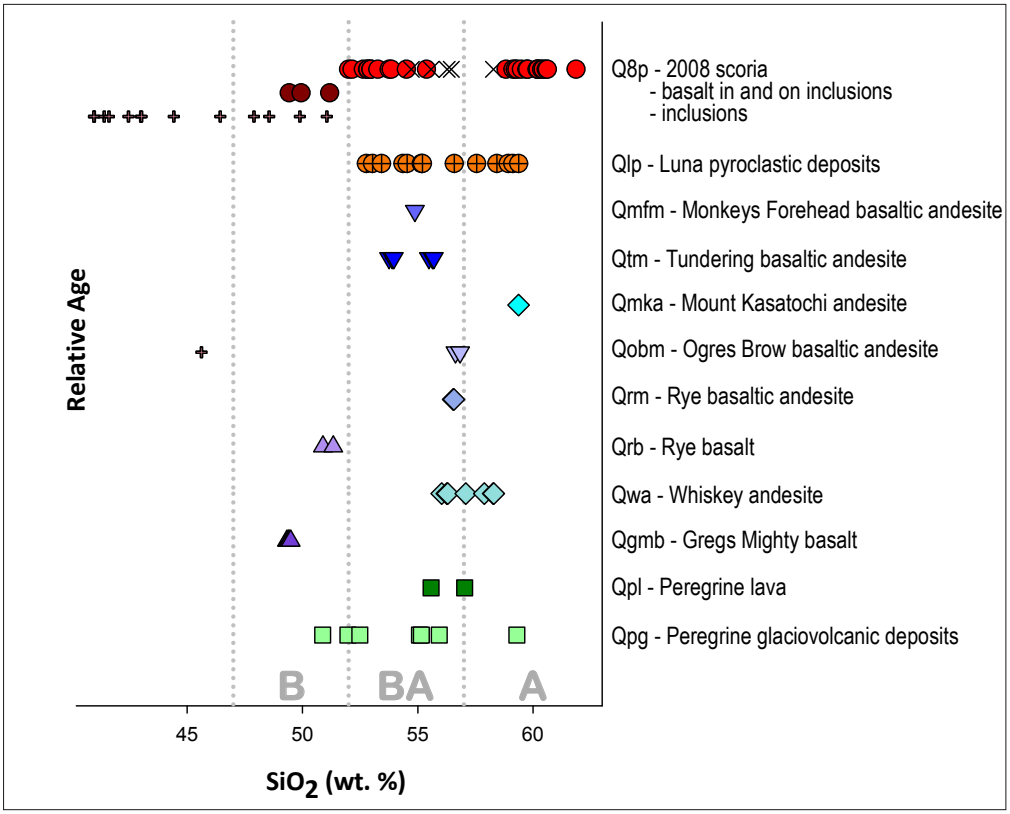

Figure 33. Whole-rock SiO_2 of Kasatochi samples by unit; data from appendix 5. B = basalt; BA = basaltic andesite; A = andesite. Banded 2008 scoria are denoted by "X". Analyses from the Peregrine glaciovolcanic deposits are scoria from individual beds.

anomalously magnesian amphiboles with Mg# greater than 95 (fig. 31).

GEOCHEMISTRY

MAJOR ELEMENT CLASSIFICATION

All Kasatochi lava and scoria samples, as a group, comprise a roughly uniformly distributed suite of basalts, basaltic andesites, and andesites (fig. 33. 34). However, field relations and geochemical data indicate that individual lava units are compositionally homogeneous within a few percent SiO_2; individual lava units are characterized by small differences in major-element concentrations, but more importantly by significant differences in trace-element concentrations (below).

The explosive, fragmental units (2008, Luna pyroclastic deposits, and Peregrine glaciovolcanic deposits), in contrast, are compositionally heterogeneous. Magmas erupted during the day-long 2008 eruption, for instance, have a combined SiO_2 range that exceeds that of all other lavas and scoria combined by more than 20 percent relative, and the 2008 basaltic andesite and andesite each span over 30 percent of the SiO_2 range of all pre-2008 lavas and scoriae (fig. 33). Thirteen juvenile scoriae from the Luna pyroclastic deposits, the other unit that appears similar to 2008 deposits in having been formed by a relatively short-lived explosive eruption, span half the entire SiO_2 range of the volcano. Compositionally distinct scoriae were collected from the same, or nearly adjacent, flow units in the Luna pyroclastic deposits, which indicates that the erupted magma was compositionally heterogeneous, rather than that the deposit is chemically zoned. Juvenile fragments from the Peregrine glaciovolcanic deposits unit span two-thirds of the total SiO_2 range of the volcano but, unlike with 2008 and Luna deposits, we did not find multiple compositionally distinct scoriae at a single field location. Thus it appears that Peregrine glaciovolcanic deposits represent sequential eruption of magmas of varying, but fairly homogeneous composition over an extended, but unknown, period of time.

Kasatochi lavas are medium-K (Gill, 1981) and have K_2O contents that increase from about 0.5 weight percent in basalts to 1.2 weight percent in silicic andesites (fig. 34). At constant SiO_2 there is scatter of 0.2–0.3 weight percent K_2O, which is especially noteworthy in basalts because it implies either that there are multiple parental magmas or that even the most mafic magmas underwent significant modification by contamination or combined assimilation and fractional crystallization (AFC) processes. Figure 34B compares Kasatochi magmas to those from other volcanoes west of the Amlia Fracture Zone, which marks a major intra-arc segment boundary. Kasatochi magmas fall within, but at the lower limit of, the western arc array.

Kasatochi magmas with >51 weight percent SiO_2 form a scattered array that crosses from the tholeiitic field to the calc-alkaline field at about 56 weight percent SiO_2 (fig. 34C). The overall trend is of only moderate increase in FeO*/MgO (FeO* is total Fe as FeO) with increasing SiO_2, and the slope of that trend is less than that of the tholeiitic–calc-alkaline dividing line. Thus the overall trend of the suite has calc-alkaline affinities despite individual basalt and basaltic andesite samples plotting in the tholeiitic field, mimicking the regional trend (fig. 34D).

At Kasatochi, basalts with less than 50 percent SiO_2 have dramatically lower FeO*/MgO than basalts with more than 50 percent SiO_2 and most higher-silica lavas. This is a result of the low-silica basalts having variably higher MgO (6–10 wt.%) at the same FeO* content (~9 wt.%) as the higher-silica basalts. The low-silica basalts have lower whole-rock Cr and Ni

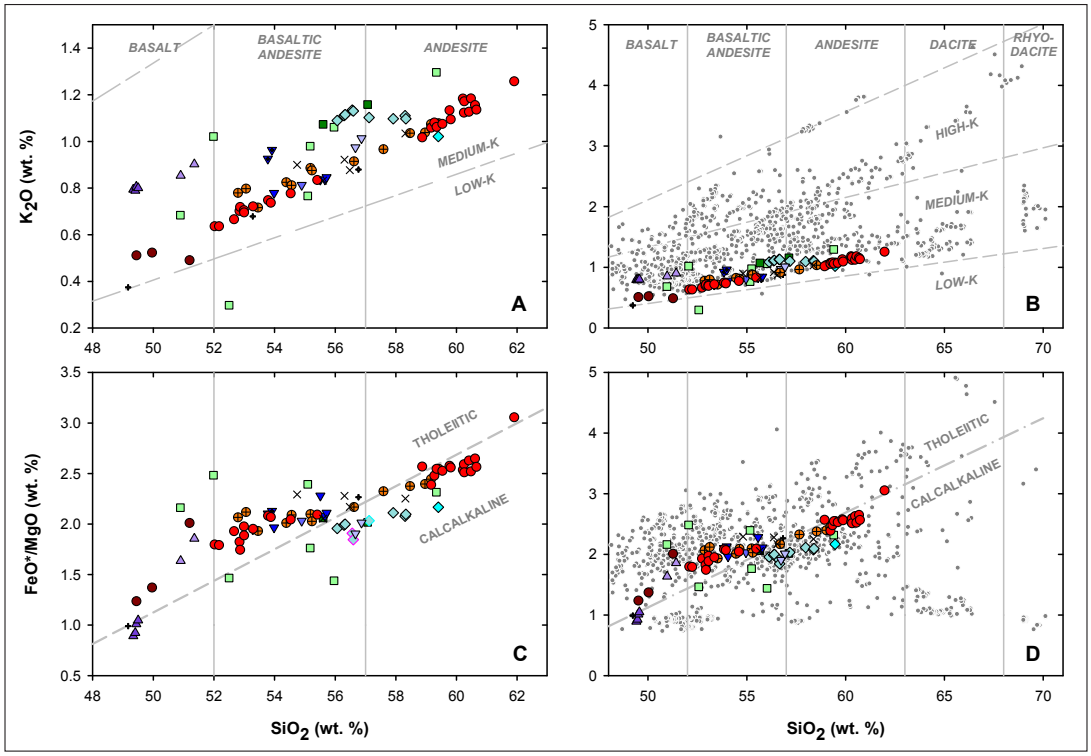

Figure 34. Major element classification diagrams of Kasatochi lava and scoria samples (A, C symbols as in fig. 33), and Kasatochi samples compared to published lava analyses from the Aleutian Arc (B, D). Gray circles are all published lava analyses from 174°W (Atka) to 189.2°W (Western Cones [Yogodzinski and others, 2015]). FeO* is total iron as FeO. K_2O–SiO_2 classification from Gill (1981); tholeiitic–calcalkaline dividing line from Miyashiro (1974). Most samples with FeO*/MgO < 1.5 are from submarine vents west of Buldir (see Yogodzinski and others, 2015).

concentrations, and lower Cr_2O_3 in pyroxenes than primary mantle-derived magmas, and thus are products of some prior fractionation.

TRACE ELEMENTS

Kasatochi magmas have broad intra-suite similarities in incompatible trace-element concentrations, described first, as well as significant second-order intra-suite differences, discussed later. Mantle-normalized concentrations are quintessentially arc-like in having high concentrations of the large-ion lithophile elements (LILE) and Th, U, and Pb, which we refer to as heavy elements (HE), and lower concentrations of rare-earth elements (REE), Y, and the high-field-strength elements (HFSE) Zr and Hf, and very low concentrations of the HFSE Nb and Ta (fig. 35). Mantle-normalized values of LILE range increase from 10 in mafic samples to 100 in silicic samples, with Cs and Ba more enriched than Rb and K. REE enrichments decrease monotonically from 6–16 times mantle in the light REE to 3–6 times mantle in the heavy REE, and REE patterns change from straight in mafic samples to slightly concave up in silicic samples. Europium anomalies are absent in all magma and scoria samples. The heavy elements (Th, U, and Pb) are, like the LILE, highly enriched with Th 20–40 times, U 30–80 times, and Pb 80–300 times mantle concentrations. The HFSE elements Nb and Ta are the least enriched of all elements, with 1.3–3 times mantle concentrations. The HFSE elements Zr and Hf are enriched 4–10 times mantle.

Mantle-normalized trace-element values are important for understanding subduction zone processes, but because they span more than two orders of magnitude—dramatically more than the variations within any single element—important intra-suite differences can be obscured in graphical displays of data. For that reason, in the following discussion we normalize the trace-element data to a composite of Kasatochi basalts, effectively reducing the vertical axes of graphs by two orders of magnitude. The basalt composite is the average of Gregs Mighty basalt, Rye basalt, Peregrine glaciovolcanic deposit basalt, basalt in and on 2008 cumulate inclusions, a single 2008 basalt scoria sample; and a single basalt lithic clast recovered from 2008 deposits. In determining the composite average (comprising 13 basalts), averages were taken for each unit with multiple analyses, and then those averages were averaged. Half of these have only a few tens of parts per million Ni and several tens of parts per million Cr, similar to silicic basalts and basaltic andesites, suggesting that even at these low silica contents those magmas were at least somewhat evolved.

Most of the basalts have lower concentrations of incompatible elements than do basaltic andesites and andesites; however, the basalts also have a wide range of concentrations (fig. 36). Compositional variation in the basalts, excluding the single Qpg sample with anomalously high concentrations of most elements, encompasses one- to two-thirds of the total variation in trace elements of the entire Kasatochi suite. We believe this is primarily due to variations in the composition of primary magmas; however, a secondary control by fractionation or other processes of magma evolution cannot be discounted.

For all samples, maximum incompatible trace-element concentrations normalized to average Kasatochi basalt range from 3.5 for Cs and 2.8 for Pb to 1.3 for the middle REE. For major groups of trace elements, basalt-normalized enrichments are in the order HE > LILE > HFSE > light REE (La–Eu) > heavy REE (Er–Lu) > middle REE (Gd–Ho). Exceptions are

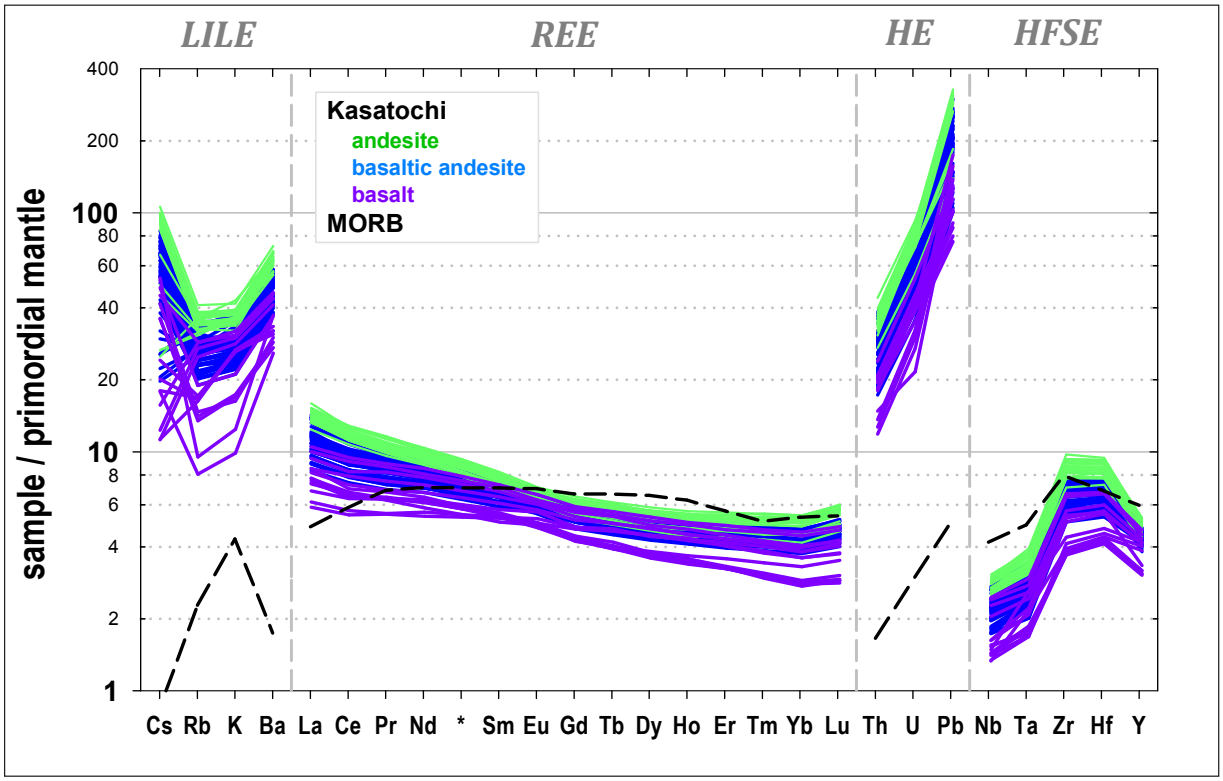

Figure 35. Multi-element variation diagram for all Kasatochi lava and scoria samples, normalized to the primordial mantle of Sun and McDonough (1989). Average East Pacific NMORB (dashed black line; Klein, 2005) is shown for reference.

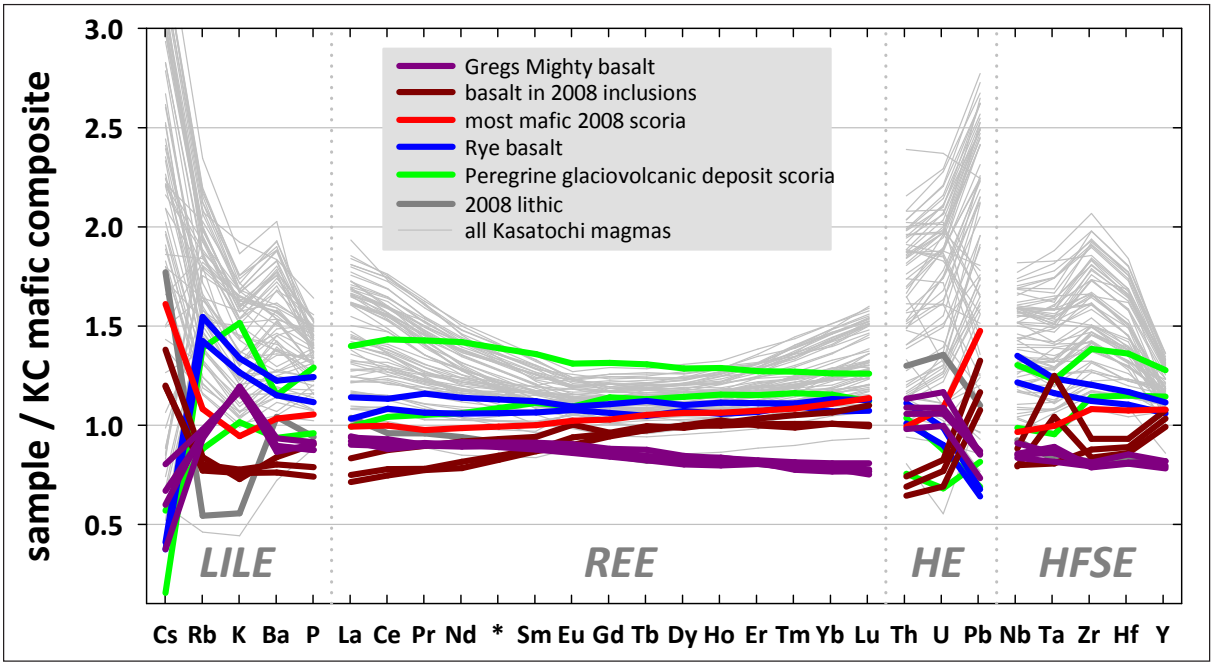

Figure 36. Multi-element variation diagram showing the range of Kasatochi basalt concentrations (colored lines), compared to each other and to all other Kasatochi analyses (gray lines). All analyses are normalized to an average Kasatochi basalt composite (see text).

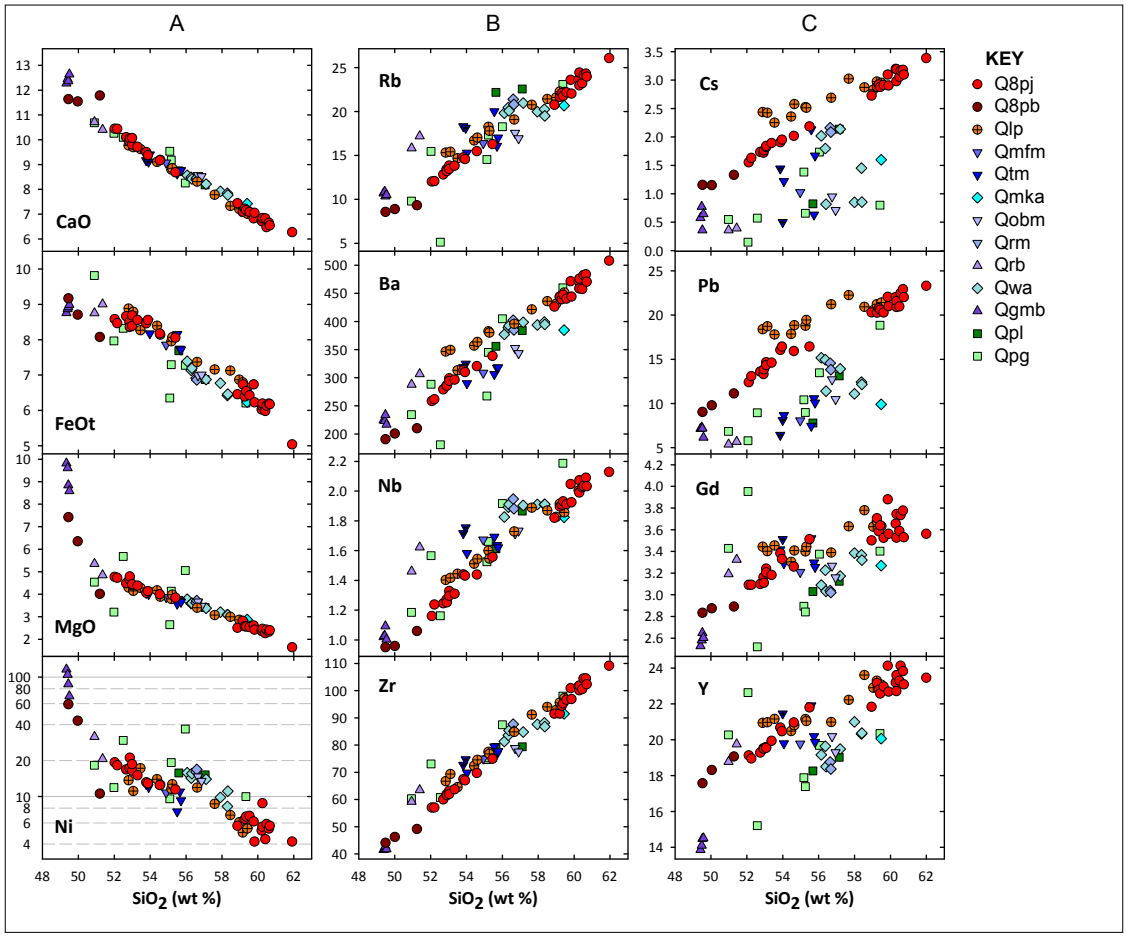

Figure 37. Selected silica variation diagrams (additional diagrams in appendix 5). Abbreviations for symbols are Q8pj = unbanded juvenile 2008 scoria; Q8pb = basalt on or in 2008 cumulate inclusions. Other abbreviations are map unit names. Column A shows compatible major and trace elements; column B shows examples of incompatible trace elements with concentration ranges that are similar for all units; column C shows examples of incompatible trace elements with concentrations that vary widely between and among units.

Zr, which overlaps LILE, and La, which is enriched more than the HFSE. Basalt-normalized REE patterns become increasingly concave-up with increasing silica; Gd/Gd* ($Gd_n/0.5[La_n+Lu_n]$) decreases regularly from 1 to 0.7 in silicic andesites, with the primary exception of Whiskey andesite, which has more deeply concave REE patterns than most other lavas of similar silica content.

In general, the Kasatochi suite is characterized by trace-element concentrations that increase linearly with increasing silica for typically incompatible elements (LILE, REE, HE, HFSE), and decrease linearly or exponentially for typically compatible elements (Mg, Cr, Ni), forming tight arrays for many, but not all, elements on silica variation diagrams (fig. 37). In many, but not all, variation diagrams samples from all map units fall along the same compositional trend. Elements for which this is true include most major elements, Ba, the light REE, Zr, Hf, Sc, and V (fig. 36, fig. A5a. 1, 2). For other elements, notably Cs and Pb, there is wide scatter of concentrations as a function of silica within some units.

2008 and Luna pyroclastic deposits samples form reasonably coherent subarrays, but samples from other units do not, either individually or in aggregate. Cs and Pb, both highly incompatible elements, are decoupled from each other and from silica. Cs/Rb is scattered between 0.06 and 0.29 in Tundering basaltic andesites and between 0.07 and 0.15 in Whiskey andesites, both over restricted silica ranges. In contrast, Cs/Rb in 2008 samples forms a tight linear array increasing from 0.12 in basalts to 0.14 in silicic andesites—a tenth of the scatter over five times the silica range of Tundering basaltic andesites.

Individual units have distinguishing features in their trace-element concentrations with respect to silica (fig. 37). As examples, Luna scoriae have the highest, and 2008 scoriae the second highest Cs/Si and Pb/Si. Qwa and Qtm both have high Nb/Si, but of the two units Qtm has higher Ni/Si and lower Y/Si. Among basalts, Rye basalt has the highest Rb, Nb, and Gd concentrations, but low Cs and Pb.

Additional distinguishing trace-element characteristics are illustrated by multi-element variation diagrams that show both the general conformity of compositions within units and important differences among units (fig. 38). 2008 and Luna scoriae have high Cs, Cs/Rb, Pb, and Pb/U over their entire compositional range, implying control by the composition of magmas parental to those units rather than fractionation from a parent in common with other units. Mount Kasatochi andesite has low concentrations of HE compared to Whiskey andesite, and Ogres Brow basaltic andesite has higher concentrations of HE than other basaltic andesites, despite both having concentrations of other incompatible trace elements similar to other andesite and basaltic andesite units, respectively. Again, these kinds of differences imply successive parent magmas with different chemical fingerprints rather than a shared common parent for all magmas. In contrast to coherent, yet distinct composi-

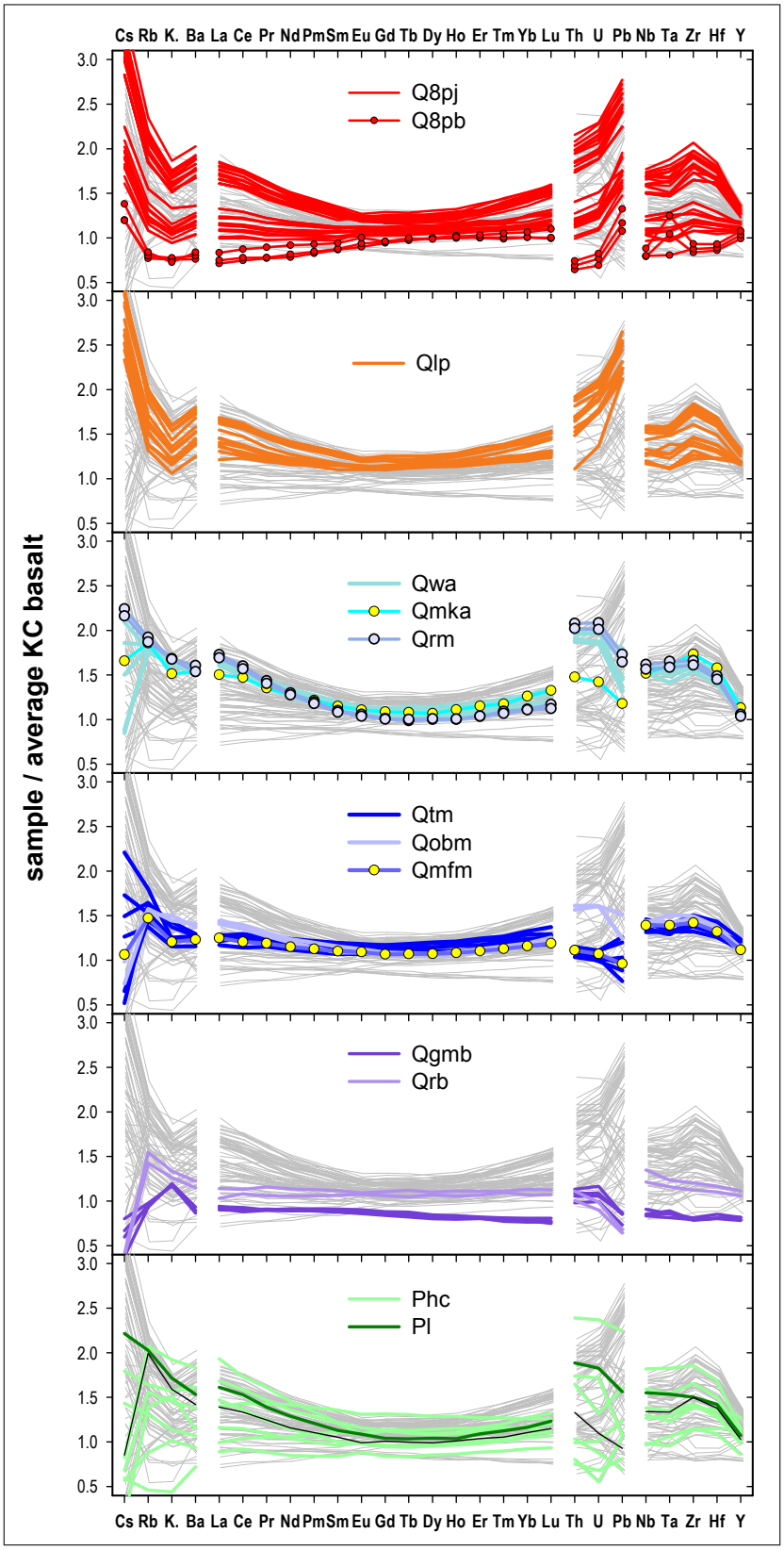

Figure 38. Multi-element variation diagrams of lava and scoria samples normalized to average Kasatochi basalt. Labels are map units except Q8pj, juvenile 2008 scoria, and Q8pb, basalt in and on inclusions in 2008 pyroclastic deposits.

tional variations between units, Whiskey andesite, Tundering basaltic andesite, and to a lesser extent juvenile lava and scoria samples from the Peregrine glaciovolcanic deposits samples have chaotic variations in Cs, while 2008 and Luna pyroclastic deposits samples do not. Cs is expected to be one of the most incompatible elements during fractionation, so the samples with dramatically depleted Cs and low Cs/Rb are especially noteworthy. The chaotic, compositionally independent variations in Cs may arise from processes other than high-temperature crystal–liquid fractionation. One candidate process is weathering or low-temperature alteration, but because these samples were visibly pristine and collected from the cores of large blocks, and because there was no outcrop-scale staining or alteration, we discount this possibility. Another, more speculative, process might be Cs partitioning into high-temperature magmatic gas that exsolved as magmas rose, and that different volumes of the erupted magma were more or less efficiently degassed. The units that have erratic Cs concentrations are those with highly corroded and reacted amphibole phenocrysts, implying slower rise than 2008 and Luna pyroclastic deposits magmas, which carried pristine amphibole phenocrysts.

CUMULATE GABBROIC AND ULTRAMAFIC INCLUSIONS

Cumulate gabbroic and ultramafic inclusions form a notable minor component of the upper, basaltic andesite scoria-bearing, 2008 pyroclastic deposits. Gabbros are much more common than ultramafic inclusions. They are texturally diverse, and consist of unzoned anorthitic plagioclase with subequal amounts of unrimmed amphibole, lesser amounts of clinopyroxene, and minor amounts of opaque minerals, olivine, orthopyroxene, voids, and basalt that fills some voids and coats some inclusions. Plagioclase and amphibole are commonly euhedral, with well-developed crystal faces bounding voids. Amphibole commonly contains subhedral to anhedral pyroxene, and may have been growing at the expense of those pyroxenes. Similar-appearing gabbroic inclusions are common minor components of beach cobbles derived from the lava units, suggesting that crystal mush, brought to the surface as these inclusions, generally has been present beneath Kasatochi throughout its eruptive history. 2008 deposits also include plagioclase-free ultramafic inclusions dominated by olivine and/or clinopyroxene that are subordinate to gabbros in volume (ultramafic inclusions are further discussed by Kentner, 2013).

We discuss major- and trace-element whole-rock chemistry of five gabbroic and seven ultramafic inclusions from 2008 pyroclastic deposits; hand-picked amphibole and plagioclase from 2008 gabbros; and a single Ogres Brow gabbroic inclusion. None of these samples represent magma compositions. The gabbros have <45 weight percent SiO_2 and >20 weight percent Al_2O_3; pyroxenites have 17–28 weight percent MgO and >15 weight percent CaO; peridotitic inclusions have about 40 weight percent MgO; all inclusions have LILE and HE concentrations that are 2–15 percent those of Kasatochi basalts. These geochemical characteristics are well outside the range of magmas in general, and Kasatochi magmas specifically. Instead, these inclusions are probably representative of the crystal mush left behind by evolving magmas. It's noteworthy that the mineral species and proportions in the cumulate inclusions are quite different than the phenocrysts in the lavas themselves, primarily in the dramatically higher modal abundance of amphibole. Compositions of magmas that evolve in equilibrium with these mushes will be quite different than compositions produced by gravitational separation of their phenocrysts.

Figure 39 shows the cumulate inclusion trace-element data normalized to Kasatochi basalt in comparison to Kasatochi lavas and scoriae. The gabbros mirror the lavas and scoriae. The 2008 gabbros are primarily a mix of plagioclase and amphibole; the average proportion of plagioclase to amphibole to clinopyroxene in the five samples for which there are modal data is 4:3:1,

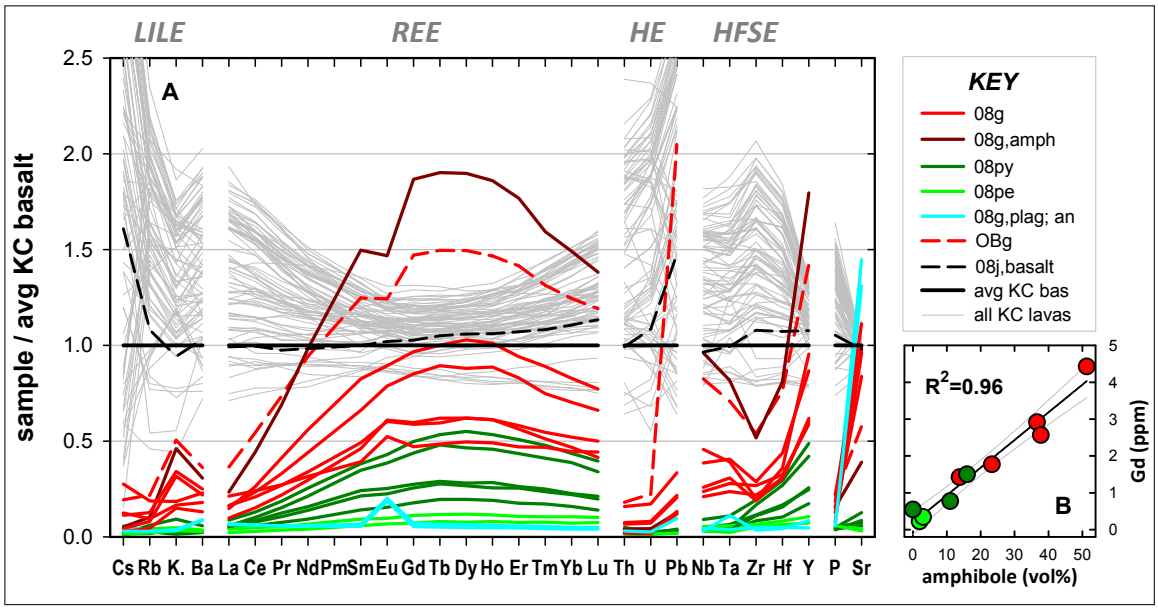

Figure 39. A. Multi-element variation diagram, showing incompatible trace-element compositions of all Kasatochi samples (thin gray lines) compared to 2008 inclusions. 08g, 2008 gabbro; 08g,amph, amphibole separate from 2008 gabbro; 08py, 2008 pyroxenitic inclusion; 08pe, 2008 peridotitic inclusion; 08g,plag, plagioclase separate from 2008 gabbro; an, anorthositic inclusion; OBg, Ogres Brow gabbro inclusion; 08j, basalt, basalt in and on 2008 inclusions; avg KC bas, Kasatochi basalt composite. The gabbros mirror the lavas in major ways, such as the REE pattern, and in detail (for example, high normalized K/Ba in the gabbro mirrors low K/Ba in the lavas, and low Zr/Nb and P/Y in the gabbros mirror high Zr/Nb and P/Y in the lavas). **B.** Gd concentrations of the cumulate inclusions vs. modal percent amphibole, showing that amphibole plays a dominant role in determining concentrations of Gd, and at least other REEs, by extension. Red circles are amphibole gabbros, green circles are plagioclase-free ultramafic inclusions.

but the data are sparse considering the textural diversity and coarse grain size of all samples. Nevertheless, visual inspection of a large number of gabbro samples indicates that they consist primarily of plagioclase with subequal amounts of amphibole, lesser amounts of pyroxene, and little to no olivine. Variations in gabbro trace-element geochemistry are primarily controlled by amphibole, which has basalt-normalized values from as low as 0.04 (Th, U) to as high as 1.9 (middle REE). In contrast, plagioclase in gabbros has uniformly low basalt-normalized trace-element values between 0.02 and 0.07, with the exception of Pb (0.1) and Eu (0.2, reflecting a positive Eu anomaly). Amphibole-poor peridotitic and pyroxenitic inclusions also have low concentrations of incompatible trace elements, implying uniformly low trace-element levels in olivine (0.02 to 0.08 times average Kasatochi basalt) and variable but low concentrations in clinopyroxene (from 0.02 for LILE, LREE, and HFSE to 0.08 for MREE, HREE, and Y). The cumulate inclusions have a large range in compositions, particularly in the middle REE. That range is governed by the modal amount of amphibole in individual samples: Gd concentrations in the inclusions have a linear correlation with modal amphibole with a correlation coefficient of 0.96 (fig. 39B). Additionally, within the inclusions there is a very strong linear correlation between Gd and the heavy REE and HFSE and a strong correlation between Gd and the LILE and light REE.

Gabbroic plagioclase has a positive Eu anomaly, and amphibole has a negative Eu anomaly of comparable magnitude. As a result of the combination of these two phases in bulk samples, gabbros with about 40 volume percent amphibole have no bulk Eu anomaly; gabbros with about 20 volume percent amphibole have slight positive Eu anomalies; and the Ogres Brow gabbro, with 50 volume percent amphibole, has a slight negative Eu anomaly. Kasatochi lavas and scoriae do not have Eu anomalies, mirroring the gabbros with about 40 volume percent amphibole.

GABBRO CONTROL OF MAGMA CHEMISTRY

The principal goals of igneous geochemistry are to understand the potentially diverse processes that produce magmatic diversity, and to constrain both the nature and temporal variability of subvolcanic plumbing systems. Volcanism delivers the end product of myriad petrogenetic processes to the surface, where the lavas can be collected and analyzed, and the analyses used to infer constraints on the processes of interest. In the process of interpreting volcanic geochemistry it is commonplace to assume that the crystals that segregated to produce the volcanic daughter magma in hand from its immediate parent are of the same species, and in roughly the same proportions as the phenocrysts in the sample. The interpretation that dioritic intrusive rocks represent the residue of fractional crystallization often follows from the first assumption. The first assumption is commonplace because having unequivocal samples of the crystalline residue of magma evolution is quite rare, both in modern samples and in the rock record. The gabbroic cumulate inclusions at Kasatochi likely are samples of the crystalline residue associated with 2008 erupted magmas, providing an uncommon opportunity to evaluate their role in magma evolution, which we consider below.

Mass balance requires that the crystalline residue of magma evolution is the complement to evolved magmas, and that the two mirror each other so that when added together they equal the initial parental magma. The fidelity with which the gabbroic inclusions mirror the evolved Kasatochi magmas is qualitatively apparent in a multi-element variation diagram (fig. 39).

There is a concave-up pattern of basalt-normalized REE in the lavas and scoriae. The concavity of the pattern progressively develops with increasing enrichment of all incompatible elements and silica, and light REE increase more than heavy REE that increase more than middle REE. Linear correlation coefficients (r^2) of REE concentrations in lavas and scoriae as a function of silica are 0.98 for La, 0.97 for Lu, and 0.86 for Gd. The patterns of lava and scoriae REE are mirrored by the gabbros, in which light REE are more depleted than heavy REE that are more depleted than middle REE. Other more subtle features of lava and scoriae enrichment are mirrored by the gabbros as well. In all lavas except Gregs Mighty basalt, K is less enriched than Rb and Ba, while in the gabbros K is more enriched than Rb and Ba. In lavas and scoriae Zr is more enriched than the other HFSE, while in the gabbros it is less enriched. Thus the multi-element variation diagram (fig. 39) provides qualitative evidence that the amphibole gabbros are the complement to the lavas and scoriae, and are the crystalline residue of magma evolution. The two primary elements for which lava enrichments are not mirrored in the gabbros are Cs and Pb. Both these elements have variable and non-systematic concentrations (often depletions with respect to other LILE and HE) in lavas, as noted above, but uniformly and consistently low concentrations in the gabbros with the exception of very high Pb values in the Ogres Brow gabbro sample.

Silica variation diagrams (fig. 40) confirm that gabbros with about 40 percent amphibole are the complement to 2008 scoria, and by extension to Kasatochi magmas in general. A linear regression through 2008 scoria passes directly through, or very near, amphibole gabbro for major elements and most LILE, REE, HE, and HFSE.

We have estimated the compositions of the phenocryst cargos for individual lava and scoria samples by summing the average compositions of each phenocryst phase multiplied by its modal proportions as determined by point counting (fig. 40). The calculated phenocryst cargos are not collinear with the 2008 scoriae, or with Kasatochi lavas and scoriae in general, in certain elements. Specifically, the phenocryst cargos are higher in Al_2O_3, and lower in FeO* and K_2O, than the trend of Kasatochi samples. Separation of the phenocryst cargos through fractional crystallization would drive evolved magmas to lower Al_2O_3, marginally lower CaO, and higher K_2O, FeO*, and FeO*/MgO than observed.

Amphibole gabbro is a reasonable complement to the lavas and scoriae, but the phenocryst loads entrained by the lavas and scoriae are not. The data indicate that Kasatochi magmas evolve in equilibrium with an amphibole gabbro crystal residue rather than by fractional crystallization of their observed phenocrysts. The strongest argument for this comes from REE geochemistry, but the argument is supported by other trace- and major-element data, as well as phenocryst modes and compositions.

If the gabbro inclusions are portions of this residue, then they indicate magma evolution took place in a crystal mush zone, or solidification front at the margins of the crustal magma storage system (Marsh, 2006) with mineralogy distinctly unlike the magma's phenocrysts. Maximum H_2O contents of ~8 weight percent in glass inclusions in phenocrysts in 2008 scoria imply a depth of 12 km or more for the magma storage zone (P.E. Izbekov, unpublished data). The model presented here of "cryptic" magma evolution driven by crystallization of minerals and mineral proportions other than those carried as phenocrysts is less common than the model of fractional crystallization of

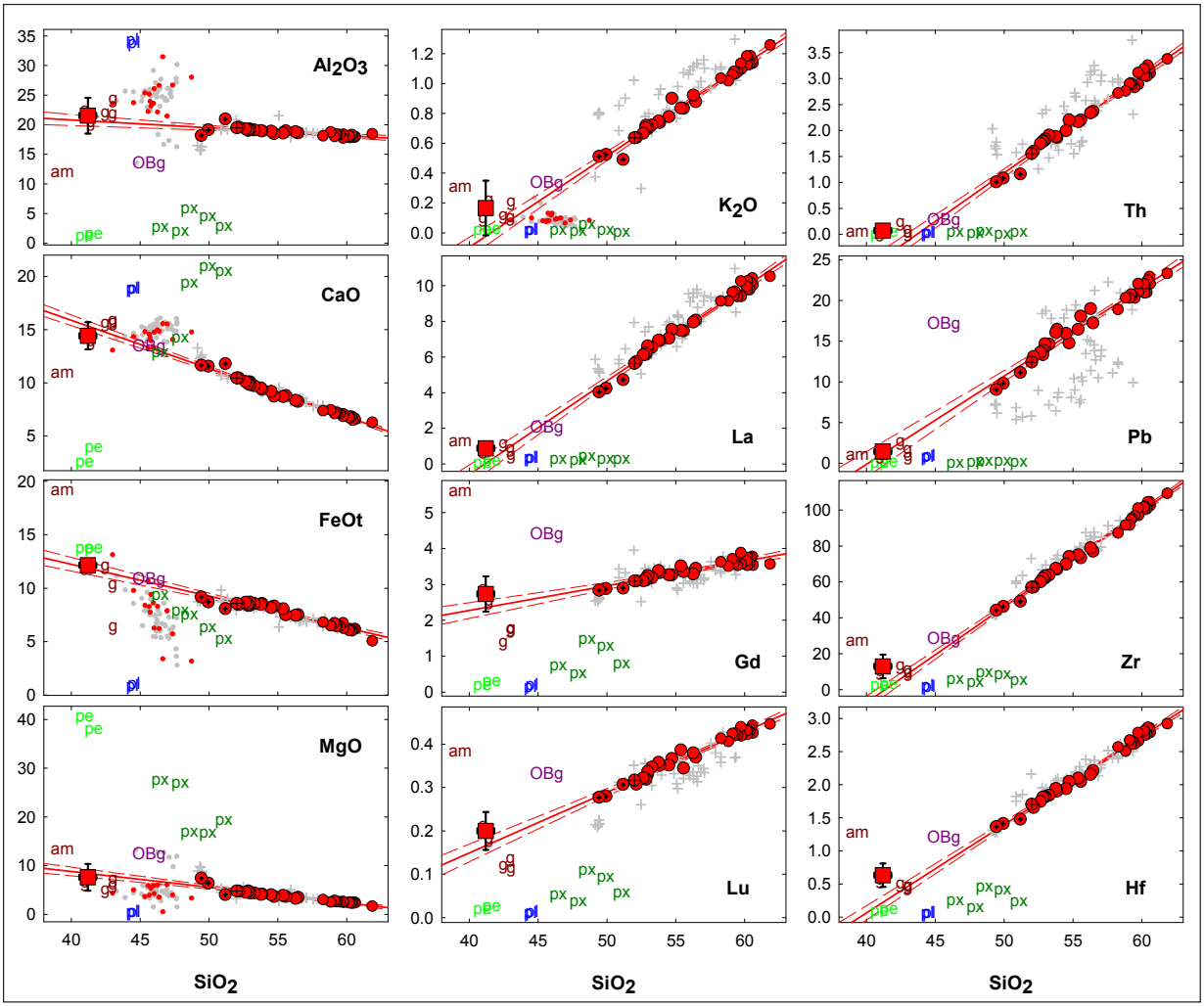

Figure 40. A selection of silica variation diagrams, showing the relation of lavas and scoriae, cumulate inclusions from the 2008 eruption, and calculated compositions of the major element composition of the total phenocryst load for each sample. Symbols: red circles = 2008 juvenile scoria (basalt scoria crossed red circle; basalt in and on gabbro red circles with crosshairs); red line = linear regression through 2008 scoria with 99 percent confidence envelope; gray plus = other lavas and scoriae; red square = average of two gabbro inclusions with about 40 percent amphibole with 2σ error; green px = pyroxenitic inclusions; green pe = peridotitic inclusions; dark red g = other amphibole gabbro samples; dark red am = amphibole separate from gabbro; blue pl = plagioclase separate from amphibole gabbro, anorthosite; purple OBg = Ogres Brow gabbro. In plots of major oxides, dots are the calculated combined phenocryst compositions for individual samples (red, 2008; grey, other units) based on modal proportions of phenocrysts in each sample and mineral compositions determined as part of this study.

a dioritic assemblage similar to the phenocryst load, but not unique to this study. Davidson and others (2007) present a general case based on REE data in lavas, and Davidson and Wilson (2011) and Kratzmann and others (2010) present specific cases.

SUMMARY

Kasatochi is a small, isolated island volcano midway between Atka and Adak, in the central Aleutian Islands and in the western quarter of the Aleutian Arc. It sits on the northernmost edge of the shallow, flat summit platform of the Aleutian Ridge—a location that was likely emergent during low Pleistocene sea levels.

The oldest geologic unit on the island is a package of Pleistocene glaciovolcanic deposits including autobrecciated lava, lahars, and a few lava masses. Volcanic facies such as these are typical products of subaqueous eruption in ice-confined vaults, and we interpret this package to have been emplaced in a lake beneath a Pleistocene ice cap. A single 131 ± 2.5 ka $^{40}Ar/^{39}Ar$ age confirms that this package is at least in part of MIS 6 glacial age, but we have no direct evidence for the total timespan represented by the unit.

The next younger group of units consists of thick, stubby basalt, basaltic andesite, and andesite lava flows produced by several, perhaps many, eruptions. A Holocene age for these is indicated by the lack of any morphologic evidence of eruption in the presence of Pleistocene ice, as well as Holocene $^{40}Ar/^{39}Ar$ ages from two of the lower units.

The penultimate eruption deposits consist of a thick package of pyroclastic deposits that make up about half of the southern crater wall; are prominent features of the lower southern flanks; and are locally widespread, although now buried elsewhere on the island, but always stratigraphically above the lava units. The age of this unit is not known quantitatively, but the lack of a well-developed sequence of soils and tephras on top of the unit suggests an age of hundreds, rather than thousands, of years. The eruption that produced these deposits likely formed the large central crater.

In 2008 Kasatochi had a major magmatic eruption for the

first time in recorded history (about 250 years). The eruption was brief, entirely explosive, and had a dramatic impact on the island. The crater was enlarged by 30 percent by the force of the explosions, and the entire island increased in area by 40 percent through emplacement of pyroclastic deposits into the sea, reaching up to 500 m beyond the pre-eruption shoreline. The eruption buried the previously lush vegetation, and importantly, buried nesting taluses used by hundreds of thousands of seabirds. Since the 2008 eruption new nesting taluses have accumulated and are in use.

The island is currently in flux, biologically and geologically. Seabirds are finding new nesting sites, but passerines have not returned in number. Vegetation is starting to regrow in places where the pre-eruption root mat has become exposed and in areas backed by outward-facing cliffs that were not deeply buried. The shoreline is adjusting by retreating on all but the south side, and by probably transient growth on the south. 2008 deposits on the island's flanks are being transported to lower alluvial fans on the south or to tidewater on other flanks by a robust system of gullies.

Two main magmas erupted in 2008: andesite followed by basaltic andesite (Neill, 2013; Neill and others, 2015). Each was chemically inhomogeneous, and mechanical mixtures of the two are present. Basaltic andesite brought a rich variety of amphibole gabbro inclusions to the surface, with a third 2008 magma, a basalt, present as a coating on the inclusions and occupying void space in the inclusions. One important lesson is that despite eruptive quiescence throughout historic time multiple magmas still existed beneath the volcano. Trace-element geochemistry indicates that, as a rule, crustal residence time of Kasatochi basalts, basaltic andesites, and andesites is sufficient for them to grow and equilibrate with an amphibole-rich, largely crystalline, chamber rind.

This study is the first to document the geology of the entire island, and presents a snapshot of the island early in its response to the 2008 eruption.

ACKNOWLEDGMENTS

Initial fieldwork was supported by the North Pacific Research Board (Project #923), the U.S. Fish and Wildlife Service, the Alaska Volcano Observatory, and the U.S. Geological Survey. Additional fieldwork was supported by AVO and the USFWS. We thank USFWS for continued encouragement and support. We especially thank Jeff Williams of the USFWS for sharing his deep knowledge of Kasatochi history, biology, and geography, and for his all-encompassing interest in Kasatochi science. Fieldwork was supported by the *M/V Tiĝlax̂*, under the able command of Captain Billy Pepper; we thank the captain and crew for comfortable and safe transport. We thank pilots Burke Mees, Jerry Morris, and Roger Clifford for taking and sharing oblique aerial photographs. Post-eruption scientific studies span a large range of biologic and geologic disciplines, and we thank the other scientists for rewarding and fruitful cross-fertilization. Chris Nye thanks Patricia Gallagher for help with ArcGIS during preparation of the map draft and for final cartography, and Nicole Kinsman for help with establishing the Kasatochi Mean Sea Level datum. Reviews by Brian Jicha and especially Michael Clynne substantially improved the report. Any use of trade, firm, or product names is for descriptive purposes only and does not imply endorsement by the State of Alaska or U.S. Government.

REFERENCES

Arnoult, K.M., Olson, J.V., Szuberla, C.A.L., McNutt, S.R., Garcés, M.A., Fee, D., and Hedlin, M.A.H., 2010, Infrasound observations of the 2008 explosive eruptions of Okmok and Kasatochi volcanoes, Alaska: Journal of Geophysical Research, v. 115, no. D2, D00L15. http://doi.org/10.1029/2010JD013987

Buchheit, R.M., and Ford, J.C., 2008, Biological monitoring in the central Aleutian Islands, Alaska in 2008—Summary appendices: Homer, AK, U.S. Fish and Wildlife Service Report, AMNWR 08/12, 141 p.

Coats, R.R., 1956, Reconnaissance geology of some western Aleutian Islands, Alaska, in Investigations of Alaskan volcanoes: U.S. Geological Survey Bulletin B 1028-E, p. 83–100, 1 sheet, scale approx. 1:1,000,000. https://pubs.er.usgs.gov/publication/b1028E

Corradini, S., Merucci, L., Prata, A.J. and Piscini, A., 2010, Volcanic ash and SO_2 in the 2008 Kasatochi eruption—Retrievals comparison from different IR satellite sensors: Journal of Geophysical Research, v. 115, no. 2, D00L21. http://doi.org/10.1029/2009JD013634

Davidson, Jon, and Wilson, Marjorie, 2011, Differentiation and source processes at Mt. Pelée and the Quill—Active volcanoes in the lesser Antilles arc: Journal of Petrology, v. 52, no. 7-8, p. 1,493–1,538. http://doi.org/10.1093/petrology/egq095

Davidson, Jon, Turner, Simon, Handley, Heather, Macpherson, Colin, and Dosseto, Anthony, 2007, Amphibole "sponge" in arc crust?: Geology, v. 35, no. 9, p. 787–790. http://doi.org/10.1130/G23637A.1

DeGange, A.R., Byrd, G.V., Walker, L.R., and Waythomas, C.F., 2010, Introduction—The impacts of the 2008 eruption of Kasatochi volcano on terrestrial and marine ecosystems in the Aleutian Islands, Alaska: Arctic, Antarctic, and Alpine Research, v. 42, no. 3, p. 245–249. http://doi.org/10.1657/1938-4246-42.3.245

Drew, G.S., Dragoo, D.E., Renner, Martin, and Piatt, J.F., 2010, At-sea observations of marine birds and their habitats before and after the 2008 eruption of Kasatochi volcano, Alaska: Arctic, Antarctic, and Alpine Research, v. 42, no. 3, p. 325–334. http://doi.org/10.1657/1938-4246-42.3.325

Drummond, B.A., and Larned, A.L., 2007, Biological monitoring in the central Aleutian Islands, Alaska in 2007–Summary appendices: Homer, AK, U.S. Fish and Wildlife Service Report, AMNWR 07/06, 155 p.

Fee, David, Steffke, Andrea, and Garcés, Milton, 2010, Characterization of the 2008 Kasatochi and Okmok eruptions using remote infrasound arrays: Journal of Geophysical Research, v. 115, no. D2, D00L10. http://doi.org/10.1029/2009JD013621

Friday, D.Z., Taylor, L.A., Eakins, B.W., Carignan, K.S., Caldwell, R.J., Grothe, P.R., and Lim, E., 2011, Digital elevation model of Atka, Alaska—Procedures, data sources and analysis: Boulder, CO, U.S. Department of Commerce, National Oceanic and Atmospheric Administration (NOAA) Technical Memorandum NESDIS NGDC-48, Boulder, CO, 20 p.

Gard, L.M., Jr., 1980, The Pleistocene geology of Amchitka Island, Aleutian Islands, Alaska: U.S. Geological Survey Bulletin 1478, 38 p. https://pubs.er.usgs.gov/publication/b1478

Gill, J.B., 1981, Orogenic andesites and plate tectonics: Berlin, Springer-Verlag, 404 p.

Grewingk, Constantine, 1850, Grewingk's geology of Alaska and the Northwest Coast of America [edited by Marvin W. Falk, translation by Fritz Jaensch published 2003]: Fairbanks, AK, Rasmuson Library Historical Translation Series 11, The University of Alaska Press, 242 p.

Grove, T.L., Gerlach, D.C., and Sando, T.W., 1982, Origin of calc-alkaline series lavas at Medicine Lake Volcano by fractionation, assimilation and mixing: Contributions to Mineralogy and Petrology, v. 80, no. 2, p. 160–182. http://doi.org/10.1007/BF00374893

Houghton, B.F. and Wilson, C.J.N., 1989, A vesicularity index for pyroclastic deposits: Bulletin of Volcanology, v. 51, p.451-462.

Karlstrom, T.N.V., compiler, 1964, Surficial geology of Alaska: U.S. Geological Survey Miscellaneous Geologic Investigations Map I-357, 2 sheets, scale 1:1,584,000. https://pubs.er.usgs.gov/publication/i357

Kay, S.M., and Kay, R.W., 1985, Aleutian tholeiitic and calcalkaline magma series I—The mafic phenocrysts: Contributions to Mineralogy and Petrology, v. 90, no. 2, p. 276–290. http://doi.org/10.1007/BF00378268

Kay, S.M., and Kay, R.W., 1994, Aleutian magmas in space and time, *in* Plafker, George, and Berg, H.C., eds., The Geology of Alaska: Geological Society of America The Geology of North America series, v. G-1, p. 687–722.

Kentner, Adrienne, 2013, Petrological constraints on the origin of enclaves from Kasatochi volcano, Aleutian Islands, Alaska: Fairbanks, AK, University of Alaska Fairbanks, MS thesis, 166 p.

Klein, E.M., 2005, Geochemistry of the igneous ocean crust, *in* Holland, H.D., Turekian, K.K., and Rudnick, R.L., eds., The Crust, Vol. 3, Treatise on Geochemistry: Oxford, Elsevier-Pergamon. p. 433–463.

Kratzmann, D.J., Carey, Steven, Scasso, R.A., and Naranjo, J.-A., 2010, Role of cryptic amphibole crystallization in magma differentiation at Hudson volcano, southern volcanic zone, Chile: Contributions to Mineralogy and Petrology, v. 159, no. 2, p. 237–264. http://doi.org/10.1007/s00410-009-0426-1

Lim, E., Eakins, B.W., and Wigley, R., 2011, Coastal relief model of southern Alaska—Procedures, data sources and analysis: National Oceanic and Atmospheric Administration Technical Memorandum NESDIS NGDC-43, 22 p.

Lindsley, D.H., 1983, Pyroxene thermometry: American Mineralogist, v. 68, p. 477–493.

Marsh, B.D., 2006, Dynamics of magmatic systems: Elements, v. 2, no. 5, p. 287–292. http://doi.org/10.2113/gselements.2.5.287

Miyashiro, Akiho, 1974, Volcanic rock series in island arcs and active continental margins: American Journal of Science, v. 274, no. 4, p. 321–355. http://doi.org/10.2475/ajs.274.4.321

Neal, Christina, and McGimsey, R.G., 1997, 1996 volcanic activity in Alaska and Kamchatka—Summary of events and response of the Alaska Volcano Observatory: U.S. Geological Survey Open-File Report OF 97-0433, 34 p. https://pubs.er.usgs.gov/publication/ofr97433

Neill, O.K., 2013, Petrologic and geochemical tracers of magmatic movement in volcanic arc systems—Case studies from the Aleutian Islands and Kamchatka, Russia: Fairbanks, AK, University of Alaska Fairbanks, Ph.D. dissertation, 188 p.

Neill, O.K., Larsen, J.F., Izbekov, P.E., and Nye, C.J., 2015, Pre-eruptive magma mixing and crystal transfer revealed

by phenocryst and microlite compositions in basaltic andesite from the 2008 eruption of Kasatochi Island volcano: American Mineralogist, v. 100, no. 4, p. 722–737, http://doi.org/10.2138/am-2015-4967

Prata, A.J., Gangale, G., Clarisse, L., and Karagulian, F., 2010, Ash and sulfur dioxide in the 2008 eruptions of Okmok and Kasatochi—Insights from high spectral resolution satellite measurements: Journal of Geophysical Research, v. 115, no. D2, D00L18. http://doi.org/10.1029/2009JD013556

Roeder, P.L., 1974, Activity of iron and olivine solubility in basaltic liquids: Earth and Planetary Science Letters, v. 23, no. 3, p. 397–410. http://doi.org/10.1016/0012-821X(74)90129-0

Ruppert, N.A., Prejean, S., and Hansen, R.A., 2011, Seismic swarm associated with the 2008 eruption of Kasatochi Volcano, Alaska—Earthquake locations and source parameters: Journal of Geophysical Research, v. 116, no. B7, B00B07. http://doi.org/10.1029/2010JB007435

Sack, R.O., Carmichael, .S.E., Rivers, M.L., and Ghiorso, M.S., 1981, Ferric-ferrous equilibria in natural silicate liquids at 1 bar: Contributions to Mineralogy and Petrology, v. 75, no. 4, p. 369–376. http://doi.org/10.1007/BF00374720

Scholl, D.W., Buffington, E.C., and Marlow, M.S, 1975, Plate tectonics and the structural evolution of the Aleutian–Bering Sea region, *in* Forbes, R.B., ed., Contributions to the Geology of the Bering Sea and Adjacent Regions: Geological Society of America Special Paper 151, p. 1–32. http://doi.org/10.1130/SPE151-p1

Scott, W.E., Nye, C.J., Waythomas, C.F., and Neal, C.A., 2010, August 2008 eruption of Kasatochi Volcano, Aleutian Islands, Alaska—Resetting an island landscape: Arctic, Antarctic, and Alpine Research, v. 42, no. 3, p. 250–259, http://doi.org/10.1657/1938-4246-42.3.250

Skilling, I.P., White, J.D.L, and McPhie, J., 2002, Peperite—A review of magma–sediment mingling: Journal of Volcanology and Geothermal Research, v. 114, no. 1-2, p. 1–17. http://doi.org/10.1016/S0377-0273(01)00278-5

Sun, S.S., and McDonough W.F., 1989, Chemical and isotopic systematics of oceanic basalts—Implications for mantle compositions and processes, *in* Saunders, A.D., and Norry, M.J., eds., Magmatism in ocean basins: Geological Society of London, Special Publication 42, p. 313–345.

Thorson, R.M., and Hamilton, T.D., 1986, Glacial geology of the Aleutian Islands, based on the contributions of Robert F. Black, *in* Hamilton, T.D., Reed, K.M., and Thorson, R.M., eds., Glaciation in Alaska—the geologic record: Alaska Geological Society, p. 171–192.

Waythomas, C.F., Scott, W.E., and Nye, C.J., 2010a, The geomorphology of an Aleutian volcano following a major eruption—the 7–8 August 2008 eruption of Kasatochi volcano, Alaska, and its aftermath: Arctic, Antarctic, and Alpine Research, v. 42, no. 3, p. 260–275, http://doi.org/10.1657/1938-4246-42.3.260

Waythomas, C.F., Scott, W.E., Prejean, S.G., Schneider, D.J., Izbekov, Pavel, and Nye, C.J., 2010b, The 7–8 August 2008 eruption of Kasatochi volcano, central Aleutian Islands, Alaska: Journal of Geophysical Research, v. 115, no. B6, B00B06, 23 p. http://doi.org/10.1029/2010JB007437

Williams, J.C., Drummond, B.A., and Buxton, R.T., 2010, Initial effects of the August 2008 volcanic eruption on breeding birds and marine mammals at Kasatochi Island, Alaska: Arctic, Antarctic, and Alpine Research, v. 42, no. 3, p. 306–314, http://doi.org/10.1657/1938-4246-42.3.306

Yogodzinski, G.M., Brown, S.T., Kelemen, P.B., Vervoort, J.D., Portnyagin, Maxim, Sims, K.W.W., Hoernle, Kaj, Jicha, B.R., and Werner, Reinhard, 2015, The role of subducted basalt in the source of island arc magmas—Evidence from seafloor lavas of the western Aleutians: Journal of Petrology, v. 56, no. 3, p. 441–492. http://doi.org/10.1093/petrology/egv006

APPENDIX 1. PANORAMIC PHOTOGRAPHS

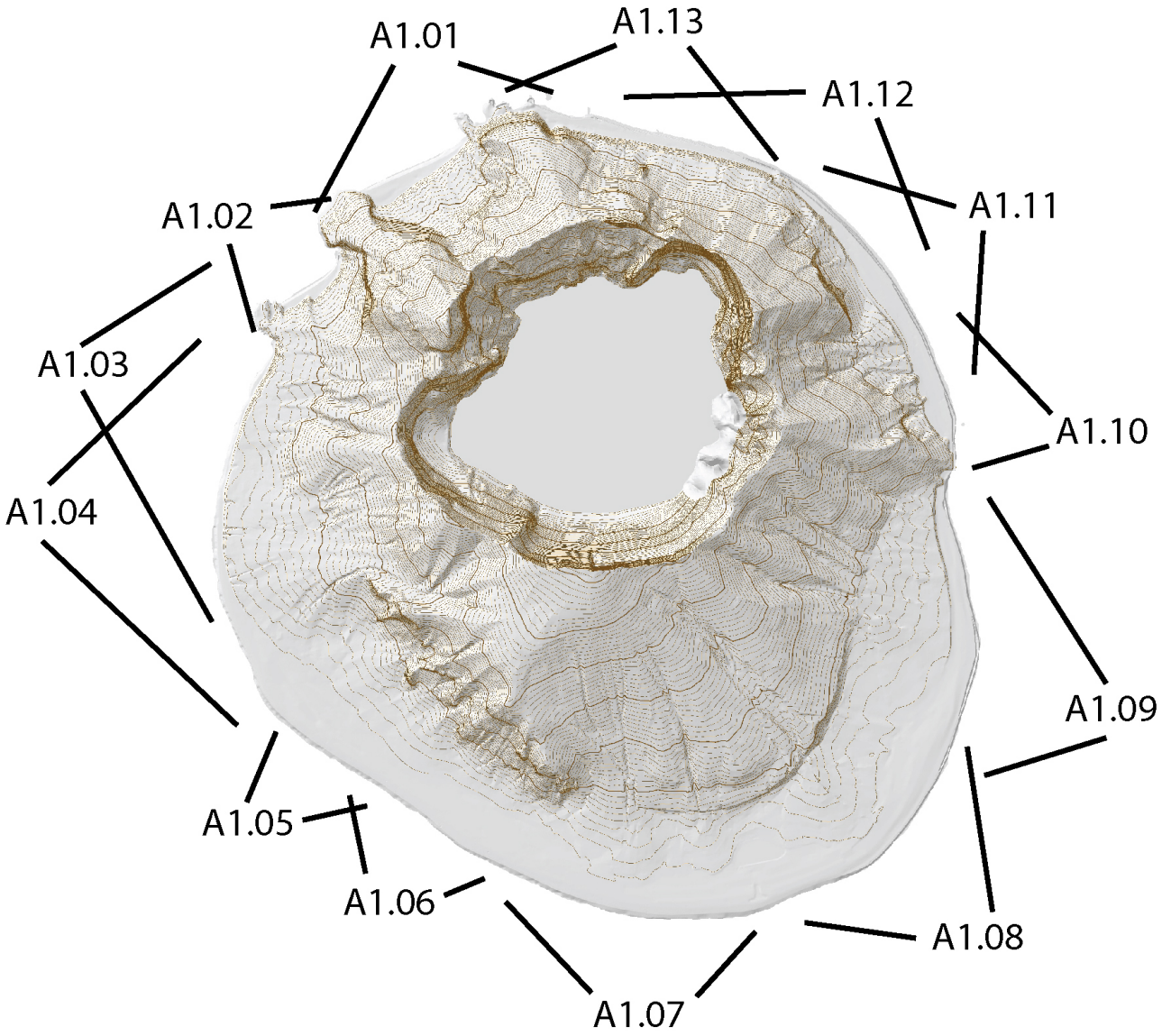

A1.00. Approximate orientation and viewshed of panoramic coastal photographs. All photographs taken from the *M/V Tiĝlax̂.* The position of the *Tiĝlax̂* during photography, represented by label location, was estimated from the photographs. High resolution versions of the images are in the digital supplement.

A1.01. Photograph of western part of north shore of Kasatochi. Sea Lion spit is to left of center and closest to camera. Note sea lions to left of Sea Lion spit. Right half of shoreline is Whiskey cove. The Monkey's Forehead is silhouetted low on left skyline. Headland on far right is Tundering head; highest point on skyline is mount Kasatochi. Photograph by J. Williams (USFWS), June 12, 2009.

A1.02. Photograph of northwestern coast of Kasatochi between Tundering head (left) and Barabara ridge (right foreground). Tundering cove is in center of photograph. Tundering talus, completely buried by 2008 eruption and with its toe partially exposed at time of this photograph, is between left side of beach and cliffs above. High foreground cloud-capped peak is mount Kasatochi. Photograph by C. Nye, August 16, 2011

A1.03. Photograph of western coast of Kasatochi. Tundering head is on far left; Barabara ridge is on left; Tundering cove is behind Barabara ridge and not visible. High points on skyline are mount Kasatochi, left; Jack peak, center; and Peregrine peak. Beach bluffs are 25 m high on left, dropping to 3 m at lowest point, and were cut into 2008 deposits during fall–winter 2008 and winter–spring 2009. Photograph by J. Williams, USFWS, June 13, 2009.

A1.04. Photograph of western coast of Kasatochi from a few hundred meters south of location where photograph in figure A1.03 was taken. Shag rock can be seen protruding above beach by a few meters on far right. The two highest points on skyline are mount Kasatochi, left, and Jack peak, center; Peregrine peak is below skyline to right of Jack peak. Photograph by C. Nye, June 12, 2009.

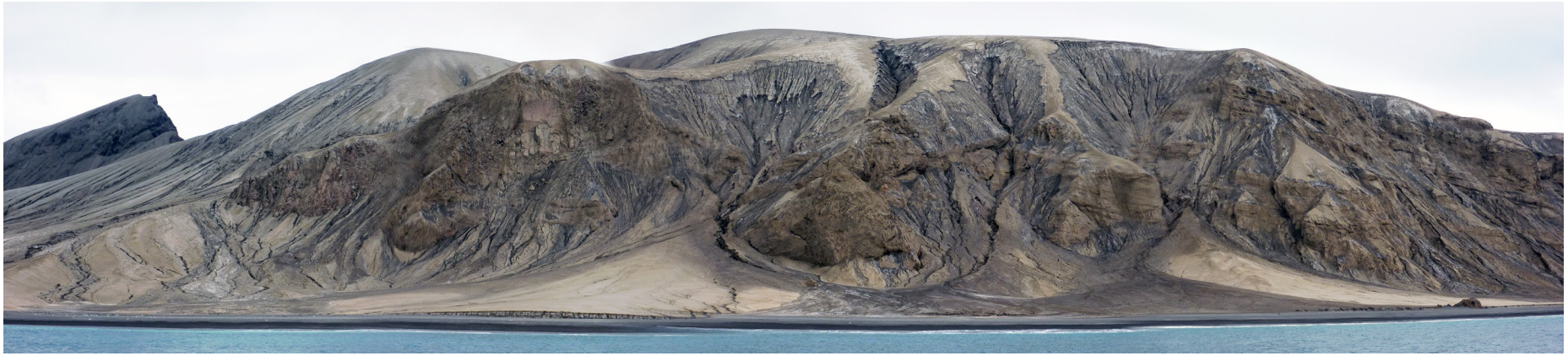

A1.05. Photograph of northern part of southwestern coast of Kasatochi. Highest point on skyline is Luna summit (center); Jack peak is second highest, to left of Luna summit. Peregrine peak is between Luna summit and Jack peak, just breaking skyline. Shag rock protrudes from the beach in lower right part of photograph. Photograph by C. Nye, June 12, 2009.

A1.06. Photograph of southwestern coast of Kasatochi. High point just right of center on the skyline is Luna summit. Peregrine peak is on left skyline, below and to left of Jack peak, in background. Photograph by C. Nye, June 12, 2009.

A1.07. Photograph of southern coast of Kasatochi. Highest point on skyline is Luna summit. Foreground bluffs at low elevation in center are pre-eruption beach bluffs. Photograph by C. Nye, June 12, 2009.

A1.08. Photograph of south–southeast coast of Kasatochi. Large gullies in center of photograph descend from a position near the rim about 200 m east of Luna summit. Clouds obscure approximately upper half of volcano. Photograph by J. Williams (USFWS), June 12, 2009.

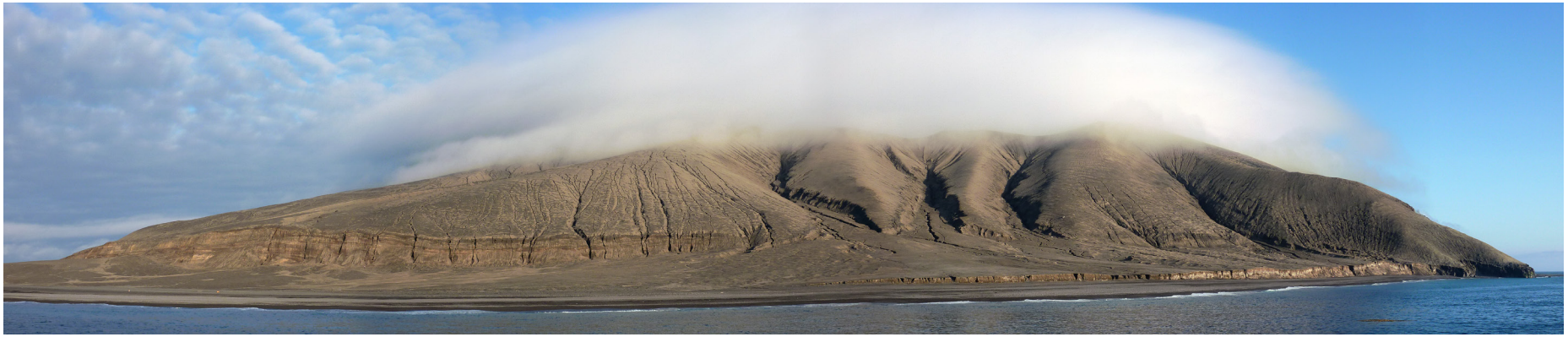

A1.09. Photograph of southeastern coast of Kasatochi. V-shaped valleys roughly perpendicular to coast and ridges between them are The Ogres Toes. Valleys are 100 to 200 m apart and 15 to 30 m deep at mid slope. Rye point is at far right of photograph. Photograph by C. Nye, June 12, 2009.

A1.10. Photograph of eastern coast of Kasatochi. Rye point is on left. East point is the rocky outcrop about three-quarters of the way from left to right. Bluffs cut into 2008 deposits form two apparent headlands on right. Two highest points on skyline are Rye summit (left) and Ogre summit (right). Photograph by C. Nye, June 12, 2009.

A1.11. Photograph of northeastern coast of Kasatochi. Rye point is at far left of photograph. Large cliff in center foreground is The Ogres Brow. Ogre summit is just off top edge of photograph. Monkey summit is on right skyline. Light-colored bluffs behind beach are 2008 deposits; these transient bluffs formed in ten months between eruption and time of this photograph. Photograph by J. Williams (USFWS), June 12, 2009.

A1.12. Photograph of north–northeast coast of Kasatochi. Rye point is silhouetted on far left; The Ogres Brow is to left of center. Northernmost point on island is on far right. Ogre summit is left of center, above most prominent gully. Steep peak on right is Monkey summit. The Monkeys Forehead is at mid slope near but below right skyline. Light-colored bluffs are 2008 deposits. Photograph by J. Williams (USFWS), June 12, 2009.

A1.13. Photograph of northern coast of Kasatochi. The Ogres Brow is silhouetted on lower left skyline. Sea Lion point is at far right. The Monkey's Forehead is large mid slope block just right of center, and Monkey summit is above—the tallest feature on skyline. Photograph by J. Williams (USFWS), June 12, 2009.

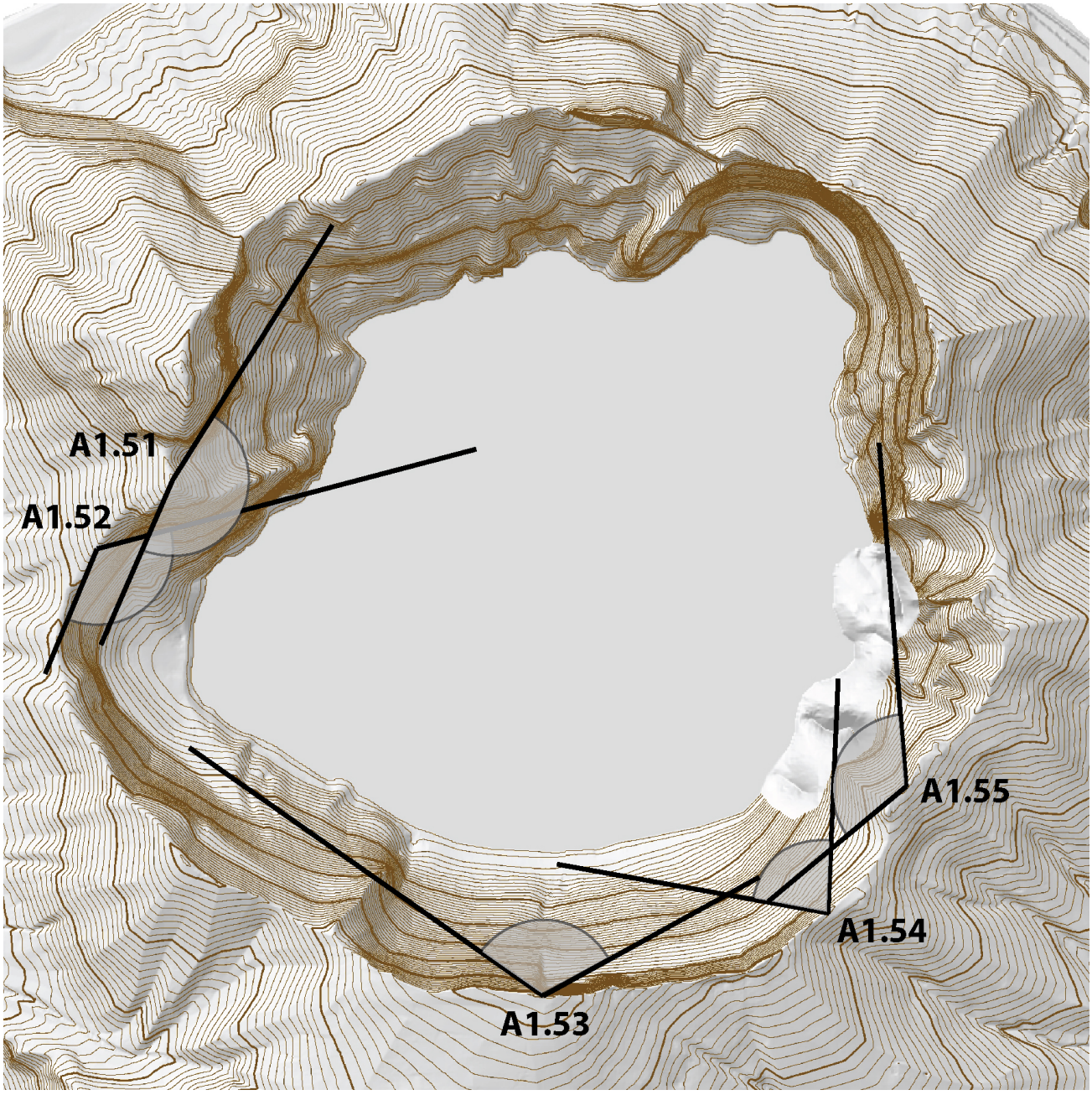

A1.50. Approximate orientation and viewshed of panoramic photographs of crater walls, taken from crater rim. Opportunities for photographing walls were severely limited by terrain and weather. This appendix contains print-resolution images (1,800 pixels wide).

A1.51. Panoramic photograph of northern, eastern, and southern crater walls, taken from crater rim immediately south of mount Kasatochi. Photograph spans about 180 degrees of arc. Monkey summit is on left skyline, lightly shrouded by cloud. Ogre (left) and Rye (right) summits are along back skyline, left of center. Luna summit and Jack peak are shrouded in clouds along right skyline. Photograph by J. Williams (USFWS), August 10, 2010.

A1.52. Panoramic photograph of southern and eastern crater walls, taken from southwest. The summit and eastern shoulder of Monkey summit are northernmost (left) visible features of the rim. Luna summit is in clouds and Jack peak is just at cloud level. Photograph by J. Williams (USFWS), August 10, 2010.

A1.53. Panoramic photograph of western, northern, and eastern crater walls taken from Luna summit, on crater's south rim. Mount Kasatochi (left) is tallest feature. Other high points on rim are, from left: Monkey summit, Ogre summit, and Rye summit. Koniuji Island is in far right distance. Photograph by J. Williams (USFWS), June 13, 2009.

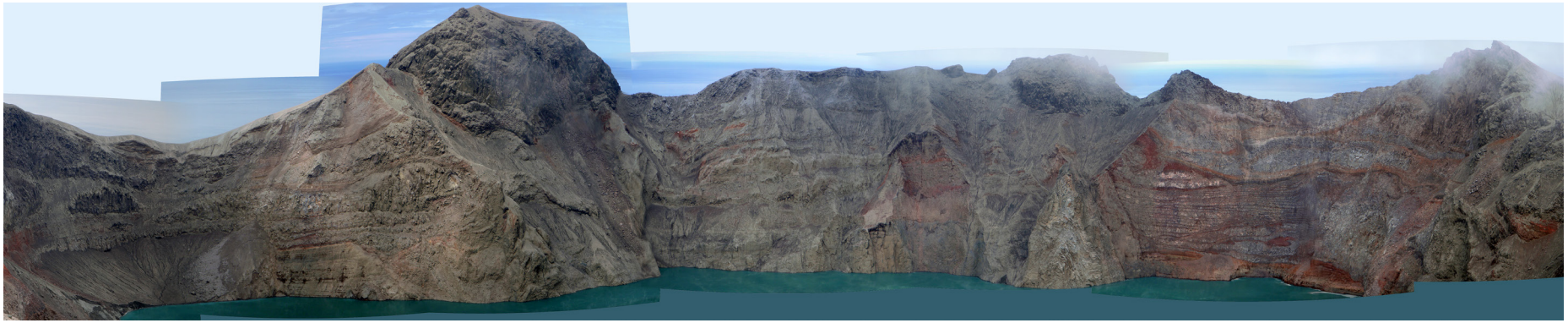

A1.54. Panoramic photograph of western and northern crater walls, taken from southeast crater rim. Features along crater rim are, from left: low point on rim, mount Kasatochi, Monkey summit, and Ogre summit at far right. Photograph by J. Williams (USFWS), June 13, 2009.

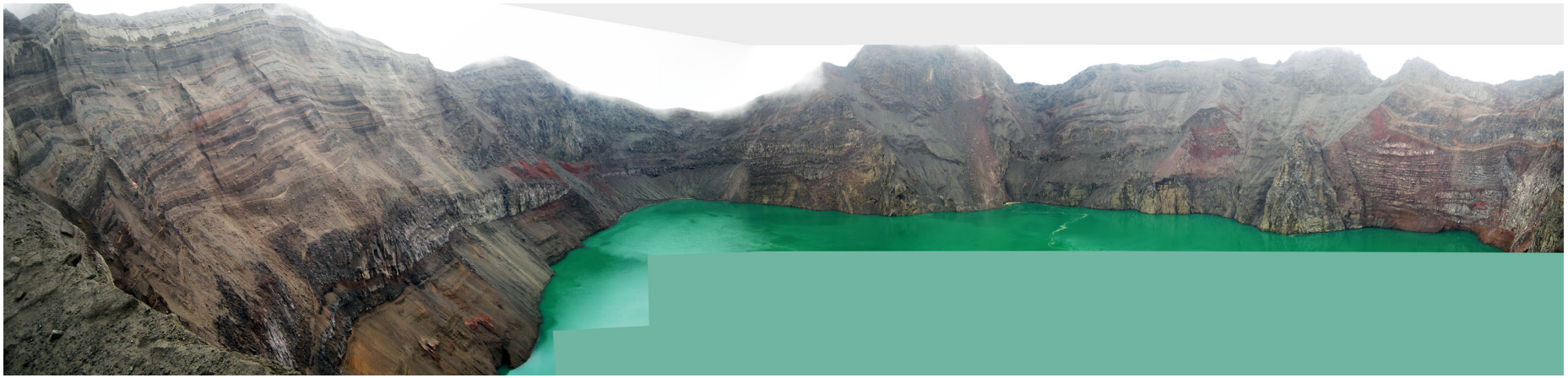

A1.55. Panoramic photograph of southern, western, and northern crater walls, taken from southeastern crater rim. Features along rim, from left: Luna summit, Jack peak, the low spot on the rim, Mount Kasatochi (upper part truncated) and Monkey summit. Photograph by W. Scott, August 11, 2010.

APPENDIX 1A.

Table A1. Full-resolution copies of the panoramic images are in Electronic Supplement E1. The following table lists the full filenames, size and resolution of each image.

file name	size (MB)	w (pixels)	h (pixels)	date	photographer
Coastal panoramas					
A1.00_PhotoOrientation_coast.jpg	1.87	1,783	1,605		
A1.01_WhiskeyCove.tif	63.8	7,858	1,626	June 12, 2009	J. Williams
A1.02_TunderingCove.tif	70.8	10,667	2,266	August 16, 2011	C. Nye
A1.03_WNWCoast.tif	138.5	16,420	2,879	June 13, 2009	J. Williams
A1.04_WCoast.tif	76.2	12,687	2,050	June 12, 2009	C. Nye
A1.05_PeregrineNorth.tif	48.2	8,543	1,925	June 12, 2009	C. Nye
A1.06_PeregrineSouth.tif	31.6	7,209	1,497	June 12, 2009	C. Nye
A1.07_SCoast.tif	43.3	9,048	1,634	June 12, 2009	C. Nye
A1.08_SECoast.tif	162.2	16,320	3,392	June 12, 2009	J. Williams
A1.09_OgresToes.tif	43.3	8,438	1,750	June 12, 2009	C. Nye
A1.10_RyePoint.tif	28.3	6,397	1,511	June 12, 2009	C. Nye
A1.11_OgresBrow.tif	125.1	15,069	2,832	June 12, 2009	J. Williams
A1.12_ENECoast.tif	55.2	9,840	1,914	June 12, 2009	J. Williams
A1.13_MonkeysForehead.tif	128.1	14,568	3,001	June 12, 2009	J. Williams
Crater wall panoramas					
A1.50_PhotoOrientation_crater.jpg	4.08	1,796	1,796		
A1.51_N_E_S_walls_fromW.tif	77.6	10,494	2,523	August 10, 2010	J. Williams
A1.52_E_S_walls_fromW.tif	115.0	11,058	3,548	August 10, 2010	J. Williams
A1.53_W_N_E_walls_fromS.tif	71.2	10,830	2,244	June 13, 2009	J. Williams
A1.54_W_N_walls_fromSE.tif	198.0	18,474	3,657	June 13, 2009	J. Williams
A1.55_S_W_N_walls_fromE.tif	330.8	21,114	5,347	August 11, 2010	W. Scott

APPENDIX 2. SATELLITE IMAGES USED IN THIS STUDY

Table A2. The following satellite images were used in this study to determine shoreline and gully geometry history. The stereo pair of images acquired April 18, 2009 were used to construct the digital elevation model from which the topographic contours were obtained, as well as for the primary base image used for mapping. Licensing restrictions do not permit distribution of the raw satellite data with this study.

DigitalGlobe Catalog_Id	Imaging Bands	Spacecraft	Acquisition date	y, m, d, post-eruption	Off-nadir angle (deg)	GSD (m)	comments
1010010002D8F600	Pan-MS1	QB02	4/9/2004	pre-eruption	12.63	0.64	Minor diffuse clouds, sea lion spit obscured.
1010010008853E00	Pan-MS1	QB02	9/3/2008	0y 0m 27d	29.46	0.78	Thick plume obscures crater and SW flank. W flank obscured by plume and its shadow to 1–200 m from shoreline. Shoreline unobscured except for ~1 km in SW, outboard of Peregrine cliffs. Sea Lion spit still covered.
1020010004607300	Pan	WV01	9/17/2008	0y 1m 11d	28.88	0.63	North half of crater, eastern rim, and upper flank obscured by plume. North flank obscured by plume shadow. Shoreline clear except for a few hundred meters near Rye point/East point. South and west flanks clear. Sea lions visible 200 m SE of Shag Rock. Sea Lion spit still covered.
1010010008A1CE00	Pan-MS1	QB02	9/29/2008	0y 1m 23d	23.05	0.71	Clear except for diffuse clouds over South point and Shag Rock area. Locally heavy shadows on north flank.
10200100064A7100	**Pan**	**WV01**	**4/18/2009**	**0y 8m 11d**	**22.82**	**0.58**	**Stereo pair used for DEM and map base. Clear except for small clouds/plume in SE crater, which are dense enough to make DEM and topography of SE crater wall unusable.**
10200100067E5500	**Pan**	**WV01**	**4/18/2009**	**0y 8m 11d**	**29.61**	**0.6**	
1020010009A7AC00	Pan	WV01	9/13/2009	1y 1m 6d	23.25	0.58	Clouds over upper east flank, Rye point, easternmost crater rim. Some shadows under cliffs on north flank. Mostly clear.
103001000AC7A900	Pan-MS1-MS2	WV02	3/9/2011	2y 7m 0d	18.13	0.51	Clouds over southwest flank cover most of lower and mid flank. Rim and coast clear everywhere.
103901900F183400	Pan-MS1-MS2	WV02	1/11/2012	3y 5m 4d	24.77	0.55	Minor very diffuse clouds over south beach. All north-facing slopes in shadow, but the shadows aren't opaque—reasonable detail visible throughout.
10300100112C3F00	PanMS1-MS2	WV02	2/2/2012	3y 5m 26d	20.58	0.52	Cloudless. All north-facing slopes in shadow, but the shadows aren't opaque—reasonable detail visible throughout.

APPENDIX 3. SAMPLE LIST AND DESCRIPTIONS

APPENDIX 3A. SAMPLE LIST AND METADATA

Table A3. Sample list. Microsoft Excel (.xlsx), tab-delimited (.txt), and comma-separated value (.csv) versions of this table are included in Electronic Supplement E3.

Sample	Map Unit	Map symbol[1]	Latitude (WGS84)	Longitude (E, WGS84)	SiO_2	Chem[2]	Mode[3]	Geologist	Date Collected
11KCon07B-5	2008 pyroclastic deposits, andesite scoria	Q8p.j,a	52.17487	-175.52933	58.83	Y	n	Neill, O. K.	8/15/2011
08cw002-1b	2008 pyroclastic deposits, andesite scoria	Q8p.j,a	52.17477	-175.53152	59.12	Y	Y	Waythomas, C. F.	8/22/2008
11KCon07B-6	2008 pyroclastic deposits, andesite scoria	Q8p.j,a	52.17487	-175.52933	59.23	Y	n	Neill, O. K.	8/15/2011
10KCon09-1	2008 pyroclastic deposits, andesite scoria	Q8p.j,a	52.18046	-175.49873	59.30	Y	Y	Neill, O. K.	8/1/2010
11KCon07B-2	2008 pyroclastic deposits, andesite scoria	Q8p.j,a	52.17487	-175.52933	59.49	Y	n	Neill, O. K.	8/15/2011
10KCon06-1	2008 pyroclastic deposits, andesite scoria	Q8p.j,a	52.18046	-175.49873	59.73	Y	n	Neill, O. K.	8/1/2010
11KCon14B-1	2008 pyroclastic deposits, andesite scoria	Q8p.j,a	52.17487	-175.52933	59.77	Y	n	Neill, O. K.	8/16/2011
11KCon17-1	2008 pyroclastic deposits, andesite scoria	Q8p.j,a	52.16724	-175.52937	60.17	Y	n	Neill, O. K.	8/17/2011
10KCwes001	2008 pyroclastic deposits, andesite scoria	Q8p.j,a	52.18077	-175.49892	60.21	Y	Y	Scott, W.E.	6/18/2010
10KCon11-1	2008 pyroclastic deposits, andesite scoria	Q8p.j,a	52.16884	-175.53114	60.22	Y	n	Neill, O. K.	8/1/2010
11KCon07B-4	2008 pyroclastic deposits, andesite scoria	Q8p.j,a	52.17487	-175.52933	60.37	Y	n	Neill, O. K.	8/15/2011
09KCnye0F1	2008 pyroclastic deposits, andesite scoria	Q8p.j,a	52.17931	-175.52646	60.44	Y	Y	Nye, C. J.	6/14/2009
10KCon07-1	2008 pyroclastic deposits, andesite scoria	Q8p.j,a	52.18046	-175.49873	60.57	Y	Y	Neill, O. K.	8/1/2010
11KCon07B-3	2008 pyroclastic deposits, andesite scoria	Q8p.j,a	52.17487	-175.52933	60.62	Y	n	Neill, O. K.	8/15/2011
11KCon07B-1	2008 pyroclastic deposits, andesite scoria	Q8p.j,a	52.17487	-175.52933	61.86	Y	n	Neill, O. K.	8/15/2011
09KCnye008a	2008 pyroclastic deposits, basaltic andesite scoria	Q8p.j,ba	52.16247	-175.52338	52.00	Y	Y	Nye, C. J.	6/13/2009
11KCon10B-1	2008 pyroclastic deposits, basaltic andesite scoria	Q8p.j,ba	52.17271	-175.53027	52.15	Y	n	Neill, O. K.	8/16/2011
11KCon13-1	2008 pyroclastic deposits, basaltic andesite scoria	Q8p.j,ba	52.16773	-175.52985	52.64	Y	n	Neill, O. K.	8/16/2011
09KCnye008c	2008 pyroclastic deposits, basaltic andesite scoria	Q8p.j,ba	52.16247	-175.52338	52.82	Y	Y	Nye, C. J.	6/13/2009
09KCnye008b	2008 pyroclastic deposits, basaltic andesite scoria	Q8p.j,ba	52.16247	-175.52338	52.84	Y	Y	Nye, C. J.	6/13/2009
10KCon03-1	2008 pyroclastic deposits, basaltic andesite scoria	Q8p.j,ba	52.16703	-175.49226	52.97	Y	Y	Neill, O. K.	8/1/2010
10KCon03-3	2008 pyroclastic deposits, basaltic andesite scoria	Q8p.j,ba	52.16703	-175.49226	52.97	Y	n	Neill, O. K.	8/1/2010
11KCon10B-2	2008 pyroclastic deposits, basaltic andesite scoria	Q8p.j,ba	52.17271	-175.53027	53.27	Y	n	Neill, O. K.	8/16/2011
10KCon18-3	2008 pyroclastic deposits, basaltic andesite scoria	Q8p.j,ba	52.16884	-175.53114	53.76	Y	n	Neill, O. K.	8/1/2010
10KCon18-1	2008 pyroclastic deposits, basaltic andesite scoria	Q8p.j,ba	52.16884	-175.53114	53.85	Y	Y	Neill, O. K.	8/1/2010
11KCon01B-3	2008 pyroclastic deposits, basaltic andesite scoria	Q8p.j,ba	52.17271	-175.53027	54.50	Y	n	Neill, O. K.	8/15/2011
11KCon20B-1	2008 pyroclastic deposits, basaltic andesite scoria	Q8p.j,ba	52.16922	-175.53043	55.38	Y	n	Neill, O. K.	8/17/2011
11KCon02B-1	2008 pyroclastic deposits, banded scoria	Q8p.j,bnd	52.17271	-175.53027	54.72	Y	n	Neill, O. K.	8/15/2011

Table A3. Sample list (cont'd).

Sample	Map Unit	Map symbol[1]	Latitude (WGS84)	Longitude (E, WGS84)	SiO_2	Chem[2]	Mode[3]	Geologist	Date Collected
09KCnye005	2008 pyroclastic deposits, banded scoria	Q8p.j,bnd	52.18003	-175.49742	55.57	Y	Y	Nye, C. J.	6/12/2009
11KCon01B-2	2008 pyroclastic deposits, banded scoria	Q8p.j,bnd	52.17271	-175.53027	56.28	Y	n	Neill, O. K.	8/15/2011
09KCwes012	2008 pyroclastic deposits, banded scoria	Q8p.j,bnd	52.17349	-175.5314	56.45	Y	Y	Scott, W.E.	6/14/2009
08cw002-1c	2008 pyroclastic deposits, banded scoria	Q8p.j,bnd	52.17477	-175.53152	58.28	Y	Y	Waythomas, C. F.	8/22/2008
09KCnye199m	2008 gabbro groundmass	Q8p.gg	52.16105	-175.51552	49.94	Y	n	Nye, C. J.	
09KCnye003m	2008 gabbro groundmass	Q8p.gg	52.17463	-175.49533	51.18	Y	n	Nye, C. J.	6/12/2009
KC12ak34m	2008 ultramafic inclusion gms	Q8p.umg	52.18111	-175.51923	49.43	Y	n	Kentner, A. (UAF)	6/17/2012
08cw002-4a	2008 pyroclastic flows - unanalyzed scoria	Q8p.na	52.17477	-175.53152	-	n	Y	Waythomas, C. F.	8/22/2008
09KCwes013	2008 pyroclastic flows - unanalyzed scoria	Q8p.na	52.17338	-175.53146	-	n	Y	Scott, W.E.	6/14/2009
09KCwes002	2008 pyroclastic flows - unanalyzed scoria	Q8p.na	52.17988	-175.49895	-	n	Y	Scott, W.E.	6/12/2009
09KCwes020	2008 pyroclastic flows - unanalyzed scoria	Q8p.na	52.17398	-175.53122	-	n	Y	Scott, W.E.	6/14/2009
10KCon10-2	2008 pyroclastic flows - unanalyzed scoria	Q8p.na	52.16884	-175.53114	-	n	Y	Neill, O. K.	8/1/2010
09KCnye001c	2008 gabbro	Q8p.gab	52.17568	-175.4937	40.98	Y	Y	Nye, C. J.	6/12/2009
09KCnye012a1	2008 gabbro	Q8p.gab	52.1799	-175.52583	41.41	Y	Y	Nye, C. J.	6/14/2009
09KCnye003	2008 gabbro	Q8p.gab	52.17463	-175.49533	42.46	Y	Y	Nye, C. J.	6/12/2009
09KCnye012a2	2008 gabbro	Q8p.gab	52.1799	-175.52583	42.99	Y	Y	Nye, C. J.	6/14/2009
09KCnye012b3	2008 gabbro	Q8p.gab	52.1799	-175.52583	43.02	Y	n	Nye, C. J.	6/14/2009
09KCnye100am	amphibole from 2008 gabbro	Q8p.g.am	52.16436	-175.51952	39.34	Y	n	Nye, C. J.	8/10/2009
09KCnye012b1	plagioclasw from 2008 gabbro	Q8p.g.pl	52.1799	-175.52583	44.54	Y	n	Nye, C. J.	6/14/2009
09KCnye100	2008 gabbro, not anlyzed	Q8p.gab.na	52.16436	-175.51952	-	n	Y	Nye, C. J.	8/10/2009
KC12ak22	2008 ultramafic inclusion	Q8p.um	52.18111	-175.51923	40.96	Y	Y*	Kentner, A. (UAF)	6/17/2012
KC12ak34	2008 ultramafic inclusion	Q8p.um	52.18111	-175.51923	41.61	Y	Y*	Kentner, A. (UAF)	6/17/2012
KC12ak11	2008 ultramafic inclusion	Q8p.um	52.17139	-175.52795	46.44	Y	Y*	Kentner, A. (UAF)	6/18/2012
KC12ak33	2008 ultramafic inclusion	Q8p.um	52.18111	-175.51923	47.90	Y	Y*	Kentner, A. (UAF)	6/17/2012
KC12ak13	2008 ultramafic inclusion	Q8p.um	52.17139	-175.52795	48.55	Y	Y*	Kentner, A. (UAF)	6/18/2012
KC12ak12	2008 ultramafic inclusion	Q8p.um	52.17139	-175.52795	49.89	Y	n	Kentner, A. (UAF)	6/18/2012
KC12ak42	2008 ultramafic inclusion	Q8p.um	52.18111	-175.51923	51.05	Y	n	Kentner, A. (UAF)	6/17/2012
KC12ak19	2008 anorthosite inclusion	Q8p.an	52.17139	-175.52795	44.43	Y	n	Kentner, A. (UAF)	6/18/2012

Table A3. Sample list (cont'd).

Sample	Map Unit	Map symbol[1]	Latitude (WGS84)	Longitude (E, WGS84)	SiO_2	Chem[2]	Mode[3]	Geologist	Date Collected
09KCwes009	Luna pyroclastic deposits	Qlp	52.16234	-175.50018	52.77	Y	Y	Scott, W.E.	6/13/2009
12KCwes001	Luna pyroclastic deposits	Qlp	52.16134	-175.51204	53.04	Y	n	Scott, W.E.	6/18/2012
05KScn002A	Luna pyroclastic deposits	Qlp	52.16059	-175.50418	53.43	Y	n	Neal, C. (USGS)	6/27/1905
10KCwes004	Luna pyroclastic deposits	Qlp	52.17082	-175.49565	54.36	Y	n	Scott, W.E.	6/18/2010
09KCwes008	Luna pyroclastic deposits	Qlp	52.16365	-175.49897	54.53	Y	Y	Scott, W.E.	6/13/2009
09KCnye009a	Luna pyroclastic deposits	Qlp	52.16072	-175.50848	55.15	Y	Y	Nye, C. J.	6/13/2009
09KCnye009b	Luna pyroclastic deposits	Qlp	52.16072	-175.50848	55.20	Y	n	Nye, C. J.	6/13/2009
09KCwes006	Luna pyroclastic deposits	Qlp	52.16639	-175.49782	56.59	Y	Y	Scott, W.E.	6/13/2009
09KCwes007	Luna pyroclastic deposits	Qlp	52.16365	-175.49897	57.56	Y	Y	Scott, W.E.	6/13/2009
09KCwes022	Luna pyroclastic deposits	Qlp	52.17543	-175.52648	58.43	Y	Y	Scott, W.E.	6/14/2009
09KCnye011a	Luna pyroclastic deposits	Qlp	52.17437	-175.5268	58.92	Y	Y	Nye, C. J.	6/14/2009
09KCnye011b	Luna pyroclastic deposits	Qlp	52.17437	-175.5268	59.12	Y	Y	Nye, C. J.	6/14/2009
09KCwes005	Luna pyroclastic deposits	Qlp	52.16907	-175.49893	59.38	Y	Y	Scott, W.E.	6/13/2009
10KCnye004	Monkeys Forehead basaltic andesite	Qmfm	52.18361	-175.50811	54.87	Y	Y	Nye, C. J.	8/11/2010
09KCwes019	Tundering basaltic andesite, Barabara R	Qtm	52.17735	-175.52911	53.75	Y	Y	Scott, W.E.	6/14/2009
09KCwes023	Tundering basaltic andesite, Barabara R	Qtm	52.17843	-175.52871	53.89	Y	Y	Scott, W.E.	6/14/2009
10KCnye002	Tundering basaltic andesite	Qtm	52.18187	-175.52307	53.96	Y	n	Nye, C. J.	6/19/2010
09KCwes024	Tundering basaltic andesite	Qtm	52.18012	-175.52525	55.48	Y	Y	Scott, W.E.	6/14/2009
09KCwes025	Tundering basaltic andesite	Qtm	52.18012	-175.52525	55.63	Y	Y	Scott, W.E.	6/14/2009
KC12nye03	Tundering basaltic andesite	Qtm	52.1817	-175.52376	55.69	Y	n	Nye, C. J.	6/19/2012
KC11nye05	Mt Kasatochi andesite	Qmka	52.17959	-175.52595	59.37	Y	Y	Nye, C. J.	8/17/2011
09KCwes003	Ogres Brow basaltic andesite	Qobm	52.17863	-175.49761	56.64	Y	Y	Scott, W.E.	6/12/2009
09KCnye108	Ogres Brow basaltic andesite	Qobm	52.17866	-175.49797	56.83	Y	Y	Nye, C. J.	8/12/2009
09KCnye107	Ogres Brow gabbro	Qobg	52.17866	-175.49797	45.62	Y	Y	Nye, C. J.	8/12/2009
09KCnye002	Rye basaltic andesite	Qrm	52.17523	-175.49533	56.53	Y	Y	Nye, C. J.	6/12/2009
09KCnye004	Rye basaltic andesite	Qrm	52.17387	-175.495	56.57	Y	Y	Nye, C. J.	6/12/2009
09KCnye006	Rye basalt	Qrb	52.17337	-175.49237	50.89	Y	Y	Nye, C. J.	6/12/2009
10KCnye001	Rye basalt	Qrb	52.17191	-175.49239	51.34	Y	Y	Nye, C. J.	6/18/2010

Table A3a. Sample list (cont'd).

Sample	Map Unit	Map symbol[1]	Latitude (WGS84)	Longitude (E, WGS84)	SiO_2	Chem[2]	Mode[3]	Geologist	Date Collected
12KCaek001	Whiskey andesite	Qwa	52.17975	-175.51788	56.04	Y	n	Kentner, A. (UAF)	6/19/2012
KC12nye01	Whiskey andesite	Qwa	52.18182	-175.51815	56.26	Y	n	Nye, C. J.	6/19/2012
KC12nye02	Whiskey andesite	Qwa	52.1835	-175.51811	56.30	Y	n	Nye, C. J.	6/19/2012
09KCnye010	Whiskey andesite	Qwa	52.1705	-175.52315	57.08	Y	Y	Nye, C. J.	6/14/2009
12KCwes004	Whiskey andesite	Qwa	52.18254	-175.51719	57.88	Y	n	Scott, W.E.	6/19/2012
12KCwes005	Whiskey andesite	Qwa	52.18118	-175.5178	58.27	Y	n	Scott, W.E.	6/19/2012
09KCnye110	Whiskey andesite	Qwa	52.18468	-175.51384	58.30	Y	Y	Nye, C. J.	8/12/2009
10KCnye005	Gregs Mighty basalt	Qgmb	52.18238	-175.50211	49.33	Y	Y	Nye, C. J.	8/11/2010
10KCnye006	Gregs Mighty basalt	Qgmb	52.18198	-175.50101	49.39	Y	Y	Nye, C. J.	8/11/2010
09KCnye109	Gregs Mighty basalt	Qgmb	52.18088	-175.49828	49.43	Y	Y	Nye, C. J.	8/12/2009
09KCwes001	Gregs Mighty basalt	Qgmb	52.17988	-175.49895	49.49	Y	Y	Scott, W.E.	6/12/2009
09KCnye007	Peregrine lava	Qpl	52.16898	-175.52399	55.57	Y	Y	Nye, C. J.	6/13/2009
05KScn001	Peregrine lava	Qpl	52.16949	-175.52388	57.04	Y	n	Neal, Christina	6/27/1905
09KCwes011	Peregrine glaciovolcanic deposits	Qpg	52.16121	-175.51354	51.97	Y	Y	Scott, W.E.	6/13/2009
09KCwes030	Peregrine glaciovolcanic deposits	Qpg	52.16129	-175.51522	52.48	Y	Y	Scott, W.E.	8/10/2009
09KCnye106	Peregrine glaciovolcanic deposits	Qpg	52.16121	-175.51354	55.07	Y	Y	Nye, C. J.	8/10/2009
09KCnye104	Peregrine glaciovolcanic deposits	Qpg	52.16536	-175.5206	55.15	Y	Y	Nye, C. J.	8/10/2009
09KCwes031	Peregrine glaciovolcanic deposits	Qpg	52.16106	-175.51361	55.93	Y	Y	Scott, W.E.	8/10/2009
10KCnye003b	Peregrine glaciovolcanic deposits	Qpg	52.16229	-175.5183	59.30	Y	Y	Nye, C. J.	8/10/2010
09KCwes018	Peregrine glaciovolcanic deposits	Qpg.Shag Rk	52.16242	-175.52339	50.87	Y	Y	Scott, W.E.	6/14/2009
10KCnye003	lava lithic in 2008 pyroclastic deposits	08l	52.18199	-175.52208	49.16	Y	Y	Nye, C. J.	8/10/2010
09KCwes017	lava lithic in 2008 pyroclastic deposits	08l	52.17253	-175.53177	53.26	Y	Y	Scott, W.E.	6/14/2009
09KCwes015	lava lithic in 2008 pyroclastic deposits	08l	52.17338	-175.53146	56.74	Y	Y	Scott, W.E.	6/14/2009

[1]Subdivisions of Q8p samples are Q8p.j,a, andesite scoria; Q8p.j,ba, basaltic andesite scoria; Q8p.j,bnd, banded scoria; Q8p.gg, gabbro groundmass; Q8p.umg, ultramafic inclusion rind; Q8p.na, unanalyzed scoria; Q8p.gab, gabbro; Q8p.g.am, amphibole from gabbro; Q8p.g.pl, plagioclase from gabbro; Q8p.gab.na, unanalyzed gabbro; Q8p.um, ultramafic inclusion; Q8p.an, anorthosite inclusion.
[2]Y indicates that major and trace-element whole-rock data were obtained and are listed in Appendix 5. 08l are lithic blocks from 2008 deposits.
[3]Y indicates that modal analysis based on petrographic identification of 1,000 points per slide was performed; results are listed in Appendix 6; y* indicates that modal data are from Kentner (2013) and are not listed in Appendix 5..

APPENDIX 3B. SAMPLE DESCRIPTIONS

Table A3b. Sample descriptions. Microsoft Excel (.xlsx), tab-delimited (.txt), and comma-separated value (.csv) versions of this table combined with the location and other data from Appendix 3a are included in Electronic Supplement E3.

Sample	Map symbol	Field notes	Laboratory hand specimen notes
11KCon07B-5	Q8p.j,a	White pumiceous clast from 11KCON07B - see above.	
08cw002-1b	Q8p.j,a		
11KCon07B-6	Q8p.j,a	White pumiceous clast from 11KCON07B - see 11KCon07B-1.	
10KCon09-1	Q8p.j,a	Hornblende- and plag-bearing white pumiceous bomb with breadcrust exterior (removed), density 990 kg/m3. Vesicles <6mm, euhedral hornblende and plag crystals, white in color. Want to see how compositionally homogeneous the white pumice is. Sample wt. 20.5 g.	
11KCon07B-2	Q8p.j,a	Grey-brown pumiceous clast from 11KCON07B - see 11KCon07B-1.	
10KCon06-1	Q8p.j,a	Hornblende- and plag-bearing white pumice clast, density 830 kg/m3. Vesicles <6mm, euhedral hornblende and plag crystals, white in color. Want to see how compositionally homogeneous the white pumice is. Lowest density clast in this analysis set. Sample wt. 10.5 g.	
11KCon14B-1	Q8p.j,a	Grey hbl-pyx-plg pumiceous clast from the base of Unit 2. Color is similar to 13-1, but more vesicular - fairly easily broken. Will show whether color is controlled by vesicularity or chemistry.	
11KCon17-1	Q8p.j,a	Whitish-grey vesicular hbl-pyx-plag clast from the upper part of Unit 3. Very vesicular, resembles the white andesite from Unit 2 (e.g. 11KCON07B-1). White pumice seems to make a re-appearance near the top of Unit 3 after being scarce in the middle - is the andesite coming back?	
10KCwes001	Q8p.j,a	Eroding cliff is near former cliffed coast in basalt flows. Within few meters of beach, pf deposits contain concentrations of rounded pumice lapilli and blocks. All look to be light gray. Collect one.	Inflated pumice, density < 1. 10% black, highly inflated w/ thready glass fibers in voids. 10's of % phenocrysts (est. void-free) of plag, px. Amph avg. 1mm, up to 3 mm.
10KCon11-1	Q8p.j,a	Hornblende- and plag-bearing grey pumice clast, density 1320 kg/m3. Vesicles <2mm, euhedral hornblende and plag crystals, grey in color. Doesn't really fit into either the "brown" or "white" categories based on physical appearance. Does chemistry match? Sample wt. 6.7 g.	
11KCon07B-4	Q8p.j,a	Grey-brown pumiceous clast from 11KCON07B - see 11KCon07B-1.	
09KCnye0F1	Q8p.j,a	Roughly spherical 10cm dia piece of pumice from NW beach. Bulk D < 1 g/cm3. This was floating, and redeposited on the beach. Very light tannish-gray (5%g). Pl, px, am supported by highly vesicular glassy groundmass. Beautiful white glass threads in larger vesicles.	Afterthought sample included just to make sure we had a sample of the floating pumice.

Table A3b. Sample descriptions (cont'd).

Sample	Map symbol	Field notes	Laboratory hand specimen notes
10KCon07-1	Q8p.j,a	Sugary-textured hornblende- and plag-bearing breadcrusted bomb (breadcrust removed), density 910 kg/m3. Somewhat friable, seems to contain higher crystal fraction, but glass is also visible. Not very dense but vesicles are <1mm. White in color but a very different texture than most "white" pumice clasts. Sample wt. 20.8 g.	
11KCon07B-3	Q8p.j,a	White pumiceous clast from 11KCON07B - see above.	
11KCon07B-1	Q8p.j,a	Vesicular hbl-pyx-plag bearing whitish-grey pumiceous clast Taken from pumice-rich horizon near the base of L2. All samples from 11KCON07B (1-6) were taken to assess the presence of more mafic material in the early deposits. White clasts are assumed to be andesite (we'll see), while grey-brown clasts may be more mafic. Not a lot of grey clasts, but enough to notice.	
09KCnye008a	Q8p.j,ba	Pumice from youngest fan, thus deepest incision of '08 deposits? Light colored fans have 1-2 m wave-cut fronts, which expose eruption stratigraphy, including persistent white layers. Despite the fact that these look like Qc (fan shapes from remobilization) they must be primary eruption deposits because they are covered with the final 08 surge/mud sequence. The younger, darker fans spill between the wave-cut fronts of the light fans and thinly cover the back-beach muds (soft walking!!!).	Dark olive gray.
11KCon10B-1	Q8p.j,ba	Dark grey-brown hbl-pyx-plag clast (probably basaltic andesite) from a surgy unit in the middle of Unit 3. Denser than the lower stuff, also darker. Picked out some gabbroic fellow travelers. Possibly slightly oxidized?	
11KCon13-1	Q8p.j,ba	Dense grey plg-pyx-hbl clast from surge-fall unit above 11KCON10B. Pretty dense/pretty hard, but significantly lighter in color than 10B-1/10B-2 - is this a compositional or textural (vesicularity?) thing.	
09KCnye008c	Q8p.j,ba	pMAX = 20x28x40 cm, yet still only a broken fragment of the original piece (probably at least half-ish).	
09KCnye008b	Q8p.j,ba	A second pumice from this deposit - more dense.	
10KCon03-1	Q8p.j,ba	Hornblende- and plag-bearing grey pumice clast, density 1170 kg/m3. Vesicles <2mm, euhedral hornblende and plag crystals, grey in color. Doesn't really fit into either the "brown" or "white" categories based on physical appearance. Does chemistry match? Sample wt. 20.1 g.	
10KCon03-3	Q8p.j,ba	Hornblende- and plag-bearing grey pumice clast, density 1320 kg/m3. Vesicles <2mm, euhedral hornblende and plag crystals, grey in color. Doesn't really fit into either the "brown" or "white" categories based on physical appearance. Does chemistry match? Sample wt. 20.4 g.	

Table A3b. Sample descriptions (cont'd).

Sample	Map symbol	Field notes	Laboratory hand specimen notes
11KCon10B-2	Q8p.j,ba	Dark grey-brown clast similar to 10B-1 (maybe slightly less vesicular). Contained one large hbl-plag gabbroic inclusion which was removed.	
10KCon18-3	Q8p.j,ba	Hornblende- and plag-bearing grey pumice clast, density 1320 kg/m3. Vesicles <2mm, euhedral and rounded hornblende and plag crystals, brown in color. Want to expand the "brown" pumice compositional sample set. Does chemistry match? Sample wt. 20.4 g.	
10KCon18-1	Q8p.j,ba	Hornblende- and plag-bearing brown pumice clast, density 1300 kg/m3. Vesicles <2mm, euhedral and rounded hornblende and plag crystals, brown in color. Want to expand the "brown" pumice compositional sample set. Sample wt. 21 g.	
11KCon01B-3	Q8p.j,ba	Whitish-brown hbl-pyx-plag bearing vesicular clast. Inferred as more silicic than 01B-1.Taken from "burnt" pumice lens in the lower part of Unit 3 - partially oxidized, but not as badly as 01B-1.	
11KCon20B-1	Q8p.j,ba	Dark grey-brown hbl-pyx-plg dense clast from the top of the Unit 2 section. Top of Unit 2 is dominated by banded pumice, most of it darker. This is one of the few homogenous clasts in the bunch. Is Basaltic Andesite starting to make inroads at the end of Unit 2? And if so, why are the burnt pumice horizons at the bottom of Unit 3 all white clasts (so it seems)?	
11KCon02B-1	Q8p.j,bnd	Whitish-brown hbl-pyx-plag bearing vesicular clast. Taken from the second-from-bottom clast-rich horizon in Unit 3. Also slightly oxidized, though not severely. Pretty vesicular.	
09KCnye005	Q8p.j,bnd	Large single pumice block from beach at base of p.f. Probably derived from more lithic rich portion half way up cliff.	
11KCon01B-2	Q8p.j,bnd	Grey-brown grey-brown hbl-pyx-plag bearing vesicular clast. Taken from "burnt" pumice lens in the lower part of Unit 3 - partially oxidized, if data seem spurious, suspect alteration.	
09KCwes012	Q8p.j,bnd	Single 20-cm pumice from lithic-rich pf that lies below lower of 2 conspicuous coarse-grained fall deposits.	
08cw002-1c	Q8p.j,bnd		
09KCnye199m	Q8p.gg	Single block 11x14x18 cm handed to me by Willie as we walked towards destination. He said "here 'ya go" or something and was surprised when I put it in my pack (heavy). Photo by Ned Rozell same afternoon which was used in GI newsletter.	Single dense gabbro block. Large (largest to date) amphiboles up to 12 x 2 x 2 cm in fine-grained matrix (~1 mm) 80%pl 20% amphibole. Block is cased in gray basalt (50%k[1]) which is sparsely phyric w/ 0.5 x 2 mm amph and 1 mm pl. Sample 09KCnye199m is the basalt, chipped from the surface of the block.

Table A3b. Sample descriptions (cont'd).

Sample	Map symbol	Field notes	Laboratory hand specimen notes
09KCnye003m	Q8p.gg	Coarse, equigranular cpx-hb-pl rock. This one sampled because it looks like it has gms/interstitial glass preserved. Question, is this interstitial melt the main-phase magma?	Coarse-grained amph plag gabbro. Color index ~60, mean grain size ~3mm. But some amphibole crystals are crystallographically coherent for up to 3.cm - these are poikilitic. This specimen is unusual compared to others in this unit because it contains zones of disseminated intergranular melt from a few mm to 1 cm across. Melt is 60%k, finely vesicular and sparsely phyric. Sample 09KCnye300m is ~7g of handpicked intergranular magma from 472 g of coarse crushed material. This separate is about 90%melt and 10% crystal fragments.
KC12ak34m	Q8p.umg		Med gray basalt sheath coating (part of) outside of cumulate peridotite block.
08cw002-4a	Q8p.na		
09KCwes013	Q8p.na	Single 20-cm brown pumice from lower of 2 conspicuous coarse-grained fall deposits; clots of large hb and plag,	Dark, brownish-gray scoria. Abt inclusions of cm-sized amph, plag, microgabbro. Also wispy banding (mm x cm) w/ lt brownish-gray magma. NOT ANALYZED because of inclusions.
09KCwes002	Q8p.na	Single 25-cm pumice bomb from 2008 pf; clots of hb mush; 1-cm oxidized rim; range of vesicularity. Pfs partly bury pre-08 sea cliff formed of lava flows.	Banded. Dominantly light tannish-gray w/ 1-2cm darker chocolate-gray bands. Sharpness of contacts is moderate.
09KCwes020	Q8p.na	Single 15-cm clast of banded brown and light-gray pumice. Collect entire clast and put in 2 bags, A and B. Collected from exposed basal unit of massive pfs.	Banded pumice/scoria with cm-scale bands with sharp to moderately sharp edges. Dark band is dark olive gray - light is 10%k with very faint yellow tinge. Dark bands have large amphiboles (up to 1 cm) not found in light bands.
10KCon10-2	Q8p.na		
09KCnye001c	Q8p.gab	Equigranular fine-grained gabbro. Jigsaw, radially fractured. Xls ~1mm to 0.5mm cpx<hb~pl gabbro.	Fine-grained equigranular gabbro. Med gray salt & pepper (~50%k). Amph prisms to 1x3mm. Plag rarely to 2mm. Holocrystalline.
09KCnye012a1	Q8p.gab	Several fragments from a large block w/ notably abundant interstitial melt and melt along channels - which become fracture surfaces. Melt appears to be in zones up to several mm wide. Question is: what is relation of this melt to erupted magma/scoria/pumice? Is melt bleeding out of these bodies and coming straight to surface or is there another magma zone in between? Or is the pumice magma acting as the transporter - the bus itself - and thus must have deeper source even though it is more silicic?	09KCnye012a1 is gabbro block with amph > plag >>>dark gray melt. Amph xls to 6.5 x 0.7 cm.
09KCnye003	Q8p.gab	Coarse, equigranular cpx-hb-pl rock. This one sampled because it looks like it has gms/interstitial glass preserved. Question, is this interstitial melt the main-phase magma?	Coarse-grained amph plag gabbro. Color index ~60, mean grain size ~3mm. But some amphibole crystals are crystallographically coherent for up to 3.cm - these are poikilitic. This specimen is unusual compared to others in this unit because it contains zones of disseminated intergranular melt from a few mm to 1 cm across. Melt is 60%k, finely vesicular and sparsely phyric. This sample also has a portion of a vein of very fine grained holocrystalline cpx plag gabbro - not sampled.

Table A3b. Sample descriptions (cont'd).

Sample	Map symbol	Field notes	Laboratory hand specimen notes
09KCnye012a2	Q8p.gab	Several fragments from a large block w/ notably abundant interstitial melt and melt along channels - which become fracture surfaces. Melt appears to be in zones up to several mm wide. Question is: what is relation of this melt to erupted magma/scoria/pumice? Is melt bleeding out of these bodies and coming straight to surface or is there another magma zone in between? Or is the pumice magma acting as the transporter - the bus itself - and thus must have deeper source even though it is more silicic?	09KCnye012a2 is a fine-grained equigranular fabric-less melt-rich gabbro with CI~80 and mm-sized amph>plag>melt>cpx>ol. Melt is intergranular throughout and in zones up to cm-scale. The presence of bottle-green cpx and honey-yellow-green ol w/ this much melt makes me wonder the extent to which amphibole in these gabbros is down-temp reaction product.
09KCnye012b3	Q8p.gab	From the 38x35x23 cm block described above. Well-developed mineralogical layering w/ "anorthosite" up to 4 cm thick and thicker hb-rich layers.	Extremely friable block -- separated b3 into individual crystals with fingertip pressure! There are 4 domains within this sample, fragments of each were handpicked for analysis. (1) 09KCnye012b1 is anorthosite, w plag ~3mm. (2) 09KCnye012b2 is coarse amphibole gabbro w amphibole to 1.5cm, plag to 7mm, and CI ~80. (3) 09KCnye012b3 is moderately coarse gabbro w/ amph to 5mm, plag to 4mm, and CI~50. (01), (02), and (03) are subparallel. (4) 09KCnye012b4 is fine-grained px gabbro – grain-size ~1mm. This crosscuts 1 and intrudes 3.
09KCnye100am	Q8p.g.am	1st day back @ Kasatochi - low ceiling - light wind. Arr Adak~17:00, left ~21:00 travel overnight, @KS in morning. Sample is 25 cm l-max piece of cumgab in slope wash. Very hb-rich regions. Only HB collected as "field mineral separate". (PLANT - just uphill from nye100 - uphill from "the rock" - single sprig of plant- orthogonal 2-fold symmetry beach-pea-looking. Growing from secondary mud and ash deposit at least a few, maybe several m thick. this plant growing in "new" soil - not from uncovered '08 or pre'08 soil.)	Equant 1-4mm amphibole w/ minor plag. Analyzed as amph separate proxy by hand picking fragments as cleanly as I could.
09KCnye012b1	Q8p.g.pl	From the 38x35x23 cm block described above. Well-developed mineralogical layering w/ "anorthosite" up to 4 cm thick and thicker hb-rich layers.	Extremely friable block -- separated b3 into individual crystals with fingertip pressure! There are 4 domains within this sample, fragments of each were handpicked for analysis. (1) 09KCnye012b1 is anorthosite, w plag ~3mm. (2) 09KCnye012b2 is coarse amphibole gabbro w amphibole to 1.5cm, plag to 7mm, and CI ~80. (3) 09KCnye012b3 is moderately coarse gabbro w/ amph to 5mm, plag to 4mm, and CI~50. (01), (02), and (03) are subparallel. (4) 09KCnye012b4 is fine-grained px gabbro – grain-size ~1mm. This crosscuts 1 and intrudes 3.
09KCnye100	Q8p.gab.na	1st day back @ Kasatochi - low ceiling - light wind. Arr Adak~17:00, left ~21:00 travel overnight, @KC in morning. Sample is 25 cm l-max piece of cumulate gabbro in slope wash. Very hb-rich regions. Only HB collected as "field mineral separate". (PLANT - just uphill from nye100 - uphill from Shag Rock - single sprig of plant- orthogonal 2-fold symmetry beach-pea-looking. Growing from secondary mud and ash deposit at least a few, maybe several m thick. this plant growing in "new" soil - not from uncovered '08 or pre'08 soil.)	Equant 1-4mm amphibole w/ minor plag. Analyzed as amph separate proxy by hand picking fragments as cleanly as I could.

Table A3b. Sample descriptions (cont'd).

Sample	Map symbol	Field notes	Laboratory hand specimen notes
09KCwes009	Qlp	Breadcrust bomb collected from dark-gray pf near base of exposed section at gully mouth; scattered oversize pl as in WES008.	Black scoria. Porphyritic. Mostly plag, cpx, opx? 0.5-1.0 mm. Occasional outrange amph (visible thick rims) and plag. Gms microcrystalline w/ tiny vesicles.
12KCwes001	Qlp	Black, plag + 2 pyx, scoriaceous andesite; almost cauliflower shape; scattered oversize plag to 7-8 mm. Unit is not basal-most of south PFs; this unit deposited after some unknown amount of south pyroclastic fan accumulated. Juvenile block from basal unit of south PFs that lie on Peregrine hc.	
05KScn002A	Qlp	Sugary, holoxtalline dark gray breadcrusted bomb with glassy rinds, plag phenos to 1 cm with ol (?).	
10KCwes004	Qlp	At or near the top of pre-2008 sea cliff is a ~70-cm-thick coarse-grained fall deposit reminiscent of 2008 lapilli falls. Clasts are up to 15 cm and include pumice, lithics, and gabbros. Collected selected larger lapilli.	Dense pumice/scoria. 30%k, brownish tinge. ~40% xls, 1-3 mm pl. px, amph, ol(?). Sample also includes poikilitic amph up to 1.5cm, with amph enclosing plag, px.
09KCwes008	Qlp	Single dark-gray scoriaceous bomb from pf deposit; scattered oversize clear plag; found at base of exposure so not certain this is pre-08.	Black scoria. plag, cpx, ol?. Xls mostly ~1mm, some larger plag. Gms microcrystalline. Sample is very fresh. WES comment - if this was inherited from preexisting surface that surface, or this bomb, must have been very young, else weathering associated w/ soil development etc. would have altered this.
09KCnye009a	Qlp	A bag of hand-picked pumices from the young pfs that formed south shore bluff prior to 2008. These from about 1 m below 08 vegetation surface.	Individual pumices present as two major groups. (a)Vesicular dark to light olive gray w/ orange-red oxidation and light olive gray rinds, glass threads and fibers in gms, very vesicular. (b) Denser med-olive-gray w/ finer vesicles and lacking obviously stretched glass fibers. Would have thought these were separate lithologies but pMax in bag (13x8x6.5 cm) has a core of (b) grading irregularly to (a) --- not obvious banding- may be diffuse banding. So (a) and (b) may be core vs rim, yet the same material - samples taken of each, just in case. These two lithologies similar to those in wes006. Chemistry sample of 009a is from pMax. 009b is two smaller pumices together.
09KCnye009b	Qlp	A bag of hand-picked pumices from the young pfs that formed south shore bluff prior to 2008. These from about 1 m below 08 vegetation surface.	Individual pumices present as two major groups. (a)Vesicular dark to light olive gray w/ orange-red oxidation and light olive gray rinds, glass threads and fibers in gms, very vesicular. (b) Denser med-olive-gray w/ finer vesicles and lacking obviously stretched glass fibers. Would have thought these were separate lithologies but pMax in bag (13x8x6.5 cm) has a core of (b) grading irregularly to (a) --- not obvious banding- may be diffuse banding. So (a) and (b) may be core vs rim, yet the same material - samples taken of each, just in case. These two lithologies similar to those in wes006. Chemistry sample of 009a is from pMax. 009b is two smaller pumices together.

Table A3b. Sample descriptions (cont'd).

Sample	Map symbol	Field notes	Laboratory hand specimen notes
09KCwes006	Qlp	Pumice lapilli in fall deposit or possibly pum-concentration zone in pf; near base of thick section of pfs; collection of pumice clasts, chiefly pinkish brown to brownish gray.	On rounded, exposed surfaces all lapilli are ~20%k. Lapillus interiors from two dominant types. (1, CHEM SAMPLE) The most numerous (~80% of sample) are medium olive gray in the interior with faintly orange tinged rinds. These are vesicular and moderately porphyritic (xls ~ 1mm) with glassy groundmass forming glass threads spanning and surrounding some vesicles. (2) The second type are denser, with lighter (10%k) microcrystalline gms and conspicuous large amphibole xls in addition to smaller plag + px.
09KCwes007	Qlp	Single dark-gray breadcrust bomb from pf deposit toward top of exposure; scattered oversize hb and plag.	Black, highly porphyritic (closer to crystal mush?). Moderately to very small vesicles in gms. Xls generally small (~0.5mm) plag, cpx, opx?, few outsized amphibole up to 1.5cm.
09KCwes022	Qlp	Pumice lapilli from ~15-cm-thick openwork pumice-concentration zone in sequence of lithic-rich pfs. Subrounded nature of pumice suggests is not a fall deposit.	Very light gray (15%k) pumice w/ ~15-20% 1-2mm-long xls of plag, cpx, opx?
09KCnye011a	Qlp	White pumice, salmon weathering, in young pre-08 pfs in little fingers and arroyos just N of old cabin site. Can see '08 deposits on top. NO SOIL, must have been peeled off and stripped during eruption, unlike S coast, where turf mat is preserved beneath thin deposits. This unit is predominantly pfs with lithic blocks up to 30 cm, typically 3-5 cm. Sample is from isolated pumice layer (discontinuous over 10's of meters horizontally) ~5-6 cm thick, pMAX ~5cm.	The bag contains two major lithologies. 09KCnye011a, approx. 70% by volume, is 20%k pumice, mostly subrounded (but pMax - 9x7x5cm is subangular) w/ ~20% phenocrysts [1mm plag, 1x2mm cpx>opx>amph]. Vesicles are irregular, gms may be microlitic. Sample of 11a from a few 2-3cm pumices. 09KCnye011b, ~30 vol% is very pale tannish-gray (10% black) and is mostly distinguished by having bulk density <1g/cm3 (it floats). Phenocrysts of plag, px, am somewhat smaller and less abundant than 011a. Vesicles less are round, abundant, and generally 0.5 mm or less. Sample of 011a from several separate pumices.
09KCnye011b	Qlp	White pumice, salmon weathering, in young pre-08 pfs in little fingers and arroyos just N of old cabin site. Can see '08 deposits on top. NO SOIL, must have been peeled off and stripped during eruption, unlike S coast, where turf mat is preserved beneath thin deposits. This unit is predominantly pfs with lithic blocks up to 30 cm, typically 3-5 cm). Sample is from isolated pumice layer (discontinuous over 10's of meters horizontally) ~5-6 cm thick, pMAX ~5cm.	The bag contains two major lithologies. 09KCnye011a, approx. 70% by volume, is 20%k pumice, mostly subrounded (but pMax - 9x7x5cm is subangular) w/ ~20% phenocrysts [1mm plag, 1x2mm cpx>opx>amph]. Vesicles are irregular, gms may be microlitic. Sample of 11a from a few 2-3cm pumices. 09KCnye011b, ~30 vol% is very pale tannish-gray (10% black) and is mostly distinguished by having bulk density <1g/cm3 (it floats). Phenocrysts of plag, px, am somewhat smaller and less abundant than 011a. Vesicles less are round, abundant, and generally 0.5 mm or less. Sample of 011a from several separate pumices.
09KCwes005	Qlp	Pumice lapilli from light yellowish-gray pf that forms S valley wall; pl+hb+cpx.	Very light gray pumice. Faint banding 5%k and 10%k, several mm to 1 cm wide. 2px, pl. Sugary gms.
10KCnye004	Qmfm	Below Monkey's Forehead. Massive conchoidal blocks of lava with gabbroic inclusions. Less px-ol rich than Greg's Mighty Rock.	Gray porphyritic andesite. ~30% xls; plag>cpx>amph. Very fine-grained sugary 30%k matrix.

Table A3b. Sample descriptions (cont'd).

Sample	Map symbol	Field notes	Laboratory hand specimen notes
09KCwes019	Qtm	Lava flow forms southernmost of 3 rocky points on lower NW flank. Pale reddish oxidization; cpx-bearing, but overall not highly porphyritic; probably same as WES023.	Dense lava. 70% black. 20-30% phenocrysts ~1mm. Plag>cpx. Orange-brown alteration widely disseminated along small cracks and grain boundaries. Occasional gabbro inclusions and outsized amph (xenocrysts?)
09KCwes023	Qtm	Dense, reddish-oxidized cpx-bearing lava flow that forms southernmost of 3 rocky points on lower NW flank. Probably same as WES019.	Dense lava. 50% purplish gray. Broadly similar to other lavas in this unit. Persistent discoloration of groundmass in shades of purple and orange.
10KCnye002	Qtm	Reddish-gms dark grey lava from talus derived from cliff to SW and sitting on top of 2008 deposits. Lava forms cliff easily 40 m tall, mostly massive 3-4m wide columns, mostly vertical w/ poorly-developed sub-horizontal parting at ~1 meter intervals. There is one noticeable diagonal parting zone. Was here in mid-late morning as thousands of auklets came on shore. Points of activity are this talus and another large talus, apparently on top of 2008 deposits to southeast - up towards crater rim.	Basalt, medium gray with purple cast; obvious phenocrysts rare. Rock largely crystalline w/ microphenocrysts down to 0.25 mm. Overall plag>>cpx.
09KCwes024	Qtm	Sugary fine-grained enclave in lava flow of WES025; reddish oxidation; inclusion is about 20x25 cm; contains scattered large vesicles.	Very fine grained (<0.5mm) equigranular xl mush. plag, cpx, and rods of some garnet-red mineral (assume alteration). Isolated round vesicles up to 5mm. Also appears to be interconnected void space along crystal faces. Like Okmok "easter eggs", but finer.
09KCwes025	Qtm	Sample of lava flow that can be traced to NW crater rim; blocky with preserved levees; must be Holocene?; host of enclave of WES024.	Dense 35% black lava. plag ~ cpx > ol. ~30% phenocrysts fairly equigranular from~0.5 -2 mm. Gms sugary, appears holocrystalline. Cleanest of '09 samples from this unit.
KC12nye03	Qtm	Massive thick cliff which forms SW Whiskey Cove boundary. Columns to 3-4m diameter w/ well defined horizontal cooling striae ~20 cm wide. This same unit can be seen dipping steeply uphill to the rim (and forming Mt. Kasatochi). Huge cliff that has dropped blocks to form Whiskey Talus.	
KC11nye05	Qmka	Large (3 to 5 m) beach boulder with radial fractures at edge 3-5 cm wide and extending 30-40 cm into interior of boulder before annealing. Massive block interior. Block itself is light matte gray grading to orangish-purple towards edges. This sample must have come off the cliffs above which form the tallest backdrop to Tundering Cove. (Hand samples KC11nye03, 04 -- collected from the base of the cliff itself ~100m asl confirm this, although they are friable ashy lava base, rather than decent samples.) This unit is distinct from all other massive lavas in that it has ABUNDANT LARGE AMPHIBOLE PHENOCRYSTS. This boulder also contains gabbro inclusions.	
09KCwes003	Qobm	Upper lava flow exposed on NE flank; lies above red breccia; sugary enclaves; oxidized; 2 pyx; forms part of NE crater wall.	40% black plag px basalt w/ wispy pink-gray sugary zones. Not sure if these are devitrified zones or not.
09KCnye108	Qobm	Sample of massive lava from "the nose" septum. Massive lava with large irregular planar, angular conchoidal fracture. Oxidized throughout to irregular wine & gray.	Weird. 40%k plag, cpx,+-ol basalt. Common cm-sized "eyes" with dark coarse interior of cpx-amph - up to 1 cm crystals - surrounded by very light pinkish-white very-fine grained holocrystalline material surrounding dark eye and streaking out to thin wisps. About half a dozen per 50 cm2 of sample surface.

Table A3b. Sample descriptions (cont'd).

Sample	Map symbol	Field notes	Laboratory hand specimen notes
09KCnye107	Qobg	Part of large xline reddish block, presumably one of cumulate/gabbroic inclusions common in this massive lava. Collected in rubble on slope below cliff. (near nose septum in Ogre's Brow).	Coarse-grained block included in lava 09KCnye108. Amph (to1.5cm enclosing much smaller plag, cpx; vitreous orange-brn) > cpx (5mm equant) > plag (1x2mm) > gms (glassy, vesicular, purple-red).
09KCnye002	Qrm	Older lava up along small ridge behind East Point seismic sta. Likely a ol, cpx, pl BA, A. This unit ~8 m thick (bottom obscured) w/ large equant conchoidal frac blocks up to 1.5-2m among smaller faceted boulders and inter-boulder red oxidized flow margin (red oxidation is brick-red; similar to cone B at Okmok and other basaltic scoria). This outcrop ~same as one to N and could well be lobate margin of large AA flow. [Blue sky, light wind (no white-caps). Constant calls of least auklets (cicada-like) and more barking/squeaking/gull like call of whiskered auklet.]	Dark gray (60%k) basalt. Phenocrysts of plag (2mm) and cpx (3mm) in coarsely crystalline gms. Phenocrysts hard to distinguish from gms because of crystallinity. Phenocrysts maybe 20%, but abt gms xls. Contains a few cm-scale gabbroic inclusions.
09KCnye004	Qrm	On top of cliff part way up side of cone and S and W of east point. Red matrix cpx, pl, dark lava. Probably same as 002.	Medium reddish-gray (~40%k) basalt similar to 09KCnye002 but with pervasive brick-red alteration in groundmass. Max gabbro inclusion in sample 5cm (hb+pl).
09KCnye006	Qrb	Porphyritic ol cpx pl lava. Probably the same as other older lava samples today (002, 004).	Light gray (25%k) basalt. Presumably similar to 02 and 04, but the lighter gms makes it easier to see mineralogy. ~20% total phenocrysts with plag (1-2mm) ~= cpx (1-2mm) > ol (1mm). Olivine is fairly abundant and coarse. Note that h.s. photo contains unusual 2cm inclusion of very fine grained (0.25mm) equigranular holocrystalline plag+ol+cpx mass w/ abt inter-crystal voids and vesicles. This was beach outcrop and it was difficult to find fresh stuff - hard to break far enough into the rock.
10KCnye001	Qrb	Lava from beach level South side Rye Pt. (farthest east point). Ol-cpx basalt w/ ~20%cpx 2-3mm. Walked S along beach, up onto 2008 deposit, to camera site, then up ridge to rim.	Dense, gray basalt, slight purple cast. plag (up to 3 mm long) > cpx (1-2mm) > ol (1-2mm). Crystalline gms. Maybe 30% Phenocrysts, but plag is hard to see.
12KCaek001	Qwa	Sample of uppermost one of flows above central Whiskey beach by Adrienne Kentner. Traverse was along bottom of Whiskey Talus then up along top of debris cones banked against large andesite cliff, topping out on crater rim. Sample was two melon-sized blocks brought back to the beach, where Willie chipped for final sample.	
KC12nye01	Qwa	Lowest lava behind central Whiskey Cove (different lavas form cliffs which bound west end of cove and sea lion rookery at east end of cove. Blocky flow, dense lava in conchoidal blocks typically to 2 m, nearly to 4 m. Not columnar. Unit 10-15 m thick. Hand sample striking 5-10% large cpx (up to 2-3mm). Plag forms smaller laths. Rexlized gms.	
KC12nye02	Qwa	Whiskey Cove east. 100m from sea lions, but walked over to edge of colony to verify that it was the same stuff. CPX OL basalt.	

Table A3b. Sample descriptions (cont'd).

Sample	Map symbol	Field notes	Laboratory hand specimen notes
09KCnye010	Qwa	Lava unit stratigraphically above massive hb dacite (nye007) -- next unit above and to N. Ol, cpx, pl BA. Equant conchoidal frac boulders to 2 m in band across hillside.	Medium gray (45%k overall, salt & pepper) cpx > plag basalt. Cpx ~2mm equant. plag 1.5x0.5mm laths and plates - plag enough small that it may be all coarse microphenocrysts or v coarse gms. Equigranular and holocrystalline (?) (i.e. identifiable groundmass not seen in hand specimen). A few% vugs lined by small white xls. Rare amphibole single xls to 10xs15mm (w/ cpx rims and inclusions of plag, cpx).
12KCwes004	Qwa	Dark-gray, slightly purplish oxidation, cpx lava; scattered cm-sized fine grained enclaves; most of flow is much more oxidized. Sample of middle of 3 lava flows exposed above bluff of 08 deposits on east side Whiskey Cove;	
12KCwes005	Qwa	Medium to dark-gray to reddish-gray cpx lava; scattered oversize cpx to 7 mm. This flow is separated from 12KCWES004 by 1 m or more of purple sandy, friable breccia; no sign of weathering; can trace flow to north crater rim at 52.18016/-175.51568; can't get to flow on rim as is covered by 1-2 m of 08 deposits.	
09KCnye110	Qwa	Eastern edge of sea lion colony. Massive cliff of this basalt est. 30-40 m high. Through-going zones of subhorizontal columns-to-platy-fracture. Whole outcrop: crude but primary long fractures and vertical conchoidal-to-planar, modest curving of joint surfaces, few meters wide for columns. Often crosscut by subhorizontal fractures and/or incipient columns 10-20 cm scale. Thick lava pond/flow w/ contorted cooling history suggests emplaced near ice/water. Rock is cpx basalt similar to others along this beach but with darker gms.	30% black over all, gms to 40% black. Fine-grained xl rich plag cpx lava. Generally equigranular w/ cpx 1mm and plag 1x2mm. Pl>cpx>>>other mafics (amph?, opx?). Gms looks nearly holocrystalline. Meets my understanding of Calvert Protocol for dating. Occasional cm-scale gabbro/mush clots are dominantly pl+cpx, ~2mm equigranular. Some amph sheathing on cpx?
10KCnye005	Qgmb	Ol-cpx basalt identical to Greg's m.r. in hand-specimen. Next available outcrop south of 004. 1-2m wide crude vertical columns w/ horizontal band/detachment surfaces a few cm wide every 10-30 cm.	Pyroxene basalt. ~30% total 1-3mm phenocrysts; cpx>ol; plag Phenocrysts of similar size rare, but 1mm plag laths are common - unclear in h.s. if these are gms or phenocrysts. Sugary 40%k gms.
10KCnye006	Qgmb	Another ol-cpx basalt similar to Greg's m.r.	
09KCnye109	Qgmb	Cpx ol basalt. V cpx-rich. From "Greg's Mighty Rock" which stuck out into water like a dock pre-eruption, was covered during June 09 trip, and is now barely exposed. Thus ~15m of retreat of cliffs of '08 pfs since June. Crude sub-horizontal columns ~20cm diameter. Columns plus pre-eruption dock-like erosion suggest this is a dike - but exposure at this time not good enough to really tell.	Cpx olivine basalt similar to 09KCwes001 but coarser and more xl rich. Cpx 3mm, ol rarely to 7mm, plag much smaller (are plag phenos or gms?)
09KCwes001	Qgmb	Lower lava flow; lies below red breccia; cpx-bearing; fine-grained enclaves; reddish oxidation and slight greenish alteration.	Cpx olivine basalt. 25% cpx (3mm equant) 10% ol (2mm stubby prisms) ~10% plag (1x2mm; much smaller than cpx.

Table A3b. Sample descriptions (cont'd).

Sample	Map symbol	Field notes	Laboratory hand specimen notes
09KCnye007	Qpl	At north end of massive pink-weathering lava in north end of a large section of bedded rx (PFs, lahars, etc.) on SW part of island. Px-bearing hb dacite. Hb up to 1.5 cm, mostly ~0.5 cm, prismatic. These massive lavas overlie more bedded coarse material which make up lower half of w-facing cliffs and slopes on cone. Massive lavas (perhaps 2 separate bodies) and therefore maybe domes or vent filling lavas. Pics from land and sea of this unit. [Auklets, constant chatter heard from groups immediately offshore. When standing at "the rock" heard lots of chatter seeming to come from base of these cliffs. Groups of ~1-200 come in and sit on 08 deposits - thick mud/surge on top) for a minute or two, then leave. As I leave this place will look back and see many hundred to a few thousand standing here. Jeff Williams will tell me that talus buried here used to be home for nocturnal auklets, not these least and whiskered.] Arroyo adjacent to 007 in valley to N is ~8-12 m deep w/ near vertical walls. Edge-parallel cracks - tension cracks - suggest active process of sloughing into gully. Top 10-50 cm (variable) is ubiquitous mud which forms mudcracks at surface and columns in x-sctn. Below is/are lithic pfs w/ up to 1 cm grains and abt lithics. Scoria mostly light. Below this much coarser w/ angular boulders up to 2 m (photo) suspended in fine matrix.	Mottled light pinkish-gray and gray amphibole (amph) plag lava. Amphibole is typically euhedral prisms ~1mm across and 5-10mm long - occasional larger xls. Amph reaction rim obvious on sawn surface w/ hand lens. Plag ~1-2mm. Amph >= plag >> px; total phenocrysts ~30%. Gms has alternating zones that are reddish and gray on scale of several mm. Cleaner sample not available at outcrop.
05KScn001	Qpl	Dense, slightly oxidized, sugary holoxtalline hbl andesite/dacite from base of 50-70 m thick flow/dome.	
09KCwes011	Qpg	Dike about 2-3 m thick cuts lithified diamicts; trend about N20E; dike exposed below shallow caves; diamicts underlie nye007	Dense, very dark gray (90k) lava. Sparsely phyric w/ plag (1x3mm) more abundant than mafic phases. Yellowish tinge to plag crystals, blue-black vesicle lining. Weathering rind ~1cm along cracks.
09KCwes030	Qpg	Single reddish-brown to gray, 10-cm weakly inflated lapillus from diamict	Peach/khaki lava clast w/ obvious euhedral clinopyroxene (cpx) and abundant smaller plag -- like most other Peregrine rocks. Assume light pumiceous color as well as softness of sample is due to alteration (dull thud when struck with hammer). Analyzed anyway, just to check.
09KCnye106	Qpg	0.75m thick scoria lag - several scoriae merged in one sample. In thick section of volcaniclastics w/ meter scale crude bedding.	Monolithologic subrounded dense scoria. Medium gray (50%k); 25%plag - stubby prisms and tablets 1x3mm; 5% cpx - equant, euhedral, to 5mm; <5% other mafic mineral -amphibole?. Groundmass (gms) clean gray, small total void space as tiny (<0.1mm) vesicles.
09KCnye104	Qpg	~1.5m l-max boulder. Visible part of mode is 4-5mm faceted cpx. These large blocks are apparent lithics in the scoriaceous "pepperite" thus >= same age. Hopefully this block is datable and should be among the oldest rocks on the island. [INSECT collected: fly on rock in vial #106919.]	Medium gray (35%k) lava with faint greenish cast. 5% stubby prisms of cpx to 3x5mm. Some ambiguity about these, black, not emerald green in hand specimen, but with hand lens they seem to be vitreous olive green, unlike amphibole -- on the other hand, some prismatic section seem to have amphibole angles]. Sparse plag phenocrysts as 3mm long laths. Abundant plag in gms. Gms fine-grained sugary holocrystalline.

Table A3b. Sample descriptions (cont'd).

Sample	Map symbol	Field notes	Laboratory hand specimen notes
09KCwes031	Qpg	Single light gray, weakly inflated clast with thin prismatically jointed rim from large block of indurated diamict that fell from near dike exposure	Medium gray lava (35%K) w/ obvious cpx and abundant smaller plag. Spotty, with yellowish green staining extending into gms surrounding mafic grains.
10KCnye003b	Qpg	In post-'08 debris flow which issues from amphitheater in Phc. Sample is from massive lava just south of Troll Talus. Medium to fine-grained cpx-pl rock (different than Troll Talus, which is hb-bearing). 40-50% xls. Groundmass is translucent milky med-gray, and brick reddish-brown on weathering. Collected as part of ongoing quest for good datable sample.	Medium gray BA, purplish-red cast, especially on weathered surfaces. Equigranular, ~40% xls, 1-2 mm, plag~cpx>>ol. Very fine-grained sugary gms is 40%k.
09KCwes018	Qpg.Shag Rk	Freshest block in lithified diamict that forms Shag Rock, which is part of or more likely fell from SW cliffs of old diamicts and lava flows(?)	Dark gray (80%k)[(4)] lava. >10% cpx to 4mm, equant. Abundant plagioclase (plag) laths (0.3 x 2 mm) which may be microphenocrysts. Dark gray groundmass - sugary but microcrystalline. Light olive cast may reflect pervasive water migration along fine voids.
10KCnye003	08l	"black rock in bluff" from GPS site -- single rock from pf. probably lithic based on hs and ts.	Greenish-black B/BA. Green alteration coating vugs and streaming though rock in cm-thick bands - like internal rinds. ~40% phenocrysts and microphenocrysts in black glassy matrix. Plag~=cpx, xls ~1mm.
09KCwes017	08l	Single dark-gray, scoriaceous bomb from upper of 2 conspicuous coarse-grained fall deposits; scattered large hb and plag xtals.	Dense, xl rich, 30%k lava,
09KCwes015	08l	Single relatively dense brown pumice from lower of 2 conspicuous coarse-grained fall deposits; clots of large hb and plag.	Dark gray to black, dense. Very xl rich (>=30%plag, 20%px, x% amph. Equigranular ~1mm.

[1]Color was estimated by comparison with a gray scale graduated from white to black in ten percent increments, and is abbreviated as (__%k).

APPENDIX 4. ^{40}AR/^{39}AR AGE DATA

^{40}AR/^{39}AR ANALYTICAL TECHNIQUES

Gray, crystalline portions of lava flows were selected for dating. Samples were crushed, ultrasonicated and sized to 250-350 μm. Dense, clean groundmass was concentrated using a Frantz magnetic separator and careful handpicking under a binocular microscope. For irradiation, 95-189 mg groundmass samples were packaged in Cu foil and placed in a cylindrical quartz vial, together with fluence monitors of known age and K-glass and fluorite to measure interfering isotopes from K and Ca. The quartz vials were wrapped in 0.5 mm-thick Cd foil to shield samples from thermal neutrons during irradiation. The samples were irradiated for one hour in the central thimble of the U.S. Geological Survey TRIGA reactor in Denver, Colorado (Dalrymple et al., 1981). The reactor vessel was rotated continuously during irradiation to avoid lateral neutron flux gradients and oscillated vertically to minimize vertical gradients. Reactor constants determined for these irradiations were indistinguishable from recent irradiations, and a weighted mean of constants obtained over the past five years yields ^{40}Ar/^{39}ArK = 0.001002±0.000379, ^{39}Ar/^{37}ArCa = 0.00071±0.00005, and ^{36}Ar/^{37}ArCa = 0.000281±0.000006. TCR-2 sanidine from the Taylor Creek Rhyolite (Dalrymple and Duffield, 1988) was used as a fluence monitor with an age of 27.87 Ma. This monitor is a secondary standard calibrated against the primary intralaboratory standard, SB-3, that has an age of 162.9 ± 0.9 Ma (Lanphere and Dalrymple, 2000). Fluence monitors were analyzed using a continuous CO_2 laser system and mass spectrometer described by Dalrymple (1989). Argon was extracted from groundmass and mica separates using a Mo crucible in a custom resistance furnace modified from the design of Staudacher et al. (1978) attached to the above mass spectrometer. Heating temperatures were monitored with an optical fiber thermometer, a PhotriX sensor and controlled with custom LabView software. Gas was purified continuously during extraction using two SAES ST-172 getters operated at 4A and 0A.

Mass spectrometer discrimination and system blanks are important factors in the precision and accuracy of ^{40}Ar/^{39}Ar age determinations of Pleistocene lavas because of low radiogenic yields. Discrimination is monitored by analyzing splits of atmospheric Ar from a reservoir attached to the extraction line and for these samples D_{1amu} = 1.00597 ± 0.00018. All isotopic ratios are mass discrimination corrected using ^{40}Ar/^{36}Ar = 295.5 (Steiger and Jager, 1977). A recent determination of atmospheric argon (^{40}Ar/^{36}Ar = 298.56 ± 0.31; Lee et al., 2006) is more precise, but acceptance is controversial and that ratio has no impact on this study because normalizing to a different value does not change the isotopic ratios. Typical system blanks including mass spectrometer backgrounds were $1.5x10^{-18}$ mol of m/z 36, $9x10^{-17}$ mol of m/z 37, $3x10^{-18}$ mol of m/z 39 and $1.5x10^{-16}$ mol of m/z 40, where m/z is mass/charge ratio.

In the incremental-heating experiments, the extraction line is isolated from pumping systems and the sample is heated to a specified temperature for 10 minutes, cooled for 3-5 minutes, and transferred to an isolated mass spectrometer. The gas is exposed to getters during the entire extraction. Isotopic ratios are measured and corrected for instrumental blanks, mass discrimination and interfering isotopes generated in the reactor. In these experiments we separated and loaded enough material to do 10-14 steps on each unknown in order to carefully characterize the argon release. The incremental heating data are plotted both as an age spectrum diagram and as an isotope correlation (isochron) diagram. For the age spectrum, apparent ages are calculated assuming that non-radiogenic Ar is atmospheric (^{40}Ar/^{36}Ar = 295.5) in composition and are plotted against the cumulative ^{39}Ar released during the experiment. In cases with several contiguous steps yielding ages within analytical error, we calculate and report plateau ages by weighing individual ages by the inverse of their analytical error. Most groundmass age experiments do not yield identical ages across the entire spectrum due to minor alteration, recoil of ^{39}Ar during irradiation (Huneke and Smith, 1976) or modest excess ^{40}Ar. Generally accepted criteria for a meaningful incremental heating age are: (1) well-defined plateau (apparent ages within 2σ error) for at least 50% of the ^{39}Ar released; (2) well-defined isochron for the plateau gas fractions; (3) concordant plateau and isochron ages; and (4) ^{40}Ar/^{36}Ar isochron intercept not significantly different from 295.5.

For isochron plots, data are not corrected using an atmospheric ratio. Isochron ages include plateau steps on well-behaved samples or a subset of data that yield a reasonable goodness of fit. We show normal isochron plots for these low-radiogenic rocks because the data are easier to visualize. Inverse isochron results are indistinguishable. The most reliable results generally include gas from the middle of the release spectrum with consistent K/Ca ratios and concordant isochron data with ^{40}Ar/^{36}Ar intercepts within error of air. Ages and isotopic ratios are reported at 2σ.

^{40}AR/^{39}AR INTERPRETATION

09KCnye002

This sample of Rye basaltic andesite yielded a disturbed age spectrum and complicated isochron diagram. Apparent ages are negative at low temperatures, and climb monotonically at higher temperatures. A statistically reasonable isochron fits the 550-850°C steps with a 148±113 ka age; however, its subatmospheric ^{40}Ar/^{36}Ar ratio is difficult to interpret and we consider the age unreliable.

09KCnye006

This Rye basalt sample yielded a strong 4.0±2.5 ka plateau age that agrees with the total gas and isochron ages. We interpret the plateau age as a reliable eruption age.

09KCnye007

This Peregrine lava sample yielded a 131±3 ka plateau age that agrees with total gas and isochron results. We interpret the plateau age as a reliable eruption age.

09KCnye010

This sample of the Whiskey andesite yields a disturbed age spectrum and isochron. Apparent ages are negative at low and high temperature and positive, but discordant, at moderate temperatures. Gas yields were high at low temperature, a result commonly seen when lavas have interacted with water or ice during emplacement. Interestingly, two well-defined linear arrays are apparent in the isochron diagram. Low temperature (550-685°C) steps define a line with an extremely low ^{40}Ar/^{36}Ar ratio (275±4) and old age (974±79 ka). High temperature (785-1150°C) steps define a line with a slightly low ^{40}Ar/^{36}Ar

ratio (293±1) and younger, but still unlikely, age (391±57 ka). Our interpretation is that the arrays represent three or more components of argon and neither isochron age is reliable.

09KCnye110

This sample of the Whiskey andesite yields apparent ages near zero, but a well-determined isochron age of 8.9±2.0 ka. As with samples 09KCnye002 and 09KCnye010 the isochron yields a slightly subatmospheric intercept; however, steps including 79% of the ^{39}Ar define the isochron line. We interpret the isochron age as a reliable eruption age.

REFERENCES

Dalrymple, G.B., 1989, The GLM continuous laser system for ^{40}Ar/^{39}Ar dating—Description and performance characteristics, in Shanks, W.C., III, and Criss, R.E., eds., New frontiers in stable isotopic research—Laser probes, ion probes, and small-sample analysis: U.S. Geological Survey Bulletin 1890, p. 89–96.

Dalrymple, G.B., and Duffield, W.A., 1988, High precision ^{40}Ar/^{39}Ar dating of Oligocene rhyolites from the Mogollon–Datil volcanic field using a continuous laser system: Geophysical Research Letters, v. 15, p. 463–366.

Dalrymple, G.B., Alexander E.C., Jr., Lanphere, M.A., and Kraker, G.P., 1981, Irradiation of samples for ^{40}Ar/^{39}Ar dating using the Geological Survey TRIGA reactor: U.S. Geological Survey Professional Paper 1176.

Huneke, J.C., and Smith S.P., 1976, The realities of recoil—^{39}Ar recoil out of small grains and anomalous patterns in ^{39}Ar-^{40}Ar dating: Geochimica et Cosmochimica Acta Supplement 7 (Proceedings of the Seventh Lunar Science Conference), p. 1,987–2,008.

Lanphere, M.A., and Dalrymple, G.B., 2000, First-principles calibration of 38Ar tracers—Implications for the ages of ^{40}Ar/^{39}Ar fluence standards: U.S. Geological Survey Professional Paper 1621, 10 p.

Lee, J., Marti, K., Severinghaus, J.P., Kawamura, K., Yoo, H., Lee, J., and Kim, J.S., 2006, A redetermination of the isotopic abundances of atmospheric Ar: Geochimica et Cosmochimica Acta, v. 70, p. 4,507–4,512.

Staudacher, T., Jessberger, E.K., Dorflinger, J., and Kiko, J., 1978, A refined ultrahigh-vacuum furnace for rare gas analysis: Journal of Physics E: Scientific Instruments, v. 11, p. 781–784.

Steiger, R.H., and Jager, E., 1977, Subcommission on geochronology—Convention on the use of decay constants in geo- and cosmochronology: Earth and Planetary Science Letters, v. 36, p. 359–362.

APPENDIX 4A. AGE TABLE

Table A4a. $^{40}Ar/^{39}Ar$ ages. Preferred ages are bold and underlined. Electronic versions of this table in Microsoft Excel (.xlsx) and tab-delimited (.txt) formats are in electronic supplement E4.

		$^{40}Ar/^{39}Ar$ Weighted mean plateau age			$^{40}Ar/^{39}Ar$ isotope correlation (isochron) age				$^{40}Ar/^{39}Ar$ total gas	
Sample	**Map unit**	**Age (ka)**	**%^{39}Ar[steps, °C]**	**MSWD**	**Age (ka)**	**%^{39}Ar[steps, °C]**	**MSWD**	**$^{40}Ar/^{36}Ar_i$**	**Age (ka)**	**Comment**
09KCnye002	Qrm	--			147.7 ± 112.7	77[550–850]	2.31	282.9 ± 10.6	-127.8 ± 5.3	Poor isochron, unreliable
09KCnye006	Qrb	**4.0 ± 2.5**	95[600–1,150]	0.63	3.6 ± 3.4	95[600–1,150]	0.71	295.6 ± 1.2	2.7 ± 2.9	Good plateau age
09KCnye007	Qpg	**131.1 ± 2.5**	99[550–1,050]	1.34	131.5 ± 3.5	99[550–1,050]	1.44	294.7 ± 4.8	129.1 ± 2.8	Good plateau age
09KCnye010	Qwa	--			--				-41.3 ± 8.9	Disturbed, unreliable
09KCnye110	Qwa	--			**8.9 ± 2.0**	79[650–1,000]	1.12	289.0 ± 1.5	-20.7 ± 2.1	Negative ages, good isochron result

APPENDIX 4B. AGE SPECTRA

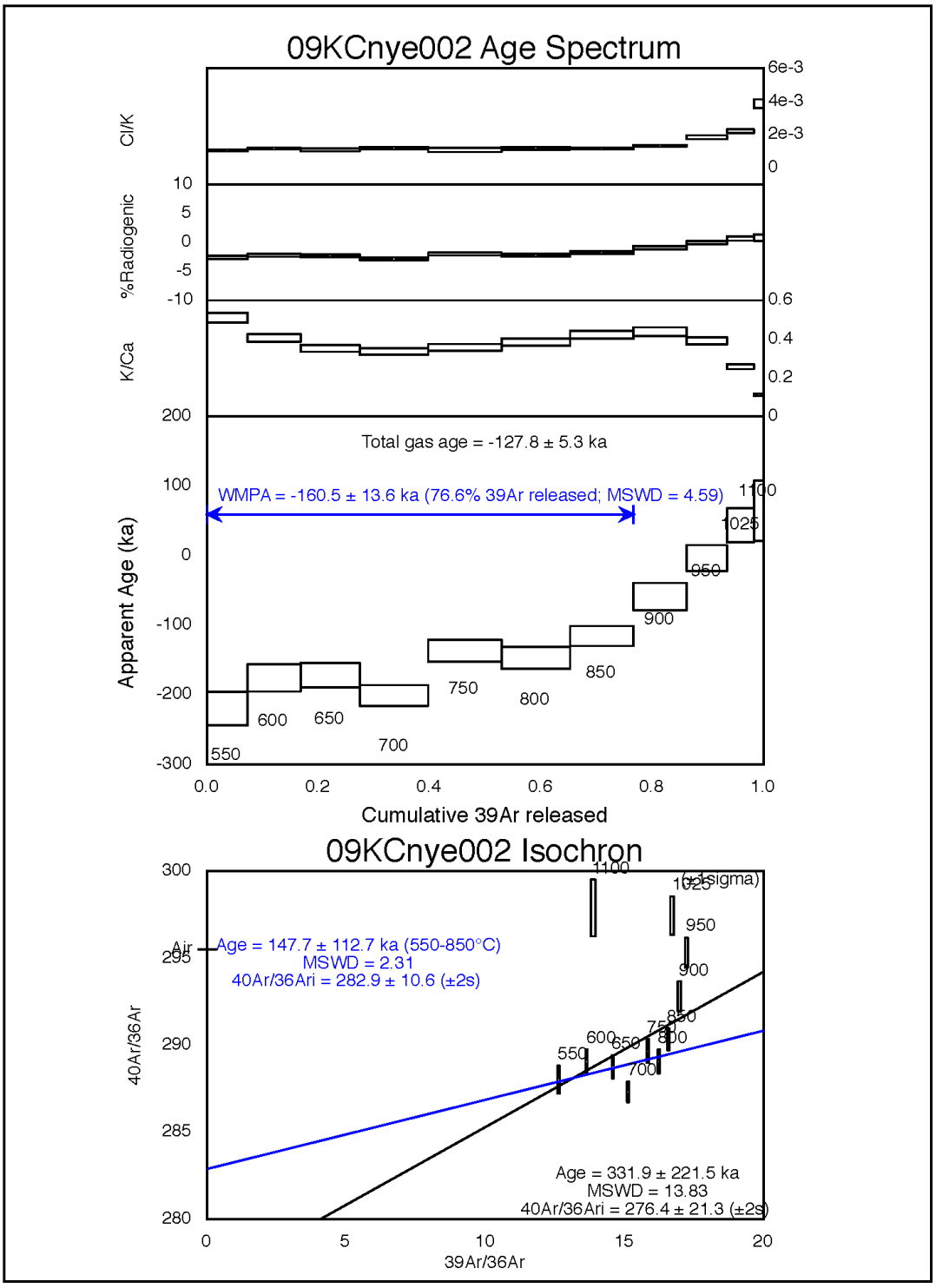

Figure A4b1. 09KCnye002 Age Spectrum.

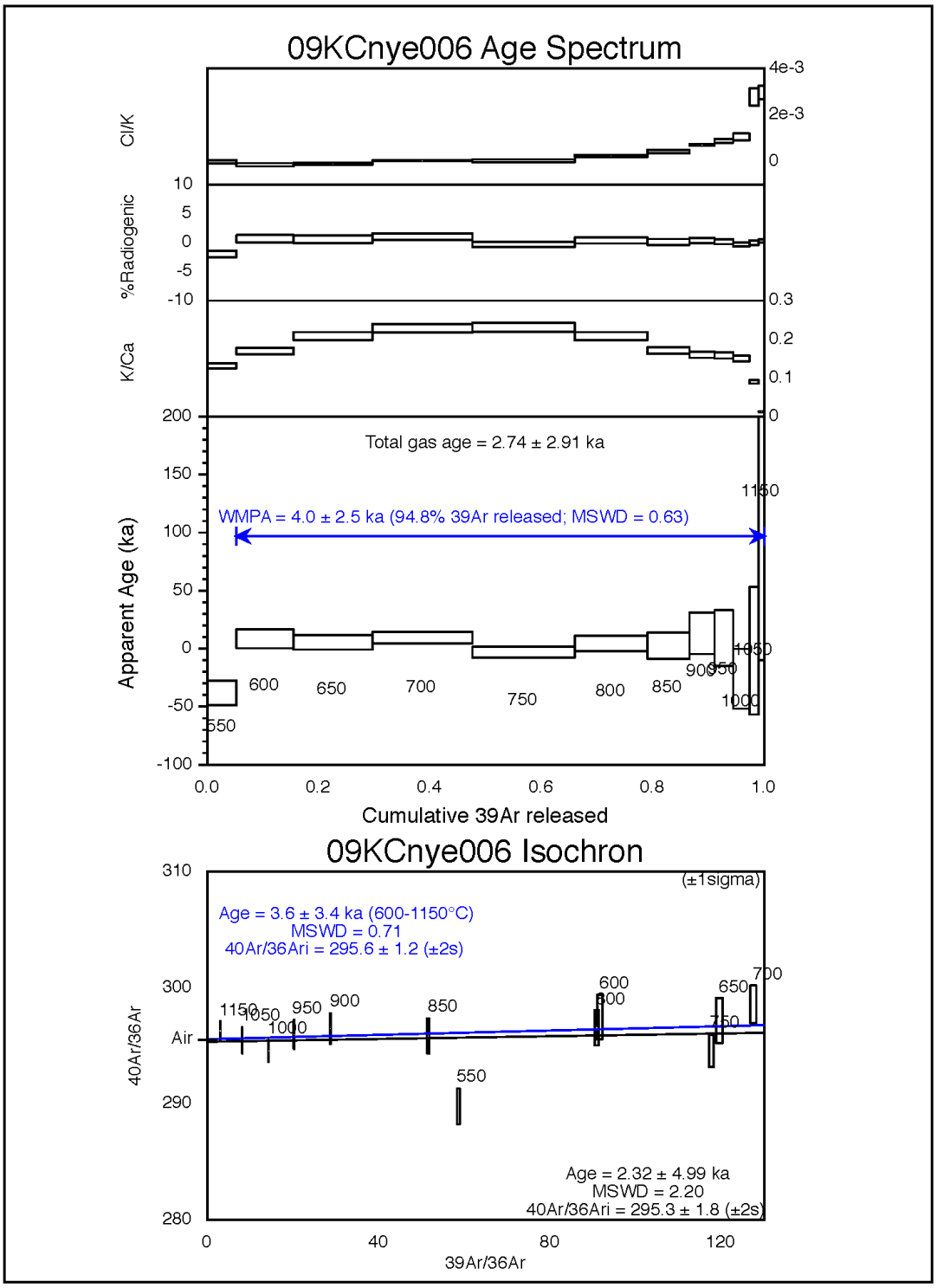

Figure A4b2. 09KCnye006 Age Spectrum.

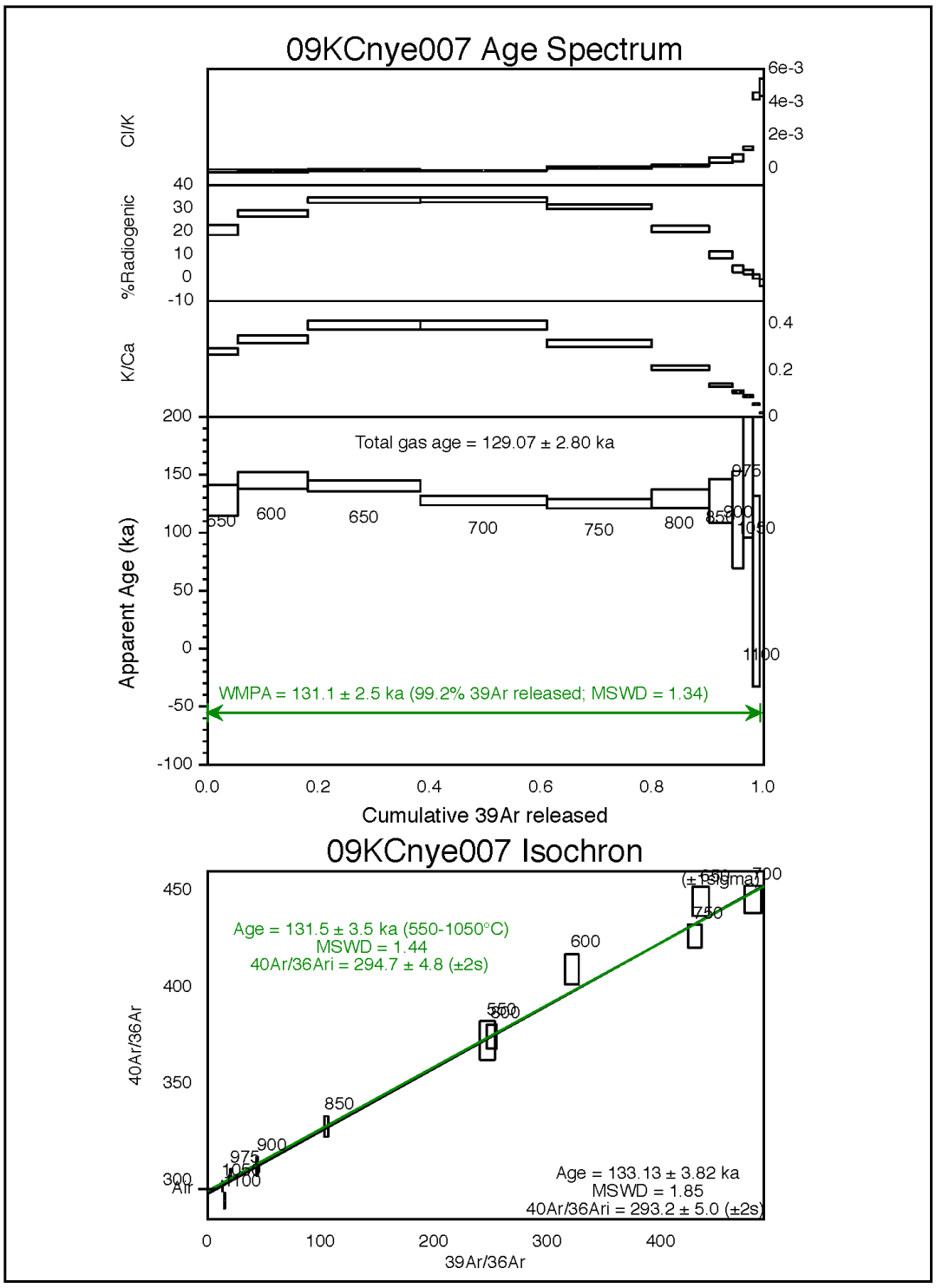

Figure A4b3. 09KCnye007 Age Spectrum.

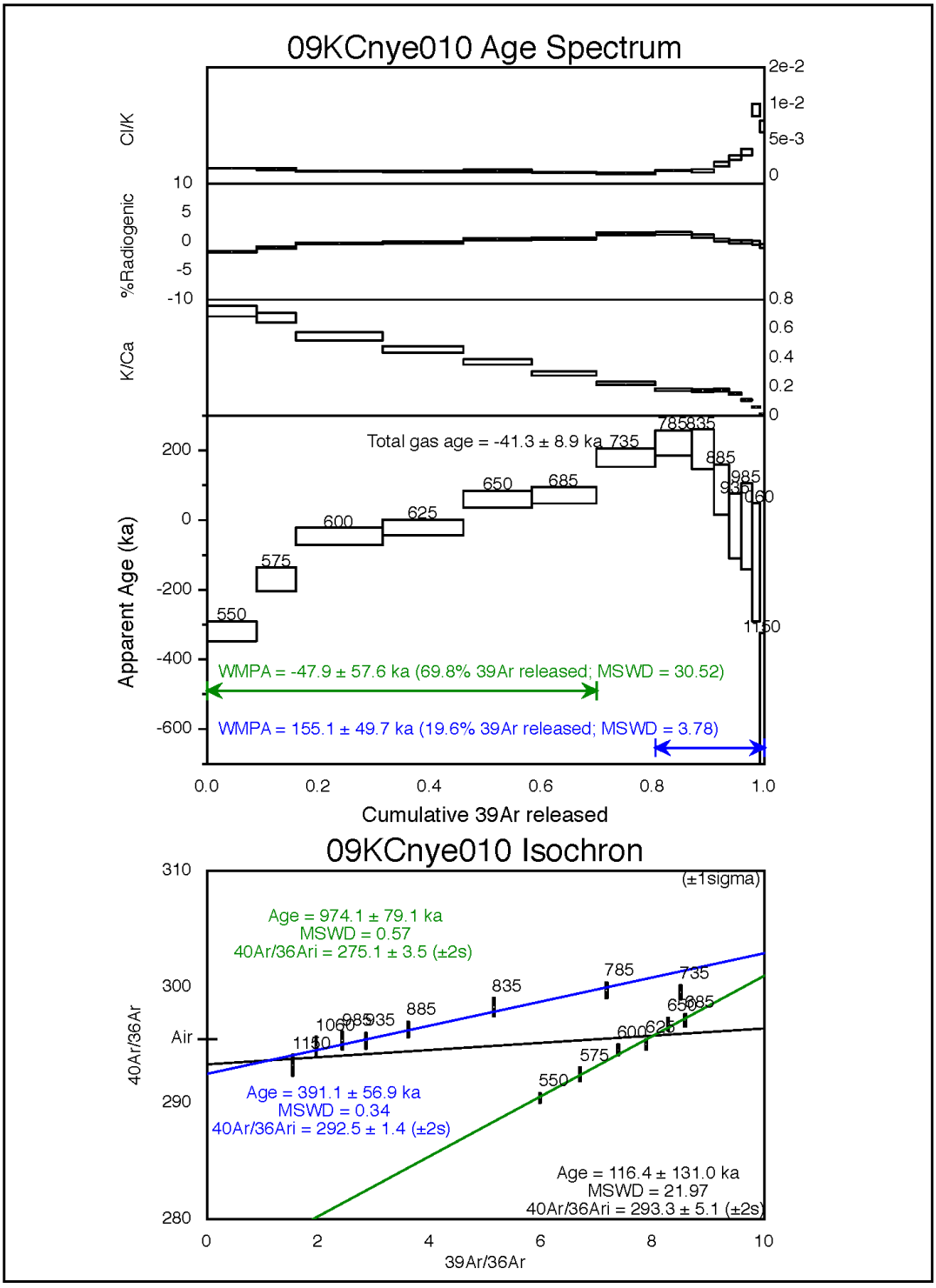

Figure A4b4. 09KCnye010 Age Spectrum.

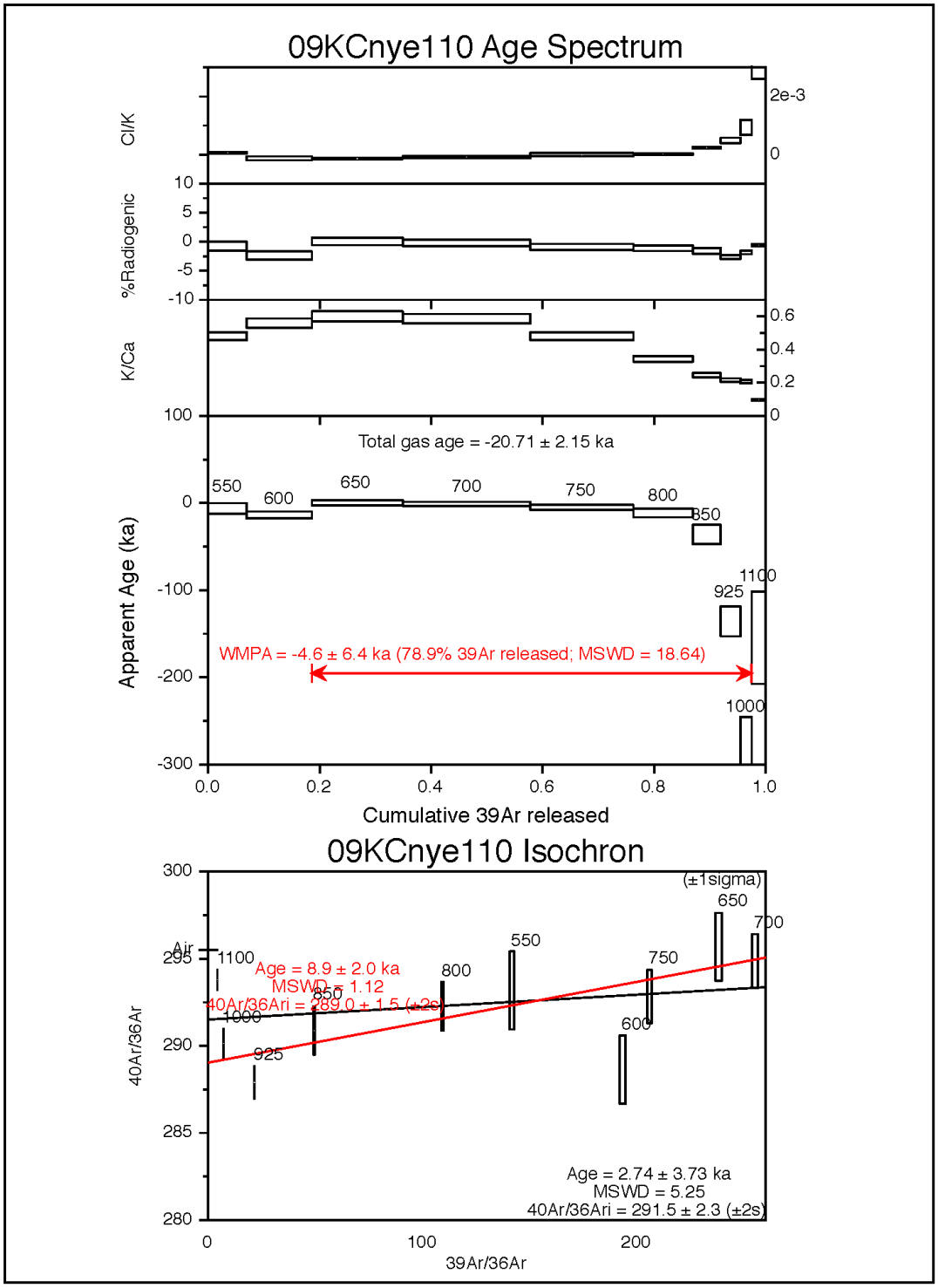

Figure A4b5. 09KCnye110 Age Spectrum.

APPENDIX 4C. $^{40}AR/^{39}AR$ RESULTS

Table A4b. Detailed results of age determinations. Electronic versions of this table in Microsoft Excel (.xlsx) and tab-delimited (.txt) formats are in electronic supplement E4.

09KCnye002

Temp(°C)	Age(ka)	$\%^{40}Ar^*$	K/Ca	K/Cl	moles $^{40}Ar^*$	$\sum^{39}Ar$	^{40}Ar	^{39}Ar	^{38}Ar	^{37}Ar	^{36}Ar
550	-220.3±24.0	-2.6	0.51	947	-3.06E-15	0.07	4.282357±0.001348	0.187882±0.000135	0.006104±0.000036	0.193067±0.000833	0.014922±0.000041
600	-175.9±19.7	-2.23	0.4	858	-3.22E-15	0.17	5.294429±0.001803	0.249836±0.000222	0.007963±0.000033	0.323514±0.001041	0.018406±0.000044
650	-171.8±17.5	-2.33	0.35	931	-3.50E-15	0.27	5.463395±0.001624	0.276037±0.000245	0.008445±0.000094	0.411643±0.000669	0.019035±0.000043
700	-201.3±14.8	-2.85	0.34	838	-4.75E-15	0.4	6.070826±0.002084	0.319891±0.000247	0.009803±0.000086	0.500193±0.000599	0.021269±0.000042
750	-137.0±16.0	-2.01	0.36	929	-3.46E-15	0.53	6.252284±0.002592	0.342177±0.000277	0.010123±0.000184	0.504215±0.000716	0.021725±0.000049
800	-147.3±15.8	-2.22	0.38	849	-3.48E-15	0.65	5.743079±0.001525	0.322761±0.000250	0.009598±0.000106	0.440629±0.000898	0.019990±0.000046
850	-115.7±14.2	-1.78	0.42	866	-2.52E-15	0.77	5.174263±0.001789	0.295449±0.000207	0.008687±0.000050	0.367235±0.001029	0.017923±0.000038
900	-59.1±19.4	-0.92	0.44	754	-1.09E-15	0.86	4.325382±0.001682	0.250848±0.000191	0.007492±0.000046	0.300085±0.001231	0.014856±0.000044
950	-3.8±18.5	-0.06	0.39	543	-5.22E-17	0.93	3.227673±0.001369	0.188383±0.000123	0.006013±0.000092	0.252977±0.001113	0.011000±0.000031
1025	43.4±24.4	0.66	0.26	453	4.02E-16	0.98	2.231218±0.000618	0.125474±0.000131	0.004246±0.000059	0.256310±0.001006	0.007573±0.000028
1100	64.0±43.3	0.8	0.11	259	2.18E-16	1	0.988691±0.000518	0.046190±0.000075	0.001996±0.000052	0.218898±0.000737	0.003380±0.000018

Packet IRR292-ZB, Experiment #11Z0203, 0.0951 g , all errors ±1σ

J = 0.000206062466±1.371E-07

$^{40}Ar^*$ is radiogenic argon, isotopes in volts (2.75e-14 moles/volt), corrected for blank, background, discrimination, and decay Calculated K2O = 1.40%wt., Calculated CaO = 4.73%wt., Calculated Cl = 2.1ppm

Total Gas Age = -127.8 ± 5.3 ka

Isochron Age = 147.7 ± 112.7 ka (±1σ, including ±J)

Isochron Age = 147.7 ± 74.1 ka (A Priori Errors, including ±J)

Isochron Age = 147.7 ± 259.8 ka (95% confidence, including ±J)

MSWD = 2.31 (Good fit, MSWD < 2.56)

$^{40}Ar/^{36}Ar$ intercept = 282.9 ± 4.6 (±1σ)

$^{40}Ar/^{36}Ar$ intercept = 282.9 ± 3.0 (A Priori)

$^{40}Ar/^{36}Ar$ intercept = 282.9 ± 10.6 (95% confidence)

Steps 7 of 11 (550,600,650,700,750,800,850°C)

Table A4b. Detailed results of age determinations (cont'd)

09KCnye006

Temp(°C)	Age(ka)	%^{40}Ar*	K/Ca	K/Cl	moles ^{40}Ar*	∑^{39}Ar	^{40}Ar	^{39}Ar	^{38}Ar	^{37}Ar	^{36}Ar
550	-38.19±10.55	-1.98	0.13	-49400	-4.90E-16	0.05	0.902882±0.000336	0.182877±0.000174	0.002987±0.000055	0.729264±0.001448	0.003320±0.000016
600	8.39±8.14	0.66	0.17	-6915	2.13E-16	0.15	1.171689±0.000538	0.361352±0.000211	0.005288±0.000108	1.117123±0.001919	0.004252±0.000024
650	5.47±6.29	0.56	0.21	-9322	1.92E-16	0.3	1.250762±0.000437	0.503673±0.000303	0.007205±0.000090	1.268855±0.003269	0.004564±0.000026
700	9.42±4.91	1.03	0.23	45748	4.19E-16	0.48	1.494190±0.000504	0.638440±0.000340	0.009421±0.000041	1.464975±0.002080	0.005414±0.000025
750	-3.09±4.65	-0.32	0.23	33895	-1.41E-16	0.66	1.621434±0.000579	0.648170±0.000351	0.009665±0.000171	1.469354±0.002503	0.005915±0.000024
800	4.53±6.52	0.36	0.21	4291	1.46E-16	0.79	1.500546±0.000566	0.460309±0.000246	0.007483±0.000085	1.159304±0.001259	0.005384±0.000025
850	2.57±11.32	0.11	0.17	2373	4.81E-17	0.87	1.529190±0.000601	0.266699±0.000174	0.004972±0.000083	0.817321±0.001432	0.005398±0.000026
900	13.23±17.93	0.33	0.16	1422	1.48E-16	0.91	1.652979±0.000559	0.160294±0.000163	0.003644±0.000023	0.525294±0.001706	0.005723±0.000025
950	9.13±23.92	0.16	0.16	1132	7.55E-17	0.94	1.722711±0.000674	0.117762±0.000128	0.003091±0.000040	0.389902±0.001160	0.005930±0.000024
1000	-25.96±25.74	-0.32	0.15	948	-1.87E-16	0.97	2.120140±0.000567	0.102708±0.000110	0.003168±0.000064	0.358213±0.001185	0.007298±0.000023
1050	-1.81±54.87	-0.01	0.09	360	-7.54E-18	0.99	2.155321±0.000619	0.059287±0.000102	0.002854±0.000094	0.344748±0.000850	0.007391±0.000028
1150	103.04±113.10	0.26	0.01	337	2.58E-16	1	3.577590±0.001278	0.036574±0.000084	0.003226±0.000044	1.487880±0.002399	0.012493±0.000033

Packet IRR292-YY, Experiment 11Z0206, 0.1888 g , all errors ±1σ
J = 0.000216412747±1.262E-07
^{40}Ar* is radiogenic argon, isotopes in volts (2.75e-14 moles/volt), corrected for blank, background, discrimination, and decay
Calculated K2O = 0.91%wt., Calculated CaO = 6.70%wt., Calculated Cl = 0.2ppm
Total Gas Age = 2.7 ± 2.9 ka

Weighted Mean Plateau Age = 4.0 ± 2.5 ka (±1 σ, including ±J), 94.8% 39Ar released

Weighted Mean Plateau Age = 4.0 ± 2.5 ka (A priori, without ±J)
MSWD = 0.63 (Good fit, MSWD < 2.05)
Steps 11 of 12 (600,650,700,750,800,850,900,950,1000,1050,1150°C)
Isochron Age = 3.6 ± 3.4 ka (±1 sigma, including ±J)
Isochron Age = 3.6 ± 3.4 ka (A Priori Errors, including ±J)
Isochron Age = 3.6 ± 7.6 ka (95% confidence, including ±J)
MSWD = 0.71 (Good fit, MSWD < 2.11)
^{40}Ar/^{36}Ar intercept = 295.6 ± 0.5 (±1σ)
^{40}Ar/^{36}Ar intercept = 295.6 ± 0.5 (A Priori)
^{40}Ar/^{36}Ar intercept = 295.6 ± 1.2 (95% confidence)
Steps 11 of 12 (600,650,700,750,800,850,900,950,1000,1050,1150°C)

Table A4b. Detailed results of age determinations (cont'd)

09KCnye007

Temp(°C)	Age(ka)	%^{40}Ar*	K/Ca	K/Cl	moles ^{40}Ar*	∑^{39}Ar	^{40}Ar	^{39}Ar	^{38}Ar	^{37}Ar	^{36}Ar
550	127.94±13.25	20.66	0.28	-7356	9.89E-16	0.05	0.174293±0.000512	0.115303±0.000122	0.001541±0.000040	0.214565±0.000711	0.000528±0.000012
600	145.13±7.22	27.79	0.33	-6217	2.63E-15	0.18	0.344569±0.000895	0.270178±0.000210	0.003532±0.000086	0.423707±0.001208	0.000960±0.000016
650	140.33±4.77	33.49	0.4	-10160	4.08E-15	0.38	0.443061±0.001045	0.432878±0.000243	0.005707±0.000099	0.572319±0.001859	0.001157±0.000016
700	127.79±3.98	33.64	0.4	-8538	4.18E-15	0.61	0.452249±0.000463	0.487494±0.000275	0.006368±0.000050	0.645319±0.001280	0.001195±0.000015
750	125.01±3.94	30.71	0.32	16897	3.39E-15	0.8	0.405053±0.000285	0.407443±0.000262	0.005652±0.000121	0.674079±0.001898	0.001138±0.000013
800	129.27±8.08	21.08	0.21	5473	1.92E-15	0.9	0.331627±0.000203	0.221626±0.000144	0.003265±0.000051	0.547844±0.001148	0.001039±0.000014
850	127.49±18.77	9.9	0.14	1968	7.74E-16	0.94	0.284465±0.000204	0.090631±0.000135	0.001559±0.000065	0.347311±0.001233	0.000965±0.000014
900	111.32±41.90	3.84	0.11	1552	3.15E-16	0.96	0.298643±0.000222	0.042295±0.000072	0.000859±0.000037	0.204251±0.000418	0.001029±0.000015
975	153.84±58.03	2.48	0.09	814	3.74E-16	0.98	0.548772±0.000249	0.036336±0.000082	0.001012±0.000016	0.212568±0.000693	0.001871±0.000017
1050	49.61±82.36	0.52	0.05	228	8.57E-17	0.99	0.604452±0.000284	0.025903±0.000070	0.001211±0.000024	0.246652±0.001292	0.002104±0.000017
1100	-166.57±116.03	-2.06	0.02	204	-1.82E-16	1	0.321441±0.000209	0.016630±0.000057	0.000780±0.000037	0.490650±0.001212	0.001248±0.000015

Packet IRR292-ZC, Experiment #11Z0204, 0.0973 g , all errors ±1σ
J = 0.000226741501±1.693E-07
^{40}Ar* is radiogenic argon, isotopes in volts (2.75e-14 moles/volt), corrected for blank, background, discrimination, and decay
Calculated K2O = 1.03%wt., Calculated CaO = 5.11%wt., Calculated Cl = 0.1ppm
Total Gas Age = 129.1 ± 2.8 ka

Weighted Mean Plateau Age = 131.1 ± 2.5 ka (±1σ, including ±J), 99.2% 39Ar released

Weighted Mean Plateau Age = 131.1 ± 2.2 ka (A priori, without ±J)
MSWD = 1.34 (Good fit, MSWD < 2.11)
Steps 10 of 11 (550,600,650,700,750,800,850,900,975,1050°C)
Isochron Age = 131.5 ± 3.5 ka (±1σ, including ±J)
Isochron Age = 131.5 ± 2.9 ka (A Priori Errors, including ±J)
Isochron Age = 131.5 ± 8.0 ka (95% confidence, including ±J)
MSWD = 1.44 (Good fit, MSWD < 2.19)
^{40}Ar/^{36}Ar intercept = 294.7 ± 2.1 (±1σ)
^{40}Ar/^{36}Ar intercept = 294.7 ± 1.7 (A Priori)
^{40}Ar/^{36}Ar intercept = 294.7 ± 4.8 (95% confidence)
Steps 10 of 11 (550,600,650,700,750,800,850,900,975,1050°C)

Table A4b. Detailed results of age determinations (cont'd)

09KCnye010

Temp(°C)	Age(ka)	%^{40}Ar*	K/Ca	K/Cl	moles ^{40}Ar*	∑^{39}Ar	^{40}Ar	^{39}Ar	^{38}Ar	^{37}Ar	^{36}Ar
550	-319.5±28.0	-1.74	0.72	917	-4.97E-15	0.09	10.368434±0.007351	0.213275±0.000229	0.010479±0.000023	0.155295±0.000939	0.035743±0.000048
575	-169.9±34.6	-1.03	0.67	1009	-2.11E-15	0.16	7.453691±0.004890	0.170530±0.000262	0.007734±0.000101	0.132649±0.000685	0.025521±0.000050
600	-46.6±24.9	-0.31	0.55	1425	-1.28E-15	0.31	6.543642±0.002857	0.163909±0.000167	0.006804±0.000045	0.157149±0.000685	0.022256±0.000035
625	-21.0±22.2	-0.15	0.46	1483	-5.36E-16	0.46	5.712131±0.001877	0.152523±0.000139	0.006069±0.000045	0.174942±0.000448	0.019408±0.000030
650	60.1±24.5	0.44	0.37	1308	1.30E-15	0.58	4.632273±0.002033	0.129206±0.000095	0.005044±0.000087	0.182914±0.000555	0.015657±0.000028
685	71.6±23.8	0.55	0.29	1816	1.46E-15	0.7	4.222152±0.001680	0.122004±0.000085	0.004553±0.000030	0.219673±0.000268	0.014271±0.000025
735	179.3±26.0	1.35	0.22	2346	3.34E-15	0.8	3.921511±0.001193	0.111403±0.000083	0.004121±0.000056	0.262849±0.000694	0.013165±0.000026
785	221.5±35.6	1.41	0.18	1284	2.56E-15	0.87	2.883443±0.000933	0.069045±0.000068	0.002941±0.000013	0.201293±0.000531	0.009677±0.000022
835	203.7±56.9	0.93	0.17	1316	1.43E-15	0.91	2.433445±0.000818	0.042040±0.000055	0.002217±0.000040	0.127229±0.000627	0.008194±0.000021
885	87.6±71.7	0.28	0.18	603	4.19E-16	0.94	2.348125±0.000557	0.028621±0.000043	0.002063±0.000038	0.084889±0.000346	0.007948±0.000018
935	-16.6±93.0	-0.04	0.15	387	-6.38E-17	0.96	2.386669±0.001210	0.023042±0.000044	0.002070±0.000029	0.079684±0.000369	0.008102±0.000019
985	-17.8±123.8	-0.04	0.11	300	-6.08E-17	0.98	2.483173±0.000780	0.020415±0.000049	0.002133±0.000041	0.098697±0.000194	0.008434±0.000022
1060	-121.1±169.5	-0.21	0.06	109	-3.06E-16	0.99	2.275837±0.000551	0.015157±0.000043	0.002236±0.000055	0.132932±0.000371	0.007755±0.000023
1150	-554.1±229.3	-0.77	0.01	145	-7.87E-16	1	1.623458±0.000556	0.008687±0.000034	0.001407±0.000029	0.304694±0.000681	0.005622±0.000017

Packet IRR292-ZA, Experiment #11Z0205, 0.152 g , all errors ±1σ
J = 0.000208705633±1.328E-07
^{40}Ar* is radiogenic argon, isotopes in volts (6.31e-14 moles/volt), corrected for blank, background, discrimination, and decay
Calculated K2O = 0.81%wt., Calculated CaO = 3.43%wt., Calculated Cl = 0.9ppm
Total Gas Age = -41.3 ± 8.9 ka
Isochron Age = 391.1 ± 56.9 ka (±1σ, including ±J)
Isochron Age = 391.1 ± 56.9 ka (A Priori Errors, including ±J)
Isochron Age = 391.1 ± 125.1 ka (95% confidence, including ±J)
MSWD = 0.34 (Good fit, MSWD < 2.56)
40Ar/36Ar intercept = 292.5 ± 0.6 (±1σ)
40Ar/36Ar intercept = 292.5 ± 0.6 (A Priori)
40Ar/36Ar intercept = 292.5 ± 1.4 (95% confidence)
Steps 7 of 14 (785,835,885,935,985,1060,1150°C)
Isochron Age = 974.1 ± 79.1 ka (±1σ, including ±J)
Isochron Age = 974.1 ± 79.1 ka (A Priori Errors, including ±J)
Isochron Age = 974.1 ± 174.1 ka (95% confidence, including ±J)
MSWD = 0.57 (Good fit, MSWD < 2.77)
^{40}Ar/^{36}Ar intercept = 275.1 ± 1.6 (±1σ)
^{40}Ar/^{36}Ar intercept = 275.1 ± 1.6 (A Priori)
^{40}Ar/^{36}Ar intercept = 275.1 ± 3.5 (95% confidence)
Steps 6 of 14 (550,575,600,625,650,685°C)

Table A4b. Detailed results of age determinations (cont'd)

09KCnye110

Temp(°C)	Age(ka)	%^{40}Ar*	K/Ca	K/Cl	moles ^{40}Ar*	∑^{39}Ar	^{40}Ar	^{39}Ar	^{38}Ar	^{37}Ar	^{36}Ar
550	-6.28±6.11	-0.79	0.48	15719	-1.52E-16	0.07	0.699370±0.000325	0.338150±0.000255	0.004991±0.000038	0.368983±0.001102	0.002488±0.000018
600	-13.62±3.99	-2.38	0.56	-7732	-5.60E-16	0.19	0.857997±0.000356	0.574593±0.000285	0.007802±0.000163	0.538840±0.000905	0.003122±0.000020
650	0.30±3.13	0.06	0.6	-7198	1.71E-17	0.35	0.993687±0.000505	0.799837±0.000418	0.010681±0.000056	0.698505±0.002549	0.003554±0.000022
700	-0.97±2.34	-0.22	0.59	-11553	-7.77E-17	0.58	1.300582±0.000445	1.124818±0.000512	0.015215±0.000145	1.007172±0.002182	0.004690±0.000022
750	-4.98±2.88	-0.91	0.48	-3E+05	-3.24E-16	0.76	1.292689±0.000529	0.908661±0.000397	0.012780±0.000212	0.993120±0.001954	0.004690±0.000022
800	-11.33±4.98	-1.1	0.34	44644	-4.24E-16	0.87	1.411835±0.000670	0.527939±0.000300	0.007912±0.000053	0.804598±0.001217	0.005055±0.000023
850	-35.93±11.03	-1.59	0.25	4233	-6.32E-16	0.92	1.448782±0.000433	0.246218±0.000196	0.004429±0.000033	0.524395±0.001121	0.005127±0.000024
925	-135.88±17.12	-2.64	0.22	2048	-1.69E-15	0.95	2.331989±0.000708	0.174299±0.000128	0.004180±0.000069	0.422489±0.000943	0.008218±0.000026
1000	-292.15±46.45	-1.85	0.21	1070	-2.09E-15	0.98	4.103351±0.001360	0.099980±0.000145	0.004364±0.000109	0.253185±0.000651	0.014214±0.000041
1100	-154.63±53.06	-0.58	0.1	352	-1.35E-15	1	8.413982±0.003134	0.122024±0.000169	0.008453±0.000122	0.651011±0.001660	0.028822±0.000056

Packet IRR292-YZ, Experiment #11Z0202, 0.1854 g Dacite, all errors ±1σ
J = 0.000212765945±1.284E-07
^{40}Ar* is radiogenic argon, isotopes in volts (2.75e-14 moles/volt), corrected for blank, background, discrimination, and decay
Calculated K2O = 1.32%wt., Calculated CaO = 3.91%wt., Calculated Cl = 9.9e-2ppm
Total Gas Age = -20.7 ± 2.1 ka

Isochron Age = 8.9 ± 2.0 ka (±1σ, including ±J)

Isochron Age = 8.9 ± 1.9 ka (A Priori Errors, including ±J)
Isochron Age = 8.9 ± 4.8 ka (95% confidence, including ±J)
MSWD = 1.12 (Good fit, MSWD < 2.56)
^{40}Ar/^{36}Ar intercept = 289.0 ± 0.6 (±1σ)
^{40}Ar/^{36}Ar intercept = 289.0 ± 0.6 (A Priori)
^{40}Ar/^{36}Ar intercept = 289.0 ± 1.5 (95% confidence)
Steps 7 of 10 (650,700,750,800,850,925,1000°C)

APPENDIX 5. WHOLE-ROCK COMPOSITIONS
APPENDIX 5A. SILICA VARIATIONS DIAGRAMS

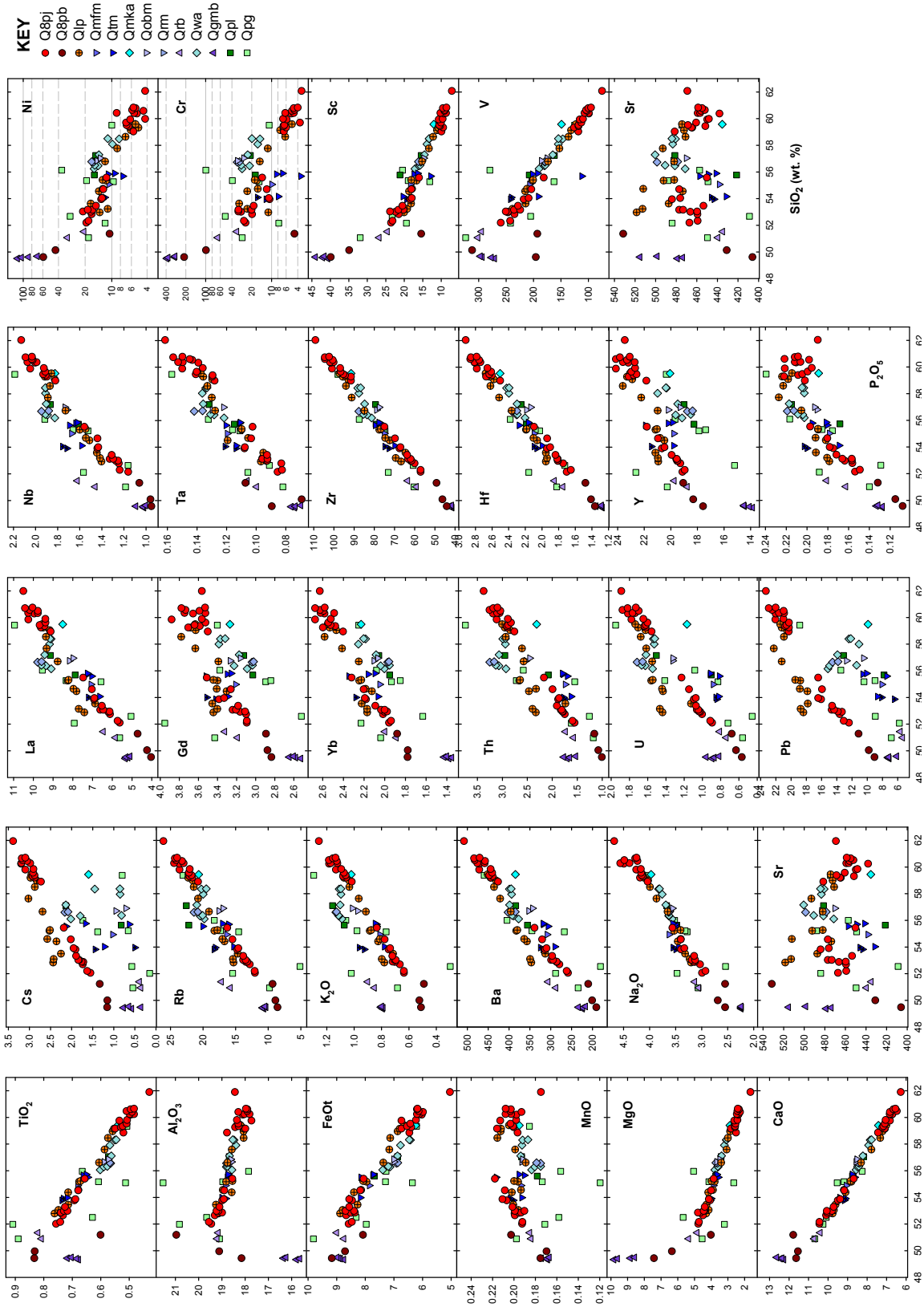

Figure A5a.1. Silica variation diagrams of major oxides (wt. %, normalized to 100%) and trace elements (ppm). 08pj, juvenile 2008 scoria; 08pb, basalt in and on inclusions in 2008 deposits; all other symbols are map units.

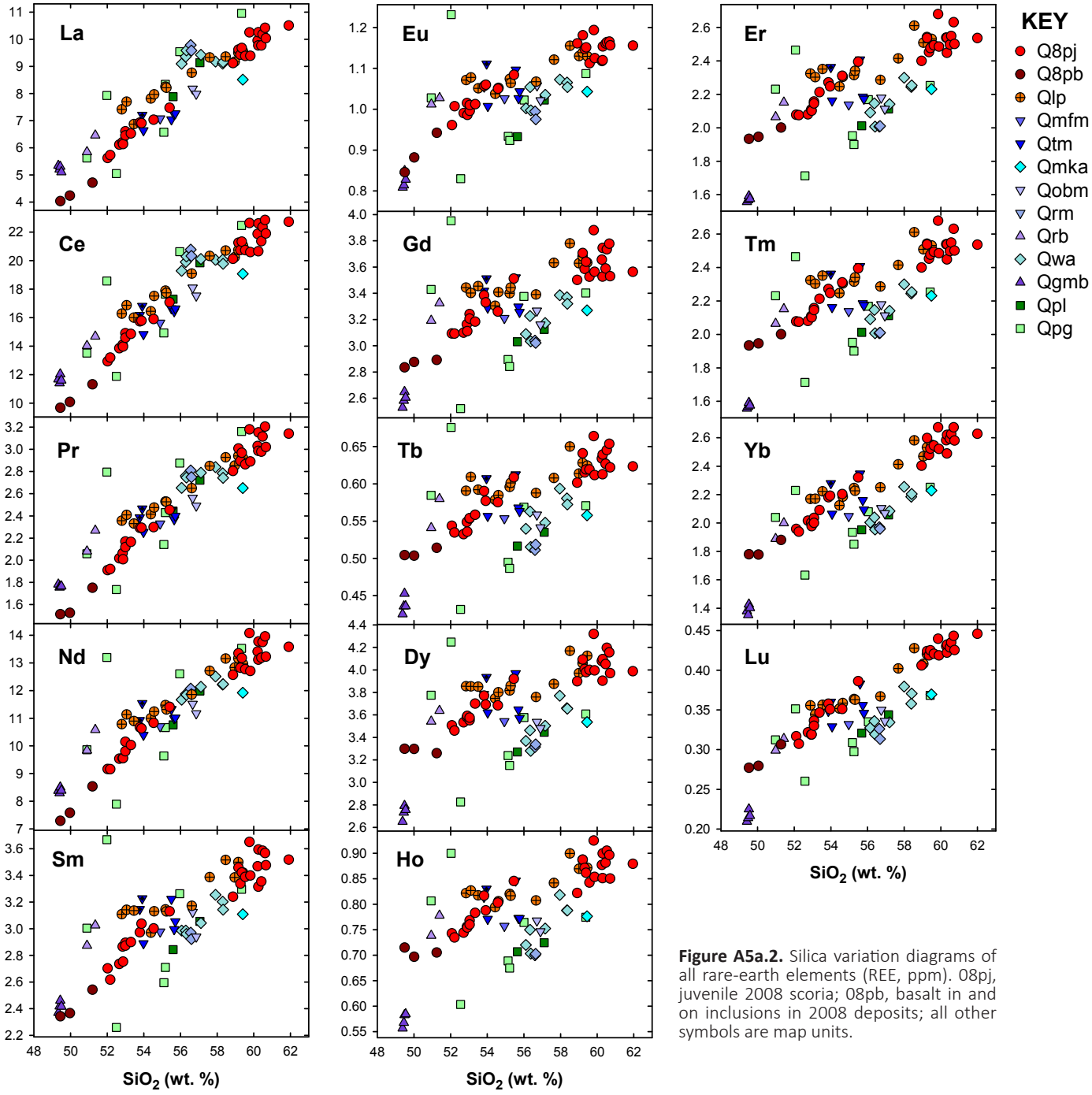

Figure A5a.2. Silica variation diagrams of all rare-earth elements (REE, ppm). 08pj, juvenile 2008 scoria; 08pb, basalt in and on inclusions in 2008 deposits; all other symbols are map units.

APPENDIX 5B. ENRICHMENT SPECTROGRAM

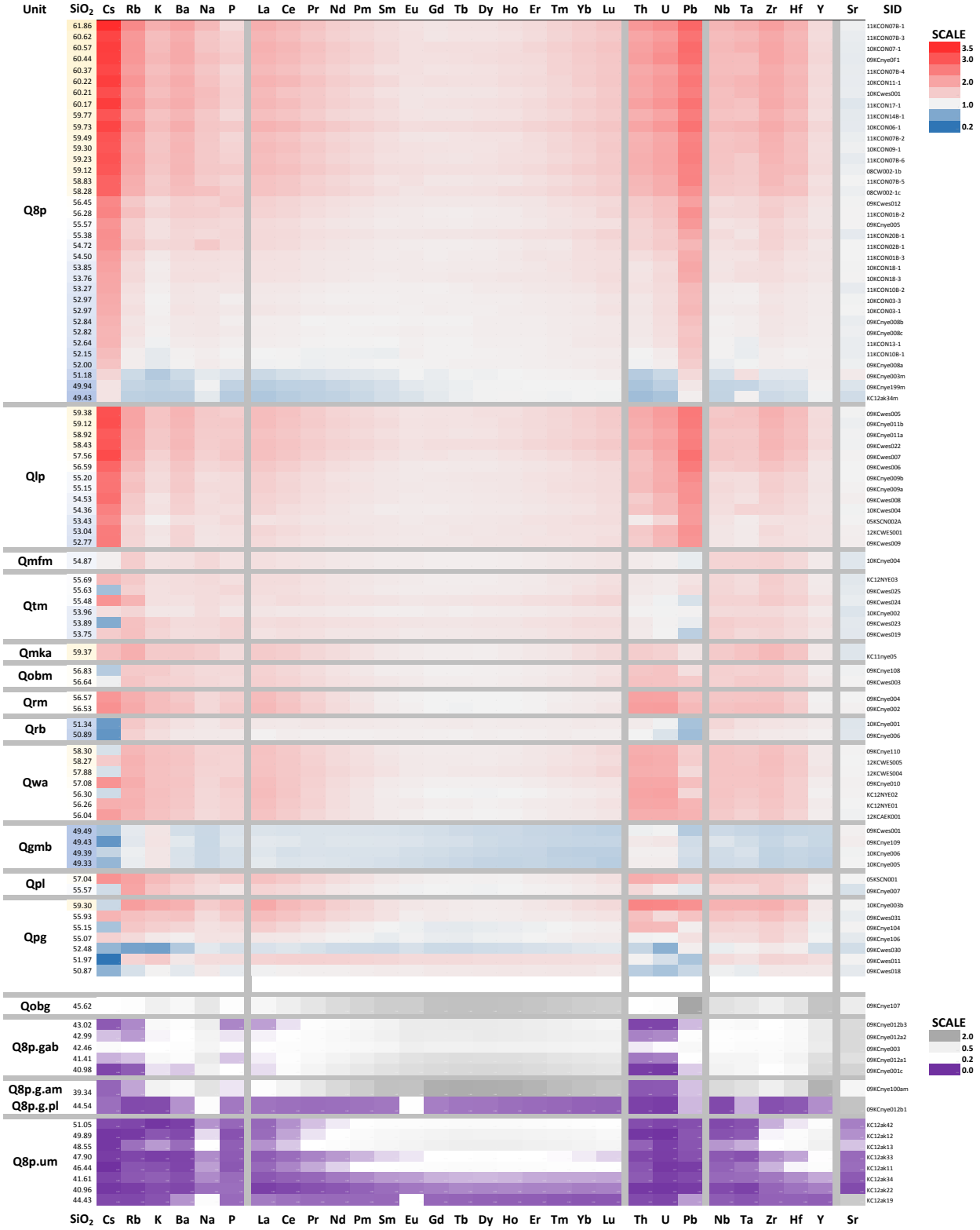

Figure A5b. Enrichment spectrogram. The enrichment spectrogram is made by normalizing all trace element concentrations to average Kasatochi basalt, then coloring the normalized values from highest to lowest. The spectrogram is similar to more familiar multi-element variation diagrams ("spider diagrams") in showing all data for all samples in a single figure, but different in that each sample is shown as a separate line, whereas in multi-element variation diagrams many crossing lines make tracking individual samples difficult. Two color scales are applied, blue to red for lava and scoria samples and purple to gray for cumulate inclusions. The diagram emphasizes that Cs and Pb behave most incompatibly, that trace element enrichment as a function of silica is consistent for Qlp and 2008 samples; that Cs and Pb are decoupled from each other and from silica in lava units; and that Qqmb has lower concentrations of all trace elements other than K, Th, and U than average Kasatochi basalt.

APPENDIX 5C. PRECISION

During analysis duplicate pellets (XRF) or solutions (ICP/MS) are made from a single powder from one sample in each batch, or one sample in every twenty from batches with more than twenty unknowns. Comparison of elemental concentrations measured from each of the duplicates provides an estimate of analytical uncertainty which includes both machine precision and pellet or solution preparation uncertainty. Uncertainties associated with producing powder from a rock sample, or taking a small sample from an outcrop are not included. Here we discuss the distribution of intra-analysis variations for all duplicates from AVO samples analyzed at the GeoAnalytic Laboratory (Washington State University) between 2004 and 2016 (105 XRF duplicates and 131 ICP/MS duplicates).

Between-duplicate variations are calculated as absolute difference between duplicates divided by the mean of the two values, in percent (100*(|a-b|/0.5(a+b))). An alternative method, not used here, would be to use the coefficient of variance between duplicates (CV; 100*(1 std/mean), which yields results that are about 30% lower.

Comparing duplicates using the differences between analyses rather than the absolute differences yields a range of values for each element which are roughly normally distributed about a value near zero. Because, it's irrelevant if one analysis or the other has the larger value, the mean of values based on arithmetic differences has no significance in terms of analytical precision. Calculating differences between duplicates using absolute variation (or, alternatively, CV) yields populations that are no-longer normally distributed because values that were negative are reflected to the positive side of distributions. Thus the range of inter-duplicate values cannot be summarized using its mean and standard deviation. Instead we summarize variations by percentiles, which can be asymmetric about the median value (Table A5c.1). The 50th percentile (median) is the value where half the values are smaller and half larger. The 68th percentile is the value where the portion of the population with smaller intra-pellet variations is roughly equivalent to ±1σ of a normally distributed population, and the 95th percentile is roughly equivalent to ±2σ. Table A5c.1 also gives the compositional range of the samples.

Table A5c.1. Summary of intra-duplicate variation and compositional range of AVO samples analyzed by the Washington State University GeoAnalytical Laboratory between 2004 and 2016. Intra-duplicate variation is calculated as absolute difference divided by the average of the two values, in percent, and provides a measure of analytical precision. Average values are given for the central 50, 68, and 95 percent, as well as the maximum value of the duplicate variation for each element. Microsoft Excel spreadsheet and Adobe PDF versions of this table are in Electronic Supplement E5.

element	Concentration range			Relative percent variation between duplicates			
	min	max	n	50%	68%	95%	max
Major oxides (wt. %) and trace elements (ppm) by XRF							
SiO_2	39.5	74.6	105	0.09	0.11	0.29	0.72
TiO_2	0.138	2.21	105	0.23	0.32	0.90	1.4
Al_2O_3	12.2	22.3	105	0.15	0.23	0.52	0.94
FeO*	1.45	18.9	105	0.70	1.2	2.7	6.0
MnO	0.052	0.245	105	0.33	0.54	1.1	1.4
MgO	0.553	13.5	105	0.37	0.46	1.4	2.9
CaO	0.903	15.7	105	0.20	0.27	0.52	0.79
Na_2O	1.09	4.85	105	0.29	0.47	1.3	2.2
K_2O	0.084	3.85	105	0.27	0.40	1.0	2.2
P_2O_5	0.023	0.529	105	0.35	0.51	2.0	4.5
Ni	1.2	114	102	6.1	11	55	88
Ni<10 ppm			*50*	*13*	*38*	*67*	*88*
Ni>10 ppm			*52*	*4.2*	*7.0*	*25*	*38*
Cr	0.54	300	101	4.7	11	69	100
Cr<10 ppm			*41*	*13*	*30*	*96*	*100*
Cr>10 ppm			*60*	*2.5*	*4.2*	*25*	*30*
Sc	4.4	81	105	2.3	3.5	7.5	30
V	12	732	105	1.0	1.5	3.0	8.7
Ba	63	1699	105	0.72	1.2	2.3	3.7
Rb	1.1	80	105	2.0	2.8	8.7	33
Sr	143	1082	105	0.39	0.62	1.7	2.7
Zr	11	267	105	0.66	0.91	2.8	6.1
Y	9.0	49	104	1.6	2.8	8.2	19
Nb	0.35	13	104	10	13	54	100
Nb<4 ppm			*54*	*16*	*24*	*81*	*100*
Nb>4 ppm			*50*	*5.4*	*8.6*	*14*	*27*
Ga	16	23	105	3.7	5.4	14	27
Cu	1.9	256	104	1.7	2.7	14	52
Zn	42	118	105	1.2	2.2	4.9	6.0
Pb	0.90	18	104	8.2	15	50	136
La	1.5	30	105	16	22	83	144
Ce	5.7	71	105	9.9	15	38	90
Th	0.20	8.4	100	20	32	105	179
Nd	4.2	40	85	9.8	13	29	37
U	0.35	3.9	41	48	72	140	141

Table A5c.1. (cont'd).

element	Concentration range			Relative percent variation between duplicates			
	min	max	n	50%	68%	95%	max
Trace elements (ppm) by ICP/MS							
La	1.2	30	131	0.80	1.2	2.6	8.4
Ce	3.2	67	131	0.76	1.1	3.2	7.8
Pr	0.54	9.2	131	0.78	1.2	3.8	12
Nd	3.0	40	131	0.86	1.3	3.9	8.5
Sm	1.1	9.8	131	1.3	1.9	3.3	4.2
Eu	0.49	2.5	131	1.4	2.1	3.6	5.4
Gd	1.4	9.8	131	1.4	1.8	3.2	4.0
Tb	0.25	1.6	131	1.0	1.6	3.3	4.7
Dy	1.5	10.0	131	1.1	1.6	3.7	5.3
Ho	0.29	2.1	131	1.0	1.5	2.9	6.1
Er	0.75	5.9	131	0.94	1.3	3.2	4.8
Tm	0.10	0.90	131	1.3	1.7	3.7	7.0
Yb	0.61	5.8	131	1.3	1.8	3.5	5.5
Lu	0.092	0.94	131	1.2	1.8	3.5	6.8
Ba	57	1767	131	0.72	1.0	2.0	13
Th	0.13	9.2	131	1.4	2.2	6.3	35
Nb	0.28	12	131	1.3	1.9	5.8	53
Y	7.2	55	131	1.0	1.6	3.4	19
Hf	0.26	9.8	131	1.2	1.5	3.1	6.5
Ta	0.023	1.1	131	1.7	3.0	8.4	92
U	0.078	4.1	131	1.4	2.1	8.5	47
Pb	0.96	29	131	1.1	2.1	5.3	75
Rb	1.0	97	131	1.4	1.8	3.4	7.0
Cs	0.084	6.6	131	1.5	2.4	7.9	77
Sr	149	1060	131	0.87	1.3	3.5	5.3
Sc	3.6	44	131	2.4	3.9	11	16

It is also important to know if analytical precision is compositionally dependent (i. e. if lower concentrations of any element have systematically poorer precision). Figures A5c.1–5 are plots of duplicate variation vs. concentration for all elements by both XRF and ICP/MS. Principle observations are:

- Major element precision (Figure A5c.1) is independent of composition and generally better than 0.5 rel. % at the 68th percentile except for iron, which is about 1.2 rel. %.
- XRF analyses of Ni, Cr and Nb (Figure A5c.2) are generally better than 10 rel. %, but increase systematically at concentrations below 10 ppm (Ni and Cr) and 4ppm (Nb). Variations approach 100% (the detection limit) at about 2 ppm (Ni and Cr) and 1 ppm (Nb). Rb and Y precision also decrease and disperses at low concentrations, but not as severely as Ni, Cr, and Nb.
- REE analyses by ICP/MS (Figure A5c.4 have precisions of better than 2 rel.% at the 68th percentile; better than 4 rel. % at the 95th percentile and are independent of concentration—as low about 5 times chondritic concentrations in the data summarized here.
- Analyses of trace elements other than REE by ICP/MS (Figure A5c.3) have precisions similar to the REE, and are also independent of concentration with the exception of Ta, Cs, and Pb which have modest increased dispersion of variation below 0.2 ppm (Ta), 1.5 ppm (Cs), and 8 ppm (Pb).
- Concentrations of a dozen trace elements are measured by both XRF and ICP/MS (Figure 5Ac.5). Ba, Rb, Sr, and Zr have similar analytical precision by both techniques. Y precision by XRF and ICP/MS is similar at concentrations greater than 25ppm, but at concentrations less than 25 ppm the XRF data are somewhat less precise. For Nb, Pb, Th, La, Ce, Nd, and U XRF precision is substantially poorer over most or all of the concentration range of AVO samples. XRF analyes of Pb, Th, La, Ce, Nd, and U for Kasatochi samples are not reported here.
- In a small number of cases there are abnormally large variations between duplicates. About 1.3% of the data lie outside 3σ of intra-duplicate variations calculated as the arithmetic difference divided by the mean of the two analyses. In most cases these outliers are widely separated from neighboring points when the data for each element are ranked by inter-duplicate variation. In the ranked data most neighboring points are less than 5% different, but in the tails of the distribution the difference between neighbors can increase to several hundreds of percent. In some cases the outliers are associated with the lowest-concentration of a particular element in the data set, but in many cases the outliers span the full concentration range of the data. For instance, Pr variation (Figure A5c.4) is mostly less than 2%, but in four cases the variation between duplicates is 9–13%. Outliers generally exist only for one element in a given duplicate pair. There are no duplicate pairs where one analysis is systematically and uniformly different across many or all elements. The implication of the existence of the outliers is that for any large data set a few of the values for a few of the elements may be aberrant for reasons unrelated to geology, petrology, or geochemistry.

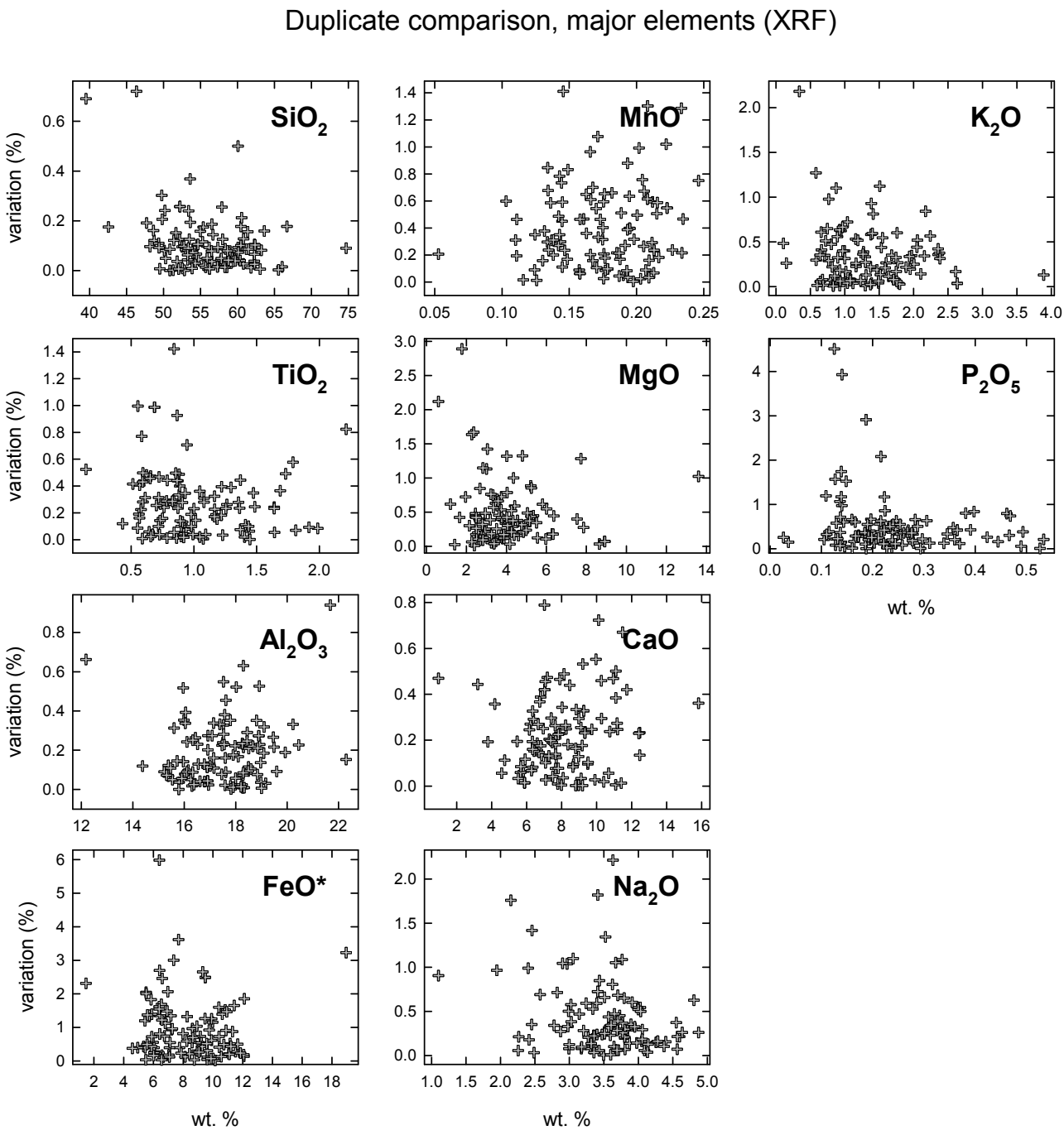

Figure A5c.1. Variation between duplicate pellets vs. concentration for major elements (normalized to 100%) measured by XRF. Variation is 100*|a-b|/((a+b)/2).

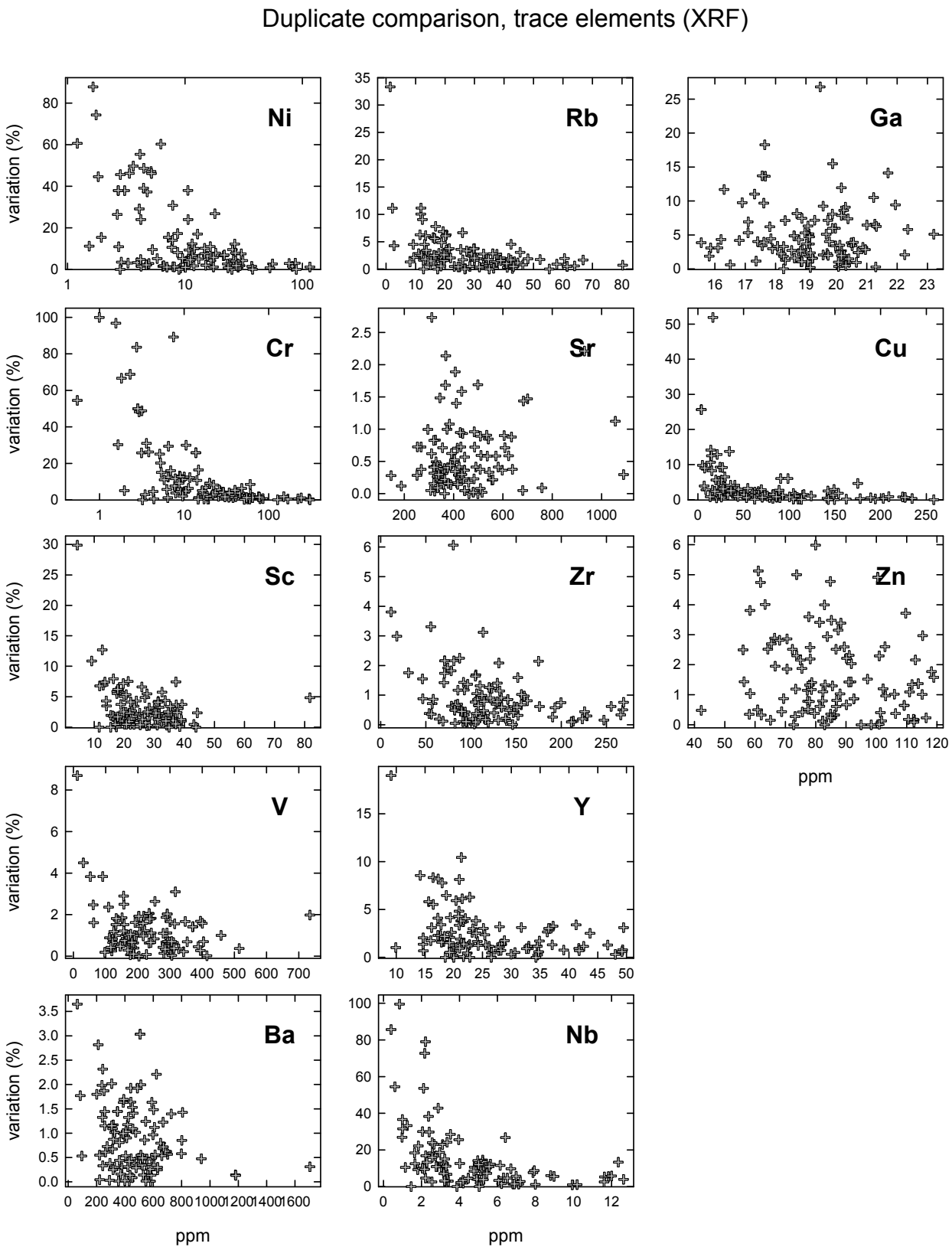

Figure A5c.2. Variation between duplicate pellets vs. concentration for trace elements measured by XRF.

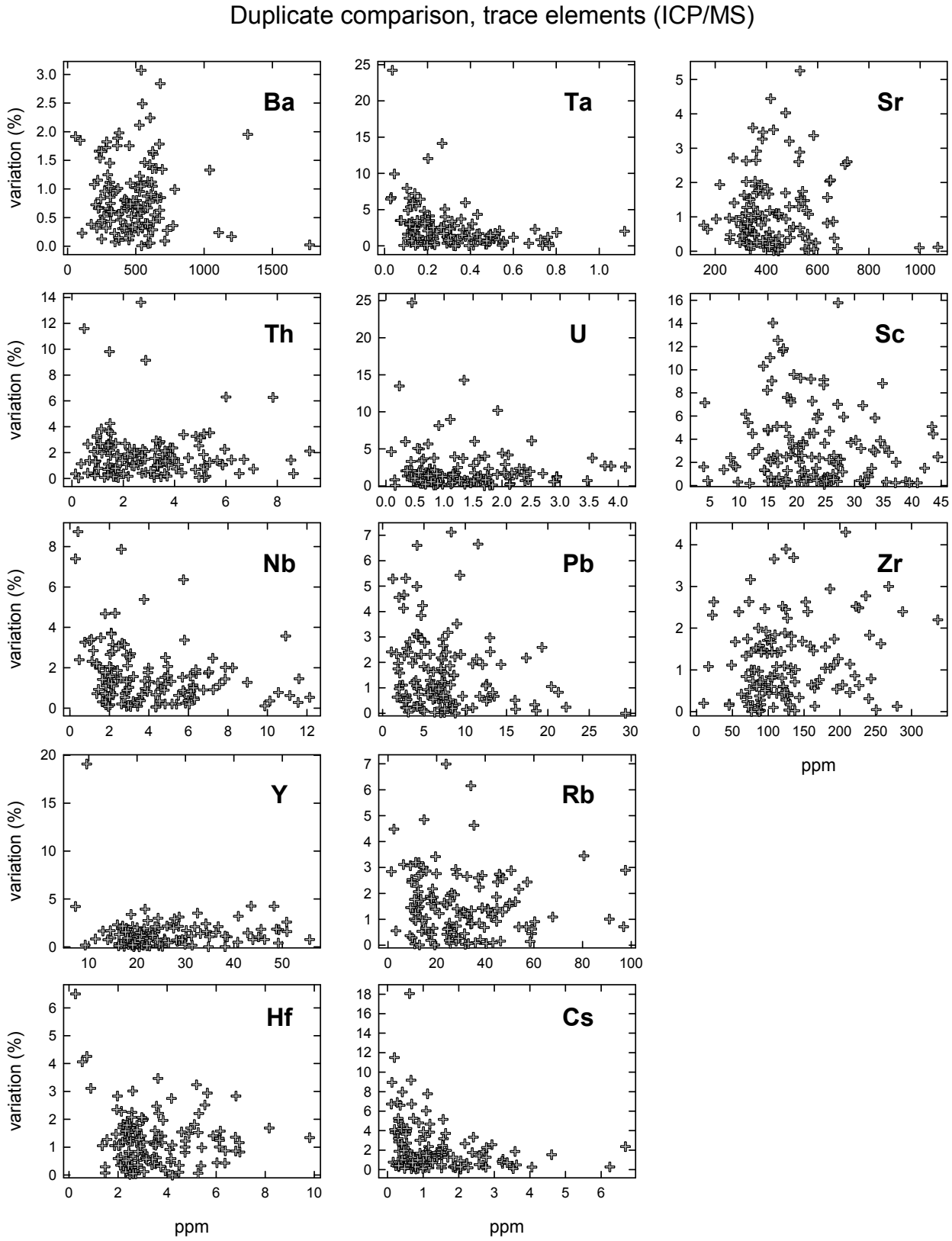

Figure A5c.3. Variation between duplicate pellets vs. concentration for trace elements other than REE measured by ICP/MS.

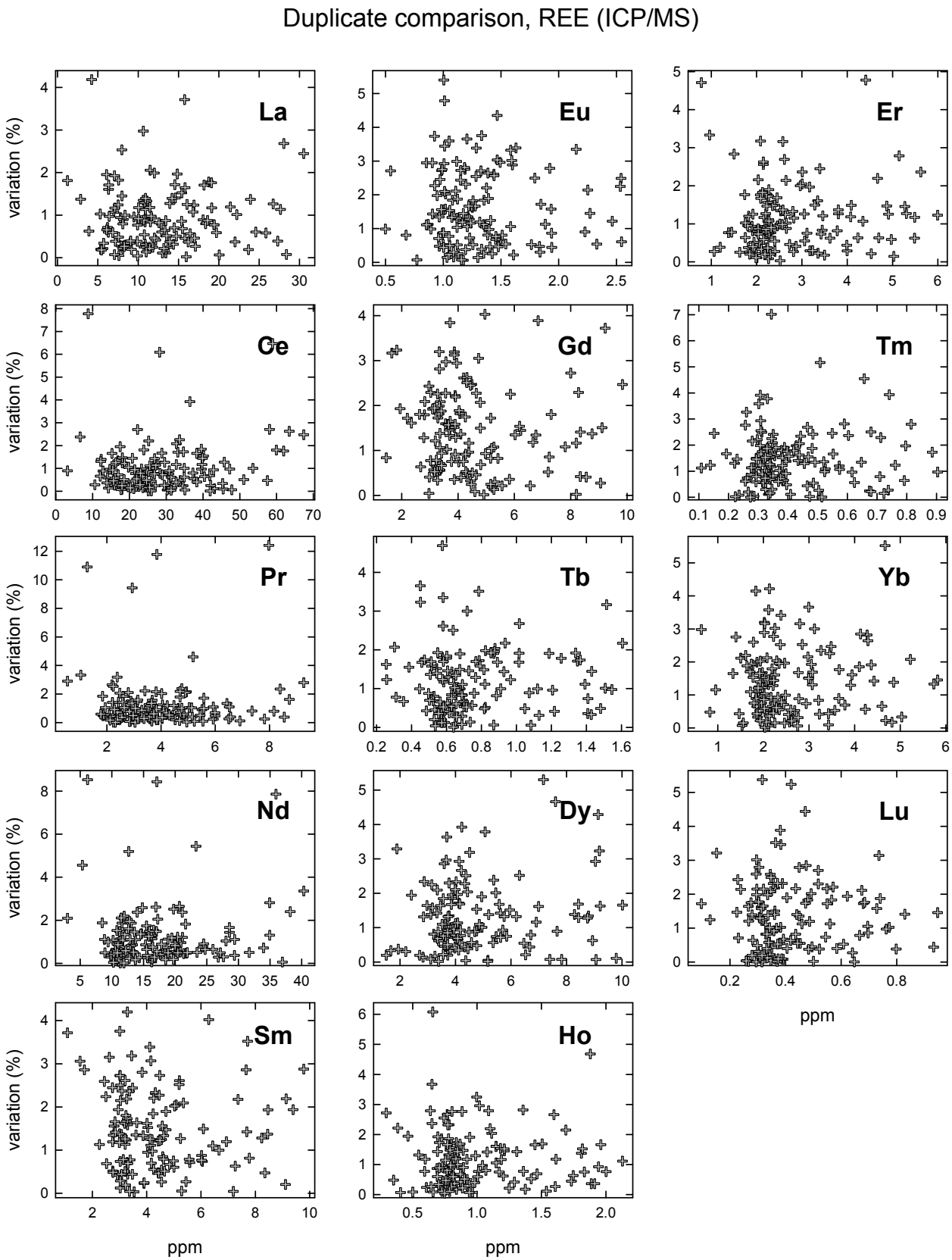

Figure A5c.4. Variation between duplicate pellets vs. concentration for rare-earth elements (REE) measured by ICP/MS.

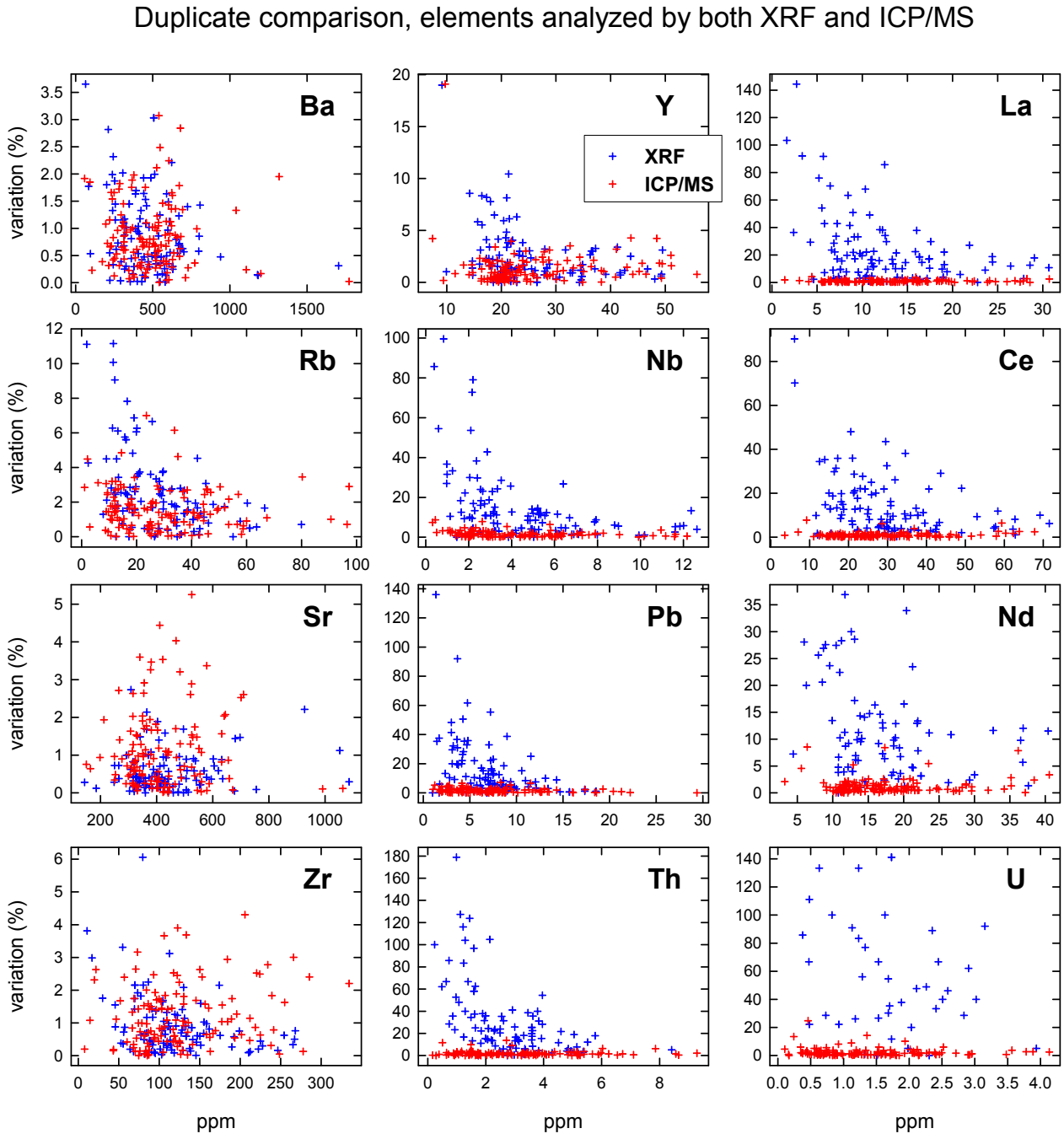

Figure A5c.5. Variation between duplicate pellets vs. concentration for trace elements measured by both XRF and ICP/MS.

APPENDIX 5D. DATA

Table A5d. Whole-rock and mineral separate analyses by XRF and ICP. All analyses by the Peter Hooper GeoAnalytical Lab at Washington State University, Pullman, WA. Electronic Supplement E5 contains these data as a Microsoft Excel spreadsheet (.xlsx) and a comma-separated value file (.csv).

Table A5d. Whole rock and mineral separate analyses.

sampleID	09KCnye008a	11KCon10B-1	11KCon13-1	09KCnye008c	09KCnye008b	10KCon03-1	10KCon03-3	11KCon10B-2	10KCon18-3
Map symbol[1]	Q8p.j,ba	Q8p.j,ba	Q8p.j,ba	Q8p.j,ba	Q8p.j,ba	Q8p.j,ba	Q8p.j,ba	Q8p.j,ba	Q8p.j,ba
Latitude[2]	52.16247	52.17271	52.16773	52.16247	52.16247	52.16703	52.16703	52.17271	52.16884
Longitude[2]	-175.52338	-175.53027	-175.52985	-175.52338	-175.52338	-175.49226	-175.49226	-175.53027	-175.53114
XRF[3]									
SiO_2	52.00	52.15	52.64	52.82	52.84	52.97	52.97	53.27	53.76
TiO_2	0.757	0.742	0.732	0.741	0.740	0.729	0.717	0.726	0.693
Al_2O_3	19.46	19.56	19.31	19.15	18.99	19.15	19.23	19.10	18.99
FeOt	8.58	8.47	8.67	8.50	8.36	8.69	8.39	8.56	8.46
MnO	0.192	0.192	0.199	0.195	0.193	0.199	0.190	0.201	0.207
MgO	4.78	4.73	4.50	4.66	4.79	4.40	4.45	4.39	4.07
CaO	10.45	10.44	10.10	9.93	10.05	9.81	10.07	9.72	9.50
Na_2O	2.99	2.93	3.03	3.13	3.15	3.19	3.13	3.14	3.40
K_2O	0.636	0.637	0.666	0.702	0.719	0.705	0.696	0.721	0.748
P_2O_5	0.154	0.149	0.156	0.164	0.157	0.166	0.157	0.172	0.175
Total	100.03	100.02	100.23	100.11	99.97	100.01	99.45	99.91	99.30
H_2O^+/LOI	--	--	--	--	--	--	--	--	--
SO_3 (≥)	--	--	--	--	--	--	--	--	--
Cl (≥)	0.06	0.05	0.04	0.06	0.10	0.07	0.05	0.05	0.20
Ni	19.4	18.3	16.9	17.3	21.2	16.5	18.7	15.1	13.2
Cr	24.8	26.3	19.8	29.1	32.0	20.1	31.8	18.7	10.7
Sc	23.8	23.7	21.4	23.0	25.1	21.4	21.0	21.0	18.4
V	259.9	242.6	234.8	246.5	250.7	235.6	224.3	228.3	218.0
Ba	267.8	266.1	278.6	293.2	296.7	294.6	294.4	300.9	308.1
Rb	13.6	12.3	13.5	15.3	15.2	15.6	14.3	14.6	15.5
Sr	467.6	474.5	477.1	468.5	460.1	475.8	473.3	471.3	477.4
Zr	60.0	55.5	59.2	66.2	68.9	65.2	62.9	63.8	67.0
Y	19.7	19.3	20.0	20.3	21.8	20.1	19.6	20.8	21.5
Nb	2.6	1.6	1.6	2.6	3.0	2.8	2.4	2.3	1.9
Ga	18.7	18.0	19.2	19.0	17.3	18.4	19.1	18.5	18.8
Cu	105.3	114.9	105.8	103.9	109.2	106.0	106.7	104.6	106.7
Zn	84.4	83.4	88.4	88.5	86.8	89.0	86.6	90.4	94.0
ICP/MS[4]									
La	5.625	5.734	6.117	6.210	6.137	6.610	6.461	6.529	6.931
Ce	12.939	13.201	13.852	14.093	13.969	14.908	14.591	14.857	15.740
Pr	1.9108	1.9208	2.0178	2.0635	2.0087	2.1692	2.1173	2.1653	2.2924
Nd	9.165	9.159	9.537	9.554	9.560	10.153	9.806	10.032	10.674
Sm	2.703	2.618	2.737	2.867	2.753	2.896	2.873	2.901	2.974
Eu	0.9611	1.0075	0.9907	1.0151	0.9863	0.9958	1.0104	1.0122	1.0571
Gd	3.093	3.093	3.100	3.164	3.111	3.242	3.207	3.184	3.385
Tb	0.5439	0.5348	0.5326	0.5489	0.5359	0.5537	0.5541	0.5585	0.5904
Dy	3.507	3.461	3.534	3.581	3.592	3.553	3.576	3.701	3.771
Ho	0.7429	0.7347	0.7443	0.7558	0.7543	0.7682	0.7601	0.7832	0.8170
Er	2.0778	2.0753	2.0802	2.1094	2.1020	2.1571	2.1454	2.2130	2.2715
Tm	0.3066	0.3094	0.3119	0.3148	0.3152	0.3185	0.3186	0.3285	0.3370
Yb	1.9586	1.9397	2.0174	2.0025	1.9779	2.0367	2.0014	2.0916	2.1813
Lu	0.3169	0.3074	0.3218	0.3190	0.3192	0.3365	0.3301	0.3467	0.3578
Ba	258.81	261.80	279.38	286.23	285.99	299.17	294.53	296.71	313.38
Th	1.5533	1.5962	1.7500	1.7869	1.7969	1.8301	1.8143	1.9081	1.8817
Nb	1.1614	1.2387	1.2462	1.2718	1.2526	1.3290	1.2974	1.3106	1.4402
Y	19.129	18.962	19.288	19.528	19.503	19.595	19.556	19.945	20.684
Hf	1.7037	1.6533	1.7449	1.8079	1.8103	1.8118	1.8170	1.8378	1.9402
Ta	0.08557	0.08259	0.08302	0.09310	0.09256	0.09590	0.09237	0.09272	0.10796
U	0.8952	0.9140	1.0042	1.0247	1.0372	1.0618	1.0456	1.0710	1.0946
Pb	12.407	13.094	13.624	13.328	13.866	14.667	14.349	14.625	16.064
Rb	12.034	12.078	12.832	13.423	13.222	13.844	13.462	13.828	14.781
Cs	1.5543	1.6327	1.7380	1.7225	1.7635	1.8226	1.8422	1.8935	1.9078
Sr	467.3	459.3	459.4	466.4	459.7	477.1	473.4	453.6	484.2
Sc	23.57	23.17	21.50	22.39	23.86	20.22	21.62	20.48	18.31
Zr	57.07	57.07	60.04	61.92	61.61	63.24	62.06	63.77	67.51
Mode[5]									
gms	55	--	--	53	47	57	--	--	--
pl	28	--	--	30	34	26	--	--	--
ol	0.2	--	--	0.0	0.7	0.0	--	--	--
cpx	6.9	--	--	5.9	6.5	8.3	--	--	--
opx	0.0	--	--	5.4	2.5	3.4	--	--	--
am	8.0	--	--	1.8	4.7	3.4	--	--	--
ox	1.8	--	--	3.0	4.0	2.1	--	--	--

Table A5d. Whole-rock and mineral separate analyses (cont'd).

Table A5d. Cont'd.

sampleID	10KCon18-1	11KCon01B-3	11KCon20B-1	11KCon07B-5	08cw002-1b	11KCon07B-6	10KCon09-1	11KCon07B-2	10KCon06-1
Map symbol	Q8p.j,ba	Q8p.j,ba	Q8p.j,ba	Q8p.j,a	Q8p.j,a	Q8p.j,a	Q8p.j,a	Q8p.j,a	Q8p.j,a
Latitude	52.16884	52.17271	52.16922	52.17487	52.17477	52.17487	52.18046	52.17487	52.18046
Longitude	-175.53114	-175.53027	-175.53043	-175.52933	-175.53152	-175.52933	-175.49873	-175.52933	-175.49873
XRF									
SiO_2	53.85	54.50	55.38	58.83	59.12	59.23	59.30	59.49	59.73
TiO_2	0.689	0.679	0.656	0.521	0.549	0.530	0.523	0.509	0.534
Al_2O_3	18.92	18.90	18.55	18.78	17.99	18.43	18.27	18.29	17.73
FeOt	8.56	8.18	8.06	6.46	6.74	6.39	6.55	6.43	6.74
MnO	0.211	0.209	0.218	0.197	0.216	0.200	0.201	0.203	0.213
MgO	4.14	4.00	3.85	2.51	2.82	2.58	2.57	2.54	2.62
CaO	9.38	9.17	8.69	7.44	7.10	7.22	7.16	7.09	6.83
Na_2O	3.33	3.40	3.56	4.04	4.19	4.13	4.15	4.16	4.26
K_2O	0.737	0.777	0.835	1.018	1.059	1.081	1.062	1.075	1.134
P_2O_5	0.178	0.181	0.197	0.202	0.222	0.209	0.205	0.199	0.221
Total	99.45	99.60	99.72	99.36	100.02	99.03	99.59	99.11	99.69
H_2O^+/LOI	--	--	--	--	--	--	--	--	--
SO_3 (≥)	--	0.02	--	--	--	--	--	--	--
Cl (≥)	0.10	0.07	0.11	0.09	--	0.14	0.13	0.12	0.16
Ni	12.9	12.5	11.5	5.7	1.4	6.5	6.8	6.9	6.2
Cr	11.0	11.8	13.9	6.5	6.0	6.6	6.4	3.7	5.9
Sc	17.5	17.2	15.6	11.1	11.2	9.9	10.5	11.1	10.2
V	209.0	204.1	181.4	118.5	126.4	118.2	118.1	113.0	115.9
Ba	304.5	322.7	343.2	424.6	441.2	433.1	442.4	440.6	468.4
Rb	14.6	15.7	17.3	21.4	21.8	22.5	22.3	23.1	24.0
Sr	475.5	475.4	468.1	487.7	455.0	469.3	467.8	464.3	448.6
Zr	68.2	68.8	74.5	91.4	94.6	93.6	95.3	94.9	102.0
Y	21.0	21.4	22.6	22.7	21.8	23.1	23.2	22.9	24.7
Nb	2.5	2.0	2.4	2.7	1.4	2.1	2.6	2.8	2.9
Ga	17.3	17.7	18.4	19.1	16.8	19.8	19.0	19.5	18.1
Cu	112.8	102.4	90.2	69.6	60.2	60.0	68.2	66.7	59.9
Zn	92.7	92.3	97.1	91.2	96.9	92.9	90.8	92.6	97.1
ICP/MS									
La	6.911	7.038	7.478	9.124	9.618	9.432	9.679	9.384	10.252
Ce	15.785	15.900	17.078	20.119	21.253	20.743	21.332	20.734	22.630
Pr	2.2934	2.2987	2.4549	2.8054	3.0067	2.8963	2.9689	2.8646	3.1799
Nd	10.634	10.832	11.413	12.573	13.347	12.826	13.181	12.775	14.082
Sm	3.038	3.003	3.131	3.240	3.459	3.339	3.422	3.389	3.651
Eu	1.0599	1.0501	1.0844	1.1610	1.1810	1.1471	1.1514	1.1125	1.1939
Gd	3.330	3.260	3.513	3.502	3.707	3.586	3.641	3.527	3.881
Tb	0.5772	0.5755	0.6088	0.6017	0.6409	0.6153	0.6193	0.6193	0.6640
Dy	3.692	3.685	3.921	3.899	4.093	4.009	3.980	4.001	4.321
Ho	0.7880	0.8030	0.8455	0.8219	0.8874	0.8711	0.8616	0.8426	0.9251
Er	2.2477	2.3112	2.3952	2.4003	2.5375	2.4527	2.4767	2.4939	2.6804
Tm	0.3391	0.3352	0.3526	0.3658	0.3938	0.3751	0.3854	0.3806	0.4064
Yb	2.1923	2.2042	2.3213	2.4036	2.5979	2.4788	2.5239	2.5454	2.6737
Lu	0.3509	0.3512	0.3863	0.4060	0.4240	0.4187	0.4251	0.4208	0.4397
Ba	310.00	320.71	338.93	426.47	443.76	439.59	447.60	440.59	471.55
Th	1.8643	1.9944	2.1678	2.7580	2.9002	2.9128	2.8823	2.8264	3.1145
Nb	1.4319	1.4393	1.5583	1.8202	1.8966	1.9087	1.9315	1.9123	2.0480
Y	20.477	20.968	21.807	21.841	23.167	22.789	22.580	22.974	24.135
Hf	1.9016	1.9379	2.0953	2.5035	2.6728	2.6035	2.6344	2.6126	2.7848
Ta	0.10769	0.10339	0.10248	0.12813	0.12974	0.12948	0.14086	0.14027	0.14999
U	1.0733	1.1474	1.2300	1.5582	1.6226	1.6359	1.6220	1.6030	1.7791
Pb	16.451	15.941	16.441	20.318	20.287	20.781	20.613	20.290	22.063
Rb	14.593	15.495	16.296	20.774	21.660	22.088	21.763	22.181	23.612
Cs	1.9527	2.0208	2.1868	2.7285	2.8810	2.9240	2.8797	2.9149	3.0980
Sr	476.1	477.2	450.3	481.5	465.1	451.7	468.6	460.7	449.9
Sc	17.99	18.09	16.02	9.95	9.49	10.32	10.51	10.08	10.67
Zr	67.04	69.79	74.99	91.58	91.59	94.51	95.33	96.68	100.94
Mode									
gms	70	--	--	--	70	--	74	--	--
pl	22	--	--	--	24	--	18	--	--
ol	0.0	--	--	--	0.2	--	0.0	--	--
cpx	3.7	--	--	--	1.5	--	1.7	--	--
opx	1.6	--	--	--	3.4	--	1.0	--	--
am	0.7	--	--	--	0.6	--	4.1	--	--
ox	2.1	--	--	--	0.8	--	0.9	--	--

Table A5d. Whole-rock and mineral separate analyses (cont'd).

Table A5d. Cont'd.

sampleID	11KCon14B-1	11KCon17-1	10KCwes001	10KCon11-1	11KCon07B-4	09KCnye0F1	10KCon07-1	11KCon07B-3	11KCon07B-1
Map symbol	Q8p.j,a	Q8p.j,a	Q8p.j,a	Q8p.j,a	Q8p.j,a	Q8p.j,a	Q8p.j,a	Q8p.j,a	Q8p.j,a
Latitude	52.17487	52.16724	52.18077	52.16884	52.17487	52.17931	52.18046	52.17487	52.17487
Longitude	-175.52933	-175.52937	-175.49892	-175.53114	-175.52933	-175.52646	-175.49873	-175.52933	-175.52933
XRF									
SiO_2	59.77	60.17	60.21	60.22	60.37	60.44	60.57	60.62	61.86
TiO_2	0.507	0.494	0.483	0.498	0.491	0.509	0.495	0.483	0.429
Al_2O_3	18.35	18.10	18.03	17.81	18.29	17.91	17.90	17.97	18.44
FeOt	6.23	6.03	6.12	6.20	5.98	6.14	6.19	6.18	5.04
MnO	0.198	0.198	0.203	0.208	0.193	0.203	0.203	0.208	0.175
MgO	2.43	2.38	2.36	2.47	2.28	2.43	2.34	2.41	1.65
CaO	7.05	6.74	6.70	6.84	6.83	6.48	6.65	6.55	6.28
Na_2O	4.17	4.49	4.57	4.39	4.24	4.49	4.28	4.25	4.68
K_2O	1.095	1.184	1.124	1.172	1.127	1.184	1.156	1.136	1.258
P_2O_5	0.195	0.210	0.212	0.206	0.198	0.222	0.212	0.209	0.190
Total	98.97	98.07	98.91	98.30	99.12	99.21	99.33	99.35	98.25
H_2O^+/LOI	--	--	--	--	--	--	--	--	--
SO_3 (≥)	--	0.10	--	--	--	--	--	--	--
Cl (≥)	0.11	0.18	0.27	0.27	0.10	0.23	0.11	0.11	0.26
Ni	4.2	5.2	5.6	8.8	4.4	5.9	5.4	5.7	4.2
Cr	6.7	5.0	4.6	6.2	4.9	4.5	4.6	4.0	3.5
Sc	10.1	9.6	9.3	11.0	9.0	10.2	10.6	10.0	7.2
V	110.0	99.4	99.6	107.2	102.7	104.2	100.2	95.3	75.2
Ba	445.9	471.3	461.5	462.4	455.5	483.3	471.8	466.5	494.5
Rb	22.5	24.5	23.9	23.9	23.3	25.1	25.2	24.0	26.4
Sr	465.6	452.6	466.8	451.0	461.6	450.7	456.8	458.7	462.6
Zr	96.0	100.6	100.4	101.0	100.9	107.7	105.2	100.5	107.7
Y	23.9	23.7	23.4	23.5	24.2	23.8	24.4	23.4	23.9
Nb	2.1	2.1	2.9	3.1	3.0	3.2	3.2	2.9	2.5
Ga	19.8	18.2	18.5	16.8	19.0	17.4	17.4	18.1	18.3
Cu	65.3	55.2	45.7	68.4	63.6	54.8	65.5	47.8	60.6
Zn	90.0	90.0	92.8	92.8	90.2	95.3	93.0	93.3	82.3
ICP/MS									
La	9.393	9.952	9.773	10.257	9.770	10.189	10.423	10.040	10.507
Ce	20.595	21.868	20.657	22.606	21.361	22.364	22.848	21.896	22.722
Pr	2.8901	3.0293	2.9862	3.1525	2.9787	3.1156	3.2050	3.0206	3.1410
Nd	12.709	13.415	13.119	13.779	13.187	13.755	13.960	13.227	13.582
Sm	3.400	3.468	3.316	3.594	3.355	3.586	3.568	3.477	3.518
Eu	1.1250	1.1181	1.1201	1.1535	1.1608	1.1640	1.1656	1.1565	1.1558
Gd	3.564	3.657	3.527	3.746	3.589	3.735	3.778	3.531	3.564
Tb	0.6118	0.6339	0.6129	0.6394	0.6268	0.6453	0.6538	0.6222	0.6234
Dy	3.996	4.079	3.905	4.096	4.052	4.197	4.157	3.971	3.989
Ho	0.8536	0.8772	0.8512	0.8997	0.8815	0.9049	0.8968	0.8505	0.8793
Er	2.4859	2.5393	2.4484	2.5386	2.4984	2.5492	2.6312	2.5010	2.5371
Tm	0.3773	0.3943	0.3807	0.3866	0.3972	0.3972	0.4092	0.3889	0.3950
Yb	2.5219	2.5829	2.4897	2.6209	2.5934	2.6263	2.6740	2.5807	2.6278
Lu	0.4187	0.4304	0.4222	0.4323	0.4288	0.4350	0.4433	0.4255	0.4460
Ba	444.29	471.88	458.68	476.34	457.68	482.38	483.82	470.59	508.23
Th	2.8885	3.1880	3.0549	3.1057	3.0413	3.2577	3.1837	3.0995	3.3763
Nb	1.9251	2.0040	1.9899	2.0734	2.0255	2.0336	2.0909	2.0331	2.1295
Y	22.686	23.202	22.718	23.603	23.298	24.136	23.831	23.091	23.464
Hf	2.6566	2.8084	2.7410	2.8132	2.7564	2.8633	2.8555	2.7870	2.9186
Ta	0.13608	0.13912	0.14965	0.15277	0.14320	0.14492	0.15610	0.14986	0.16159
U	1.6475	1.8158	1.7384	1.7654	1.6990	1.8767	1.8206	1.7300	1.8891
Pb	21.012	22.034	20.923	21.602	20.983	22.490	22.933	22.042	23.315
Rb	22.047	23.643	22.977	24.449	23.235	24.166	24.313	23.982	26.094
Cs	2.9051	3.1975	2.9832	3.1905	3.0578	3.1677	3.1821	3.0992	3.3892
Sr	448.3	438.0	459.1	456.8	456.0	452.2	455.0	458.7	469.2
Sc	9.62	9.23	8.69	10.21	9.12	9.09	9.54	8.60	7.12
Zr	96.92	101.55	100.18	101.94	100.59	104.46	104.53	102.37	109.20
Mode									
gms	--	--	78	--	--	86	73	--	--
pl	--	--	21	--	--	12	16	--	--
ol	--	--	0.0	--	--	0.0	0.0	--	--
cpx	--	--	0.3	--	--	0.8	6.9	--	--
opx	--	--	0.0	--	--	1.5	2.3	--	--
am	--	--	0.3	--	--	0.0	0.3	--	--
ox	--	--	0.7	--	--	0.0	1.2	--	--

Table A5d. Whole-rock and mineral separate analyses (cont'd).

Table A5d. Cont'd.

sampleID	11KCon02B-1	09KCnye005	11KCon01B-2	09KCwes012	08cw002-1c	09KCnye199m	09KCnye003m	KC12ak34m	09KCnye001c
Map symbol	Q8p.j,bnd	Q8p.j,bnd	Q8p.j,bnd	Q8p.j,bnd	Q8p.j,bnd	Q8p.gg	Q8p.gg	Q8p.umg	Q8p.gab
Latitude	52.17271	52.18003	52.17271	52.17349	52.17477	52.16105	52.17463	52.18111	52.17568
Longitude	-175.53027	-175.49742	-175.53027	-175.53140	-175.53152	-175.51552	-175.49533	-175.51923	-175.49370
XRF									
SiO_2	54.72	55.57	56.28	56.45	58.28	49.94	51.18	49.43	40.98
TiO_2	0.660	0.636	0.594	0.612	0.568	0.832	0.601	0.833	1.157
Al_2O_3	18.47	18.96	18.79	18.60	18.09	19.11	20.96	18.16	22.62
FeOt	8.32	7.48	7.45	7.50	6.81	8.71	8.08	9.17	12.14
MnO	0.215	0.202	0.209	0.218	0.216	0.170	0.203	0.175	0.153
MgO	3.63	3.64	3.27	3.46	3.02	6.35	4.02	7.43	6.62
CaO	8.73	8.80	8.34	8.24	7.36	11.55	11.79	11.64	14.87
Na_2O	4.16	3.69	3.95	3.83	4.41	2.69	2.55	2.55	1.32
K_2O	0.900	0.832	0.922	0.877	1.034	0.523	0.491	0.512	0.102
P_2O_5	0.196	0.193	0.200	0.220	0.216	0.115	0.132	0.108	0.027
Total	97.26	98.97	97.46	99.07	99.58	99.85	98.73	100.14	99.41
H_2O^+/LOI	--	--	--	--	--	--	--	--	--
SO_3 (≥)	--	--	--	--	--	--	--	--	--
Cl (≥)	0.66	0.12	0.32	0.13	--	0.07	0.07	--	0.01
Ni	10.4	13.2	8.5	9.7	0.0	43.2	10.6	59.5	27.5
Cr	12.0	14.2	11.2	8.7	11.2	99.2	4.5	212.4	31.8
Sc	14.8	17.8	13.2	13.1	11.7	35.7	17.2	39.9	34.9
V	196.1	183.4	156.9	162.4	138.3	312.0	193.1	304.5	474.7
Ba	344.4	351.1	366.3	369.3	424.8	203.6	211.6	195.9	36.1
Rb	17.7	16.7	18.4	18.1	21.2	8.8	9.6	10.1	0.4
Sr	476.5	485.7	482.1	485.4	454.6	428.4	499.6	406.2	506.2
Zr	73.0	76.1	76.5	81.3	90.2	48.5	50.2	44.7	12.6
Y	20.9	21.1	20.9	21.3	21.0	17.5	18.0	18.2	17.5
Nb	2.2	2.2	2.2	2.8	1.1	1.6	2.1	1.7	2.4
Ga	19.1	18.1	20.2	19.4	16.2	17.7	16.6	16.7	22.3
Cu	116.5	109.3	76.9	88.4	74.0	95.5	134.2	123.8	90.2
Zn	100.2	90.0	94.7	97.1	98.2	74.1	82.0	74.5	70.5
ICP/MS									
La	7.529	7.457	7.947	8.053	9.125	4.242	4.718	4.036	0.843
Ce	16.777	16.614	17.652	17.914	20.187	10.086	11.330	9.681	3.415
Pr	2.3969	2.3821	2.4879	2.5565	2.8505	1.5256	1.7519	1.5132	0.8107
Nd	10.994	10.892	11.334	11.667	12.874	7.581	8.540	7.292	5.215
Sm	3.036	3.011	3.049	3.159	3.391	2.367	2.543	2.344	2.231
Eu	1.0334	1.0592	1.0560	1.0865	1.1161	0.8819	0.9423	0.8460	0.8413
Gd	3.261	3.352	3.287	3.447	3.629	2.877	2.892	2.835	2.910
Tb	0.5598	0.5683	0.5614	0.5909	0.6251	0.5035	0.5142	0.5044	0.5178
Dy	3.643	3.700	3.650	3.810	4.053	3.298	3.260	3.300	3.405
Ho	0.7852	0.7804	0.7854	0.8182	0.8871	0.6970	0.7054	0.7150	0.7067
Er	2.2579	2.2097	2.2805	2.3003	2.4833	1.9461	2.0014	1.9343	1.8234
Tm	0.3262	0.3372	0.3391	0.3539	0.3805	0.2847	0.2972	0.2794	0.2522
Yb	2.2184	2.1687	2.2012	2.2699	2.5120	1.7777	1.8806	1.7800	1.4644
Lu	0.3664	0.3443	0.3796	0.3698	0.4129	0.2796	0.3067	0.2772	0.2154
Ba	340.79	346.32	366.60	363.88	419.73	200.92	210.22	190.77	33.04
Th	2.1999	2.1992	2.3368	2.3660	2.7172	1.0791	1.1597	1.0080	0.0323
Nb	1.4942	1.4622	1.5868	1.5543	1.8037	0.9602	1.0604	0.9514	0.5507
Y	20.524	20.805	20.737	21.316	22.503	18.318	19.071	17.579	16.941
Hf	2.0478	2.0470	2.1525	2.2089	2.5678	1.4106	1.4776	1.3640	0.5709
Ta	0.11051	0.10711	0.11485	0.11446	0.12627	0.06928	0.10728	0.08949	0.03373
U	1.2460	1.2781	1.3310	1.3451	1.5533	0.6327	0.6795	0.5688	0.0146
Pb	14.781	18.065	18.990	17.240	18.893	9.802	11.140	9.052	1.127
Rb	17.265	16.117	18.487	17.213	20.508	8.906	9.332	8.574	0.508
Cs	2.1678	2.1293	2.3279	2.2712	2.7309	1.1528	1.3323	1.1581	0.0273
Sr	476.5	486.0	486.5	476.3	464.4	431.0	531.6	406.0	530.5
Sc	14.51	15.99	13.04	13.37	10.95	34.91	15.42	39.68	34.83
Zr	73.99	73.32	78.93	76.94	87.19	46.27	49.20	44.15	10.62
Mode									
gms	--	56	--	54	68	--	--	--	0
pl	--	32	--	29	21	--	--	--	51
ol	--	0.0	--	0.0	0.0	--	--	--	0.0
cpx	--	5.0	--	2.7	2.4	--	--	--	5.6
opx	--	3.2	--	5.6	3.0	--	--	--	0.0
am	--	1.0	--	6.3	1.6	--	--	--	36.6
ox	--	2.8	--	2.1	3.8	--	--	--	7.0

Table A5d. Whole-rock and mineral separate analyses (cont'd).

Table A5d. Cont'd.

sampleID	09KCnye012a1	09KCnye003	09KCnye012a2	09KCnye012b3	09KCnye100am	09KCnye012b1	KC12ak22	KC12ak34	KC12ak11
Map symbol	Q8p.gab	Q8p.gab	Q8p.gab	Q8p.gab	Q8p.g.am	Q8p.g.pl	Q8p.um	Q8p.um	Q8p.um
Latitude	52.17983	52.17463	52.17983	52.17983	52.16436	52.17983	52.18111	52.18111	52.17139
Longitude	-175.52556	-175.49533	-175.52556	-175.52556	-175.51952	-175.52556	-175.51923	-175.51923	-175.52795
XRF									
SiO_2	41.41	42.46	42.99	43.02	39.34	44.54	40.96	41.61	46.44
TiO_2	1.346	0.882	0.880	0.955	2.198	0.062	0.082	0.120	0.247
Al_2O_3	20.48	22.24	21.97	24.50	12.13	33.94	1.34	1.72	2.81
FeOt	12.15	12.18	10.50	6.53	19.20	1.08	13.83	13.88	9.41
MnO	0.129	0.130	0.128	0.074	0.233	0.016	0.230	0.231	0.175
MgO	8.57	5.17	6.24	7.44	13.45	0.72	40.72	38.11	27.66
CaO	13.97	15.70	16.00	15.79	10.99	18.95	2.65	4.06	12.96
Na_2O	1.70	1.08	1.16	1.47	2.11	0.65	0.16	0.22	0.27
K_2O	0.231	0.125	0.112	0.214	0.311	0.022	0.023	0.032	0.025
P_2O_5	0.019	0.032	0.022	0.012	0.023	0.010	0.009	0.009	0.006
Total	99.09	99.87	99.94	99.14	98.38	99.70	99.63	99.52	100.00
H_2O^+/LOI	--	--	--	--	--	--	-0.98	-0.87	-0.26
SO_3 (≥)	--	--	--	--	--	--	--	--	--
Cl (≥)	0.02	0.02	0.03	0.01	0.01	0.01	--	--	--
Ni	34.6	24.8	31.4	47.4	74.8	6.1	944.3	869.2	437.5
Cr	6.9	4.9	44.0	33.3	149.4	5.4	1967.0	2052.8	1943.0
Sc	47.2	26.4	34.8	51.9	83.4	5.0	17.2	20.8	64.6
V	552.0	512.0	434.4	339.1	739.3	30.4	55.7	67.7	137.2
Ba	68.9	61.8	48.0	56.8	84.3	27.8	18.0	16.0	12.1
Rb	1.9	2.4	2.0	1.1	1.3	0.0	0.1	0.0	0.4
Sr	387.0	457.1	471.1	460.3	183.8	667.0	14.8	21.5	27.3
Zr	17.3	16.5	14.9	11.4	29.9	4.6	2.4	3.4	7.1
Y	15.7	9.8	10.9	11.5	32.9	1.5	2.2	3.3	6.0
Nb	1.9	1.3	2.8	1.4	3.2	0.6	0.7	0.0	1.6
Ga	18.7	20.0	19.0	16.3	18.2	18.1	2.6	1.4	4.7
Cu	23.2	64.9	19.4	6.3	13.0	6.3	14.8	31.9	10.2
Zn	53.7	62.8	51.3	23.4	103.5	4.5	80.3	80.7	47.9
ICP/MS									
La	0.921	1.213	0.932	0.563	1.330	0.365	0.133	0.236	0.316
Ce	3.043	3.138	2.717	1.973	5.755	0.800	0.381	0.647	1.020
Pr	0.6501	0.5347	0.5308	0.4302	1.3526	0.1153	0.0717	0.1060	0.2094
Nd	4.109	2.947	3.168	2.773	9.165	0.564	0.385	0.631	1.297
Sm	1.787	1.062	1.331	1.248	4.047	0.180	0.160	0.253	0.580
Eu	0.7414	0.4934	0.5679	0.5746	1.3809	0.1895	0.0642	0.0914	0.2123
Gd	2.563	1.419	1.769	1.799	5.618	0.220	0.220	0.338	0.772
Tb	0.4624	0.2510	0.3081	0.3211	0.9840	0.0343	0.0416	0.0606	0.1435
Dy	2.912	1.641	2.054	2.051	6.278	0.217	0.258	0.394	0.884
Ho	0.6203	0.3433	0.4280	0.4279	1.3002	0.0422	0.0561	0.0810	0.1795
Er	1.6098	0.9122	1.1267	1.0922	3.4259	0.1120	0.1487	0.2084	0.4945
Tm	0.2120	0.1328	0.1548	0.1450	0.4513	0.0156	0.0220	0.0298	0.0669
Yb	1.2448	0.7891	0.9224	0.8284	2.6375	0.0895	0.1282	0.1859	0.3910
Lu	0.1845	0.1238	0.1397	0.1158	0.3857	0.0137	0.0210	0.0287	0.0554
Ba	62.71	57.68	45.27	55.11	77.17	22.24	7.20	9.05	6.88
Th	0.1061	0.2493	0.1188	0.0431	0.0663	0.0381	0.0281	0.0699	0.0624
Nb	0.4656	0.2861	0.2538	0.3124	1.1566	0.0362	0.0380	0.0671	0.0605
Y	15.393	10.444	10.996	10.698	31.874	1.524	1.308	1.891	4.382
Hf	0.6954	0.5174	0.4798	0.4948	1.2870	0.0688	0.1018	0.1326	0.2665
Ta	0.03491	0.02405	0.02040	0.02648	0.07028	0.00970	0.00210	0.00502	0.00567
U	0.0601	0.1418	0.0669	0.0224	0.0358	0.0169	0.0129	0.0193	0.0140
Pb	1.734	2.820	1.833	1.014	1.065	1.003	0.169	0.265	0.174
Rb	1.414	2.101	1.062	0.909	1.156	0.348	0.243	0.472	0.441
Cs	0.1097	0.2668	0.1209	0.0421	0.0507	0.0586	0.0164	0.0258	0.0109
Sr	399.2	470.6	472.9	458.2	186.3	690.1	15.2	20.9	28.2
Sc	47.06	25.78	34.30	55.86	84.92	4.75	17.70	21.97	65.89
Zr	15.25	14.16	11.61	10.03	27.34	1.92	2.80	3.53	6.08
Mode									
gms	7	3	4	--	--	--	--	--	--
pl	51	58	47	--	--	--	--	--	--
ol	0.0	0.0	1.9	--	--	--	--	--	--
cpx	3.0	20.5	19.3	--	--	--	--	--	--
opx	0.0	0.0	0.0	--	--	--	--	--	--
am	37.8	13.8	23.3	--	--	--	--	--	--
ox	1.2	3.9	4.8	--	--	--	--	--	--

Table A5d. Whole-rock and mineral separate analyses (cont'd).

Table A5d. Cont'd.

sampleID	KC12ak33	KC12ak13	KC12ak12	KC12ak42	KC12ak19	09KCwes009	12KCwes001	05KScn002A	10KCwes004
Map symbol	Q8p.um	Q8p.um	Q8p.um	Q8p.um	Q8p.an	Qlp	Qlp	Qlp	Qlp
Latitude	52.18111	52.17139	52.17139	52.18111	52.17139	52.16234	52.16134	52.16059	52.17082
Longitude	-175.51923	-175.52795	-175.52795	-175.51923	-175.52795	-175.50018	-175.51204	-175.50418	-175.49565
XRF									
SiO_2	47.90	48.55	49.89	51.05	44.43	52.77	53.04	53.43	54.36
TiO_2	0.172	0.515	0.438	0.263	0.045	0.762	0.749	0.714	0.714
Al_2O_3	2.13	5.95	4.70	2.97	34.43	19.15	19.17	19.25	18.58
FeOt	7.99	7.60	6.44	5.29	0.90	8.88	8.79	8.27	8.40
MnO	0.151	0.144	0.131	0.112	0.013	0.199	0.196	0.201	0.202
MgO	27.08	17.15	16.88	19.51	0.56	4.30	4.15	4.28	4.18
CaO	14.32	19.44	21.08	20.54	18.92	9.77	9.70	9.62	9.11
Na_2O	0.23	0.57	0.40	0.24	0.69	3.21	3.23	3.32	3.46
K_2O	0.015	0.063	0.027	0.010	0.026	0.780	0.798	0.716	0.825
P_2O_5	0.007	0.007	0.006	0.008	0.008	0.179	0.181	0.192	0.182
Total	99.86	100.15	99.83	99.70	99.78	99.63	100.07	99.65	99.15
H_2O^+/LOI	-0.15	0.27	0.50	0.29	--	--	--	--	--
SO_3 (≥)	--	--	--	--	--	--	--	--	--
Cl (≥)	--	--	--	--		0.06	--	--	0.06
Ni	408.2	177.8	158.2	192.9	7.0	13.7	11.1	17.3	14.0
Cr	2500.3	1114.3	1844.7	1455.2	6.6	11.2	23.4	31.1	23.4
Sc	65.3	111.2	117.0	95.9	3.4	20.5	19.6	20.6	19.5
V	107.8	268.3	240.4	152.9	17.1	246.8	238.3	214.5	215.2
Ba	11.8	19.7	13.7	12.1	21.0	355.8	357.0	319.4	359.8
Rb	0.7	1.0	0.3	0.1	1.2	16.3	16.7	15.3	17.8
Sr	26.1	59.5	41.7	34.1	616.3	512.7	510.7	491.8	479.0
Zr	4.5	10.6	9.1	5.3	1.0	70.6	70.5	69.5	73.6
Y	4.3	9.6	9.5	5.1	1.7	22.4	22.0	21.3	21.4
Nb	0.5	0.3	1.0	0.6	1.3	2.5	2.3	2.3	2.1
Ga	3.3	6.2	5.5	4.7	16.1	20.1	18.1	19.0	18.1
Cu	14.8	38.7	28.7	8.6	9.2	64.9	85.2	60.6	73.5
Zn	42.4	31.5	23.9	21.8	3.2	91.0	89.4	86.8	89.8
ICP/MS									
La	0.258	0.503	0.332	0.310	0.397	7.416	7.699	6.872	7.817
Ce	0.768	1.699	1.334	1.129	0.808	16.277	16.868	15.998	16.448
Pr	0.1497	0.3672	0.2998	0.2464	0.1131	2.3578	2.4098	2.3315	2.4154
Nd	0.869	2.381	1.988	1.477	0.527	10.787	11.138	10.900	11.002
Sm	0.381	1.034	0.943	0.656	0.149	3.109	3.143	3.136	2.971
Eu	0.1463	0.4051	0.3631	0.2385	0.1766	1.0714	1.0779	1.0512	1.0375
Gd	0.538	1.500	1.319	0.830	0.163	3.443	3.403	3.455	3.305
Tb	0.1015	0.2766	0.2487	0.1505	0.0267	0.5908	0.6095	0.5921	0.5785
Dy	0.650	1.825	1.538	0.931	0.164	3.855	3.854	3.852	3.747
Ho	0.1338	0.3737	0.3208	0.1987	0.0337	0.8217	0.8268	0.8174	0.7942
Er	0.3418	0.9857	0.8444	0.5109	0.0919	2.3242	2.3028	2.3512	2.2468
Tm	0.0487	0.1354	0.1163	0.0709	0.0123	0.3381	0.3446	0.3479	0.3360
Yb	0.2823	0.7716	0.6868	0.3998	0.0725	2.1705	2.1706	2.2236	2.1242
Lu	0.0391	0.1107	0.0949	0.0592	0.0115	0.3558	0.3444	0.3564	0.3518
Ba	6.57	14.57	7.91	5.82	22.39	346.65	349.46	313.16	357.12
Th	0.0456	0.0792	0.0245	0.0529	0.0497	2.3286	2.3948	1.7390	2.4682
Nb	0.0515	0.1101	0.0453	0.0364	0.0545	1.4038	1.4173	1.4454	1.5123
Y	3.094	8.658	7.482	4.574	0.842	20.943	20.975	21.168	20.491
Hf	0.1652	0.4694	0.4291	0.2480	0.0798	1.9537	1.9398	1.9538	2.0590
Ta	0.00316	0.00949	0.00379	0.00325	0.00341	0.09683	0.09582	0.09524	0.11931
U	0.0180	0.0184	0.0105	0.0226	0.0222	1.4382	1.4670	1.1255	1.4330
Pb	0.311	0.335	0.346	0.294	0.810	18.398	18.743	17.811	17.865
Rb	0.311	0.689	0.204	0.310	0.328	15.325	15.416	14.686	16.706
Cs	0.0197	0.0160	0.0154	0.0299	0.0293	2.4385	2.4267	2.2528	2.3584
Sr	27.0	60.9	41.4	34.8	624.1	518.5	512.8	487.3	473.7
Sc	63.95	113.01	118.99	99.36	2.38	20.05	19.23	18.16	18.71
Zr	4.46	10.22	8.84	5.90	2.68	66.79	69.41	64.59	72.44
Mode									
gms	--	--	--	--	--	47	--	--	--
pl	--	--	--	--	--	39	--	--	--
ol	--	--	--	--	--	0.3	--	--	--
cpx	--	--	--	--	--	7.6	--	--	--
opx	--	--	--	--	--	3.0	--	--	--
am	--	--	--	--	--	0.0	--	--	--
ox	--	--	--	--	--	3.0	--	--	--

Table A5d. Whole-rock and mineral separate analyses (cont'd).

Table A5d. Cont'd.

sampleID	09KCwes008	09KCnye009a	09KCnye009b	09KCwes006	09KCwes007	09KCwes022	09KCnye011a	09KCnye011b	09KCwes005
Map symbol	Qlp	Qlp	Qlp	Qlp	Qlp	Qlp	Qlp	Qlp	Qlp
Latitude	52.16365	52.16072	52.16072	52.16639	52.16365	52.17543	52.17437	52.17437	52.16907
Longitude	-175.49897	-175.50848	-175.50848	-175.49782	-175.49897	-175.52648	-175.52680	-175.52680	-175.49893
XRF									
SiO_2	54.53	55.15	55.20	56.59	57.56	58.43	58.92	59.12	59.38
TiO_2	0.678	0.676	0.671	0.606	0.587	0.575	0.559	0.553	0.525
Al_2O_3	18.96	18.82	18.55	18.76	18.57	18.06	18.07	18.04	18.20
FeOt	8.14	7.96	8.07	7.37	7.16	7.13	6.87	6.80	6.64
MnO	0.193	0.196	0.200	0.189	0.199	0.216	0.213	0.212	0.205
MgO	3.90	3.79	3.99	3.40	3.08	3.00	2.87	2.78	2.61
CaO	9.19	8.80	8.85	8.31	7.78	7.33	7.21	7.09	7.01
Na_2O	3.40	3.53	3.41	3.66	3.87	3.99	4.03	4.11	4.14
K_2O	0.812	0.886	0.876	0.915	0.967	1.036	1.038	1.075	1.078
P_2O_5	0.192	0.189	0.189	0.206	0.227	0.223	0.218	0.224	0.215
Total	100.03	99.29	99.19	98.99	99.45	99.04	99.58	98.83	99.34
H_2O^+/LOI	--	--	--	--	--	--	--	--	--
SO_3 (≥)	--	--	--	--	--	--	--	--	--
Cl (≥)	0.08	0.13	0.08	0.10	0.08	0.11	0.09	0.10	0.10
Ni	12.6	11.6	12.7	11.9	8.7	7.0	6.1	5.0	5.4
Cr	16.2	16.7	18.0	15.1	11.4	6.2	7.4	6.6	4.9
Sc	18.4	18.5	18.1	16.2	13.9	12.6	12.6	11.3	11.0
V	212.0	202.3	200.7	173.8	152.9	136.4	131.7	123.2	122.7
Ba	370.8	389.7	384.0	398.8	431.2	437.9	440.1	445.1	452.7
Rb	18.2	19.5	19.5	20.0	21.4	21.9	22.5	22.6	23.9
Sr	507.2	485.7	478.2	480.9	488.0	463.5	463.8	462.3	472.1
Zr	78.7	81.0	80.8	88.4	95.8	96.2	96.9	99.2	101.7
Y	21.6	22.0	21.6	20.9	22.1	23.9	24.0	24.4	22.8
Nb	2.9	2.7	2.3	3.1	3.3	2.4	2.7	2.6	3.1
Ga	19.3	19.3	19.5	18.5	19.3	20.0	18.2	19.9	18.7
Cu	90.8	62.1	78.4	27.0	42.4	67.5	60.8	64.1	61.7
Zn	87.9	91.0	87.4	86.8	93.8	99.4	96.3	97.1	93.0
ICP/MS									
La	7.973	8.256	8.212	8.768	9.332	9.360	9.174	9.502	9.555
Ce	17.513	17.888	17.739	19.090	20.323	20.703	20.243	20.742	21.048
Pr	2.4747	2.5299	2.5278	2.6494	2.8503	2.9277	2.8534	2.9400	2.9221
Nd	11.240	11.476	11.319	11.858	12.715	13.160	12.835	13.165	12.967
Sm	3.131	3.145	3.130	3.172	3.387	3.516	3.385	3.500	3.421
Eu	1.0520	1.0740	1.0640	1.0675	1.1214	1.1554	1.1301	1.1385	1.1293
Gd	3.409	3.401	3.444	3.391	3.632	3.781	3.629	3.681	3.633
Tb	0.5848	0.5959	0.6013	0.5877	0.6080	0.6499	0.6138	0.6280	0.6246
Dy	3.802	3.818	3.859	3.760	3.876	4.170	3.972	4.060	4.125
Ho	0.8059	0.8202	0.8167	0.8075	0.8418	0.8996	0.8696	0.8871	0.8714
Er	2.3045	2.3150	2.3406	2.2868	2.4152	2.6107	2.5088	2.5425	2.5319
Tm	0.3416	0.3529	0.3504	0.3438	0.3683	0.3929	0.3842	0.3812	0.3857
Yb	2.1859	2.2470	2.2268	2.2510	2.4131	2.5819	2.4695	2.5322	2.5510
Lu	0.3588	0.3636	0.3629	0.3670	0.4023	0.4278	0.4082	0.4203	0.4220
Ba	363.53	382.50	380.30	395.93	421.46	436.19	431.59	444.30	451.54
Th	2.3259	2.6597	2.6447	2.5735	2.6069	2.9329	2.8434	2.9517	3.0045
Nb	1.5446	1.6003	1.5465	1.7285	1.8887	1.8696	1.8270	1.9149	1.8571
Y	20.812	21.155	21.043	20.989	22.227	23.612	22.907	23.297	23.074
Hf	2.1017	2.1919	2.1846	2.3647	2.5163	2.6205	2.5799	2.6327	2.6781
Ta	0.10552	0.10994	0.10985	0.12781	0.13004	0.13303	0.12976	0.13578	0.13744
U	1.4424	1.5617	1.5444	1.5512	1.6157	1.6762	1.6239	1.7056	1.7373
Pb	18.856	18.795	19.457	21.233	22.270	20.938	20.564	21.233	21.427
Rb	17.040	18.260	17.795	19.095	20.768	21.425	21.597	22.276	22.236
Cs	2.5778	2.5264	2.5134	2.6901	3.0238	2.8730	2.8332	2.9756	2.9531
Sr	512.1	492.3	482.0	482.0	493.1	471.0	472.5	464.5	474.5
Sc	17.89	16.66	18.10	15.21	13.33	12.20	11.13	10.78	10.53
Zr	74.62	77.53	76.77	84.89	91.24	94.04	92.90	95.59	97.28
Mode									
gms	51	62	--	61	63	66	67	82	64
pl	35	28	--	24	28	28	25	14	27
ol	0.0	0.1	--	0.0	0.0	0.0	0.1	0.0	0.0
cpx	9.5	5.9	--	8.7	6.5	2.0	4.5	2.3	4.0
opx	2.6	2.2	--	2.4	0.6	2.6	1.3	0.4	1.9
am	0.2	0.0	--	0.9	0.0	1.2	0.1	1.1	1.2
ox	2.1	2.2	--	2.6	1.7	0.6	2.0	0.2	1.8

Table A5d. Whole-rock and mineral separate analyses (cont'd).

Table A5d. Cont'd.

sampleID	10KCnye004	09KCwes019	09KCwes023	10KCnye002	09KCwes024	09KCwes025	KC12nye03	KC11nye05	09KCwes003
Map symbol	Qmfm	Qtm	Qtm	Qtm	Qtm	Qtm	Qtm	Qmka	Qobm
Latitude	52.18361	52.17735	52.17843	52.18187	52.18012	52.18012	52.18170	52.17959	52.17863
Longitude	-175.50811	-175.52911	-175.52871	-175.52307	-175.52525	-175.52525	-175.52376	-175.52595	-175.49761
XRF									
SiO_2	54.87	53.75	53.89	53.96	55.48	55.63	55.69	59.37	56.64
TiO_2	0.681	0.736	0.731	0.717	0.645	0.662	0.651	0.541	0.588
Al_2O_3	18.84	18.95	18.83	19.00	18.77	18.75	18.74	18.17	18.58
FeOt	7.86	8.52	8.52	8.17	8.16	7.74	7.72	6.24	6.99
MnO	0.193	0.201	0.204	0.193	0.217	0.190	0.195	0.195	0.193
MgO	3.87	4.05	4.00	4.16	3.58	3.72	3.66	2.88	3.67
CaO	9.07	9.17	9.11	9.40	8.63	8.76	8.77	7.42	8.57
Na_2O	3.63	3.49	3.55	3.44	3.50	3.50	3.56	3.97	3.61
K_2O	0.813	0.926	0.963	0.779	0.836	0.837	0.846	1.021	0.974
P_2O_5	0.179	0.200	0.203	0.169	0.181	0.195	0.182	0.189	0.190
Total	99.54	99.40	99.91	99.74	99.22	100.00	99.74	99.79	100.02
H_2O^+/LOI	--	--	--	--	--	--	--	--	--
SO_3 (≥)	--	--	--	--	--	--	--	--	--
Cl (≥)	0.11	0.05	0.02	0.05	0.04	0.02	--	--	0.02
Ni	10.8	12.7	12.0	13.2	7.5	11.0	9.3	5.5	14.7
Cr	9.9	12.1	16.4	7.9	3.6	8.4	6.8	6.4	33.0
Sc	18.5	19.3	19.9	21.6	13.8	19.3	17.5	12.1	17.4
V	207.2	242.1	240.5	191.1	112.2	201.9	192.6	149.1	185.7
Ba	309.7	327.6	332.4	296.9	313.2	326.9	320.5	385.0	359.3
Rb	16.8	19.3	19.1	16.9	21.0	17.3	18.2	20.8	18.6
Sr	445.5	443.7	444.8	444.5	453.5	453.3	443.6	431.0	481.6
Zr	76.6	76.7	77.6	70.9	83.3	81.3	80.1	91.7	81.8
Y	20.1	21.7	22.0	20.8	22.0	21.3	20.5	20.9	20.0
Nb	2.7	2.1	3.2	2.3	3.1	2.8	2.6	3.1	3.0
Ga	19.4	18.5	19.6	19.4	18.3	18.5	18.0	17.6	18.7
Cu	82.4	52.4	78.0	91.8	76.4	46.5	50.3	39.4	63.5
Zn	84.5	90.1	87.2	83.5	94.2	84.4	85.0	84.1	81.2
ICP/MS									
La	7.075	6.884	7.210	6.640	7.039	7.240	7.267	8.515	8.173
Ce	15.636	16.173	16.811	14.834	16.639	16.430	16.631	19.072	18.098
Pr	2.3302	2.3862	2.4648	2.2542	2.4493	2.3679	2.3997	2.6508	2.5621
Nd	10.704	10.927	11.539	10.398	11.324	10.994	11.020	11.922	11.514
Sm	2.978	3.146	3.227	2.890	3.223	2.996	3.055	3.109	3.124
Eu	1.0264	1.0548	1.1113	1.0074	1.0962	1.0266	1.0435	1.0431	1.0579
Gd	3.210	3.418	3.512	3.290	3.520	3.297	3.256	3.270	3.267
Tb	0.5536	0.5893	0.6073	0.5567	0.6126	0.5680	0.5633	0.5579	0.5586
Dy	3.543	3.786	3.936	3.620	3.969	3.647	3.572	3.536	3.537
Ho	0.7572	0.8140	0.8303	0.7709	0.8460	0.7726	0.7722	0.7764	0.7676
Er	2.1378	2.2660	2.3622	2.1620	2.4076	2.1854	2.1726	2.2311	2.1791
Tm	0.3195	0.3415	0.3495	0.3263	0.3586	0.3292	0.3330	0.3328	0.3273
Yb	2.0480	2.1928	2.2797	2.0642	2.3468	2.1606	2.0948	2.2295	2.1046
Lu	0.3319	0.3484	0.3601	0.3289	0.3830	0.3560	0.3461	0.3697	0.3501
Ba	308.79	318.45	324.73	290.02	306.33	317.88	318.20	384.68	352.68
Th	1.7402	1.7523	1.7761	1.6224	1.6975	1.7816	1.7988	2.3133	2.5237
Nb	1.6740	1.7159	1.7551	1.5832	1.6924	1.6365	1.6214	1.8241	1.7150
Y	19.781	20.517	21.463	19.798	21.908	20.196	19.871	20.067	20.195
Hf	2.0950	2.0624	2.0945	1.9982	2.2740	2.1596	2.1642	2.5056	2.1852
Ta	0.11954	0.11361	0.12104	0.11357	0.12044	0.11116	0.11089	0.13816	0.12965
U	0.8814	0.8417	0.8525	0.8227	0.8147	0.9137	0.9135	1.1706	1.3253
Pb	8.076	6.443	8.121	8.662	7.454	10.585	10.093	9.913	12.720
Rb	16.383	18.312	18.122	15.294	20.019	16.077	17.012	20.670	17.553
Cs	1.0266	1.4428	0.5018	1.2204	2.1324	0.6317	1.6700	1.6002	0.9508
Sr	438.1	443.3	445.9	431.5	457.2	449.0	441.3	435.4	483.2
Sc	18.34	19.34	18.18	20.32	12.85	17.38	16.41	12.02	15.16
Zr	75.00	72.73	74.76	69.84	79.48	76.84	77.75	91.53	78.89
Mode									
gms	59	63	55	--	21	45	--	56	55
pl	28	26	34	--	54	41	--	35	34
ol	0.1	2.1	2.8	--	0.0	0.7	--	0.0	0.0
cpx	5.0	5.1	5.4	--	14.4	7.5	--	3.2	6.2
opx	1.9	0.3	0.0	--	3.1	1.6	--	1.2	2.1
am	3.9	0.0	0.0	--	1.7	0.5	--	3.3	1.3
ox	2.1	3.7	3.2	--	6.0	3.6	--	1.9	1.3

Table A5d. Whole-rock and mineral separate analyses (cont'd).

Table A5d. Cont'd.

sampleID	09KCnye108	09KCnye107	09KCnye002	09KCnye004	09KCnye006	10KCnye001	12KCaek001	KC12nye01	KC12nye02
Map symbol	Qobm	Qobg	Qrm	Qrm	Qrb	Qrb	Qwa	Qwa	Qwa
Latitude	52.17866	52.17866	52.17523	52.17387	52.17337	52.17191	52.17975	52.18182	52.18350
Longitude	-175.49797	-175.49797	-175.49533	-175.49500	-175.49237	-175.49239	-175.51788	-175.51815	-175.51811
XRF									
SiO_2	56.83	45.62	56.53	56.57	50.89	51.34	56.04	56.26	56.30
TiO_2	0.573	1.504	0.565	0.568	0.809	0.821	0.602	0.590	0.577
Al_2O_3	18.62	13.54	18.80	18.67	19.21	19.16	18.57	18.81	18.77
FeOt	7.01	10.89	6.91	6.87	8.75	9.01	7.39	7.14	7.20
MnO	0.192	0.193	0.175	0.179	0.184	0.185	0.183	0.181	0.175
MgO	3.48	12.50	3.62	3.72	5.36	4.85	3.78	3.59	3.60
CaO	8.53	13.48	8.40	8.46	10.72	10.41	8.57	8.49	8.42
Na_2O	3.56	1.90	3.64	3.62	3.06	3.14	3.57	3.63	3.63
K_2O	1.013	0.341	1.134	1.130	0.853	0.902	1.090	1.111	1.115
P_2O_5	0.193	0.032	0.219	0.213	0.163	0.181	0.203	0.204	0.209
Total	99.59	98.88	100.06	99.30	100.48	100.08	100.22	99.60	99.18
H_2O^+/LOI	--	--	--	--	--	--	--	--	--
SO_3 (≥)	--	--	--	--	--	--	--	--	--
Cl (≥)	0.01	0.02	0.06	0.05	0.04	0.01	--	--	--
Ni	13.5	108.1	16.1	16.9	31.7	20.7	15.9	14.3	15.6
Cr	26.4	328.2	33.2	30.5	65.9	33.9	28.1	21.6	29.0
Sc	14.7	78.1	16.1	15.5	28.1	24.8	16.5	16.2	15.3
V	175.2	509.3	179.5	179.6	301.6	295.2	190.0	180.4	178.7
Ba	360.7	98.2	405.7	394.3	297.8	313.5	387.9	396.4	395.5
Rb	18.7	2.2	21.8	21.2	16.9	18.6	22.5	22.2	21.4
Sr	483.4	276.5	495.2	487.8	440.6	447.1	476.0	484.1	484.6
Zr	82.9	30.7	90.1	89.4	62.2	64.2	89.4	87.0	87.2
Y	21.3	26.7	19.6	19.1	19.0	21.4	20.6	19.9	18.9
Nb	2.5	2.6	2.8	3.0	2.4	2.2	2.5	2.3	2.7
Ga	18.6	15.0	19.3	18.3	18.3	19.4	18.1	17.1	17.6
Cu	37.7	176.7	38.5	53.0	110.7	47.6	46.4	33.1	45.9
Zn	81.5	64.9	82.5	82.7	76.5	75.1	83.8	81.1	76.8
ICP/MS									
La	7.988	2.071	9.787	9.585	5.848	6.464	9.099	9.363	9.590
Ce	17.536	7.076	20.765	20.322	14.033	14.690	19.281	19.901	20.285
Pr	2.4914	1.4453	2.8096	2.7495	2.0802	2.2697	2.6522	2.7602	2.7452
Nd	11.172	8.791	12.074	11.870	9.838	10.585	11.669	11.874	11.851
Sm	2.939	3.375	2.971	2.923	2.875	3.027	2.987	2.986	2.961
Eu	1.0217	1.1693	0.9946	0.9753	1.0121	1.0275	1.0023	1.0541	0.9971
Gd	3.161	4.427	3.039	3.022	3.193	3.326	3.090	3.227	3.033
Tb	0.5414	0.7748	0.5111	0.5185	0.5412	0.5801	0.5398	0.5631	0.5151
Dy	3.482	4.945	3.315	3.338	3.542	3.639	3.369	3.463	3.280
Ho	0.7466	1.0259	0.6999	0.7025	0.7386	0.7779	0.7200	0.7500	0.7030
Er	2.1125	2.7429	2.0071	2.0103	2.0645	2.1526	2.0913	2.1466	2.0073
Tm	0.3161	0.3720	0.3092	0.3028	0.3106	0.3140	0.3162	0.3182	0.3051
Yb	2.0681	2.2034	1.9714	1.9594	1.8902	2.0002	2.0042	2.0404	1.9550
Lu	0.3360	0.3328	0.3261	0.3133	0.2990	0.3137	0.3274	0.3360	0.3194
Ba	343.41	90.87	402.21	385.06	288.13	306.67	377.09	388.97	392.36
Th	2.4515	0.2846	3.2539	3.1655	1.5776	1.7395	2.9284	3.0714	3.1324
Nb	1.7333	0.9929	1.9470	1.8817	1.4618	1.6231	1.8261	1.8922	1.9105
Y	19.294	25.169	18.765	18.369	18.774	19.755	19.163	19.641	18.509
Hf	2.1355	1.2103	2.3633	2.3027	1.7502	1.8527	2.2042	2.3052	2.2955
Ta	0.12203	0.06095	0.14192	0.13623	0.09981	0.10610	0.12179	0.12845	0.13093
U	1.3241	0.1853	1.7174	1.6566	0.7409	0.8133	1.5467	1.6268	1.6668
Pb	10.493	17.232	14.562	13.838	5.382	5.685	15.176	14.964	11.404
Rb	16.942	2.442	21.398	20.810	15.834	17.202	19.823	20.469	20.074
Cs	0.7138	0.1881	2.1628	2.0867	0.3600	0.3941	2.0200	1.7956	0.8176
Sr	470.2	274.1	498.8	478.7	439.8	435.1	471.4	481.3	490.8
Sc	14.71	79.76	15.53	16.19	26.83	24.62	17.12	16.08	15.71
Zr	77.59	28.49	87.71	85.11	59.28	63.55	81.37	83.64	85.42
Mode									
gms	56	9	49	53	36	45	--	--	--
pl	30	12	37	33	46	42	--	--	--
ol	0.0	1.1	0.1	0.0	4.1	2.2	--	--	--
cpx	8.3	25.1	10.3	7.6	11.0	8.3	--	--	--
opx	2.3	0.0	1.6	3.5	0.0	0.0	--	--	--
am	1.9	51.3	0.1	0.6	0.0	0.0	--	--	--
ox	1.7	1.6	2.8	1.5	2.4	2.3	--	--	--

Table A5d. Whole-rock and mineral separate analyses (cont'd).

Table A5d. Cont'd.

sampleID	09KCnye010	12KCwes004	12KCwes005	09KCnye110	10KCnye005	10KCnye006	09KCnye109	09KCwes001	09KCnye007
Map symbol	Qwa	Qwa	Qwa	Qwa	Qgmb	Qgmb	Qgmb	Qgmb	Qpl
Latitude	52.17050	52.18254	52.18118	52.18468	52.18238	52.18198	52.18088	52.17988	52.16898
Longitude	-175.52315	-175.51719	-175.51780	-175.51384	-175.50211	-175.50101	-175.49828	-175.49895	-175.52399
XRF									
SiO_2	57.08	57.88	58.27	58.30	49.33	49.39	49.43	49.49	55.57
TiO_2	0.563	0.568	0.551	0.546	0.678	0.685	0.718	0.704	0.655
Al_2O_3	18.67	18.40	18.48	18.53	15.80	15.65	16.36	16.25	18.70
FeOt	6.88	6.77	6.43	6.46	8.76	8.87	8.93	8.99	7.69
MnO	0.194	0.193	0.192	0.187	0.169	0.170	0.174	0.167	0.178
MgO	3.38	3.21	3.09	3.09	9.83	9.61	8.85	8.59	3.73
CaO	8.22	7.92	7.84	7.77	12.28	12.45	12.37	12.64	8.75
Na_2O	3.69	3.76	3.83	3.81	2.24	2.25	2.24	2.24	3.48
K_2O	1.103	1.097	1.110	1.098	0.794	0.789	0.806	0.800	1.073
P_2O_5	0.217	0.203	0.203	0.205	0.128	0.128	0.133	0.132	0.168
Total	99.46	99.51	99.43	99.94	100.02	99.69	100.29	100.37	98.54
H_2O^+/LOI	--	--	--	--	--	--	--	--	--
SO_3 (≥)	--	--	--	--	--	--	--	--	--
Cl (≥)	0.04	--	--	0.02	0.04	0.06	0.01	0.02	0.02
Ni	14.0	9.9	8.3	11.1	116.4	105.1	87.6	69.5	15.8
Cr	23.1	16.3	15.0	19.9	391.0	373.0	300.0	293.2	17.6
Sc	15.0	15.1	12.7	14.6	41.4	43.2	43.7	45.1	21.3
V	165.1	154.9	147.0	154.8	271.4	277.3	293.8	297.3	207.9
Ba	404.8	397.6	398.3	406.4	228.0	223.7	241.3	223.5	368.1
Rb	22.0	20.5	20.8	19.6	11.5	11.8	11.5	10.9	23.4
Sr	498.9	473.9	472.3	474.0	493.4	485.7	507.9	501.3	418.4
Zr	87.4	87.3	88.9	90.9	41.9	41.4	45.2	44.9	85.9
Y	20.7	21.8	20.4	22.0	14.4	15.2	14.4	16.2	18.8
Nb	2.5	2.2	3.1	2.6	1.2	1.9	2.3	2.2	2.9
Ga	18.8	18.7	16.9	18.1	16.8	15.8	16.5	16.3	18.4
Cu	33.5	35.1	48.8	19.2	127.5	98.6	147.3	108.7	74.1
Zn	87.4	81.7	81.3	82.0	68.3	68.7	70.9	64.8	80.6
ICP/MS									
La	9.427	9.179	9.100	9.158	5.346	5.208	5.312	5.106	7.883
Ce	20.110	20.053	20.064	19.779	11.678	11.409	12.042	11.604	17.296
Pr	2.7895	2.8403	2.7842	2.7436	1.7823	1.7556	1.7641	1.7656	2.4424
Nd	12.136	12.512	12.217	12.233	8.384	8.297	8.507	8.390	10.764
Sm	3.043	3.255	3.203	3.143	2.370	2.419	2.463	2.417	2.843
Eu	1.0352	1.0723	1.0655	1.0542	0.8085	0.8142	0.8493	0.8280	0.9329
Gd	3.174	3.385	3.369	3.321	2.529	2.582	2.649	2.605	3.031
Tb	0.5480	0.5938	0.5807	0.5725	0.4253	0.4359	0.4529	0.4361	0.5165
Dy	3.504	3.770	3.661	3.656	2.651	2.733	2.794	2.757	3.271
Ho	0.7523	0.8183	0.7881	0.7877	0.5566	0.5678	0.5828	0.5846	0.7069
Er	2.1419	2.2994	2.2446	2.2536	1.5579	1.5686	1.5922	1.5758	2.0121
Tm	0.3233	0.3489	0.3403	0.3356	0.2220	0.2191	0.2299	0.2291	0.2986
Yb	2.0844	2.2556	2.1857	2.2045	1.3807	1.3531	1.4279	1.4024	1.9535
Lu	0.3345	0.3794	0.3578	0.3707	0.2095	0.2140	0.2251	0.2168	0.3208
Ba	398.81	393.79	399.11	394.80	224.51	223.61	234.06	216.94	356.03
Th	3.0663	2.9399	2.9922	2.9381	1.7030	1.6537	1.7737	1.5341	2.0817
Nb	1.9036	1.9106	1.9096	1.9114	1.0203	1.0287	1.0935	1.0039	1.6131
Y	19.483	21.003	20.330	20.377	13.864	14.111	14.487	14.511	18.263
Hf	2.3001	2.3982	2.4271	2.3953	1.2767	1.2854	1.3522	1.2862	2.1876
Ta	0.13585	0.13643	0.13416	0.13326	0.07408	0.07650	0.07371	0.07001	0.11478
U	1.6198	1.5298	1.5380	1.5224	0.8955	0.8716	0.9608	0.8204	0.9047
Pb	13.922	11.096	12.424	12.174	7.152	7.313	7.189	6.157	7.802
Rb	20.973	19.986	20.266	19.511	10.693	10.877	10.365	10.518	22.177
Cs	2.1380	0.8507	1.4511	0.8551	0.5770	0.7742	0.3614	0.6452	0.8233
Sr	500.6	483.5	480.8	484.3	479.0	473.9	515.4	498.7	421.4
Sc	14.55	13.88	13.26	13.29	40.72	42.13	44.09	41.69	21.18
Zr	84.85	87.66	88.17	86.82	41.54	41.74	42.82	41.83	79.15
Mode									
gms	43	--	--	53	51	53	50	51	49
pl	42	--	--	35	23	23	28	22	30
ol	0.1	--	--	0.1	9.0	7.9	6.5	7.0	0.1
cpx	6.8	--	--	6.9	16.4	16.5	14.6	20.2	1.7
opx	2.9	--	--	3.7	0.0	0.0	0.0	0.0	0.0
am	1.5	--	--	0.0	0.0	0.0	0.0	0.0	18.3
ox	3.7	--	--	1.7	0.5	0.2	0.2	0.1	1.0

Table A5d. Whole-rock and mineral separate analyses (cont'd).

Table A5d. Cont'd.

sampleID	05KScn001	09KCwes011	09KCwes030	09KCnye106	09KCnye104	09KCwes031	10KCnye003b	09KCwes018	10KCnye003
Map symbol	Qpl	Qpg	Qpg	Qpg	Qpg	Qpg	Qpg	Qpg.Shag rock	08l
Latitude	52.16906	52.16121	52.16129	52.16121	52.16536	52.16106	52.16229	52.16242	52.18199
Longitude	-175.52442	-175.51354	-175.51522	-175.51354	-175.52060	-175.51361	-175.51830	-175.52339	-175.52208
XRF									
SiO_2	57.04	51.97	52.48	55.07	55.15	55.93	59.30	50.87	49.16
TiO_2	0.573	0.909	0.629	0.513	0.608	0.665	0.508	0.890	0.698
Al_2O_3	18.68	20.83	19.66	21.53	18.96	17.85	18.38	19.10	16.48
FeOt	6.87	7.97	8.32	6.35	7.30	7.28	6.21	9.82	8.76
MnO	0.193	0.171	0.158	0.120	0.174	0.156	0.186	0.198	0.204
MgO	3.41	3.21	5.68	2.66	4.14	5.06	2.68	4.54	8.85
CaO	8.18	10.26	10.10	9.54	9.18	8.26	7.18	10.68	13.28
Na_2O	3.68	3.48	2.54	3.28	3.32	3.52	4.02	3.07	2.06
K_2O	1.158	1.021	0.298	0.767	0.980	1.061	1.296	0.684	0.375
P_2O_5	0.215	0.188	0.129	0.176	0.186	0.217	0.239	0.140	0.137
Total	98.74	95.90	94.90	96.27	98.54	97.58	100.25	98.34	95.39
H_2O^+/LOI	--	--	--	--	--	--	--	--	--
SO_3 (≥)	--	--	--	--	--	--	--	--	--
Cl (≥) --		0.01	0.00	0.07	0.01	0.04	0.00	0.02	0.04
Ni	15.2	11.9	29.6	9.6	19.3	36.8	10.0	18.3	123.9
Cr	21.0	7.8	50.6	15.5	39.4	99.7	10.9	28.0	415.5
Sc	15.4	19.6	23.1	13.9	19.5	21.5	11.7	33.5	38.3
V	162.1	242.1	205.3	162.8	202.7	279.7	125.2	324.0	262.8
Ba	389.4	286.2	185.9	264.8	348.1	409.0	457.2	238.3	258.0
Rb	24.1	16.6	6.1	15.0	19.2	19.8	25.2	10.6	6.3
Sr	484.3	470.2	399.9	441.0	482.5	456.4	493.7	438.2	540.4
Zr	85.0	75.0	62.3	76.7	78.2	91.9	99.5	62.3	42.4
Y	19.4	22.0	14.5	18.2	18.2	20.2	21.7	20.1	14.1
Nb	2.5	2.6	2.4	2.5	2.4	3.1	2.5	1.9	1.9
Ga	18.1	19.1	17.4	17.9	17.4	17.3	17.7	17.9	14.4
Cu	42.6	150.4	133.6	19.6	61.4	91.8	32.8	142.0	127.2
Zn	82.4	83.7	81.6	70.7	76.4	79.4	87.2	85.0	69.9
ICP/MS									
La	9.139	7.928	5.051	6.573	8.343	9.545	10.956	5.626	5.873
Ce	19.839	18.571	11.885	14.923	17.646	20.620	22.458	13.515	12.448
Pr	2.7225	2.7949	1.7354	2.1411	2.4300	2.8761	3.1608	2.0586	1.8762
Nd	11.987	13.197	7.895	9.641	10.663	12.606	13.530	9.865	8.742
Sm	3.055	3.668	2.259	2.596	2.710	3.263	3.296	3.005	2.390
Eu	1.0224	1.2315	0.8300	0.9335	0.9236	1.0225	1.0873	1.0279	0.8169
Gd	3.125	3.953	2.521	2.895	2.842	3.376	3.403	3.429	2.546
Tb	0.5352	0.6757	0.4317	0.4947	0.4866	0.5688	0.5709	0.5846	0.4240
Dy	3.446	4.249	2.827	3.240	3.151	3.577	3.609	3.776	2.710
Ho	0.7244	0.8998	0.6034	0.6887	0.6748	0.7641	0.7744	0.8066	0.5606
Er	2.1129	2.4651	1.7134	1.9525	1.9005	2.1684	2.2532	2.2310	1.5573
Tm	0.3181	0.3593	0.2541	0.2961	0.2858	0.3184	0.3395	0.3287	0.2234
Yb	2.0577	2.2298	1.6335	1.9356	1.8505	2.0797	2.2525	2.0400	1.3690
Lu	0.3439	0.3513	0.2603	0.3089	0.2974	0.3351	0.3684	0.3124	0.2144
Ba	384.16	288.48	180.90	267.75	345.18	404.96	459.95	234.54	261.19
Th	2.9517	1.6201	1.2601	1.5525	2.7213	2.5802	3.7413	1.1814	2.0334
Nb	1.8663	1.5667	1.1629	1.5257	1.6618	1.9167	2.1882	1.1858	1.1105
Y	19.024	22.634	15.214	17.890	17.394	19.691	20.354	20.276	14.012
Hf	2.2528	2.1601	1.7263	2.0288	2.0803	2.3820	2.6754	1.8239	1.3087
Ta	0.13194	0.10563	0.09116	0.11100	0.11605	0.13239	0.15704	0.08204	0.07109
U	1.5053	0.7212	0.4552	0.8307	1.4146	1.0846	1.9525	0.5606	1.1162
Pb	13.135	5.793	8.954	10.432	8.993	13.479	18.862	6.849	9.247
Rb	22.561	15.464	5.128	14.547	17.328	18.271	23.087	9.801	6.043
Cs	2.1392	0.1487	0.5722	1.3821	0.6571	1.7338	0.7997	0.5488	1.7088
Sr	481.3	484.0	408.9	449.2	488.1	457.3	474.7	449.7	538.7
Sc	15.44	19.43	23.30	13.13	18.95	20.49	11.32	31.95	38.64
Zr	79.41	73.09	60.76	74.72	75.34	87.48	98.04	60.36	43.25
Mode									
gms	--	61	57	67	47	37	62	59	53
pl	--	34	30	30	40	42	28	33	25
ol	--	0.1	0.1	0.0	0.0	3.2	0.0	3.4	11.1
cpx	--	3.1	10.6	1.8	7.9	11.0	6.2	3.3	11.1
opx	--	0.0	0.0	1.0	3.6	4.1	1.5	0.0	0.0
am	--	0.0	0.1	0.0	0.0	0.0	0.1	0.0	0.0
ox	--	2.0	1.9	0.5	1.8	2.6	2.0	1.2	0.1

Table A5d. Whole-rock and mineral separate analyses (cont'd).

Table A5d. Cont'd.		
sampleID	09KCwes017	09KCwes015
Map symbol	08l	08l
Latitude	52.17253	52.17338
Longitude	-175.53177	-175.53146
XRF		
SiO_2	53.26	56.74
TiO_2	0.698	0.602
Al_2O_3	19.29	18.76
FeOt	8.07	7.38
MnO	0.247	0.212
MgO	4.19	3.26
CaO	10.11	8.19
Na_2O	3.28	3.76
K_2O	0.679	0.879
P_2O_5	0.170	0.219
Total	99.33	99.24
H_2O^+/LOI	--	--
SO_3 (≥)	--	--
Cl (≥)	0.08	0.07
Ni	17.7	8.0
Cr	22.7	9.0
Sc	22.0	14.0
V	233.3	157.8
Ba	272.4	372.7
Rb	14.6	19.0
Sr	460.8	492.1
Zr	66.6	81.7
Y	19.5	22.0
Nb	3.0	2.4
Ga	20.9	19.4
Cu	95.6	41.2
Zn	83.2	95.2
ICP/MS		
La	6.149	8.137
Ce	14.174	18.253
Pr	2.0819	2.6166
Nd	9.672	11.925
Sm	2.712	3.170
Eu	0.9932	1.1110
Gd	3.040	3.444
Tb	0.5291	0.5974
Dy	3.399	3.848
Ho	0.7241	0.8159
Er	1.9762	2.3222
Tm	0.2984	0.3518
Yb	1.9148	2.2715
Lu	0.3048	0.3791
Ba	262.56	372.21
Th	1.4713	2.3818
Nb	1.4053	1.5893
Y	18.751	21.544
Hf	1.8502	2.2186
Ta	0.09955	0.11308
U	0.7488	1.3831
Pb	7.188	18.084
Rb	12.920	17.632
Cs	1.3379	2.3105
Sr	457.9	492.2
Sc	20.47	13.48
Zr	64.27	79.49
Mode		
gms	56	50
pl	31	32
ol	0.0	0.2
cpx	3.5	6.6
opx	1.4	5.1
am	3.7	2.6
ox	3.9	3.3

[1]Subdivisions of Q8p samples are Q8p.j,a, andesite scoria; Q8p.j,ba, basaltic andesite scoria; Q8p.j,bnd, banded scoria; Q8p.gg, gabbro groundmass; Q8p.umg, ultramafic inclusion rind; Q8p.gab, gabbro; Q8p.g.am, amphibole from gabbro; Q8p.g.pl, plagioclase from gabbro; Q8p.um, ultramafic inclusion; Q8p.an, anorthosite inclusion.
[2]Datum is WGS84, longitude values are degrees east.
[3]Major oxides are normalized to 100%; total is original analytical total; SO3 and Cl are minimum values, and not normalized. Oxides in weight percent, trace elements in parts per million.
[4]Data in parts per million. The number of decimal places is set so the lowest concentration value for each element is reported with sufficient precision. Values which exceed the lowest value by a factor of ten or more are reported with excess precision. See Appendix 5C for precision values.
[5]Summary of modes. Detailed information is in Appendix 6.

APPENDIX 6. MODAL DATA

APPENDIX 6A. METHODS AND DISCUSSION

Modal data was obtained by identifying 1,000 random points in one thin section from each sample using transmitted light microscopy with a standard automated point-counting carriage attached to the microscope stage. Errors on the modes have not been determined. In addition to normal point counting statistics (e.g. Neilson and Brockman, 1977) there is unknown error in the highly inflated scoria samples derived from the observed facts that some points were on surfaces or edges less than 30 microns thick.

APPENDIX 6B. MODE SUMMARY BY UNIT

Table A6.1. Average modal data by unit based on petrographic determination of 1,000 points per thin section. Detailed modal analyses are in Electronic Supplement Table_A6c_modes.xlsx or Table_A6c_modes.csv.

Unit[1]	n[2]	SiO_2 (avg)[3]	Groundmass		Volume percent, normalized void-free[4]					
			Min	Max	Pl	Ol	Cpx	Opx	Ox	Am
Q8p.j,ba	5	53.3	47	70	28.1	0.2	6.2	2.6	2.6	3.7
Q8p.j,a	5	60.0	70	86	18.1	0.0	2.2	1.6	0.7	1.1
Q8p.j,bnd	3	56.3	54	68	27.3	0.0	3.4	3.9	2.9	3.0
Q8p.na	5		48	70	27.5	0.0	4.2	2.8	1.6	2.1
Q8p.gab	4	42.2	0	7	51.8	0.5	9.3	2.8	4.2	27.9
Qlp	9	56.0	47	82	27.6	0.1	5.7	1.9	1.8	0.5
Qmfm	1	54.9	59	59	28.1	0.1	5.0	1.9	2.1	3.9
Qtm	4	54.7	21	63	38.7	1.4	8.1	1.3	4.2	0.6
Qmka	1	59.4	56	56	34.8	0.0	3.2	1.2	1.9	3.3
Qobm	2	56.7	55	56	31.9	0.0	7.3	2.2	1.5	1.6
Qobg	1	45.6	9	9	11.7	1.1	21.9	3.2	1.6	51.3
Qrm	2	56.6	49	53	34.9	0.1	9.0	2.5	2.2	0.3
Qrb	2	51.1	36	45	44.2	3.1	9.6	0.0	2.3	0.0
Qwa	2	57.2	43	53	38.2	0.1	6.8	3.3	2.7	0.8
Qgmb	4	49.4	50	53	23.9	7.6	16.9	0.0	0.3	0.0
Qpl	1	56.3	49	49	29.6	0.1	1.7	0.0	1.0	18.3
Qpg	6	55.0	37	67	34.2	0.6	6.8	1.7	1.8	0.0
Qpg.Shag Rk	1	50.9	59	59	33.0	3.4	3.3	0.0	1.2	0.0
08l	3	53.1	50	56	29.4	3.8	7.0	2.2	2.4	2.1
total	61									

[1]Subdivisions of Q8p samples are Q8p.j,a, andesite scoria; Q8p.j,ba, basaltic andesite scoria; Q8p.j,bnd, banded scoria; Q8p.na, unanalyzed scoria; and Q8p.gab, gabbro.
[2]Number of thin sections analyzed.
[3]Average silica content for each unit.
[4]Mineral abbreviations are Pl, plagioclase; Ol, olivine, Cpx, clinopyroxene; Opx, orthopyroxene; Ox, opaque oxides; Am, amphibole.

APPENDIX 7. PHOTOMICROGRAPHS

Figures A7.1–8 are plane-polarized transmitted light photomicrographs of samples grouped by map unit. Whole-rock SiO_2 concentrations (wt. %) are in black text with yellow borders. SiO_2 concentrations are not given for gabbroic samples because meaningful values at thin section scale do not exist. Images are about seven times actual size and about 2,800 pixels per inch of thin section. All samples were impregnated with blue epoxy prior to cutting the thin sections. Tiff versions of each figure are in the electronic supplement.

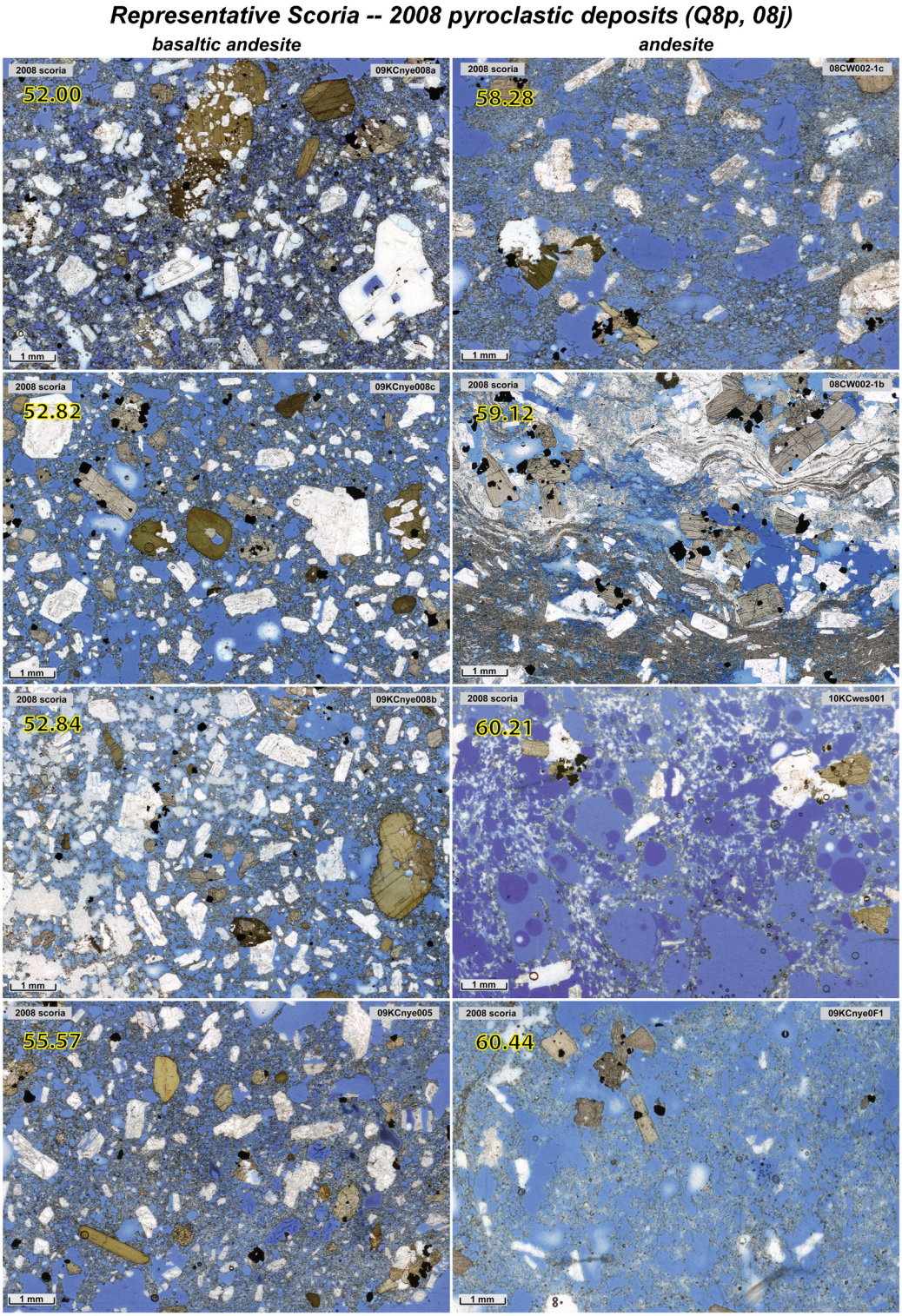

Figure A7.1. Plane-polarized photomicrographs of representative samples of 2008 scoria (Q8p).

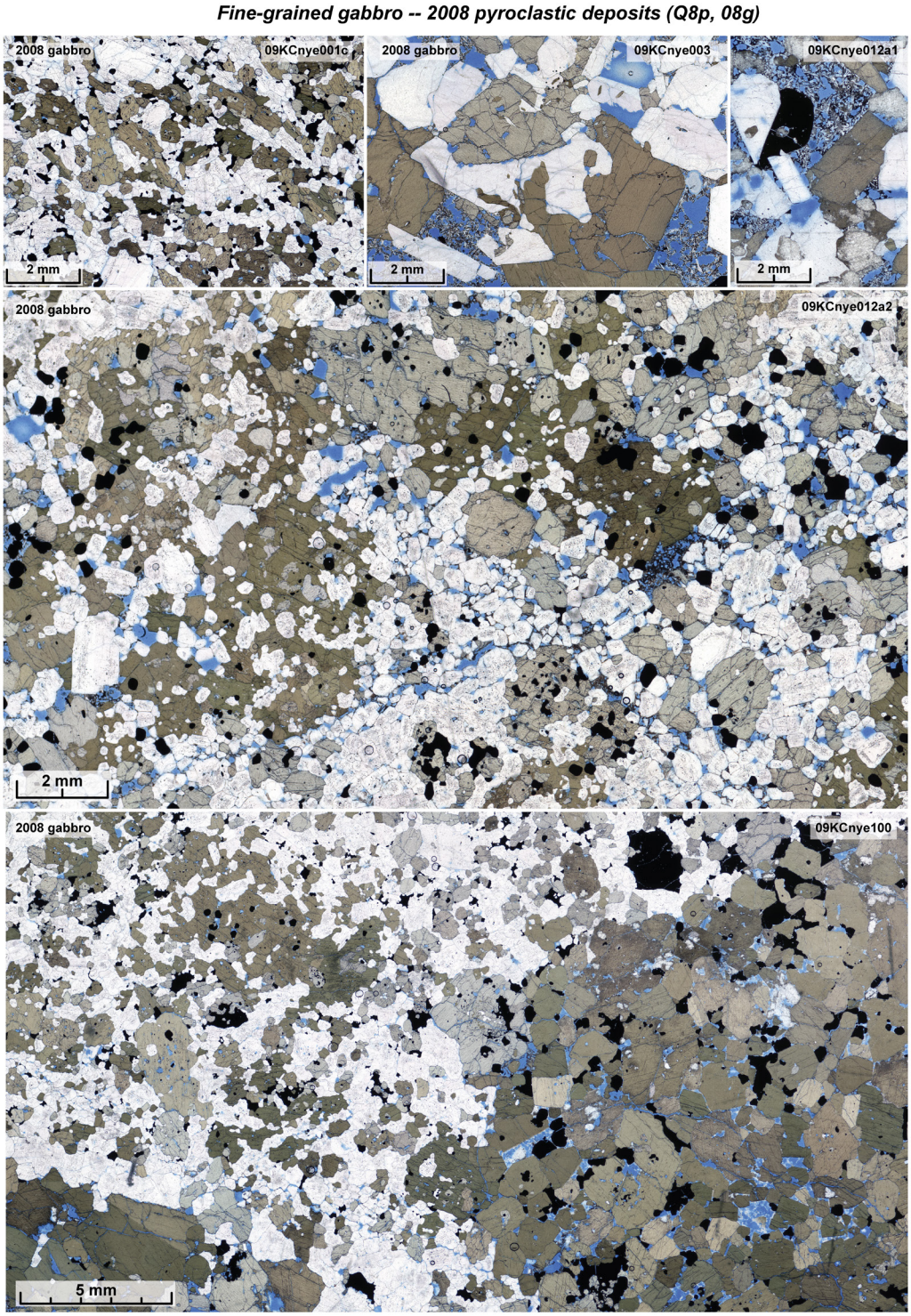

Figure A7.2. Plane-polarized photomicrographs of representative samples of amphibole gabbro inclusions in 2008 pyroclastic deposits (08g) .

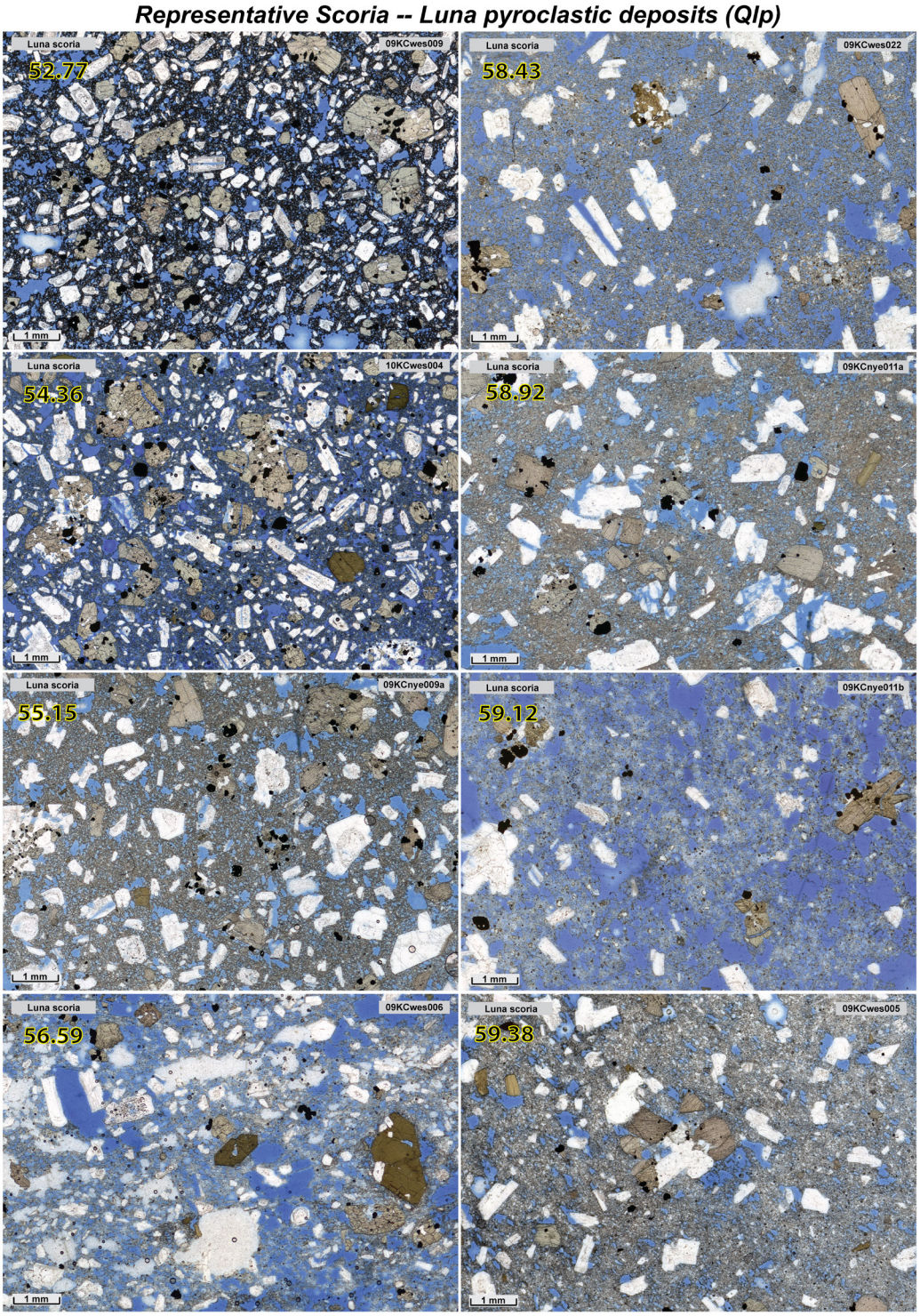

Figure A7.3. Plane-polarized photomicrographs of representative samples of Luna pyroclastic deposits (Qlp).

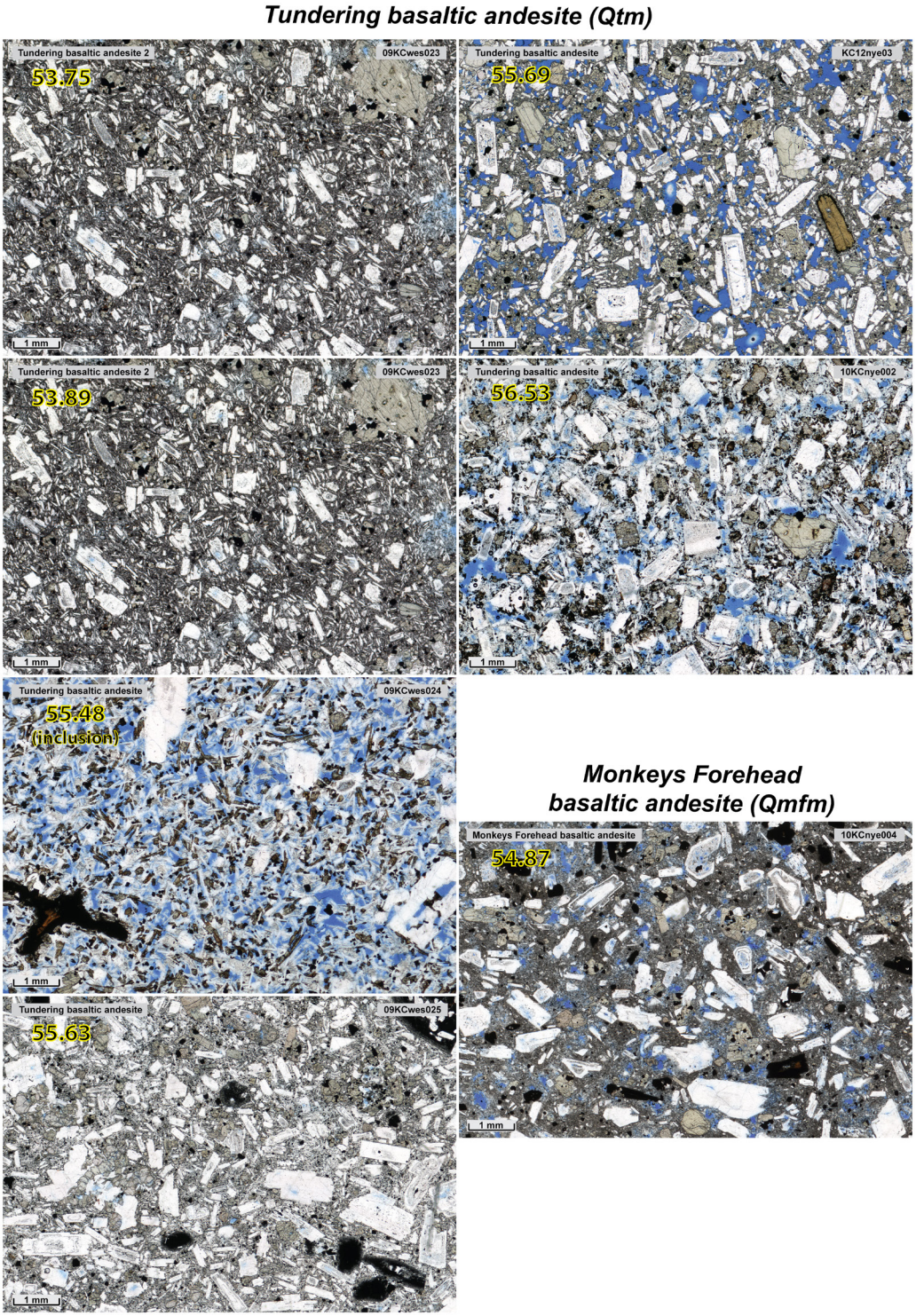

Figure A7.4. Plane-polarized photomicrographs of samples of Tundering basaltic andesite (Qtm) and Monkeys Forehead basaltic andesite (Qmfm).

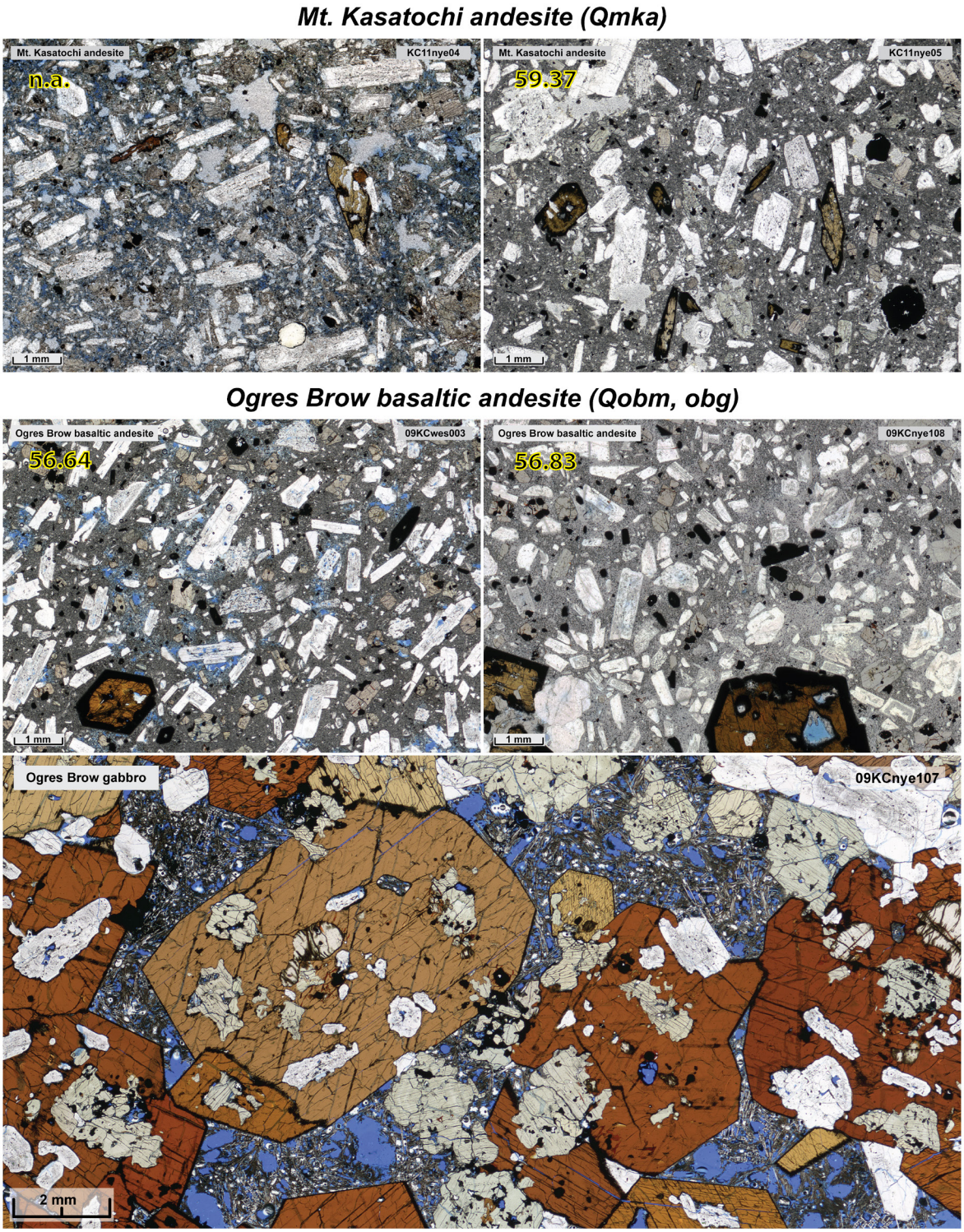

Figure A7.5. Plane-polarized photomicrographs of samples of Mount Kasatochi andesite (Qmka), Ogres Brow basaltic andesite (Qobm), and a gabbroic inclusion in Ogres Brow basaltic andesite (Qobg).

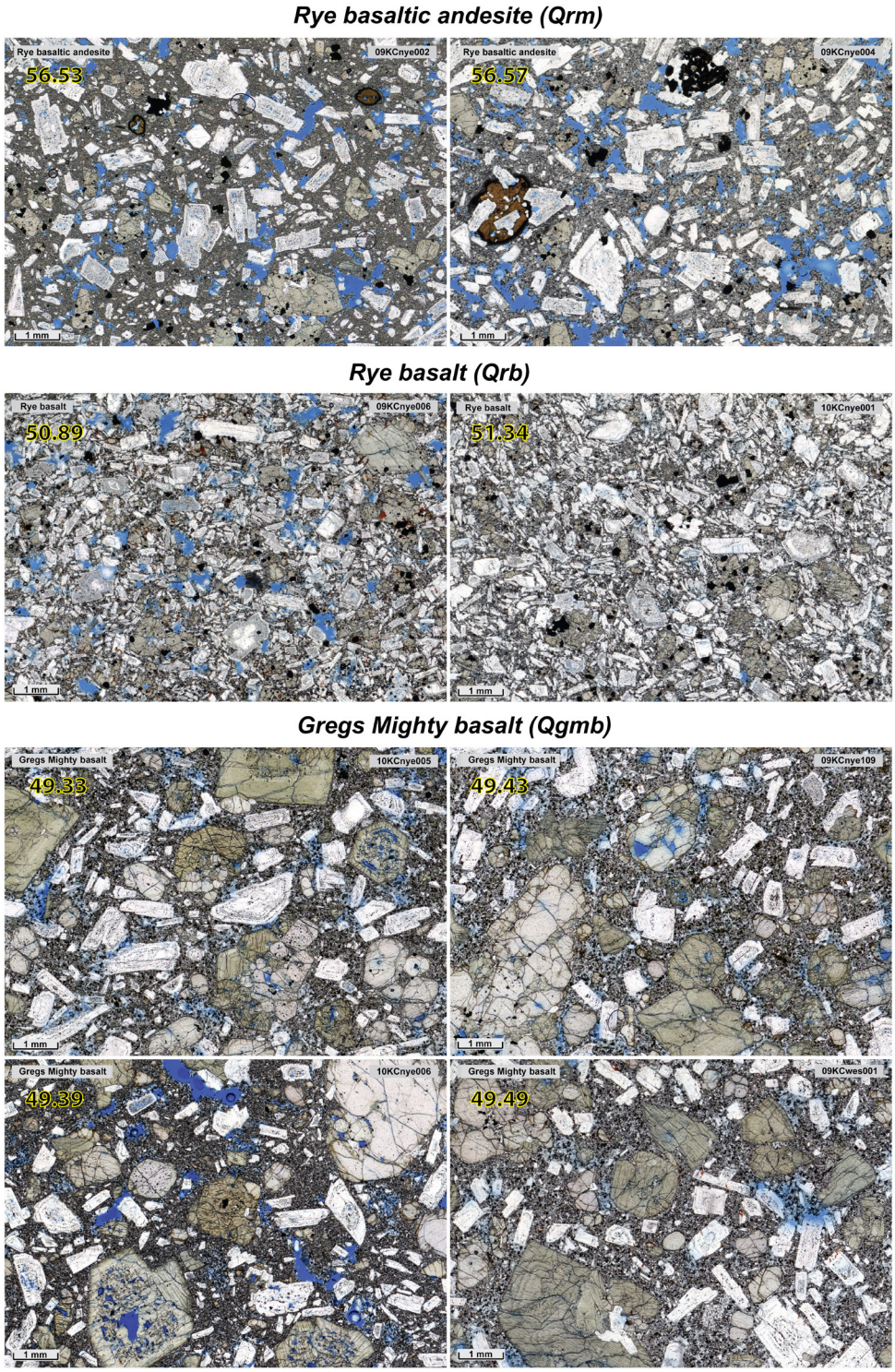

Figure A7.6. Plane-polarized photomicrographs of samples of Rye basaltic andesite (Qrm), Rye basalt (Qrb), and Gregs Mighty basalt (Qgmb).

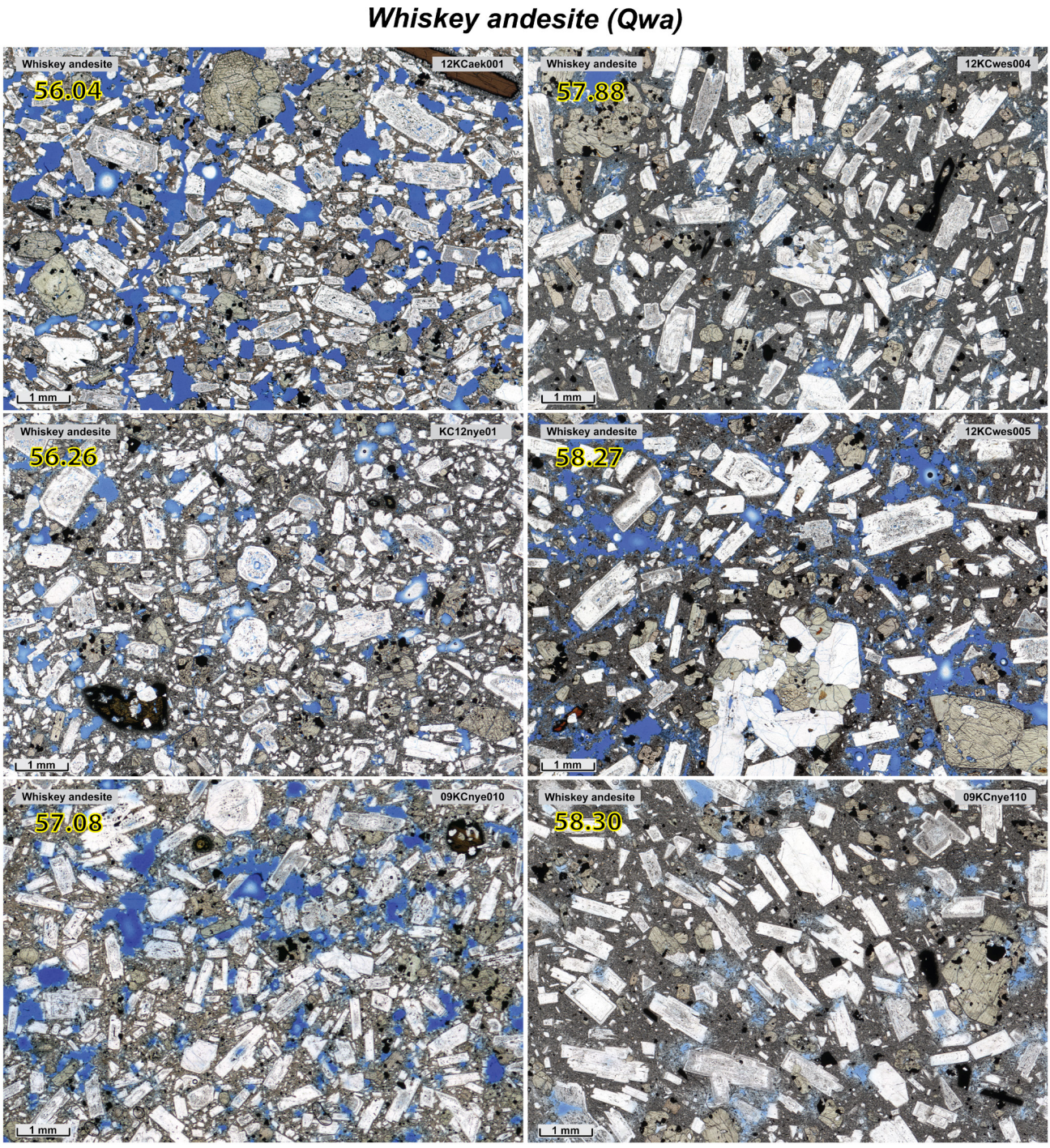

Figure A7.7. Plane-polarized photomicrographs of samples of Whiskey andesite (Qwa).

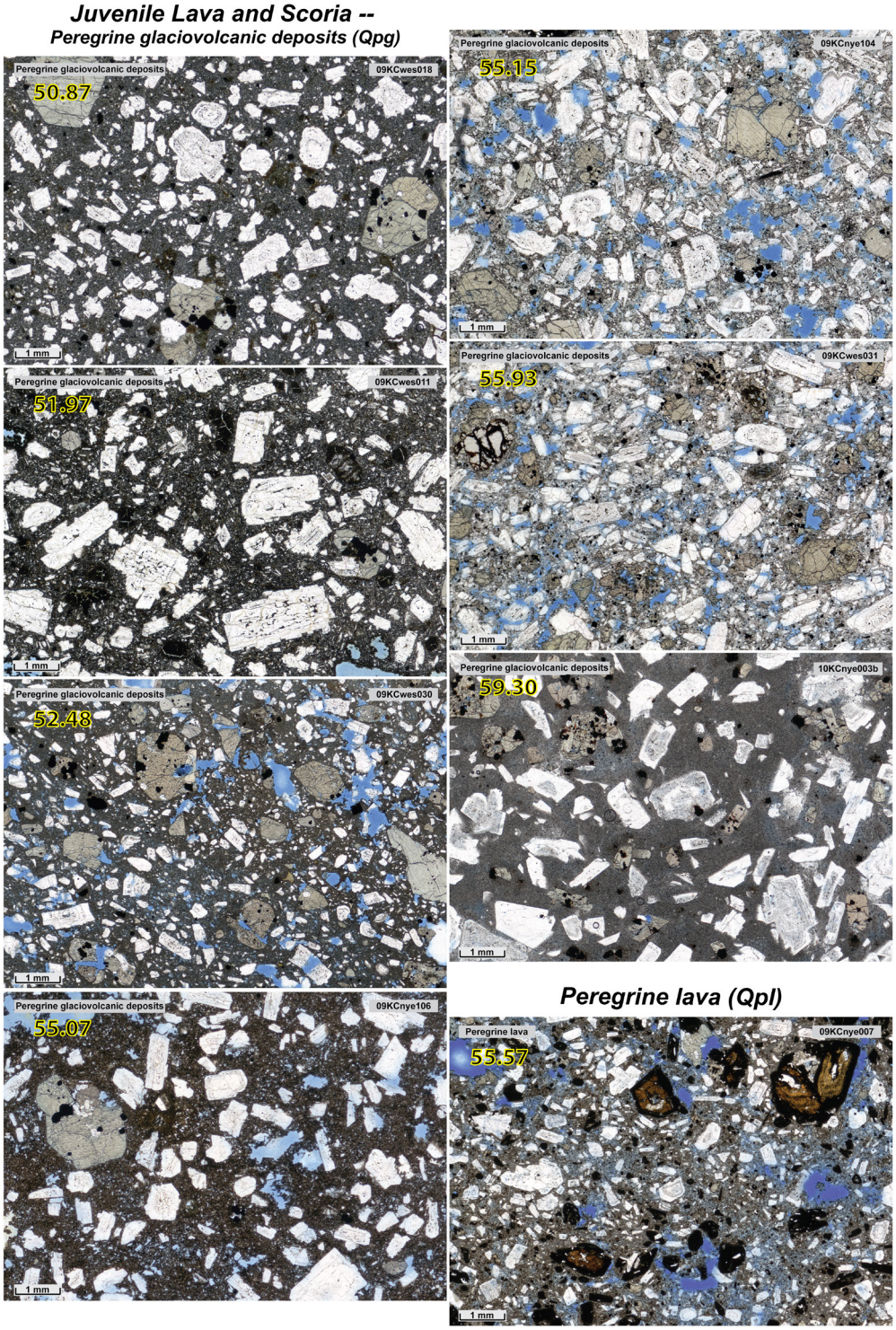

Figure A7.8. Plane-polarized photomicrographs of juvenile clasts in Peregrine glaciovolcanic deposits (Qpg) and Peregrine lava (Qpl) samples.

Lithic fragments in 2008 pyroclastic deposits (Q8p)

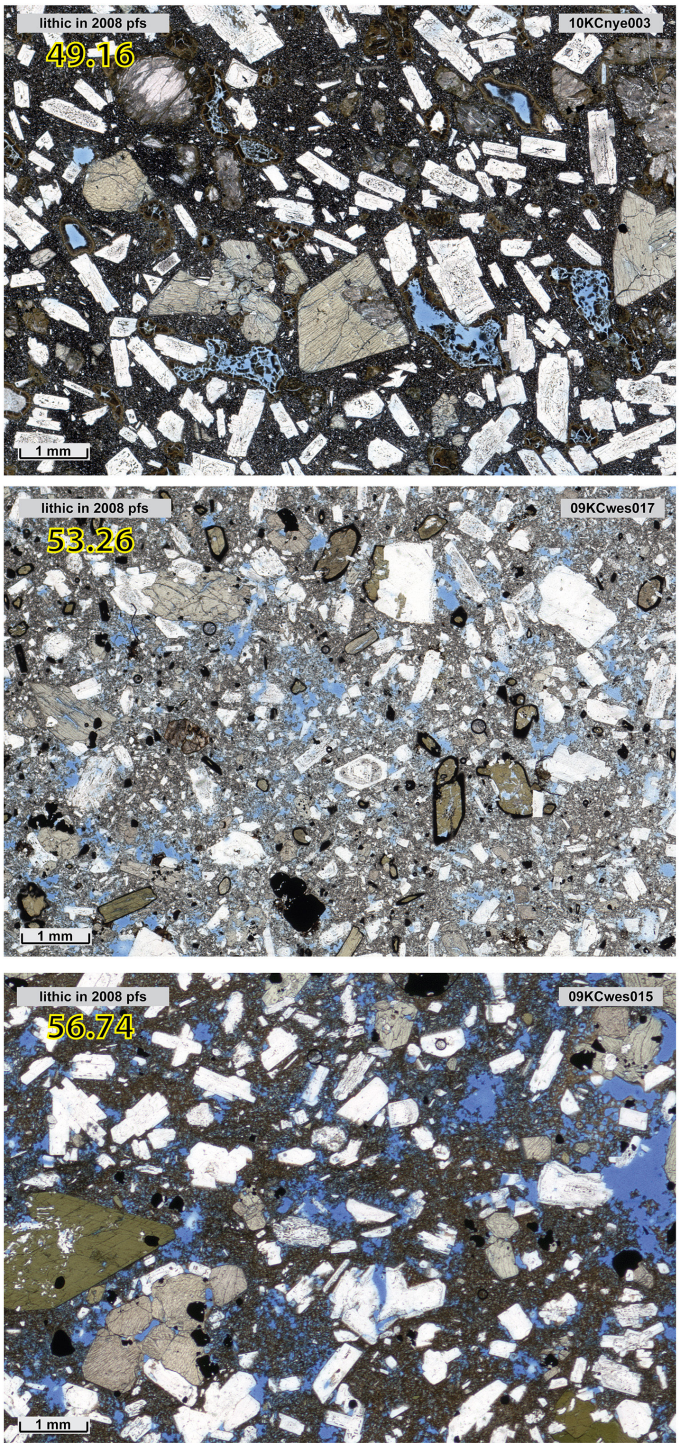

Figure A7.9. Plane-polarized photomicrographs of lithic clasts in 2008 pyroclastic deposits derived from pre-existing portions of the volcanic edifice.

APPENDIX 8. MINERAL COMPOSITIONS

APPENDIX 8A. DATA SUMMARY

Table A8. Numbers of points analyzed by sample and phase. Quench plagioclase microlites from basalt in and on Ogres Brow and 2008 gabbros are denoted by ".micro".

Key#	Unit	SID	Plagioclase		Olivine		Clinopyroxene		Orthpyroxene		Amphibole		Oxide	Glass	**Total**
			Core	Rim	Core	Rim	Core	Rim	Core	Rim	Core	Rim			
7	Q8p.j,ba	10KCON03-2	48	48	--	--	5	--	4	--	6	--	7	21	**139**
11	Q8p.j,ba	10KCON18-1	50	50	--	--	6	--	7	--	11	--	8	22	**154**
17	Q8p.j,a	10KCON09-1	42	42	--	--	5	--	5	--	9	--	--	30	**133**
26	Q8p.j,a	10KCON07-1	49	49	--	--	9	--	11	--	2	--	9	21	**150**
33	Q8p.j,bnd	08CW002-1C	--	--	--	--	--	--	--	--	--	--	--	20	**20**
35	Q8p.gg	09KCnye003m	17	--	--	--	--	--	--	--	--	--	--	--	**17**
37	Q8p.gg	09KCnye012a2m	6	--	--	--	--	--	--	--	--	--	--	--	**6**
43	Q8p.gab	09KCnye001b	--	--	--	--	2	--	--	--	5	--	--	--	**7**
46	Q8p.gab	09KCnye003	35	33	--	--	43	40	--	--	15	15	--	--	**181**
47	Q8p.gab	09KCnye012a2	29	29	11	7	42	39	--	--	19	16	--	--	**192**
51	Q8p.gab.na	09KCnye100	31	31	--	--	38	38	--	--	35	34	--	--	**207**
60	Qlp	09KCwes009	35	35	--	--	43	43	10	9	--	--	--	--	**175**
68	Qlp	09KCwes007	31	31	--	--	16	15	18	20	2	--	--	--	**133**
72	Qlp	09KCwes005	31	31	--	--	25	23	23	23	19	17	--	--	**192**
74	Qtm	09KCwes019	39	37	12	13	32	36	2		--	--	--	--	**171**
80	Qmka	KC11nye05	38	36	--	--	20	16	23	23	29	--	--	--	**185**
83	Qobg	09KCnye107	31	31	1	1	43	43			29	--	--	--	**179**
83.5	Qobg.g	09KCnye107m	42	--	--	--	--	--	--	--	--	--	--	--	**42**
84	Qrm	09KCnye002	36	37	--	--	29	33	15	14	2	--	--	--	**166**
91	Qwa	09KCnye010	34	34	--	--	30	28	13	10	2	--	--	--	**151**
94	Qwa	09KCnye110	34	33	--	--	22	25	18	13	--	--	--	--	**145**
95	Qgmb	10KCnye005	36	34	45	37	35	34			--	--	--	--	**221**
99	Qpl	09KCnye007	42	42	--	--	36	37	1		15	--	--	--	**173**
102	Qpg	09KCwes030	38	38	--	--	29	29	17	16	7	6	--	--	**180**
108	08l	10KCnye003	37	36	5	--	41	40	--	--	--	--	--	--	**159**
		Total	**811**	**737**	**74**	**58**	**551**	**519**	**167**	**128**	**207**	**88**	**24**	**114**	**3478**

APPENDIX 8B. PLOT OF COMPOSITIONS

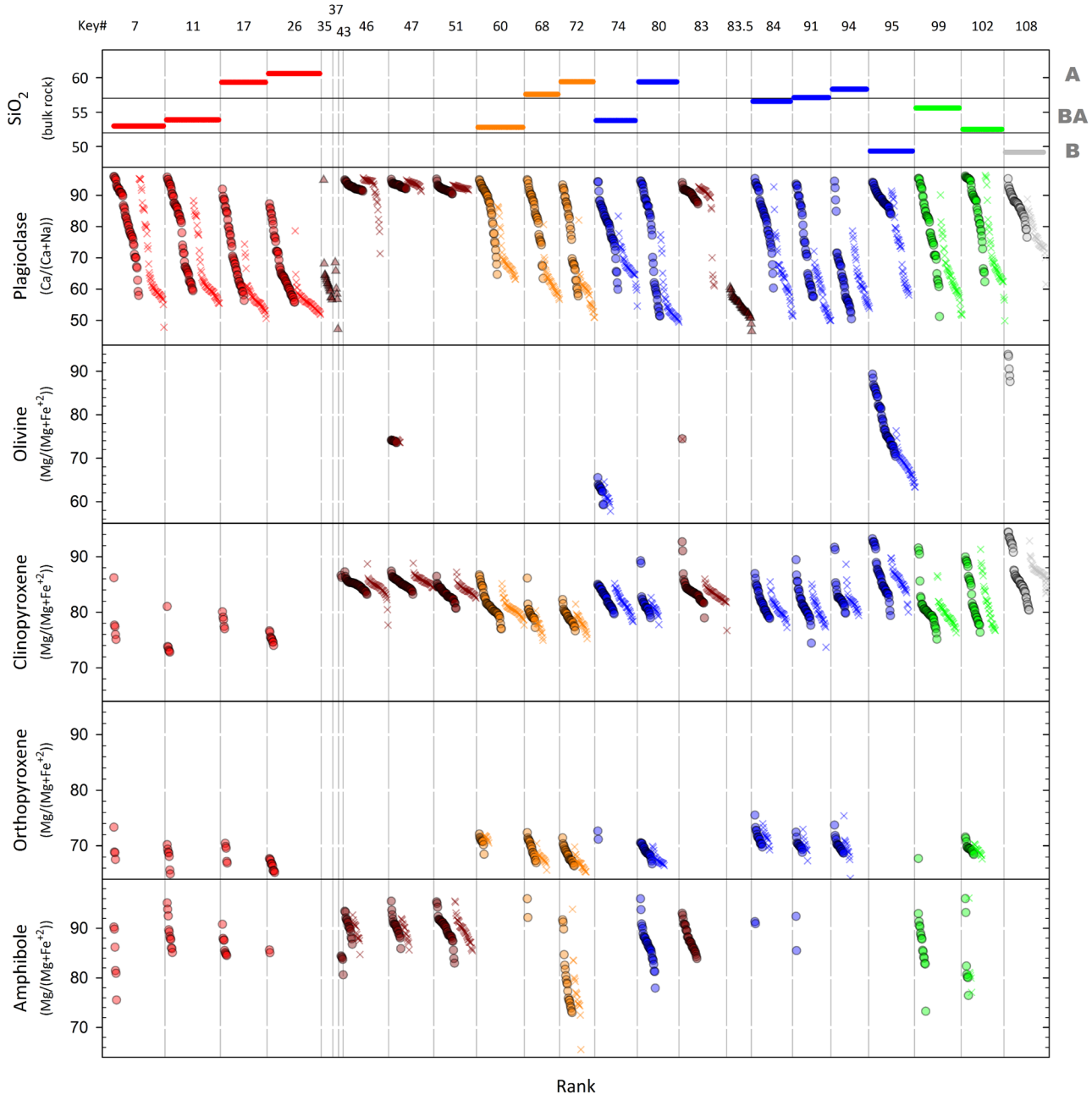

Figure A8. Mineral analyses by sample and rank. "Key#" cross references with table A8a, providing a key to sample identification numbers and map units. Symbols: circles = phenocryst cores; X's = phenocryst rims; triangles = plagioclase microlites in basalt in and on 2008 and Ogres Brow gabbros. Colors: red = 2008 pyroclastic deposits; dark red = gabbros; orange = Luna pyroclastic deposits; blue = lava units; green = Peregrine units; and gray = a lithic fragment entrained in 2008 deposits. Whole-rock SiO_2 for each sample is in the top panel, and the letters A, BA, and B indicate andesite, basaltic andesite, and basalt.

8C. ANALYTICAL DETAILS

Microprobe detection limits (wt%)

	Element											
	SiO_2	TiO_2	Al_2O_3	FeO	MnO	MgO	CaO	Na_2O	K_2O	Cr_2O_3	NiO	Cl
Amphibole	0.0685	0.2202	0.0472	0.1274	0.1485	0.0497	0.0448	0.0566	0.0325	n.a.	n.a.	0.0320
Pyroxene	0.0414	0.0264	0.0269	0.0949	0.0769	0.0304	0.0255	0.0232	n.a.	0.0830	n.a.	n.a.
Olivine	0.0300	n.a.	n.a.	0.0373	0.0220	0.0265	0.0070	n.a.	n.a.	n.a.	0.0267	n.a.
Plagioclase	0.0941	n.a.	0.0624	0.0875	n.a.	n.a.	0.0364	0.0324	0.0398	n.a.	n.a.	n.a.

Detection limits are the calculated concentration at three standard deviations above background.
n.a., not analyzed

Analytical Conditions for Electron Microprobe Analyses

Analytical conditions for analyses of solid phases by wavelength-dispersive X-ray spectrometry via electron microprobe.
Analytical uncertainty (2 standard deviations) was calculated from repeated measurements of the indicated working standard.

Plagioclase

Instrument	Date	Intensity Correction	Accelerating Voltage	Beam Current	Beam Size	Working Standard
UAF/AIL CAMECA SX-50	25-28 May, 2012	ZAF (Armstrong-Love/Scott)	15 kV	10 nA	Focused	Lake Co. Labradorite - USNM 115900

Element	Counting Time (Peak)	Counting Time (Low Background)	Counting Time (High Background)	Uncertainty (2σ) (Absolute, wt. %)	Uncertainty (2σ) (Relative %)	Calibration Standard
SiO_2	15 s	7.5 s	7.5 s	1	1	Wollastonite (C.M. Taylor)
Al_2O_3	15 s	7.5 s	7.5 s	0.3	1.1	Anorthite - USNM 137041
FeO	50 s	15 s	15 s	0.10	22.32	Orthoclase (C.M. Taylor)
CaO	15 s	7.5 s	7.5 s	0.2	1.8	Anorthite - USNM 137041
Na_2O	50 s	15 s	15 s	0.1	3.6	Orthoclase (C.M. Taylor)
K_2O	15 s	7.5 s	7.5 s	0.07	32.09	Amelia Albite (C.M. Taylor)

Olivine

Instrument	Date	Intensity Correction	Accelerating Voltage	Beam Current	Beam Size	Working Standard
UAF/AIL CAMECA SX-50	6 June, 2012	ZAF (Armstrong-Love/Scott)	20 kV	50 nA	Focused	San Carlos Olivine - USNM 1113127444

Element	Counting Time (Peak)	Counting Time (Low Background)	Counting Time (High Background)	Uncertainty (2σ) (Absolute, wt. %)	Uncertainty (2σ) (Relative %)	Calibration Standard
SiO_2	20 s	10 s	10 s	0.3	0.8	Ney Co. Cr-Augite - NMNH 164905
Cr_2O_3	30 s	10 s	10 s	0.02	77.58	Chromite-55
FeO	15 s	7.5 s	7.5 s	0.2	1.6	Rockport Fayalite - USNM 85276
NiO	20 s	10 s	10 s	0.05	13.75	San Carlos Olivine - USNM 1113127444
MnO	20 s	10 s	10 s	0.02	13.79	Sepessartine SPGA (C.M. Taylor)
MgO	20 s	10 s	10 s	0.7	1.4	Olivine (C.M. Taylor)
CaO	50 s	25 s	25 s	0.01	14.93	San Carlos Olivine - USNM 1113127444

Clinopyroxene

Instrument	Date	Intensity Correction	Accelerating Voltage	Beam Current	Beam Size	Working Standard
UAF/AIL CAMECA SX-50	17-21 May 2012	ZAF (Armstrong-Love/Scott)	15 kV	30 nA	Focused	Ney Co. Cr-Augite - NMNH 164905

Element	Counting Time (Peak)	Counting Time (Low Background)	Counting Time (High Background)	Uncertainty (2σ) (Absolute, wt. %)	Uncertainty (2σ) (Relative %)	Calibration Standard
SiO_2	15 s	7.5 s	7.5 s	0.4	0.9	Diopside - USNM 117733
TiO_2	20 s	10 s	10 s	0.03	6.80	Sphene (C.M. Taylor)
Al_2O_3	20 s	10 s	10 s	0.1	1.6	Kakanui Augite - USNM 122142
Cr_2O_3	10 s	5 s	5 s	0.1	15.3	Chromite-55
FeO	10 s	5 s	5 s	0.3	7.2	Rockport Fayalite - USNM 85276
MnO	10 s	5 s	5 s	0.08	57.06	Rockport Fayalite - USNM 85276
MgO	15 s	7.5 s	7.5 s	0.3	1.6	Diopside - USNM 117733
CaO	15 s	7.5 s	7.5 s	0.2	0.9	Kakanui Augite - USNM 122142
Na_2O	20 s	10 s	10 s	0.04	5.04	Kakanui Augite - USNM 122142

Orthopyroxene

Instrument	Date	Intensity Correction	Accelerating Voltage	Beam Current	Beam Size	Working Standard
UAF/AIL CAMECA SX-50	17-21 May 2012	ZAF (Armstrong-Love/Scott)	15 kV	30 nA	Focused	Hypersthene - USNM 746

Element	Counting Time (Peak)	Counting Time (Low Background)	Counting Time (High Background)	Uncertainty (2σ) (Absolute, wt. %)	Uncertainty (2σ) (Relative %)	Calibration Standard
SiO_2	15 s	7.5 s	7.5 s	0.9	1.6	Ney Co. Cr-Augite - NMNH 164905
TiO_2	20 s	10 s	10 s	0.05	33.13	Hypersthene - USNM 746
Al_2O_3	20 s	10 s	10 s	0.1	8.9	Hypersthene - USNM 746
Cr_2O_3	10 s	5 s	5 s	0.1	12.9	Chromite-55
FeO	10 s	5 s	5 s	1.1	7.2	Rockport Fayalite - USNM 85276
MnO	10 s	5 s	5 s	0.10	20.42	Rockport Fayalite - USNM 85276
MgO	15 s	7.5 s	7.5 s	0.7	2.6	Garnet - USNM 87375
CaO	15 s	7.5 s	7.5 s	0.08	5.51	Hypersthene - USNM 746
Na_2O	20 s	10 s	10 s	0.03	92.76	Amelia Albite (C.M. Taylor)

Amphibole

Instrument	Date	Intensity Correction	Accelerating Voltage	Beam Current	Beam Size	Working Standard
UAF/AIL CAMECA SX-50	1-2 June, 2012	ZAF (Armstrong-Love/Scott)	15 kV	10 nA	Focused	Arenal Hornblende - USNM 111356

Element	Counting Time (Peak)	Counting Time (Low Background)	Counting Time (High Background)	Uncertainty (2σ) (Absolute, wt. %)	Uncertainty (2σ) (Relative %)	Calibration Standard
SiO_2	25 s	10 s	10 s	0.6	1.5	San Carlos Olivine - USNM 1113127444
TiO_2	10 s	5 s	5 s	0.5	37.6	Sphene (C.M. Taylor)
Al_2O_3	25 s	10 s	10 s	0.4	2.3	Arenal Hornblende - USNM 111356
FeO	15 s	7.5 s	7.5 s	0.9	8.4	Synthetic Almandine
MnO	10 s	5 s	5 s	0.2	95.6	Willimite (C.M. Taylor)
MgO	25 s	10 s	10 s	0.3	2.1	San Carlos Olivine - USNM 1113127444
CaO	10 s	5 s	5 s	0.3	2.4	Sphene (C.M. Taylor)
Na_2O	25 s	10 s	10 s	0.09	4.59	Orthoclase (C.M. Taylor)
K_2O	15 s	7 s	7 s	0.05	21.68	Orthoclase (C.M. Taylor)

APPENDIX 8D. MICROPROBE DATA

Microprobe data are in the electronic supplement as a current Microsoft Excel spreadsheet (A8d_microprobe_analyses.xlsx) and as comma-separated value file (Table_A8d_microprobe_analyses_v3.csv). All data are given as analyzed oxides, calculated atomic proportions, and derived mineral parameter values in a single sheet 67 columns wide and 3,484 rows long.

APPENDIX 9. COMPONENTRY OF 2008 PYROCLASTIC DEPOSITS

Lithology, size and density componentry data were collected from two composite stratigraphic sections through 2008 Unit 2 and Unit 3 pyroclastic deposits. In the section collected in 2010 about a hundred clasts were counted of both juvenile scoria and lithic clasts. These data provide a robust estimate of the lithic content, which comprises about 70% of the deposit, but a much less robust estimate of the proportions of the different juvenile lithologies because of their lower abundance. In the section collected in 2011 between 35 and 90 juvenile clasts were counted, but lithics were cavalierly tossed aside. This results in much more precise estimates of the relative proportions of juvenile lithologies.

Electronic copies of componentry data are in electronic supplement E9 as current Microsoft Excel (.xlsx) and comma separated value (.csv) files.

APPENDIX 9A. LITHOLOGIC COMPONENTS

Table A9a. Clast counts from composite stratigraphic sections through Units 2 and 3 of 2008 pyroclastic deposits. All componentry determined using clasts from the -4 phi (16-32mm) size fraction.

								number of clasts						% of clasts				
Sample	**Subsample**	**Type**	**Unit**	**Relative Strat. Pos.**	**Purpose**	**N (°)**	**E (°)**	**White**	**Banded**	**Brown**	**Gabbro**	**Lithic**	**Total Clasts**	**White**	**Banded**	**Brown**	**Gabbro**	**Lithic**
2011 samples. Counts of 35 to 90 juvenile clasts.																		
11KCON16	N/A	Pumice separate	Unit 3/22	16 (Top)	Pumice separate for componentry, densitry, permeability. -4phi and some bigger	52.167240	-175.529370	21	23	28	0	N/A	72	29.2%	31.9%	38.9%	0.0%	N/A
11KCON17	N/A	Pumice separate	Unit 3/20	15	Pumice separate for componentry, densitry, permeability. -4phi and some bigger	52.167240	-175.529370	51	11	28	0	N/A	90	56.7%	12.2%	31.1%	0.0%	N/A
11KCON18	N/A	Pumice separate	Unit 3/16	14	Pumice separate for componentry, densitry, permeability. -4phi and some bigger	52.167240	-175.529370	12	23	21	1	N/A	57	21.1%	40.4%	36.8%	1.8%	N/A
11KCON06	A	Pumice separate	Unit 3/14	13	Pumice separate for componentry, densitry, permeability. 06A = -4phi, 06B = >-5phi	52.170780	-175.530500	1	21	49	0	N/A	71	1.4%	29.6%	69.0%	0.0%	N/A
11KCON13	N/A	Pumice separate	Unit 3/12	12	Pumice separate for componentry, densitry, permeability. -4phi and some bigger	52.167730	-175.529850	1	9	60	0	N/A	70	1.4%	12.9%	85.7%	0.0%	N/A
11KCON11	N/A	Pumice separate	Unit 3/10	11	Pumice separate for componentry, densitry, permeability. No pumice >-4phi	52.172710	-175.530270	0	28	26	0	N/A	54	0.0%	51.9%	48.1%	0.0%	N/A
11KCON10	A	Pumice separate	Unit 3/9	10	Pumice separate for componentry, densitry, permeability. 10A = -4phi, 10B = >-5phi.	52.172710	-175.530270	0	7	51	0	N/A	58	0.0%	12.1%	87.9%	0.0%	N/A
11KCON01	A	Pumice separate	Unit 3/7	9	Pumice separate for componentry, densitry, permeability. 01A = -4phi, 01B = >-5phi	52.172710	-175.530270	1	25	37	0	N/A	63	1.6%	39.7%	58.7%	0.0%	N/A
11KCON09	N/A	Pumice separate	Unit 3/5	8	Pumice separate for componentry, densitry, permeability. ~30 clasts (later is ~all lithics)	52.172710	-175.530270	7	26	2	0	N/A	35	20.0%	74.3%	5.7%	0.0%	N/A
11KCON02	A	Pumice separate	Unit 3/4	7	Pumice separate for componentry, densitry, permeability. 02A = -4phi, 02B = >-5phi	52.172710	-175.530270	57	21	0	1	N/A	79	72.2%	26.6%	0.0%	1.3%	N/A
11KCON08	N/A	Pumice separate	Unit 3/4	6	Pumice separate for componentry, densitry, permeability. 08A = -4phi, 08B = >-5phi. Supplements 11KCON02	52.172710	-175.530270	26	8	2	0	N/A	36	72.2%	22.2%	5.6%	0.0%	N/A
11KCON19	A	Pumice separate	Unit 2 (top)	5	Pumice separate for componentry, densitry, permeability. 19A = -4phi, 19B = >-5phi.	52.169219	-175.530430	13	33	16	0	N/A	62	21.0%	53.2%	25.8%	0.0%	N/A
11KCON20	A	Pumice separate	Unit 2 (top - 1m)	4	Pumice separate for componentry, densitry, permeability. 20A = -4phi, 20B = >-5phi.	52.169219	-175.530430	15	30	17	0	N/A	62	24.2%	48.4%	27.4%	0.0%	N/A
11KCON15	N/A	Pumice separate	Unit 2 (+3.5m)	3	Pumice separate for componentry, densitry, permeability. -4phi and some bigger	52.174870	-175.529330	60	6	0	0	N/A	66	90.9%	9.1%	0.0%	0.0%	N/A
11KCON07	A	Pumice separate	Unit 2 (+10cm)	2	Pumice separate for componentry, densitry, permeability. 07A = -4phi, 07B = >-5phi	52.174870	-175.529330	60	5	1	0	N/A	66	90.9%	7.6%	1.5%	0.0%	N/A
11KCON14	A	Pumice separate	Unit 2 (+0cm)	1 (Bottom)	Pumice separate for componentry, densitry, permeability. 14A = -4phi, 14B = >-5phi.	52.174870	-175.529330	61	8	0	0	N/A	69	88.4%	11.6%	0.0%	0.0%	N/A
													average (2011)	36.9%	30.2%	32.6%		
													1 sd (2011)	35.47%	19.67%	30.41%		

Table A9a. Clast counts from composite stratigraphic sections through Units 2 and 3 of 2008 pyroclastic deposits (cont'd).

								number of clasts						% of clasts				
Sample	**Subsample**	**Type**	**Unit**	**Relative Strat. Pos.**	**Purpose**	**N (°)**	**E (°)**	**White**	**Banded**	**Brown**	**Gabbro**	**Lithic**	**Total Clasts**	**White**	**Banded**	**Brown**	**Gabbro**	**Lithic**
2010 samples. Counts of about 100 total clasts per sample. Samples are dominated by lithic clasts, thus counts of juvenile lithologies are low and imprecise.																		
10KCON04	N/A	~3Kg Bag	Unit 3	12 (Top)	Density/Componentry/Grain Size on upper, more pumiceous part of this Unit 3 section.	52.167030	-175.492260	18	1	18	2	46	85	21.2%	1.2%	21.2%	2.4%	54.1%
10KCON21	N/A	~3Kg Bag	Unit 3	11	Density/Componentry/Grain Size of the lower part of Unit 3 taken from up higher on the volcano.	52.162220	-175.510090	2	0	17	3	68	90	2.2%	0.0%	18.9%	3.3%	75.6%
10KCON16	N/A	~3Kg Bag	Unit 3	10	Density/Componentry/Grain Size on the upper massive PF section.	52.168840	-175.531140	1	2	4	5	88	100	1.0%	2.0%	4.0%	5.0%	88.0%
10KCON15	N/A	~3Kg Bag	Unit 3	9	Density/Componentry/Grain Size on lithic-rich layer between upper massive PF and upper massive PF.	52.168840	-175.531140	3	3	12	8	75	101	3.0%	3.0%	11.9%	7.9%	74.3%
10KCON11	N/A	~3Kg Bag	Unit 3	8	Density/Componentry/Grain Size on the upper part of the low, massive PF - seems to be finer/more pumiceous than the rest of the lower section?	52.168840	-175.531140	17	1	18	0	22	58	29.3%	1.7%	31.0%	0.0%	37.9%
10KCON10	N/A	~3Kg Bag	Unit 3	7	Density/Componentry/Grain Size on a massive PF near the base of the Unit 3 sequence.	52.168840	-175.531140	12	0	9	0	85	106	11.3%	0.0%	8.5%	0.0%	80.2%
10KCON22	N/A	~3Kg Bag	Unit 3	6	Density/Componentry/Grain Size of lower part of Unit 3 section from the SW cliffs.	52.168090	-175.492460	10	0	3	0	77	90	11.1%	0.0%	3.3%	0.0%	85.6%
10KCON05	N/A	~3Kg Bag	Unit 3	5	Density/Componentry/Grain Size on lower more lithic-rich part of this Unit 3 section.	52.167030	-175.492260	0	0	2	0	100	102	0.0%	0.0%	2.0%	0.0%	98.0%
10KCON20	N/A	~3Kg Bag	Unit 2	4	Density/Componentry/Grain Size on the upper part of the much-thicker western Unit 2 section.	52.170110	-175.521010	11	9	10	0	72	102	10.8%	8.8%	9.8%	0.0%	70.6%
10KCON01	N/A	~3Kg Bag	Unit 2	3	Density/Componentry/Grain Size on massive Unit 2 PF layers near the top of Unit 2 section.	52.175100	-175.493100	10	4	7	0	80	101	9.9%	4.0%	6.9%	0.0%	79.2%
10KCON02	N/A	~3Kg Bag	Unit 2	2	Density/Componentry/Grain Size on massive Unit 2 PF layers nearer to the bottom of the section - NOTE: originally took 2 samples of this because I believed there was a contact - that may have been the water table, not a deposit contact.	52.175100	-175.493100	16	6	8	0	70	100	16.0%	6.0%	8.0%	0.0%	70.0%
10KCON06	N/A	~3Kg Bag	Unit 2	1 (Bottom)	Density/ComponentyGrain Size on the bottom of the massive Unit 2 section.	52.180460	-175.498730	71	2	8	0	23	104	68.3%	1.9%	7.7%	0.0%	22.1%
																	average (2010)	70%
																	1 sd (2010)	22%

APPENDIX 9B. CLAST-SIZE DISTRIBUTION

Table A9b. Particle-size distribution of samples from 2008 Units 2 and 3 pyroclastic deposits.

Grain Size (phi)	10KCON06	10KCON02	10KCON01	10KCON20	10KCON05	10KCON22	10KCON10	10KCON11	10KCON15	10KCON16	10KCON21	10KCON04
Total Mass (g)												
-6	0	0	0	0	0	0	0	0	0	614	0	0
-5	134	222	349	0	1507	457	691	50	578	110	0	0
-4	109	93	260	79	521	145	334	80	953	186	55	57
-3	130	285	250	291	405	178	322	65	682	254	149	133
-2	183	307	248	335	247	206	280	167	424	281	184	184
-1	204	333	257	338	255	228	288	214	336	317	251	249
0	250	343	259	338	273	264	317	253	310	356	282	305
1	243	438	313	394	340	347	437	238	266	390	425	435
2	428	483	338	405	370	416	451	462	203	405	331	584
3	153	269	169	209	184	243	221	188	95	240	115	338
4	202	247	126	152	134	182	184	143	69	205	80	312
<4	450	434	180	173	82	131	203	244	61	149	88	205
Total	2486	3454	2749	2714	4318	2797	3728	2104	3977	3507	1960	2802
Mass%												
-6	0.0	0.0	0.0	0.0	0.0	0.0	0.0	0.0	0.0	17.5	0.0	0.0
-5	5.4	6.4	12.7	0.0	34.9	16.3	18.5	2.4	14.5	3.1	0.0	0.0
-4	4.4	2.7	9.5	2.9	12.1	5.2	9.0	3.8	24.0	5.3	2.8	2.0
-3	5.2	8.3	9.1	10.7	9.4	6.4	8.6	3.1	17.1	7.2	7.6	4.7
-2	7.4	8.9	9.0	12.3	5.7	7.4	7.5	7.9	10.7	8.0	9.4	6.6
-1	8.2	9.6	9.3	12.5	5.9	8.2	7.7	10.2	8.4	9.0	12.8	8.9
0	10.1	9.9	9.4	12.5	6.3	9.4	8.5	12.0	7.8	10.2	14.4	10.9
1	9.8	12.7	11.4	14.5	7.9	12.4	11.7	11.3	6.7	11.1	21.7	15.5
2	17.2	14.0	12.3	14.9	8.6	14.9	12.1	22.0	5.1	11.5	16.9	20.8
3	6.2	7.8	6.1	7.7	4.3	8.7	5.9	8.9	2.4	6.8	5.9	12.1
4	8.1	7.2	4.6	5.6	3.1	6.5	4.9	6.8	1.7	5.8	4.1	11.1
<4	18.1	12.6	6.5	6.4	1.9	4.7	5.4	11.6	1.5	4.2	4.5	7.3
Unit	**2**	**2**	**2**	**2**	**3**	**3**	**3**	**3**	**3**	**3**	**3**	**3**
Relative StratIgraphic Position	**Bottom**	**2**	**3**	**4**	**5**	**6**	**7**	**8**	**9**	**10**	**11**	**Top**

APPENDIX 9C. DENSITY OF JUVENILE SCORIA

Table A9c. Clast density measured after Houghton and Wilson (1989), using clasts from the-4 phi (16-32mm) size fraction, wrapped in parafilm.

			# of Clasts Per Density Bin (kg m^{-3})																					
Sample	**Unit**	**Relative Stratigraphic Position**	**500**	**600**	**700**	**800**	**900**	**1000**	**1100**	**1200**	**1300**	**1400**	**1500**	**1600**	**1700**	**1800**	**1900**	**2000**	**2100**	**2200**	**2300**	**2400**	**2500**	**>2500**	**total**
11KCON16	Unit 3/22	16 (Top)	0	0	0	0	0	0	1	0	4	6	5	6	4	5	8	10	10	1	6	3	3	0	72
11KCON17	Unit 3/20	15	0	0	2	6	2	7	15	6	9	4	3	3	4	3	8	5	4	1	1	4	2	1	90
11KCON18	Unit 3/16	14	0	0	0	0	0	2	2	1	2	2	3	4	2	4	6	3	4	7	9	3	1	1	56
11KCON06a	Unit 3/14	13	0	0	0	0	0	0	0	0	1	2	0	7	8	18	14	12	5	1	1	2	0	0	71
11KCON13	Unit 3/12	12	0	0	0	0	0	0	1	0	0	0	1	0	11	10	17	11	9	3	0	0	5	2	70
11KCON11	Unit 3/10	11	0	0	0	0	0	0	0	0	0	0	0	0	4	6	14	19	7	2	1	0	0	0	53
11KCON10a	Unit 3/9	10	0	0	0	0	0	0	0	0	0	2	2	3	6	14	10	12	7	1	1	0	0	0	58
11KCON01a	Unit 3/7	9	0	0	0	0	0	0	1	0	0	2	2	6	8	11	15	10	2	1	3	0	0	2	63
11KCON09	Unit 3/5	8	0	0	0	0	0	0	1	0	4	4	3	1	6	6	4	1	2	2	1	0	0	0	35
11KCON02a	Unit 3/4	7	0	0	1	1	6	6	13	16	18	8	4	1	1	1	0	1	0	0	1	0	0	0	78
11KCON08	Unit 3/4	6	0	0	0	1	1	5	4	7	8	4	1	2	1	1	1	0	0	0	0	0	0	0	36
11KCON19a	Unit 2 (top) Unit	5	0	0	0	1	0	6	3	13	8	5	14	4	3	2	2	0	1	0	0	0	0	0	62
11KCON20a	2 (top - 1m) Unit	4	0	0	0	0	1	0	4	9	11	4	11	8	6	4	1	1	0	0	1	0	0	1	62
11KCON15	2 (+3.5m) Unit 2	3	0	0	1	2	6	7	5	6	11	5	7	6	6	3	0	0	1	0	0	0	0	0	66
11KCON07a	(+10cm) Unit 2	2	0	0	2	6	5	13	13	3	7	7	2	6	2	0	0	0	0	0	0	0	0	0	66
11KCON14a	(+0cm)	1 (Bottom)	2	0	1	9	6	10	11	6	7	7	6	2	2	0	0	0	0	0	0	0	0	0	69